TREE RINGS AND OXYGEN ISOTOPES AS CLIMATIC INDICATORS IN THE U.S. PACIFIC NORTHWEST

Karly R. Schmidt-Simard

A dissertation submitted to the faculty at the University of North Carolina at Chapel Hill in partial fulfillment of the requirements for the degree of Doctor of Philosophy in the Department of Geography.

Chapel Hill
2022

Approved by:

Erika K Wise

Adam Z. Csank

Charles Konrad

Diego Riveros-Iregui

Donna Surge

ABSTRACT

Karly R. Schmidt-Simard: Tree Rings and Oxygen Isotopes as Climatic Indicators in the U.S. Pacific Northwest
(Under the direction of Erika K. Wise)

The U.S. Pacific Northwest (PNW) relies on precipitation, much of which falls during the winter and is stored as snowpack until spring, for hydropower that provides over half the region's electricity. Recently, record-breaking heat waves have increased demand for air conditioning while winter snowpack and summer precipitation have decreased, causing a mismatch between hydropower supply and demand. As this mismatch is projected to worsen under climate change, a more complex understanding of seasonal precipitation patterns in the region becomes crucial. Climate proxies provide a means of revealing the nuances of these patterns across space and time.

This dissertation examines three climate proxies and their ability to capture seasonal climate to better understand climate-proxy relationships, identify each proxy's advantages and limitations, and investigate how they may be combined to improve seasonal climate reconstructions in the PNW. I first examine the relationship between oxygen isotope ratios in precipitation at five sites in the U.S. PNW and air mass trajectories to characterize the ways in which these trajectories influence precipitation isotope ratios. I then establish the extent to which annual and subannual (earlywood, latewood, and adjusted latewood) ring-width measurements of trees located near three of the five sites capture seasonal variations in precipitation and temperature. Lastly, I determine the precipitation, temperature, and source water signals captured

by the oxygen isotope ratios stored in the earlywood and latewood of those same trees, which theoretically reflect the precipitation examined as the first proxy.

In this research, I show that oxygen isotope ratios in precipitation in the PNW largely reflect air mass trajectories, but this relationship is complicated by other factors. I demonstrate that subannual tree-ring widths capture temperature and precipitation during the current and prior growing seasons, and I also show that subannual tree-ring isotope ratios strengthen summer climate capture while providing promise for reconstructions of growing-season and winter source water, which are linked with atmospheric circulation. Taken together, these findings demonstrate that subannual tree-ring widths and oxygen isotope ratios capture unique and complementary climate signals, and the combination of these two proxies stands to provide nuanced seasonal climate histories in the U.S. PNW.

To my husband, Etienne; and my parents, Lisa and Arnie: thank you for always believing in me and teaching me to believe in myself.

ACKNOWLEDGEMENTS

As the saying goes, it takes a village—this dissertation would not have been possible without the contributions, big and small, of so many mentors, colleagues, family members, and friends. This is your accomplishment, too.

I first wish to thank my advisor, Dr. Erika Wise, for her guidance, patience, and commitment to mentoring underrepresented students. I would also like to thank the other members of my committee—Drs. Adam Csank, Chip Konrad, Diego Riveros-Iregui, and Donna Surge—for their support and insight. I also thank Adam for his guidance in laboratory techniques at the Desert Research Institute and Donna for our collaborative work. I thank Drs. Melissa Berke (Department of Biological Sciences) and Dana Biasatti (Center for Environmental Science and Technology) at the University of Notre Dame for sharing their time, equipment, and expertise with me to perform my own stable isotope analyses and Dr. Drew Coleman (UNC Earth, Marine and Environmental Sciences) for use of laboratory equipment. I also wish to acknowledge funding support from the UNC Graduate School and Department of Geography, the US Climate Variability and Predictability Program, and the National Science Foundation.

The work you see in this dissertation is the tip of the iceberg of my time spent at UNC, and I am grateful for the transformative opportunities I was given to grow outside of my research. To Drs. Gigi Taylor and Marc Howlett at the UNC Writing & Learning Centers: thank you for your support over the years, providing a voice of reason during hard times, and teaching me how to apply my knowledge and skills to new contexts. To Dr. Dawn Henderson and Phil

Edwards: thank you for teaching me leadership with kindness, compassion, and humanity during our time together at the UNC Center for Faculty Excellence. To my students: thank you for sharing your time and your perspectives with me—learning from you has made me a better educator and a better person.

I also wish to thank everyone who has worked alongside me, both figuratively and literally, as I wrote this dissertation. To my fellow C-TRĒS students—Dr. Angélica Gómez, Dr. Manny Hernandez, and Carl Jurkowski—I am grateful for the years we have been able to grow together as scholars, and I thank you for your feedback and always helping me to see things from different perspectives. A special thanks goes to Dr. Maia Call, Asta Feng, Dr. Alexis Howard, Michelle Padley, and Staci Whiteside, who have always been there when the going gets tough. And to my Accountabilibuddies, especially our fearless leaders, Dr. Farnosh Mazandarani and Stefani Baca-Atlas: going through the dissertation-writing process with you all has been a privilege, and our friendships have been the silver lining on these cloudy pandemic years.

Last but certainly not least, I thank my family. To my mom and dad, Lisa and Arnie Schmidt: thank you for always believing in me and for the sacrifices you have made to get me to this point. You have never let me doubt that I make you proud, and your unconditional support and love have helped me to achieve the education you weren't given the privilege to pursue. And to my husband, best friend, and unrelenting hype man, Etienne Simard: thank you for your unwavering support and commitment, even in my darkest hours, in sickness and in health. You uprooted yourself to build a life with me in a different country so I could do this thing, and for that I will forever be grateful. What a long, strange trip it's been!

TABLE OF CONTENTS

LIST OF TABLES

LIST OF FIGURES

LIST OF ABBREVIATIONS AND SYMBOLS

AM	April-May
AMO	Atlantic multidecadal oscillation
AMSL	Above mean sea level
BI	Blue intensity
DJ	December-January
ENSO	El Niño-Southern Oscillation
EPS	Expressed population signal
EW	Earlywood width
FM	February-March
GHCN	Global Historical Climate Network
GMWL	Global Meteoric Water Line
ITRDB	International Tree-Ring Data Bank
JJAS	June-July-August-September
LW	Latewood width
LW_{adj}	Adjusted latewood
MXD	Maximum latewood density
NADP	National Atmospheric Deposition Program
NARR	North American Regional Reanalysis
NCEP	National Centers for Environmental Prediction
NCAR	National Center for Atmospheric Research
NOAA	National Oceanic and Atmospheric Administration

ON	October-November
PDO	Pacific decadal oscillation
PNA	Pacific/North American
PNW	Pacific Northwest
PRISM	Parameter-elevation Regressions on Independent Slopes Model
R	Pearson correlation coefficient
SMOW	Standard Mean Ocean Water
SOI	Southern Oscillation Index
TRW	Total ring width
USGS	United States Geological Survey
USNIP	United States Network for Isotopes in Precipitation
SLAP	Standard Light Antarctic Precipitation
VSMOW	Vienna Standard Mean Ocean Water
WPI	West Pacific teleconnection index
^{12}C	Carbon-12
^{13}C	Carbon-13
^{16}O	Oxygen-16
^{18}O	Oxygen-18
$\delta^{13}C$	Ratio of ^{13}C:^{12}C
$\delta^{18}O$	Ratio of ^{18}O:^{16}O
$\delta^{18}O_{cellulose}$	Ratio of ^{18}O:^{16}O of tree-ring cellulose
$\delta^{18}O_{EW}$	Ratio of ^{18}O:^{16}O of tree-ring earlywood
$\delta^{18}O_{LW}$	Ratio of ^{18}O:^{16}O of tree-ring latewood

$\delta^{18}O_P$	Ratio of ^{18}O:^{16}O of precipitation
$\delta^{18}O_{SW}$	Ratio of ^{18}O:^{16}O of source water

CHAPTER 1: INTRODUCTION

The Pacific Northwest (PNW, defined here as the U.S. states of Washington, Oregon, and Idaho and the Canadian province of British Columbia) contains a broad range of climates ranging from the rainforests of the Olympic Peninsula to the arid Columbia River Basin thanks to its complex topography (Mote *et al.*, 2014) and the convergence of marine, continental, and arctic air masses (Ferguson, 1999). The region's population depends heavily on hydropower (Bonneville Power Administration, 2019; Electricity Canada, 2012) that is driven primarily by winter precipitation (Hunter *et al.*, 2006), which determines snowpack accumulation that feeds spring streamflow and impacts hydropower generation (U.S. Energy Information Administration, 2021). As recent record-breaking heat waves (Philip *et al.*, 2021) have led to rapidly increasing demand for air conditioning (United States Census Bureau, 2019; Balk, 2021), the region's reliance on hydropower for cooling has continued to increase while the supply of this resource has become more tenuous. Precipitation patterns are already changing in the PNW (Zhang *et al.*, 2021), a trend that is projected to continue under climate change (Hamlet *et al*., 2010; Bartos and Chester, 2015). Summer hydropower shortfalls are projected to increase in a changing climate with intensifying seasonal mismatches between power supply and demand (Turner *et al.*, 2019), making a comprehensive understanding of seasonal precipitation and climate patterns increasingly important in this region. Climate proxies that capture variability in precipitation, temperature, and synoptic-scale climate at a seasonal scale are crucial to refining this understanding, and an in-depth understanding of the factors influencing these proxies is needed to improve their interpretation. To this end, this dissertation examines the relationships between

seasonal climate and three climate proxies— $\delta^{18}O$ values of rainfall, subannual tree-ring width measurements, and subannual $\delta^{18}O$ values of tree cellulose—at three sites in the U.S. PNW across space and time to contribute to this understanding.

Background

Climate proxy data refer to measurements from indirect recorders of climate, such as ice cores, corals, lake and ocean sediment cores, and trees, that can be used to understand past climate when instrumental records are unavailable (NCEI, 2022). Climate reconstructions from proxy data have been determined to provide reliable approximations of past climate within a range of uncertainty (Mann *et al.*, 2005), and tree-ring widths in particular have been used for over a century to approximate past climatic variability (Douglass, 1919). The annual resolution of trees' growth rings along with their widespread distribution and sensitivity to climatic variations make them particularly useful for examining short-term, high-frequency variability (Briffa *et al.*, 1996). Separate measurements of earlywood and latewood widths have also proven to be fruitful for seasonal reconstructions (Meko and Baisan, 2001; Stahle *et al.*, 2009; Griffin *et al.*, 2013; Ziaco *et al.*, 2020), including at sites in the PNW (Dannenberg and Wise, 2016).

Beyond the simple measurement of full and partial ring widths, analytical advances have expanded the tree-ring scientist's toolkit to include metrics such as maximum latewood density (MXD) (e.g., Briffa *et al.*, 1988; D'Arrigo *et al.*, 1992), measurements of blue intensity (BI) (e.g., McCarroll *et al.*, 2002; Buckley *et al.*, 2018), positioning of intra-annual density fluctuations (IADFs) (e.g., Campelo *et al.*, 2007; Vieira *et al*., 2010), and the isotopic composition of whole wood and wood components (primarily of $\delta^{18}O$ and $\delta^{13}C$ values of cellulose) (e.g., Anderson *et al.*, 1998; Saurer *et al.*, 2008; Andreu-Hayles *et al*. 2017). Although

these methods are inherently more cost- and labor-intensive than traditional ring-width measurements, oxygen isotope ratios in particular have been demonstrated to capture climatic variability in regions such as the tropics (Rozendaal and Zuidema, 2011) where ring-width measurements often do not (Jacoby, 1989), and they may also isolate and enhance seasonal climate signals and provide finer-scale climate histories (McCarroll and Loader, 2004 and references therein).

Because trees' primary moisture source is meteoric water, they generally provide a representation of the isotopic composition of precipitation within the cellulose they produce from this water (Edwards and Fritz, 1986; Reynolds-Henne *et al*., 2007) and can be powerful proxy archives for subannual climatic reconstructions using stable isotope ratios. Therefore, in many locations, stable isotope analyses of tree rings may provide climate information not available from other proxies and be worth the extra investment for improving these reconstructions. However, to appropriately interpret stable isotope records within tree-ring cellulose, the relationship between atmospheric conditions, source water, and ultimately the isotopic signature of source water must be understood both from a broad mechanistic standpoint and in the context of local, site-specific influences.

The distinct isotopic signatures of different source waters (due to rainout, temperature-dependent effects, trajectory paths, and evaporation, amongst other factors), and particularly the oxygen isotope composition of precipitation and ocean water, have been studied for over fifty years (e.g., Craig, 1961; Dansgaard, 1964; Craig and Gordon, 1965, Rozanski *et al*., 1993; Dutton *et al*., 2005). Building on the work of Epstein and Mayeda (1953) and Friedman (1953), Craig's (1961) extensive investigation and eventual definition of the linear correlation between δ^2H and $\delta^{18}O$ values introduced the idea that the relative depletion of the heavier isotopes (i.e.,

deuterium and ^{18}O) in meteoric water could be used to identify the water's source. This depletion is defined by relative abundance of the rare, heavier isotopologue (^{2}H or ^{18}O) over the lighter, more common isotopologue (H or ^{16}O) and considered relative to Vienna Standard Mean Ocean Water, or VSMOW (a recalibration of Craig's "standard mean ocean water," or SMOW; VSMOW remains the current standard (Coplen, 1996)). Craig's findings are summarized in a formula called the Global Meteoric Water Line, defined as:

$$\delta D = 8\,\delta O^{18} + 10$$

This relationship is still eminent in the study of stable isotopes in precipitation, and Rozanski *et al*. (1993) and others have noted how differing hydroclimatic conditions at different locations produce local meteoric water lines that deviate from the GMWL (e.g., Voelker *et al.*, 2014). The establishment of these relationships has enabled researchers to draw inferences about the source of precipitation based on its stable isotope ratio (e.g., Araguás-Araguás *et al.*, 1998; Kurita *et al.*, 2009; Berkelhammer *et al.*, 2012; Putman *et al.*, 2017), resulting in a rich body of research over the past half-century on a variety of spatial and temporal scales.

To better appreciate these relationships, it is necessary to understand the variables controlling isotopic fractionation. These include climatic controls and a process called the amount effect (Ramesh *et al.*, 1986). Plotting of *in situ* observations of $\delta^{18}O$ and $\delta^{2}H$ values from sites around the world at varying latitudes clearly demonstrates that source waters in warmer regions exhibit higher, less negative isotope ratios than source waters in colder regions, which exhibit increasingly lower and more negative isotope ratios (Figure 1). This relationship is further evidenced by the exceptionally low proportions of ^{18}O found in polar ice (Rozanski *et al*., 1993). However, it should be noted that the relationship between isotope ratios of precipitation and climatic variables does not fully account for variations in isotope ratios of precipitation in

the mid- and high latitudes, and therefore other factors must be considered (Rozanski *et al*., 1993).

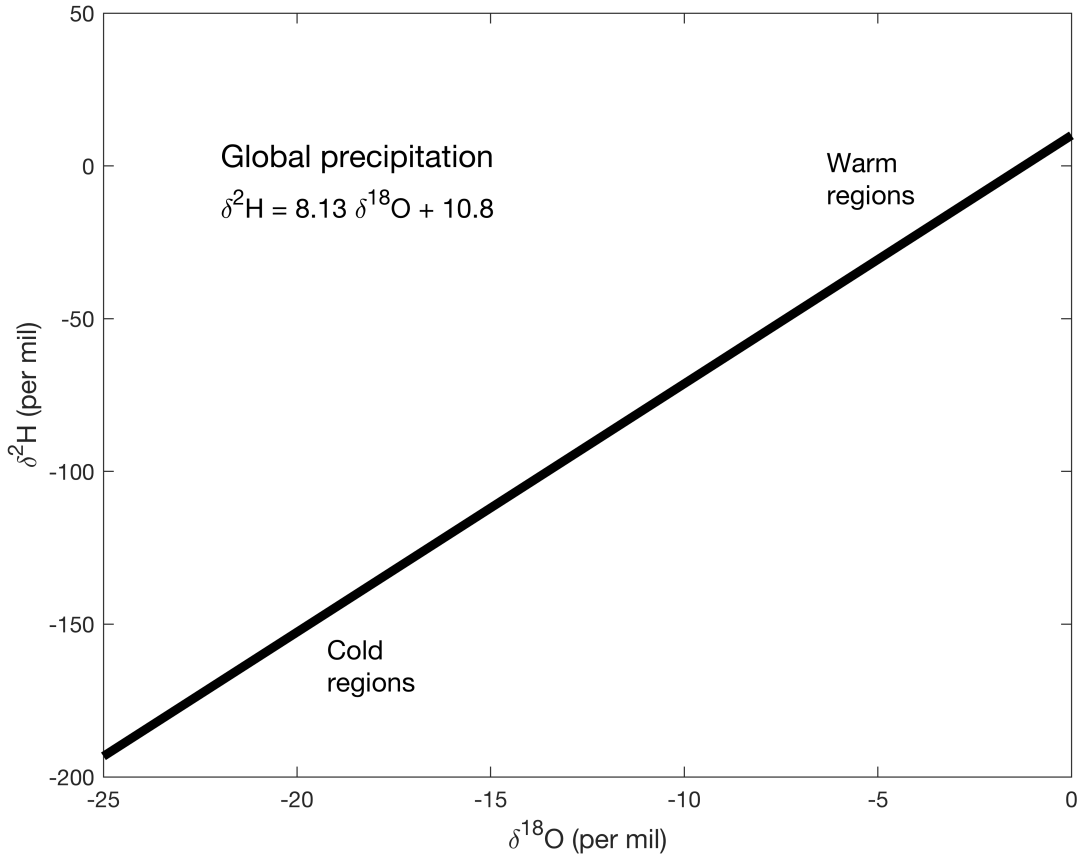

Figure 1.1. Visualization of the temperature effect on $\delta^{18}O$ values. Modeled after *Environmental Isotopes in Hydrogeology*, Clark and Fritz, 1997 as compiled in Rozanski *et al*., 1993.

In addition to climatic controls, the primary physical process affecting fractionation is the amount effect, which is used to describe the changes in isotopic composition that result from rainout (Dansgaard, 1964). The amount effect refers to the preferred rainout of molecules that contain heavier stable isotopes (including ^{18}O and D) over the course of a rain event; this preferred rainout is a result of Rayleigh fractionation (Dansgaard, 1964). Figure 2 demonstrates the practical ramifications of this process.

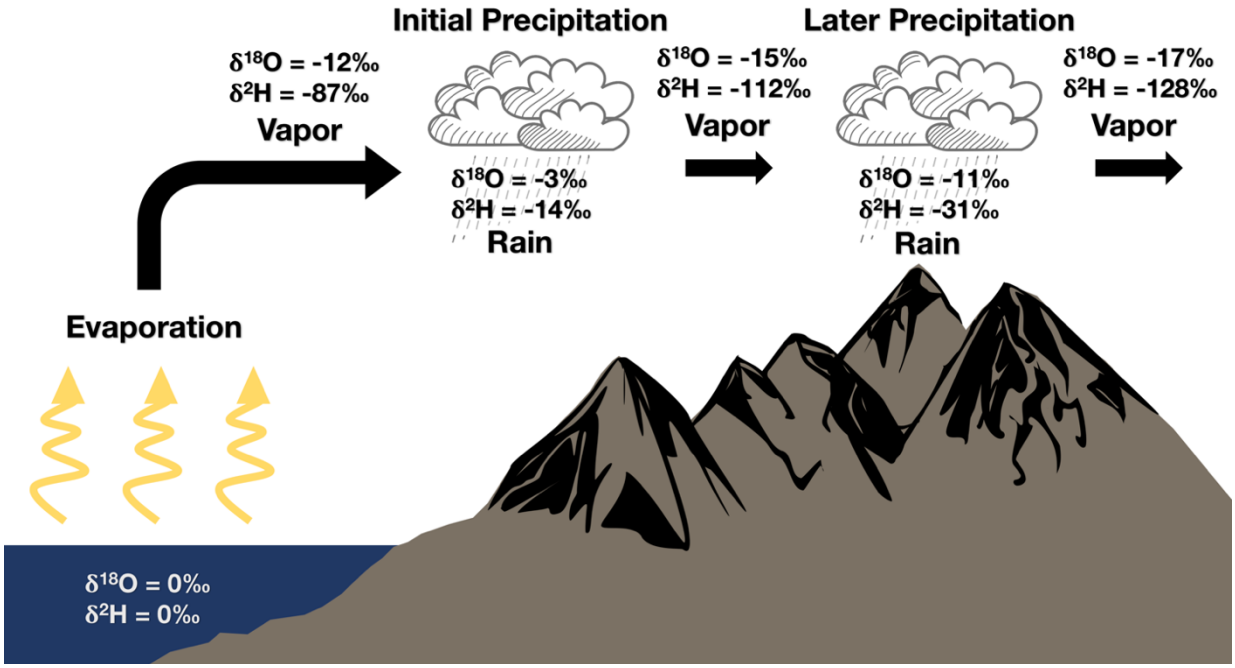

Figure 1.2. Demonstration of the effect of rainout on stable isotope signatures of precipitation. Modeled after Hoefs' *Stable Isotope Geochemistry*, 1997.

It should be noted that the impact of the amount effect has been challenged in extra-tropical and inland regions, where the majority of isotopic paleoarchives occur (Tindall *et al*., 2009), and by model-based studies in the context of multi-decadal to millennial-scale paleoclimatic reconstructions (e.g., Schmidt *et al*., 2007; LeGrande and Schmidt, 2009; Eastoe and Dettman, 2016). However, in several cases where the amount effect has been identified as not significantly impacting isotopic composition, researchers have pointed to moisture source regions and water vapor transport pathways as possible controlling factors (e.g., Schmidt *et al*., 2007; LeGrande and Schmidt, 2009; Dayem *et al*., 2010; Lewis *et al*., 2010), highlighting the potential utility of isotopic composition to reconstruct moisture source region. Other researchers have further investigated the impacts of rainout to explain what they refer to as the continental effect (Vaz de Oliveira and Lima, 2010; Winnick *et al*., 2014), in which the stable isotope ratio becomes lower (more negative) with inland movement. Altitude has also been demonstrated to

influence stable isotope ratios of precipitation (Poage and Chamberlain, 2001). In short, temperature controls and moisture source exert considerable influence on the stable isotope ratio of many meteoric waters throughout the world, but this seemingly straightforward relationship is often complicated by other factors that drive rainout and may promote isotopic exchange with water vapor (Kohn and Welker, 2005).

Despite these complications, a considerable body of work has emerged that assesses this relationship and utilizes stable isotopes as tracers of synoptic-scale flow using tools such as back-trajectory analysis. While studies combining modern precipitation and back-trajectory analysis are useful in the interpretation of modern trends in precipitation source and transport pathways, they must be combined with proxy records to understand long-term hydroclimatic variability and to characterize present conditions in respect to this variability. While physical and biochemical effects on fractionation can complicate this relationship and its interpretation, several mechanistic models have been developed to better understand and quantify the impacts of these processes on changes to the stable isotope ratios of tree-ring cellulose (e.g., Yapp and Epstein, 1982; Roden *et al*., 2000; Anderson *et al.*, 2002; Ogée *et al*., 2009) and leaf water (Flanagan *et al*., 1991). Comparing the outputs of these models with *in situ* values is an important means of testing assumptions about the processes that control the isotope ratios of tree cellulose at a given locale (Anderson *et al.*, 2002).

Climate information such as temperature, humidity, and precipitation has been derived from isotope ratios measured from tree-ring cellulose both with and without the consideration of these models. Much of this research has focused on the Tibetan Plateau and proximal areas, where $\delta^{18}O$ values of tree-ring cellulose have been demonstrated to correlate with summer moisture variability (Shi *et al*., 2012), cloud cover (Liu *et al*., 2014), relative humidity

(Grießinger *et al*., 2017; Wernicke *et al*., 2017; Liu *et al.*, 2019) and Palmer Drought Severity Index (Qin *et al*., 2015). The relationship between tree-ring $\delta^{18}O$ values and temperature, relative humidity, and precipitation has also been examined throughout Europe (Lipp *et al*., 1991; Robertson *et al.*, 2001; Loader *et al*., 2003; Rinne *et al.*, 2013; Young *et al.*, 2015), and the temporal stability of these relationships has been explored to better understand the reliability of reconstructions (Reynolds-Henne *et al.*, 2007). Elsewhere, researchers have employed mechanistic models to consider the influence of biological factors on the uptake and transformation of the isotope ratios found in meteoric water (Lorrey *et al*., 2016; Kurita *et al*., 2016), which can further strengthen resultant analyses. Models have also been refined to calculate the isotope ratio of source water based on tree-ring $\delta^{18}O$ values in Switzerland (Anderson *et al*., 2002) and separately quantify temperature and precipitation from tree-ring $\delta^{18}O$ values at thirty-three sites globally (Schubert and Jahren, 2015).

In North America, most tree-ring isotope records have been used to examine the potential for climate reconstructions or perform reconstructions of multidecadal- to centennial-scale (rather than annual or decadal-scale) climate variability. Burk and Stuiver (1981) first examined the tree isotope-climate relationship in Washington State, and other studies have since furthered this exploration in the region (Roden *et al.*, 2005; Shu *et al.*, 2005; Marshall and Monserud, 2006; Feng *et al.*, 2007; Roden and Ehleringer, 2007; de Boer *et al.*, 2019). Reconstructions in the PNW have emerged more recently, including a reconstruction of growing-season relative humidity and winter temperature in the eastern Rocky Mountains and northern Great Plains (Edwards *et al.*, 2008) and temperature in the southern Rocky Mountains (Berkelhammer and Stott, 2012) at multidecadal to centennial scales. Few studies have focused on annual scales, with one study in far northeastern Canada reconstructing temperature and precipitation $\delta^{18}O$ values

annually from Pliocene wood (Csank *et al.*, 2013) and another reconstructing modern spring-summer temperature in northwestern Canada (Porter *et al.*, 2014). Only three published studies have investigated oxygen isotopes in the U.S. PNW at subannual scales (Roden and Ehleringer, 2000; Roden *et al.*, 2005; Roden and Ehleringer, 2007), and none have (to our knowledge) examined both earlywood and latewood for a period of longer than two years, though subannual tree-ring cellulose measurements have shown potential for reconstructing seasonal climate elsewhere (Liu *et al.*, 2009; An *et al.*, 2012; Labotka *et al.*, 2016; Zhu *et al.*, 2021).

Despite the aforementioned advances, subannual tree-ring oxygen isotope records have not been used for climate reconstructions in the U.S. Pacific Northwest, where the fine resolution of these records stands to make an impactful contribution to our understanding of regional climate. However, the relationship between stable isotope ratios in precipitation and moisture source in the region must be understood to accurately interpret such a reconstruction, and simpler metrics such as subannual tree-ring width measurements may provide similar information at little expense and should also be explored. Therefore, a multi-proxy investigation that considers subannual tree-ring width and $\delta^{18}O$ values, moisture source, stable isotope ratios in precipitation, temperature and precipitation, and the factors integrated into mechanistic models at different sites across diverse environments stands to contribute to our understanding of the climate signals captured by these proxies and how they can be more accurately interpreted.

Dissertation Structure and Contributions

In this dissertation, I use instrumental, *in situ*, and proxy-based data at a targeted network of sites to examine the degree to which: 1) stable isotope ratios in precipitation; 2) subannual tree-ring widths; and 3) stable isotope ratios in subannual tree rings capture climate variability in

the U.S. Pacific Northwest. The main goal of this dissertation is to better understand the unique advantages and limitations of $\delta^{18}O$ values as a climatic indicator across diverse sites in the PNW. Each chapter is focused on an individual climate-proxy relationship and its variation across space and time. Below is an overview of each chapter's research questions, objectives and methods, and key findings along with a brief summary of overall contributions of this work as a whole.

Summary of Chapter 2

Research Questions: Does the stable isotope ratio of precipitation reflect air mass origins and transport pathways at our sites? Does the air mass trajectory–stable isotope relationship differ on the windward and leeward sides of the Cascade Range? Do spatial and temporal (seasonal) patterns exist in these relationships?

Objective and Methods: I assess relationships between the stable isotope ratios of precipitation at five sites in the Pacific Northwest and the trajectories of air masses that likely produced that precipitation. I select extreme (top and bottom 10%) values from a weekly dataset of stable oxygen isotope measurements of precipitation samples collected by the National Atmospheric Deposition Program (NADP) and use the HYSPLIT model to generate 72-hour-long back trajectories using NCEP/NCAR reanalysis data to estimate precipitation source region and transport for these samples. I perform cluster analyses of different site/season combinations and visualize these and other trajectories to quantitatively and qualitatively explore differences between these groupings at seasonal time scales.

Key Findings: Air mass trajectories leading to precipitation with $\delta^{18}O$ values in the top 10% of seasonal values at our sites more frequently originate in southerly/southwesterly regions, while trajectories leading to precipitation with $\delta^{18}O$ values in the bottom 10% of seasonal values

frequently originate in northerly regions. This finding suggests that stable isotope ratios of precipitation in the Pacific Northwest are largely driven by the origins and paths taken by air masses in the 72 hours prior to rainout, suggesting a linkage between synoptic-scale flow and the stable isotope ratio of precipitation. However, the trajectory–isotope relationship in precipitation is complex in this region, and many examples do not follow the more common trends. This is likely due to the region's complex topography and rainout during heavy precipitation events, and event-level isotope data are needed to further understand this relationship.

Summary of Chapter 3

Research Questions: Do earlywood (EW), latewood (LW), and adjusted latewood (LW_{adj}) measurements enhance overall climate signal capture at our sites when compared with total ring width (TRW) alone? Do EW measurements reflect moisture from early growing season and prior to the growing season at our sites, with LW and LW_{adj} measurements reflecting moisture later in the growing season? Does LW_{adj} isolate summer precipitation signals at our sites?

Objective and Methods: I establish the extent to which seasonal variations in total precipitation and average temperature are captured by TRW, EW, LW, and LW_{adj} of *Pinus ponderosa* trees at three newly-sampled sites in the U.S. Pacific Northwest that are located in close proximity to the NADP precipitation collection sites examined in Chapter 2. Using the MATLAB function Seascorr, I correlate monthly and seasonal temperature and precipitation data from the PRISM climate dataset with subannual growth metrics from trees at our sites and examine patterns in these relationships across sites and seasons.

Key Findings: Subannual tree-ring width measurements capture monthly- and seasonal-scale precipitation signals at our sites, with earlywood and latewood primarily reflecting prior-

summer and current-summer precipitation signals, respectively. Higher summer temperatures produce increased LW at our wettest site, while they produce increased LW early in the growing season and decreased LW during the driest part of the year at our two drier sites. TRW and EW width are not significantly affected by high summer temperatures. Subannual tree-ring widths capture more robust climate signals than traditional TRW signals alone, and different subannual ring-width metrics better capture climate at different times of the year. LW and LW_{adj} perform particularly well and show promise for seasonal climate reconstructions at our sites with little additional work and no specialized equipment or additional costs required.

Summary of Chapter 4

Research Questions: Do $\delta^{18}O_{cellulose}$ values capture seasonal temperature and precipitation signals at our sites? Are $\delta^{18}O_{cellulose}$ values a reliable indicator of source water (and hence meteoric water) that should be explored for source water reconstruction at our sites? How do subannual tree-ring widths and tree-ring $\delta^{18}O$ values compare as climatic indicators at our sites?

Objective and Methods: I examine the extent to which seasonal precipitation and temperature are captured by the $\delta^{18}O$ values of tree-ring earlywood and latewood cellulose from the same trees examined in Chapter 3. I also use tree-ring $\delta^{18}O$ values as inputs in a mechanistic model to predict the isotope ratios of source water captured by $\delta^{18}O_{cellulose}$ values and compare modeled values with amount-weighted *in situ* values from the NADP sites from Chapter 2 to explore whether modeled values might be reliable for source water reconstructions. I examine the synoptic conditions that prevailed during years that produced anomalous tree-ring $\delta^{18}O$ values to determine the extent to which synoptic drivers may explain variability in year-to-year variations in this metric.

Key Findings: $\delta^{18}O_{cellulose}$ values capture summer precipitation signals at our sites and also capture a degree of prior-summer, prior-winter, and current-summer temperature. Temperature signals are strengthened when considering source water $\delta^{18}O$ values modeled from $\delta^{18}O_{cellulose}$ values, though part of this strengthening may be explained by the input of growing-season relative humidity in the model. However, strong alignment between modeled $\delta^{18}O$ values of source water and measured, *in situ* values of presumed source water suggests that the climate-isotope relationship is not an artefact of the modeling process. Our modeling suggests that trees draw on both prior-winter and current-growing-season precipitation at our study sites, and our driest site demonstrates much stronger coherence with prior-season $\delta^{18}O_{precipitation}$ values than with current-season values. This aligns with the finding from Chapter 3 that moisture stored from prior seasons is particularly important at this site, especially for latewood formation. I also find that although especially anomalous synoptic-scale conditions seem likely to be captured by tree-ring cellulose, the relationship is complex and may be better represented at longer time scales.

Overall contributions of this dissertation

Taken together, the three examinations of climate proxies outlined above provide insight into the nuances of climate-proxy relationships in the PNW, especially as they relate to our understanding of the complex ways in which the $\delta^{18}O$ proxy serves as an indicator of air mass trajectories and broader synoptic-scale circulation, temperature, and precipitation patterns. The direct comparison of tree-ring widths, $\delta^{18}O$ values of precipitation, and $\delta^{18}O$ values of tree rings from a targeted network of sites is necessary for improving the interpretation of climate proxy records in a given region and is a particular asset of this work. Ultimately, the findings of this work show promise for reconstruction of precipitation patterns in the PNW and contribute to a

more sophisticated interpretation of oxygen isotope-based climate proxies in the region, particularly at seasonal scales. Enhanced understanding of seasonal-scale climate is increasingly important in this region with highly seasonal precipitation patterns that are projected to change with a changing climate and create a mismatch between water resource availability and demand.

CHAPTER 2: OXYGEN ISOTOPES IN PRECIPITATION AS INDICATORS OF AIR MASS TRAJECTORIES IN THE U.S. PACIFIC NORTHWEST

Introduction

Storm tracks play a significant role in controlling the amount and timing of precipitation in the Pacific Northwest (Hamlet *et al*., 2005; Berkelhammer and Stott, 2008; 2011). There is also a well-established connection between local hydroclimate and large-scale atmospheric flow and teleconnections in the U.S. Pacific Northwest, which refers here to the states of Washington and Oregon and includes the Cascade Range and the Columbia River Basin (McAfee and Wise, 2016). However, these synoptic-scale drivers of precipitation patterns in the region have begun to shift due to climate change, leading to an intensification of and northward shift in the Pacific storm track and a strengthening of the Aleutian Low (Chang *et al.*, 2012; Chang, 2013; Chang, 2014). These changes impact both the amount and seasonality of precipitation by driving a continuing increase in winter precipitation (Rupp *et al*., 2013; Warner *et al*., 2015) and decrease in minimum streamflow as more fall and early-winter precipitation falls as rain due to increasing temperatures (Tohver *et al.*, 2014; Marlier *et al.*, 2017). These projected changes highlight the importance of better understanding the complex hydroclimate of the U.S. Pacific Northwest over a variety of spatial and temporal scales.

The stable isotope composition of source water is a powerful and well-established tool for examining hydroclimate (Craig, 1961; Dansgaard, 1964; Craig and Gordon, 1965; Rozanski *et al*., 1993; Dutton *et al*., 2005), as $\delta^{18}O$ and $\delta^{2}H$ values are tracers of hydrologic processes in both meteoric water in the present (Craig and Gordon, 1965) and in proxies such as tree rings

that captured and assimilated meteoric water in the past (McCarroll and Loader, 2004). These stable isotope proxy records are important for contextualizing current hydroclimate within long-term variability (Anderson *et al*., 2002); however, the complex and interwoven signals captured by these proxies can make them difficult to untangle and interpret (Sjostrom and Welker, 2009). Coupling stable isotope analysis of *in situ* precipitation samples with air parcel back-trajectory analysis is one promising method for contributing to the interpretation of these records by examining the relationship between air mass trajectories and stable isotope ratios in precipitation over different spatial and temporal scales. Although stable isotope analysis provides some information about the moisture source region on its own, the addition of back-trajectory modeling contextualizes these findings with meteorological reanalysis. This coupling also allows for the identification of spatial and temporal patterns that can be quantified and analyzed to determine the probability that a given precipitation sample followed a given air mass trajectory, providing important context about how shifts in storm tracks and seasonal precipitation patterns are reflected in precipitation and the paleoclimate proxies that assimilate this precipitation.

There is a substantial body of work utilizing isotope ratios in precipitation to investigate patterns in synoptic-scale atmospheric circulation and moisture source regions (e.g., Welker, 2000; Friedman *et al.*, 2002; Strong *et al*., 2007; Birks and Edwards, 2009; Sjostrom and Welker, 2009; Field, 2010; Vachon *et al.*, 2010a; Liu *et al.*, 2011; Berkelhammer and Stott, 2012; Liu *et al.*, 2013; Bailey *et al*., 2015; McCabe-Glynn *et al*., 2016; Puntsag *et al*., 2016; Putman *et al.*, 2017; Bailey *et al.*, 2019). Many of these studies provide information on hydroclimate variability during the instrumental period, whereas others use stable isotope ratios captured by climate proxy records, such as tree rings, to reconstruct moisture source regimes over longer timescales

(e.g., Reynolds-Henne *et al*., 2007; Berkelhammer and Stott, 2008; 2011; Sidorova *et al*., 2010; Sano *et al*., 2012; Saurer *et al*., 2012).

Lagrangian back trajectory analysis has frequently been used to examine the source of air parcels, primarily in studies of air quality that assess the source and dispersion of particulate matter and aerosols (e.g., Covert *et al*., 1996; Karaca *et al*., 2005; Yerramilli *et al*., 2012). This type of analysis has also been used to investigate the moisture source of extreme individual precipitation events (Brimelow and Reuter, 2005; Moore *et al*., 2012) and to assess and categorize seasonal variations in moisture source at a given location (Fernau and Samson, 1990; Diem and Brown, 2006; Hondula *et al*., 2010; Diem *et al.*, 2019).

The combination of back-trajectory analysis to simulate air parcel movement with stable isotope ratios has emerged as a powerful tool in the identification of storm tracks, which refer both to areas where cyclones tend to travel and to the paths of individual storms such as mid-latitude cyclones and tropical cyclones (e.g., Buda and DeWalle, 2009; Ersek *et al*., 2010). Air parcel back-trajectory analysis can also be used as a tool to identify spatial and temporal patterns in the $\delta^{18}O$ value of precipitation and relate these patterns to precipitation amount, moisture source region, and large-scale atmospheric circulation (e.g., Sjostrom and Welker, 2009; Sánchez-Murillo *et al*., 2013; Bailey *et al*., 2015; Puntsag et al. 2016). In particular, the classification of trajectories leading to events with distinct isotope ratios has allowed researchers to link the stable isotope ratios of single precipitation samples with source regions, including at study sites in the western United States (Berkelhammer *et al.*, 2012), and identify seasonal patterns in these linkages (Sjostrom and Welker, 2009).

To assess and quantify relationships between the stable isotope ratio of precipitation in the Pacific Northwest and the trajectories of air masses leading to that precipitation, we have

analyzed δ^2H and $\delta^{18}O$ values of weekly composited precipitation samples from 2007-2016 at five locations in and around the Columbia River Basin and on either side of the Cascade Range. This extensive dataset, to our knowledge the longest continuous weekly precipitation isotope time series dataset in the Pacific Northwest, provides the opportunity to study precipitation delivery over an entire decade. It also affords us the unique ability to investigate both short-term and longer-term patterns and make comparisons across a large mountain range, which has not been possible with studies using temporally discontinuous datasets, such as some based on the United States Network for Isotopes in Precipitation (USNIP) (e.g., Vachon *et al.*, 2010a), or studies focused on a single site (e.g., Marchetti and Marchetti, 2019). Lastly, the proximity of the sites to one another allows for examination of changes in the stable isotope ratio across complex topography at a fine spatial scale using *in situ* data, where other studies of this type have often been limited by reliance on interpolation (e.g., Liu *et al.*, 2013). The physical processes that impact isotopic fractionation of orographic precipitation have been modeled and examined (e.g., Moore et al., 2016; Smith, 2019), including in the Pacific Northwest (Smith *et al*., 2005), but uncertainties remain about the variability of these impacts across space and time. Pairing isotope ratios with back-trajectory analysis stands to further elucidate this impact by using *in situ* samples from precipitation events to identify patterns in these impacts that may not be apparent from shorter-term and single-site studies.

Here, we use this unique dataset to identify spatial and temporal patterns in air mass trajectories and their relationship with isotope ratios of precipitation based on 72-hour back-trajectories terminating at five sites. The varying elevations and continentality of these locations on both sides of the Cascade Range enables the comparison of moisture sources and their variability among locations with different climatic controls. This comparison contributes to the

growing understanding of the linkages between moisture source and stable isotope ratios of meteoric water and how these linkages are altered by complex topography. Improving this understanding will help to refine isotope-enabled models and overall understanding of past hydroclimate in the Pacific Northwest and in other mountainous regions by identifying patterns in how topography impacts the moisture source-isotope relationship.

Data and Methods

Site overview

Our study sites are part of the National Atmospheric Deposition Program's National Trends Network (NADP NTN), which provides a long-term record of high-quality precipitation samples across the United States. Our selected sites are located on both sides of the Cascade Range and at elevations ranging from 233 to 1253 meters above sea level (m AMSL) (Figure 2.1 and Table 2.1).

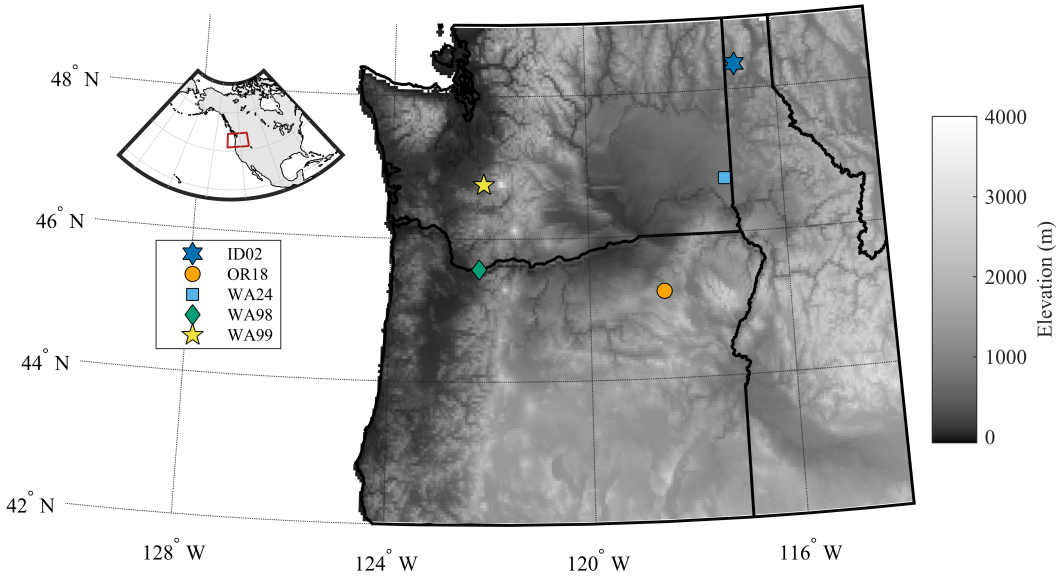

Figure 2.1. Location and elevation of study sites within the U.S. Pacific Northwest.

Table 2.1. Summary of site attributes.

NADP Site ID	Site Name	State	Latitude	Longitude	Elev. (m)
ID02	Priest River Experimental Forest	Idaho	48.3518	-116.8397	726
OR18	Starkey Experimental Forest	Oregon	45.2247	-118.5130	1253
WA24	Palouse Conservation Farm	Washington	46.7606	-117.1847	766
WA98	Columbia River Gorge	Washington	45.5694	-122.2100	233
WA99	Mount Rainier National Park	Washington	46.7582	-122.1243	424

The sites at Columbia River Gorge (NADP site WA99) and Mount Rainier National Park (WA98) in Washington are both at relatively low elevation on the windward side of the Cascades, while the sites at Priest River Experimental Forest (ID02) in Idaho, Palouse Conservation Farm (WA24) in Washington, and Starkey Experimental Forest (OR18) in Oregon are located on the leeward side of the Range at relatively higher elevations (for simplicity, NADP site IDs are used in Figure 1 and from this point forward). We selected these sites to examine differences in air mass trajectories and their overall patterns across the complex topography of the Pacific Northwest. They also provide longer-term weekly precipitation sampling with good spatial coverage, particularly on the eastern side of the Cascades.

The NADP collects precipitation samples in collectors that automatically open during wet weather at 257 active sites within the network, and site operators replace the collection bucket weekly, resulting in weekly resolution of precipitation samples (NADP, 2020a). Daily precipitation amount and type are also recorded at each site. The NADP Program Office implements a strict protocol for data analysis and quality control, resulting in a robust and closely monitored dataset that is suitable for chemical analysis (NADP, 2020b). However, the NADP only shares samples with external researchers when they have excess volume or are discarding samples. Therefore, we were not always able to obtain samples if there was only a small amount of precipitation. Consequently, summer sample depth was reduced by about one

half at our sites, and we chose to combine June-August samples into a single period with similar sample depth as the other two-month periods we developed and used throughout this study.

Selecting and analyzing precipitation samples and data

We requested all available weekly precipitation samples for January 2007 through December 2016 at each of our five study sites from the NADP. Samples from 2007 and 2008 were analyzed at Nipissing University in North Bay, ON; samples from 2009-2013 were analyzed at the Desert Research Institute in Reno, Nevada; and samples from 2014-2016 were analyzed at in the Stable Isotope Laboratory at the University of Nevada, Reno. All samples were analyzed for δ^2H and $\delta^{18}O$ values, and all three laboratories used a Picarro L-1102i WS-CRDS analyzer for sample analysis. International reference standards (IAEA, Vienna, Austria) were used to calibrate each instrument to the VSMOW-SLAP scale (wherein $\delta^{18}O$ values are expressed relative to Vienna Standard Mean Ocean Water [VSMOW], which has a $\delta^{18}O$ value of 0 ‰). Stable isotope ratios are expressed in delta notation in per mil (‰) relative to VSMOW . Working standards (USGS45: δ^2H= -10.3 ‰, $\delta^{18}O$= -2.24 ‰ and USGS46: δ^2H= -235.8 ‰, $\delta^{18}O$= -29.8 ‰) were used with each analytical run to correct for instrumental drift, and six injections per sample were run (three of which were measured) to ensure stability in the analysis. Average analytical accuracy ranged from 0.07 – 0.11‰ for all laboratories. Data that fell more than one standard deviation from the Local Meteoric Water Line were excluded from the dataset. Although these outlier values may be indicative of environmental evaporation or other dynamic processes, they may also be an artifact of evaporation that occurs while a bucket is open for collection during a rain event or from improperly sealed containers during storage or transport.

These values represent approximately 1% of samples at each site and therefore do not considerably impact the comprehensiveness of the dataset.

Daily precipitation data, including amount and type, were downloaded from the NADP NTN for each study site for 26 December 2006 through 31 December 2016 to correspond with the dates leading up to and including the collection of the precipitation isotope samples. This dataset includes the starting and ending date and hour (in local time) of each collection followed by the precipitation amount in inches and precipitation type coded as rain (including hail), snow, mixture, or unknown. Missing and trace precipitation are also noted and account for 2.25% to 4.44% of values within the datasets for our chosen sites. Daily precipitation data were downloaded from PRISM (PRISM Climate Group, Oregon State University, https://prism.oregonstate.edu/) to account for missing data from the NADP NTN dataset.

The resulting combined dataset of weekly $\delta^{2}H$ and $\delta^{18}O$ values of precipitation and daily precipitation amount and type over the 2006-2016 period for each study site was divided into five periods: October-November, December-January, February-March, April-May, and June-September. Using these periods allows us to identify patterns beyond seasonal variation. The longer period of June through September reflects the limited data availability during the dry summer months at the study sites; at each site, these four months contained approximately the same number of weekly precipitation samples as each of the two-month periods. Sampling periods that fell across two periods were assigned to the period containing a greater proportion of the accumulated precipitation.

To identify days that likely produced anomalous precipitation isotope ratios, we isolated the weeks of precipitation that produced the lowest and highest 10% of weekly $\delta^{18}O$ values at each site within each season after removing any flagged values; we then focused our analyses on

these anomalous values. Due to the robust correlation between δ^2H and $\delta^{18}O$ values at our study sites (r = 0.98 at all sites), we used $\delta^{18}O$ values to identify weeks with anomalous isotope ratios to be explored using the HYSPLIT model. Within the chosen weeks, we used the daily precipitation record provided by the NADP for each site to identify days where precipitation of greater than 5 mm occurred to analyze only those days that were likely to significantly contribute to the isotope ratio of the given week's precipitation sample.

Lastly, we calculated deuterium excess (d-excess) for each weekly sample using the following equation defined by Dansgaard (1964):

$$d = \delta^2H - 8 \cdot \delta^{18}O$$

This second-order isotopic variable is used to assist our interpretation by providing additional information about the likely impact of moisture source and kinetic processes (Zhang *et al.*, 2010; Guan *et al.*, 2013). We also calculated summary statistics for $\delta^{18}O$ values by period and site to contextualize our other findings.

Generating and analyzing back trajectories

We used Version 4 of the Air Resources Laboratory's HYSPLIT model (Draxler and Hess, 1997; Draxler and Hess, 1998; Draxler *et al.*, 1999; Stein *et al*., 2015) to calculate back trajectories of 72-hour duration every three hours (i.e., 0300, 0600, 0900, 1200, 1500, 1800, and 2100) for days where non-trace precipitation was recorded within weeks that produced anomalous precipitation isotope ratios at each site. The HYSPLIT model uses wind field or barometric pressure measurements as the inputs for model runs that simulate the air parcel trajectory through a three-dimensional space, and we input the NCEP/NCAR global reanalysis available through NOAA's Air Resources Laboratory (Kalnay *et al.*, 1996). We calculated back

trajectories for each location and time step with terminal heights adjusted to 5500 meters above mean sea level (AMSL), accounting for differences in elevation between sites. This terminal height corresponds with a pressure of approximately 500 hPa, which is commonly analyzed for identification of middle-tropospheric pressure centers and other large-scale atmospheric features (Wallace and Gutzler, 1981). We choose this atmospheric level because we are interested in examining variations in zonal versus meridional flow and how these variations compare with known seasonal patterns in the Pacific storm track (e.g., Nakamura *et al.*, 1992; Chang *et al.*, 2002) and atmospheric circulation controls on precipitation isotope ratios in adjacent regions (Birks and Edwards, 2009). However, storms may approach at different elevations, and our experimental framework may not allow us to identify variability due to storm height as we do not directly measure or model condensation height (see Putman *et al.*, 2017). The 72-hour duration has been employed in comparable studies (e.g., Sjostrom and Welker, 2009; Hondula *et al*., 2010; Moore *et al*., 2011; Berkelhammer *et al*., 2012; McCabe-Glynn *et al*., 2016; Puntsag *et al*., 2016) and captures synoptic-scale processes while minimizing the error that typically results from longer trajectory duration (Stohl, 1998). The NCEP/NCAR global reanalysis, which has been used in similar studies (e.g., Diem and Brown, 2006; McCabe-Glynn *et al*., 2016; Puntsag *et al*., 2016; Diem *et al.*, 2019), provides consistent spatial and temporal coverage for the entire study area and has been processed into a HYSPLIT-compatible format. The reanalysis contains data for 17 pressure levels (18 sigma levels) on a 2.5 ° latitude-longitude grid at a resolution of six hours (Kalnay *et al.*, 1996). The use of global, rather than regional, reanalysis ensures that no spatial or temporal data are missing within the generated back trajectories and that all resulting trajectory points can be used as inputs in cluster analysis. Our preliminary analyses (not shown) demonstrated that the NCAR/NCEP dataset produced comparable results to the higher-resolution

but spatially-limited North American Regional Reanalysis (NARR) dataset (Mesinger *et al*., 2006).

To identify the trajectories associated with anomalous isotopic values, we performed two cluster analyses for each site for each period: one for all trajectories computed for all precipitation days within the weeks that produced the lowest 10% of $\delta^{18}O$ values and one for all trajectories computed for all precipitation days within the weeks that produced the highest 10% of $\delta^{18}O$ values (selected values are provided in Tables A1-A5). This resulted in a total of fifty cluster analyses (two conditions * five periods * five sites). The cluster analysis function in HYSPLIT uses an iterative process in which trajectories are paired, cluster spatial variance is calculated, and subsequent trajectories are either added to an existing cluster or form the basis of a new cluster based upon change in total spatial variance (Draxler *et al.*, 1999). After performing an initial cluster analysis, the model produces an output of the change in total spatial variance (TSV) with each additional cluster. The user must then choose a number of clusters based on this output, and the program assigns all trajectories to one of the clusters. As suggested by the HYSPLIT developers, we selected the number of clusters immediately prior to a large increase in TSV to maximize meaningful clustering for each set of trajectories. However, it must be noted that cluster analyses introduce an unavoidable element of subjectivity as the user must select the number of clusters, and in other studies, cluster maxima have been set at anywhere from two or four (Bazzano, *et al.*, 2021) to five (Wang *et al.*, 2010) or even eight (Su *et al.*, 2015) clusters. We minimize this subjectivity in our study by enforcing a maximum of five clusters per analysis, as in earlier analyses, we found that HYSPLIT tended to compute individual precipitation events as separate clusters when a larger number of clusters (six or more) was allowed. By limiting the number of clusters below this threshold, we maximize the meaningfulness of our clusters by

identifying patterns that are characteristic of overall pathways rather than individual event trajectories.

We used two methods to quantify the differences between the mean cluster trajectories for the highest and lowest 10% of $\delta^{18}O$ values at each site during each period (hereafter referred to as the *period mean trajectories*). First, we used a two-sample Hotelling's T^2 test statistic to test for statistically significant ($\alpha = 0.05$) differences between the period mean trajectories computed above for the extreme $\delta^{18}O$ values at each site, allowing us to determine whether the two groups result from significantly different mean storm-track trajectories. The Hotelling's T^2 test statistic is a method of multivariate analysis of variance (MANOVA) that considers the difference between two vectors and therefore is suitable for comparing two-dimensional populations such as back-trajectory cluster means (see Hondula *et al.*, 2010). The population for each period mean trajectory is comprised of the latitude and longitude of that trajectory at each hourly interval during the 72-hour duration for a total of 144 data points per population. Second, we calculated how many hours of its 72-hour duration each period mean trajectory spent over land to infer the degree of rainout.

Results

Overview

The results of our quantitative and qualitative analyses allow us to group the five sites into two groups. One group consists of the three sites east of the Cascade Range (ID02, OR18, and WA24), which are similar to each other and notably different from the second group consisting of the two sites west of the range (WA98 and WA99). The trajectories determined from these two groups differed from each other in their hours spent over land. Although there are

differences between these groups in terms of their elevation and position relative to the Cascades, the differences between them are likely driven by their continentality, and we cannot definitively claim that spatial patterns are driven exclusively by one factor. Therefore, we minimize our discussion of these results as they relate to elevation and focus on patterns in quantitative and qualitative similarities and differences between the five sites and two groups (western/windward and eastern/leeward) across space and time. We discuss these patterns within two sets of trajectories: period mean trajectories (as defined above) and cluster mean trajectories, which refer to the outputs of the cluster analysis performed on each grouping of period mean trajectories.

Patterns in stable isotope data

As expected based on the temperature effect described by Dansgaard (1964), the period average $\delta^{18}O$ values of precipitation were lowest during the cool season (defined here as October-March) and highest during the warm season (defined here as April-September) at all five sites (Tables A6-A10). Site mean $\delta^{18}O$ values ranged from -8.9‰ at WA99 to -13.8‰ at ID02, and the per-site sample range was between 17.4 and 26.6‰. Site mean $\delta^{18}O$ values decreased with increasing distance inland and elevation. Local meteoric water lines also demonstrate this decrease and show a larger range in isotope values for the sites on the eastern side of the Cascades (Figure 2.2). June-September was the driest period at each of the study sites, with periods of no measurable or obtainable precipitation.

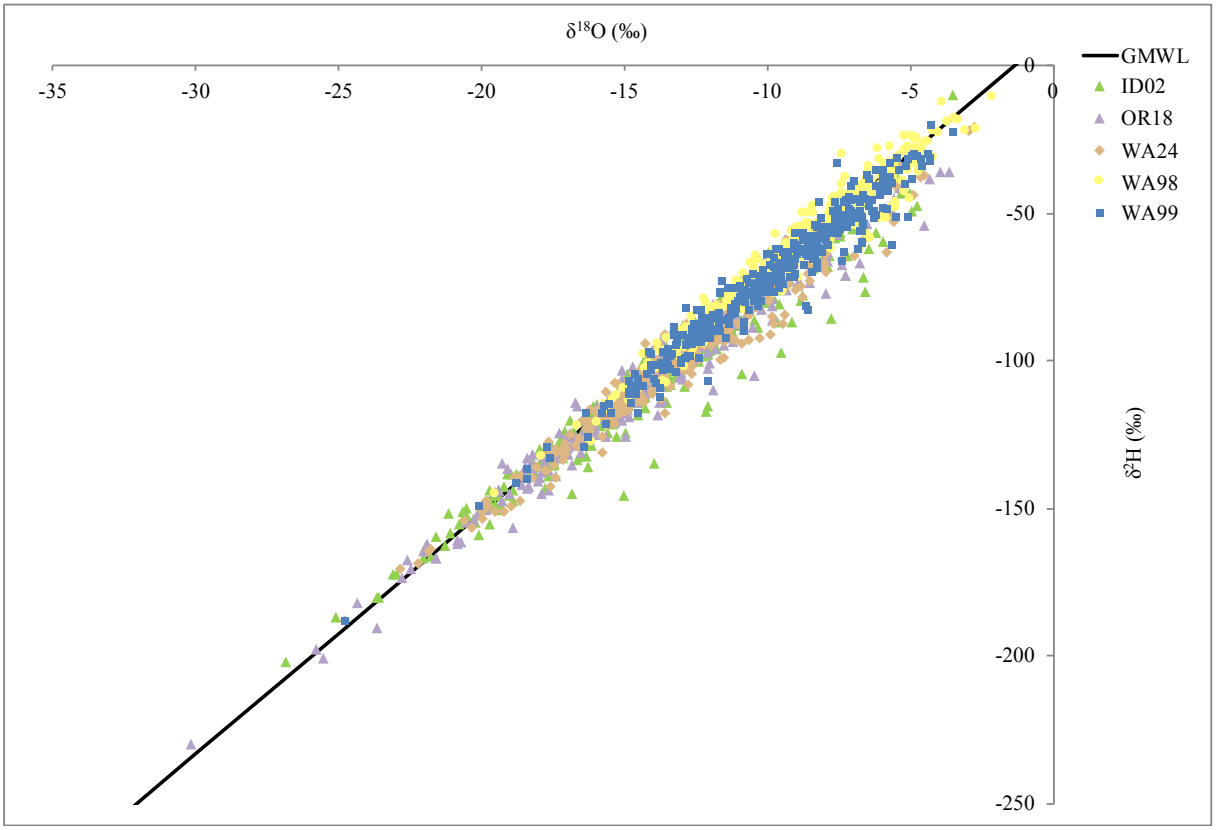

Figure 2.2. Global and local meteoric water lines.

Mean and median deuterium-excess values are positive for all sites and periods, and they decrease during warmer months across all sites. The values are more variable at the leeward sites than the windward sites in all periods, and there is a marked divergence between values for the windward and leeward sites during the warm months. Beginning in April-May, the leeward sites exhibit more weeks where deuterium-excess values are negative, and this pattern intensifies during June-September.

Period mean trajectories

Although all period mean trajectories are westerlies from the Pacific, there are distinct differences in the trajectories delivering precipitation with the highest and lowest $\delta^{18}O$ values at

each site and between stations on the eastern and western sides of the Cascades. Figure 2.3 shows that period mean trajectories for WA98 and WA99, both located on the windward side of the Cascades, are notably more direct and faster moving than the trajectories for the three leeward sites, as they travel a greater distance over their 72-hour duration. The windward sites also both show a tendency toward southwesterly flow for precipitation with high $\delta^{18}O$ values in the cool season as opposed to westerly zonal flow for precipitation with low $\delta^{18}O$ values during the same time of year. During the warm season, the two windward sites exhibit shorter, slower-moving period mean trajectories and show a westerly and at times northwesterly origin, especially for trajectories producing precipitation with low $\delta^{18}O$ values at WA99 (Figure 2.3).

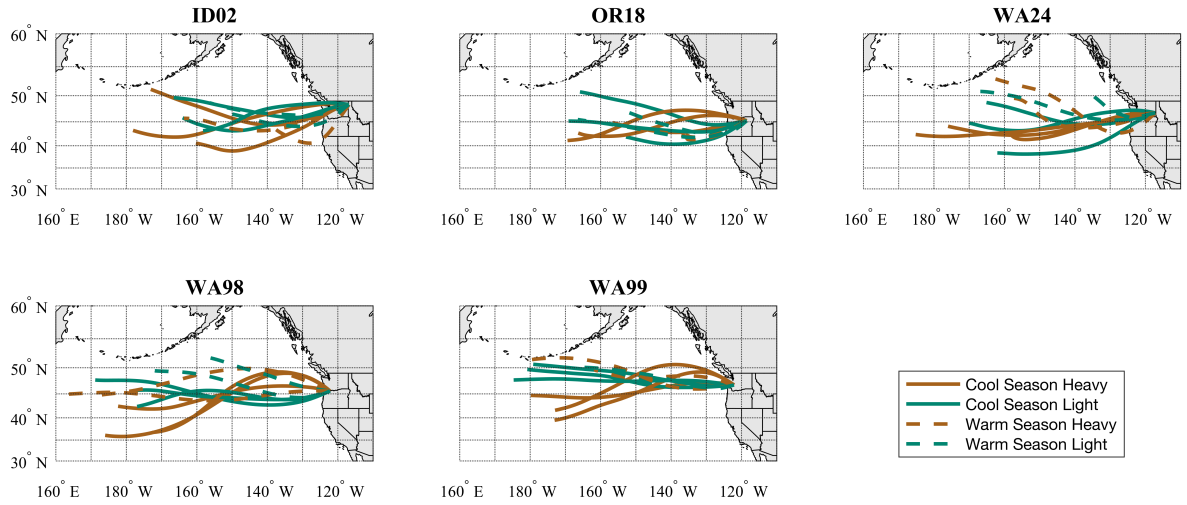

Figure 2.3. Seasonal mean trajectories across all sites and seasons. Cool season includes December-March, and warm season includes April-September. For the cool (warm) season, solid (dashed) green trajectories show storm tracks for the precipitation days from the bottom decile of stable isotope ratios ('light' precipitation), and solid (dashed) brown trajectories show storm tracks for the precipitation days from the top decile of stable isotope ratios ('heavy' precipitation).

On the eastern side of the Cascades (ID02, OR18, and WA24), trajectories are shorter than for the windward sites and follow more markedly curved paths, especially in the warm season. They tend to spend considerably more time over land due both to distance and curvature

of the paths. Precipitation with high $\delta^{18}O$ values in the cool season is associated with relatively more zonal flow than the windward sites but spans a broad latitudinal range. Precipitation with low $\delta^{18}O$ values in the same period ranges broadly in origin and trajectory. There are also distinct differences between sites. In the warm season, trajectories for ID02 and OR18 originate between around 42°N and 48°N, while all of the trajectories for WA24 originate north of 48°N.

Calculation of the two-sample Hotelling's T^2 test statistic demonstrates significantly different period mean trajectories for all but two of the 20 combinations of sites and periods at the $\alpha = 0.05$ significance level (for test statistic values, see Figures 2.4-2.8). There were significant differences between mean trajectories for precipitation with high and low $\delta^{18}O$ values in all seasons at ID02, WA24, and WA99. The period cluster means calculated for OR18 and WA98 exhibit significant differences between these categories for all periods but February-March at OR18 and June-September at WA98. Therefore, significant differences are apparent at all sites during the fall and winter months, and it is only during the spring and summer months that the period mean trajectories for the precipitation with high and low $\delta^{18}O$ values do not exhibit statistically significant difference at some sites.

Seasonal patterns in mean trajectories

The general pattern that emerges from analyses of the October-November period mean trajectories is one of relatively zonal flow where trajectories begin over the Pacific Ocean and move eastward toward the Pacific Northwest (Figure 2.4), which aligns with the overall Pacific storm track during this time of year (Chang *et al.*, 2002). Though the period mean trajectories for October-November are relatively zonal at all sites, they exhibit modest differences with a slight northerly bend for the light trajectories and a slight southerly bend for the heavy trajectories

(Figure 2.4). Starting points for the period mean trajectories for low $\delta^{18}O$ values for all five sites are located north of 45°N near the Aleutian Islands; the period mean trajectory for high $\delta^{18}O$ values at ID02 displays a similar pattern. The starting points for the period mean trajectories for high $\delta^{18}O$ values at the remaining sites originate south of 45°N. WA98 and WA99 both demonstrate longer, faster-moving trajectories than the three higher-elevation inland sites.

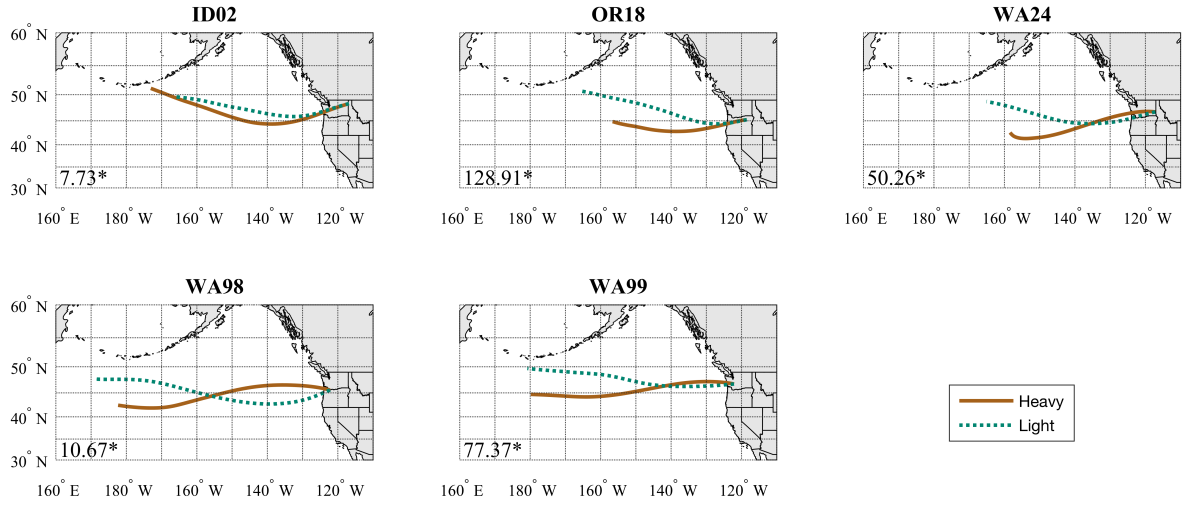

Figure 2.4. Seasonal mean trajectories for October-November. Dotted green trajectories show storm tracks for the precipitation days from the bottom decile of stable isotope ratios ('light' precipitation), and solid brown trajectories show storm tracks for the precipitation days from the top decile of stable isotope ratios ('heavy' precipitation). Results of two-sample Hotelling's T^2 test statistics for the two seasonal mean trajectories at each site are in the lower left corner of each map. Values with asterisks indicate significantly different mean trajectories for the pairing.

During December-January, the mean pattern for period mean trajectories for low $\delta^{18}O$ values remains relatively zonal, although there is a slight southward shift in trajectory origin relative to October-November (Figure 2.5). The trajectories originate between 40°N and 50°N. The period mean trajectories for high $\delta^{18}O$ values for the lower-elevation sites west of the Cascade Range exhibit more meridional flow, and these mean trajectories for all sites originate south of 45°N, suggesting that slightly warmer source waters with high $\delta^{18}O$ values may be at

least partially responsible for this trend. OR18 is the only site where the trajectory for low $\delta^{18}O$ values originates and tracks over generally lower latitudes than the trajectory for high $\delta^{18}O$ values, which could be related to its location as the lowest-latitude site. The high-value and low-value trajectories at WA24 and ID02 follow very similar paths, though the low-value trajectory at ID02 is considerably less direct than the high-value trajectory.

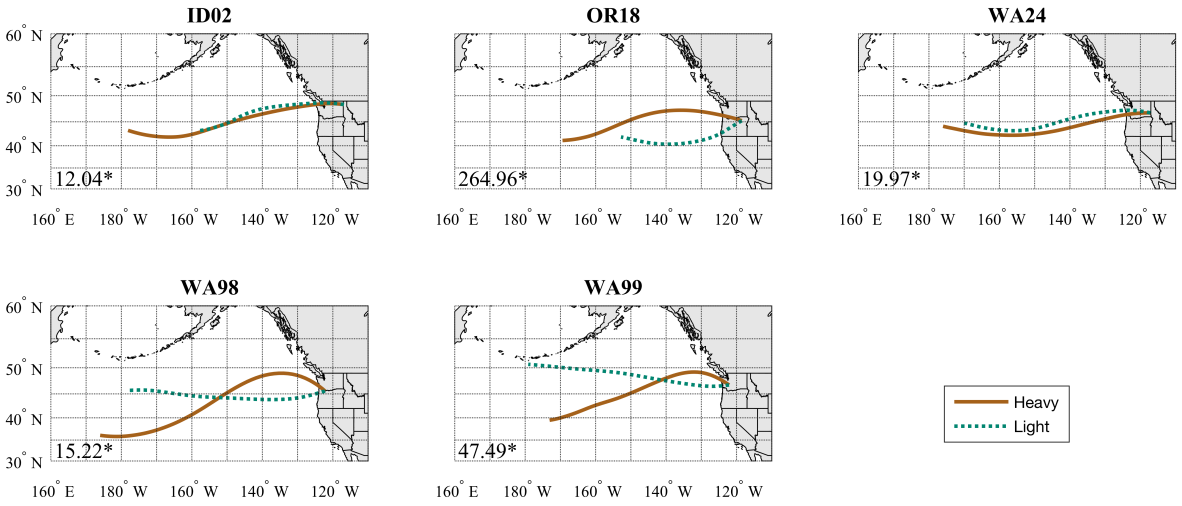

Figure 2.5. Seasonal mean trajectories for December-January. Dotted green trajectories show storm tracks for the precipitation days from the bottom decile of stable isotope ratios ('light' precipitation), and solid brown trajectories show storm tracks for the precipitation days from the top decile of stable isotope ratios ('heavy' precipitation). Results of two-sample Hotelling's T^2 test statistics for the two seasonal mean trajectories at each site are in the lower left corner of each map. Values with asterisks indicate significantly different mean trajectories for the pairing.

In February-March, there is considerable flow from the southwest, particularly for the cluster mean trajectories for high $\delta^{18}O$ values (Figure 2.6). Here, ID02 and WA24 demonstrate far less similarity than throughout the rest of the cool season. While the trajectories for high $\delta^{18}O$ values originate at lower latitudes for ID02, the trajectories for WA24 follow a zonal path and originate at higher latitudes. Meanwhile, the trajectory for low $\delta^{18}O$ values at WA24 originates at relatively low latitudes and resembles the high-value trajectory for ID02 during this period.

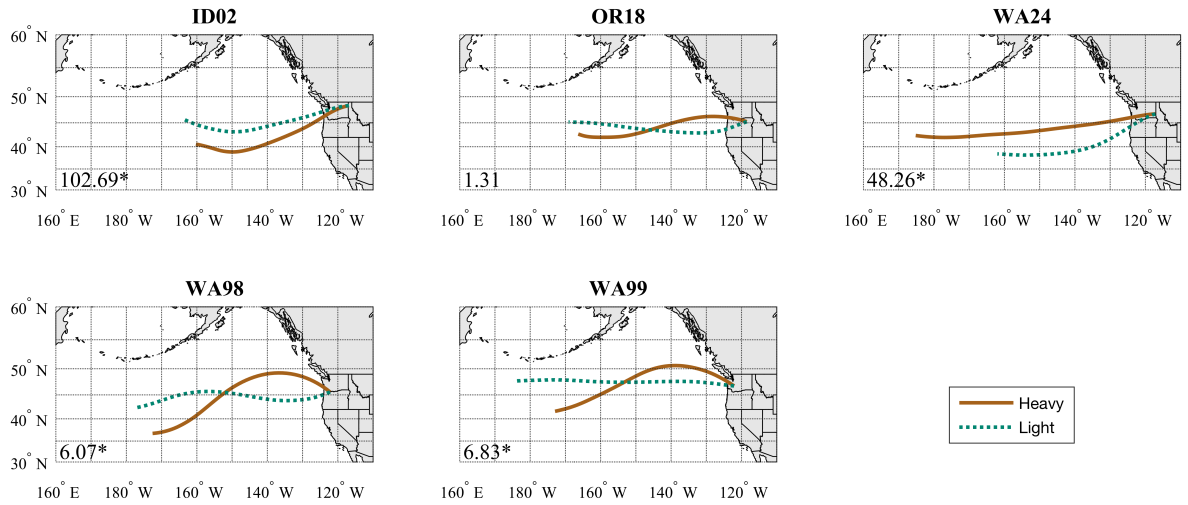

Figure 2.6. Seasonal mean trajectories for February-March. Dotted green trajectories show storm tracks for the precipitation days from the bottom decile of stable isotope ratios ('light' precipitation), and solid brown trajectories show storm tracks for the precipitation days from the top decile of stable isotope ratios ('heavy' precipitation). Results of two-sample Hotelling's T^2 test statistics for the two seasonal mean trajectories at each site are in the lower left corner of each map. Values with asterisks indicate significantly different mean trajectories for the pairing.

During April-May, many of the period mean trajectories originate around 50°N, farther north than many of the cooler-season trajectories (Figure 2.7). Several of these trajectories are also considerably shorter than for other periods, suggesting slower movement and more local origin (a notable exception is the heavy trajectory for WA99). The period mean trajectories for low $\delta^{18}O$ values originate in more northwesterly locales than during much of the rest of the year and exhibit more curved and notably less zonal flow patterns. Again, WA98 and WA99 are similar to each other, while the three higher-elevation inland sites exhibit similar characteristics.

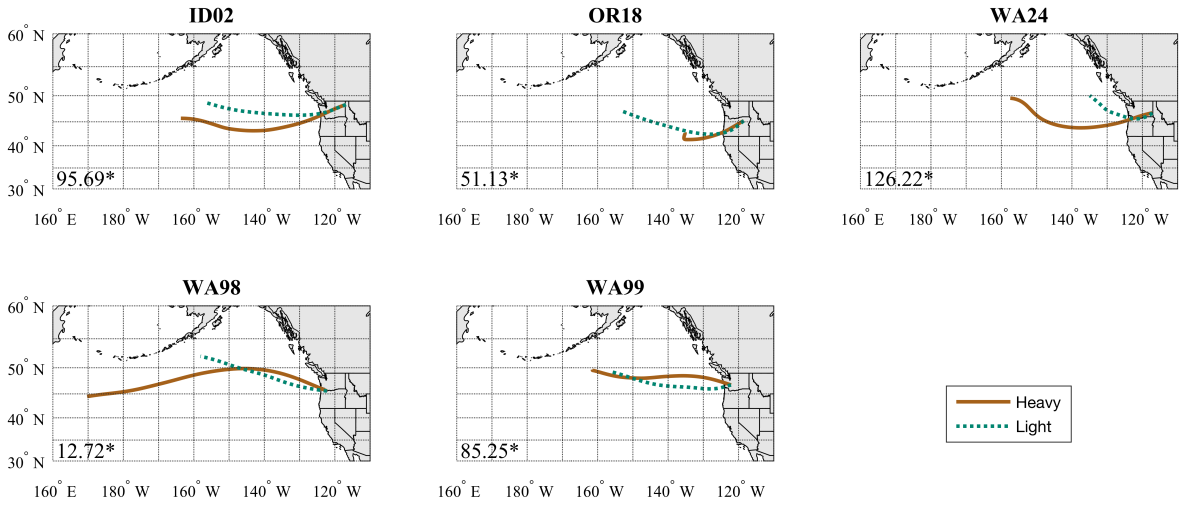

Figure 2.7. Seasonal mean trajectories for April-May. Dotted green trajectories show storm tracks for the precipitation days from the bottom decile of stable isotope ratios ('light' precipitation), and solid brown trajectories show storm tracks for the precipitation days from the top decile of stable isotope ratios ('heavy' precipitation). Results of two-sample Hotelling's T^2 test statistics for the two seasonal mean trajectories at each site are in the lower left corner of each map. Values with asterisks indicate significantly different mean trajectories for the pairing.

In June-September, there is a distinctly meridional, southerly/southwesterly trajectory for precipitation with high $\delta^{18}O$ values at the three leeward sites and relatively zonal trajectories for precipitation with low $\delta^{18}O$ values at most sites (Figure 2.8). At OR18, both period mean trajectories follow nearly identical paths, though the low-value trajectory is considerably longer and faster moving than the high-value trajectory. At WA98 and WA24, the high-value trajectory originates well above 50°N, higher north than the low-value trajectory. This could be impacted by a single precipitation event or could be indicative of precipitation that is less driven by mid-latitude cyclones, especially compared with the common trajectories in the cooler months when winter storms produce most of the region's annual precipitation.

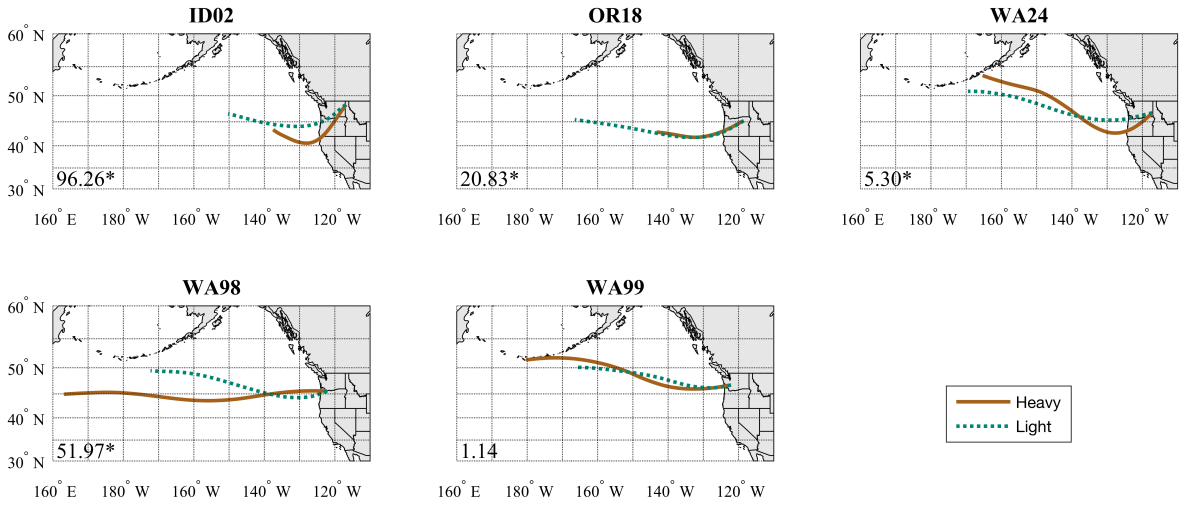

Figure 2.8. Seasonal mean trajectories for June-September. Dotted green trajectories show storm tracks for the precipitation days from the bottom decile of stable isotope ratios ('light' precipitation), and solid brown trajectories show storm tracks for the precipitation days from the top decile of stable isotope ratios ('heavy' precipitation). Results of two-sample Hotelling's T^2 test statistics for the two seasonal mean trajectories at each site are in the lower left corner of each map. Values with asterisks indicate significantly different mean trajectories for the pairing.

Hours over land

Of their 72-hour duration, period mean trajectories spend between two and 24 hours over land. Trajectories leading to precipitation with low $\delta^{18}O$ values, warm-season trajectories, and trajectories terminating at the three leeward sites generally spend more time over land than their high- $\delta^{18}O$-value-producing, cool-season, and windward-site counterparts (Table 2.2). For example, the site with the highest average time spent over land is ID02 (site mean: 11.8 hours), where the site average period mean trajectory spends more than four times longer over land than for WA99 (site mean: 2.7 hours). This characteristic could potentially lead to the leeward sites exhibiting, on average, precipitation with lower $\delta^{18}O$ values than at other sites due to rainout over the course of transport inland. The leeward sites are also likely to experience more within-cloud processes as precipitating air masses spend more time over land, particularly during the warmer months. The windward sites exhibit very little variation in this metric (ranging from two

to eight hours across all periods), while the three inland sites show much larger ranges across periods. When only the inland sites are considered, the difference between cool and warm season time over land increases from 4.2 hours to 6.5 hours. This longer time spent over land could allow for more convective activity and moisture recycling at these sites during the warm season.

Table 2.2. Hours spent over land by seasonal mean trajectories.

Site	Decile	ON	DJ	FM	AM	JJAS	Site Avg. by Decile	Site Avg.
ID02	Top	9	6	10	9	21	11 ± 5.8	11.8 ± 5.6
	Bottom	8	7	10	19	19	12.6 ± 5.9	
OR18	Top	9	6	6	10	19	10 ± 5.3	10.5 ± 4.1
	Bottom	8	11	9	16	11	11 ± 3.1	
WA24	Top	8	9	7	9	12	9 ± 1.9	10.5 ± 5.0
	Bottom	11	7	9	24	8	11.8 ± 7.0	
WA98	Top	2	3	3	2	2	2.4 ± 0.5	2.7 ± 0.7
	Bottom	2	3	3	4	3	3 ± 0.7	
WA99	Top	3	4	3	4	3	3.4 ± 0.5	3.9 ± 1.6
	Bottom	3	3	3	8	5	4.4 ± 2.2	
	Average	6.3 ± 3.4	5.9 ± 2.7	6.3 ± 3.1	10.5 ± 7.1	10.3 ± 7.3		

Cluster mean trajectories

Our discussion of cluster mean trajectories will focus on examples of clusters that are representative of overall patterns among sites or that exhibit deviations from expected patterns. We also include some probabilistic results to convey the frequency of certain air mass trajectories and to emphasize the process of quantifying patterns using HYSPLIT. While the individual cluster means provide information not otherwise available by looking at period means, only some of the clusters for each site/period/decile combination represent distinct pathways when compared with the other decile for the same site and period.

Seasonal patterns in cluster mean trajectories

In October-November, the cluster mean trajectories exhibit more differences than would be assumed by looking at the period mean trajectories. Several of the low-$\delta^{18}O$-value cluster mean trajectories originate north of Alaska at greater than 70°N and travel considerable distances over land, while none of the high-$\delta^{18}O$-value cluster mean trajectories exhibit this pattern (Figure 2.9). Conversely, several high-value cluster mean trajectories (notably for the sites farther inland) originate near southern California and Baja California and follow short, meridional paths across the interior of the western United States. These southerly trajectories comprise anywhere from 14% to 24% of all trajectories within a given site/period combination of high-value trajectories, and an additional 19-30% originate near Hawaii. Overall, while some clusters for both the low-value and high-value trajectories exhibit westerly flow, each of the two sets includes some clusters that exhibit patterns not seen in the other set.

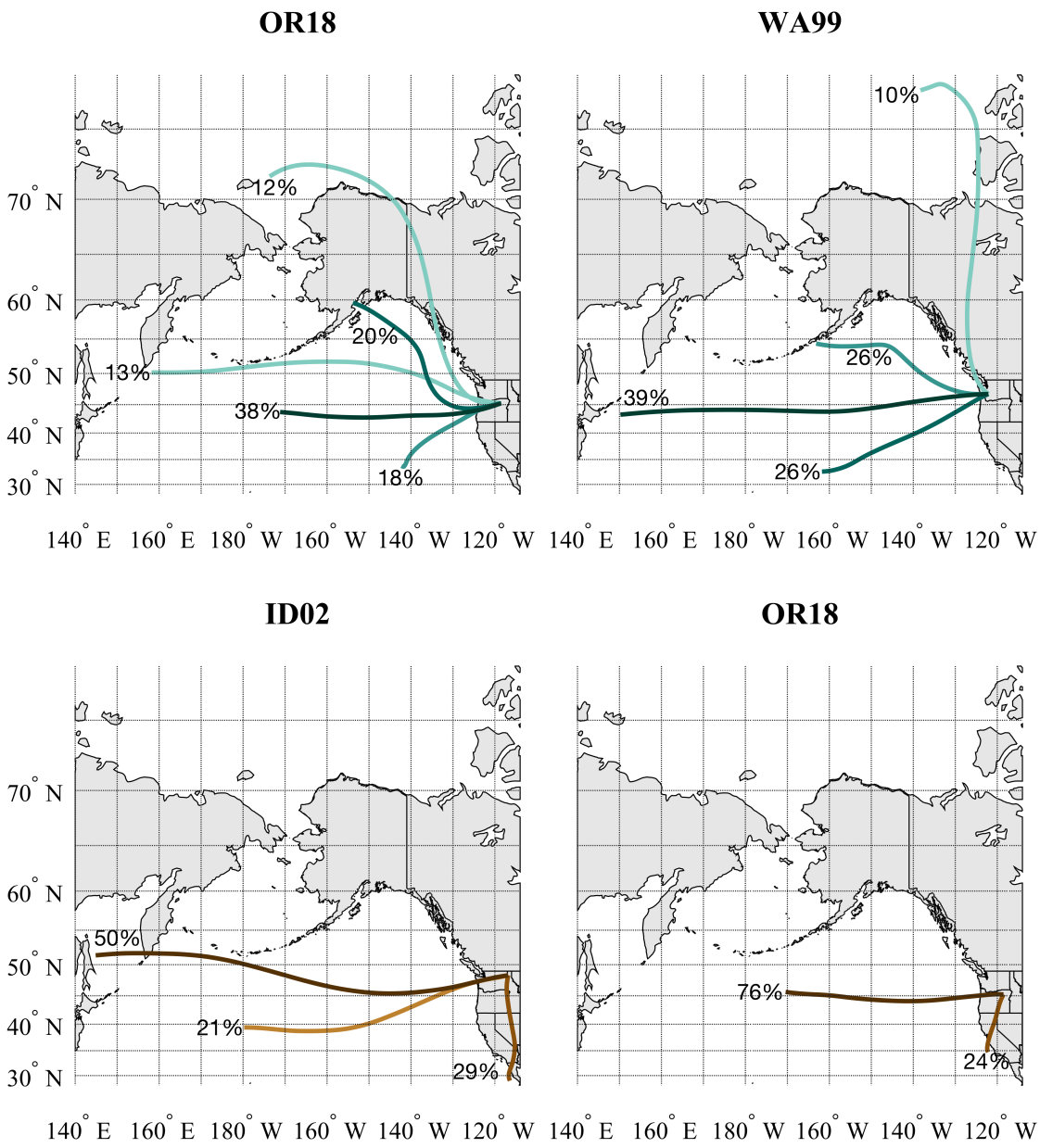

Figure 2.9. Selected cluster mean trajectories that produced precipitation with low $\delta^{18}O$ values (top) and high $\delta^{18}O$ values (bottom) precipitation during October-November. Each cluster mean is labeled with the percentage of trajectories represented by the given cluster.

Differences in cluster mean trajectories for December-January do not demonstrate the same patterns as for October-November. However, a low-value cluster mean for OR18 (representing 11% of total trajectories for the site/period/decile combination) is the only

trajectory that spends nearly the full 72 hours over the interior of the continental United States, and there is one cluster for WA24 (representing 13% of total trajectories for the site/period/decile combination) that exhibits strongly meridional flow and passes inland over western Canada for nearly the full 72 hours (Figure 2.10). The high-value cluster means do not demonstrate this overland passage, though many do originate at latitudes above 50°N, such as several clusters for OR18 (24% of total) and WA98 (16% of total) (Figure 2.10). Several cluster means for both low-value and high-value trajectories originate near Hawaii (Figure 2.10) and comprise anywhere from 35% to 55% of total trajectories.

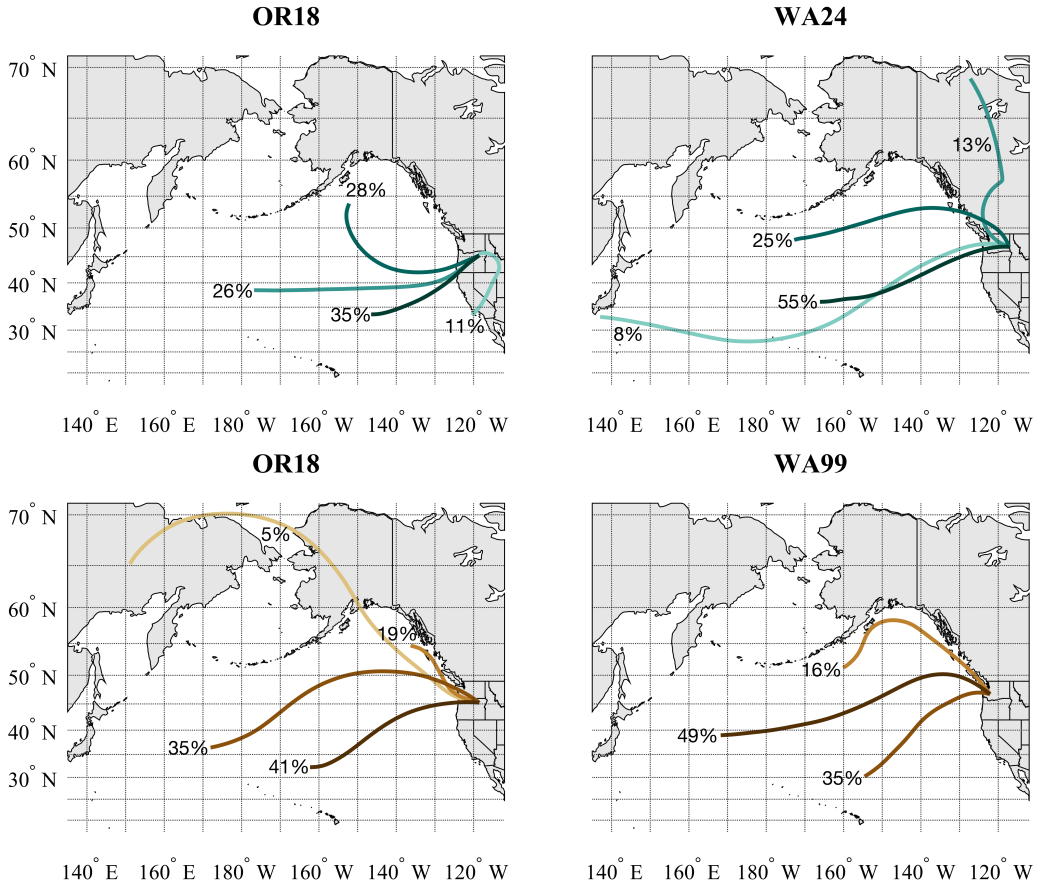

Figure 2.10. Selected cluster mean trajectories that produced precipitation with low $\delta^{18}O$ values (top) and high $\delta^{18}O$ values (bottom) precipitation during December-January. Each cluster mean is labeled with the percentage of trajectories represented by the given cluster.

In February-March, there are notable southwesterly cluster means originating close to Hawaii that produce precipitation with high $\delta^{18}O$ values at all five sites and represent anywhere from 19% to 41% of the trajectories for a given site and period (Figure 2.11). While there is a large proportion of southwesterly trajectory means for the samples with low $\delta^{18}O$ values (up to 48%), they do not originate near Hawaii and tend to demonstrate a shorter, more curved pattern and originate well north of 30°N (Figure 2.11). Some clusters representing both deciles demonstrate zonal flow originating near Russia along with relatively meridional flow originating near the Aleutian Islands, making the shape and origin of the southwesterly trajectories the most defining factor between deciles during this period.

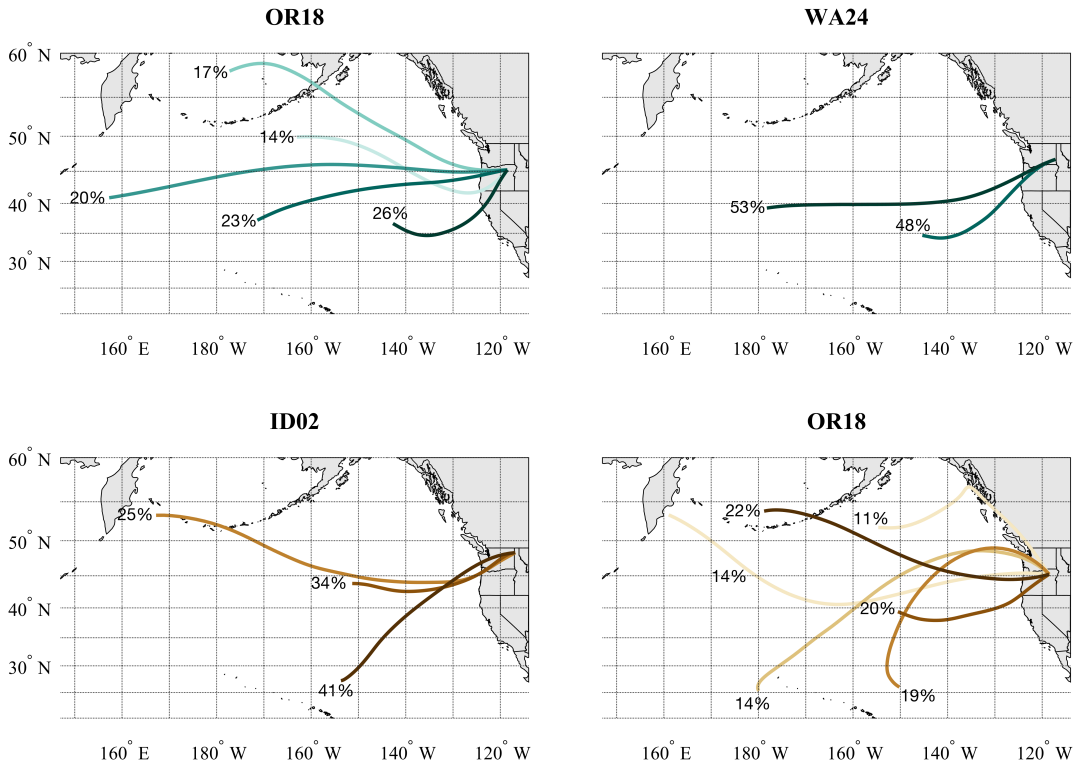

Figure 2.11. Selected cluster mean trajectories that produced precipitation with low $\delta^{18}O$ values (top) and high $\delta^{18}O$ values (bottom) precipitation during February-March. Each cluster mean is labeled with the percentage of trajectories represented by the given cluster.

Several cluster mean trajectories for precipitation with low $\delta^{18}O$ values, notably those for WA24 and WA99, demonstrate excursions into the interior in April-May (Figure 2.12). These cluster mean trajectories for WA24 and WA99 represent 36% and 67% of the low-$\delta^{18}O$-value trajectories for each of those sites during this period, indicating that these tracks (which likely experienced considerable rainout during their extended time over the interior) are likely common features during this period rather than the influence of a single precipitation day or event. Notably, there are no southwesterly tracks for the low-$\delta^{18}O$-value cluster means, though several of the high-$\delta^{18}O$-value clusters originate south of 35°N whereas all of the low-$\delta^{18}O$-value cluster means originate north of 40°N (Figure 2.12). At four of the five sites, high-$\delta^{18}O$-value precipitation was produced by clusters with southwesterly flow that accounted for between 7% and 53% of trajectories.

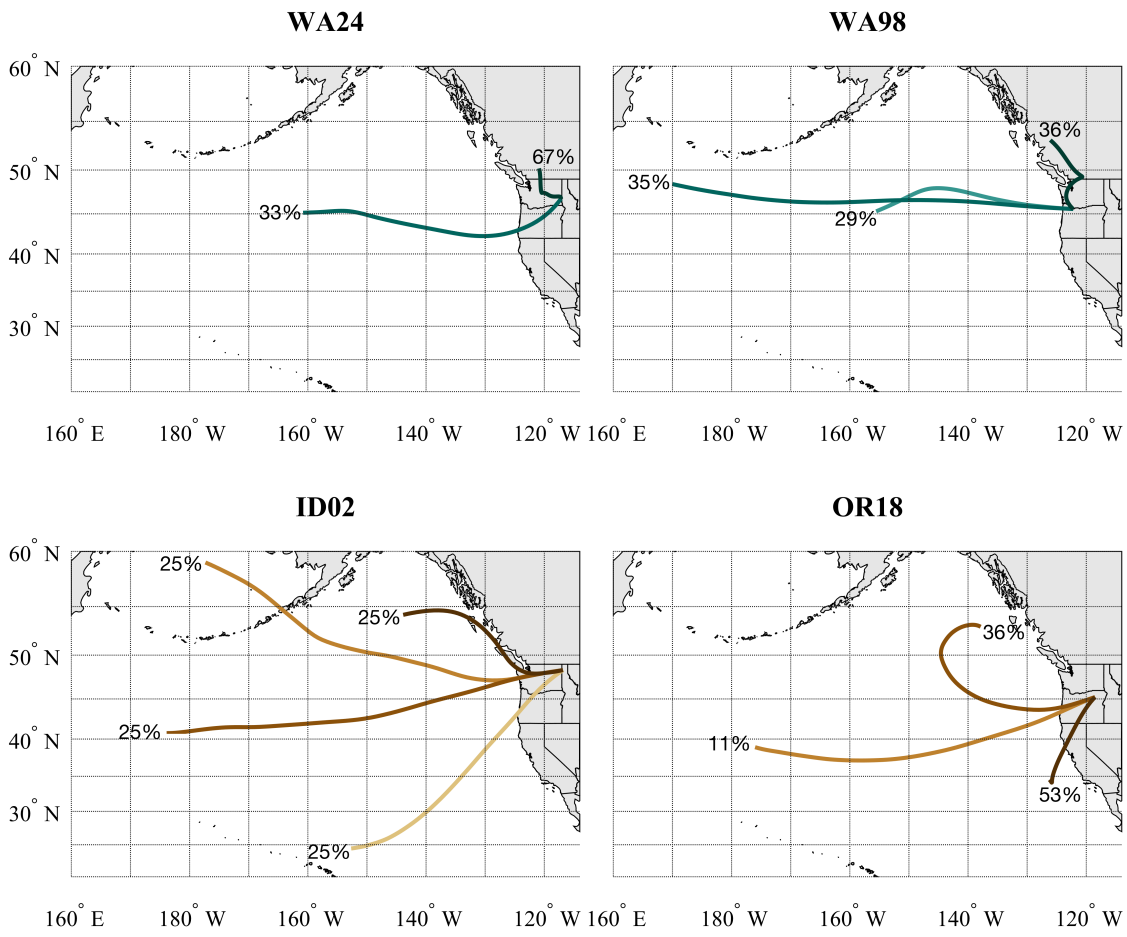

Figure 2.12. Selected cluster mean trajectories that produced precipitation with low $\delta^{18}O$ values (top) and high $\delta^{18}O$ values (bottom) precipitation during April-May. Each cluster mean is labeled with the percentage of trajectories represented by the given cluster.

In June-September, the cluster mean trajectories exhibit several of the patterns demonstrated in other period, including interior excursions that produced precipitation with low $\delta^{18}O$ values (e.g., ID02 and WA24) and nearly southerly trajectories originating near the coast of southern California that spent considerable time over the interior before producing precipitation with high $\delta^{18}O$ values (Figure 2.13). ID02 and OR18 provide examples of the latter trend, with 80% and 45% of trajectories from southerly sources, respectively. However, as with several other periods, cluster means for both sites exhibited westerly and relatively zonal flow, and in

many cases these clusters represented a majority of trajectories for the given site/period/decile combination.

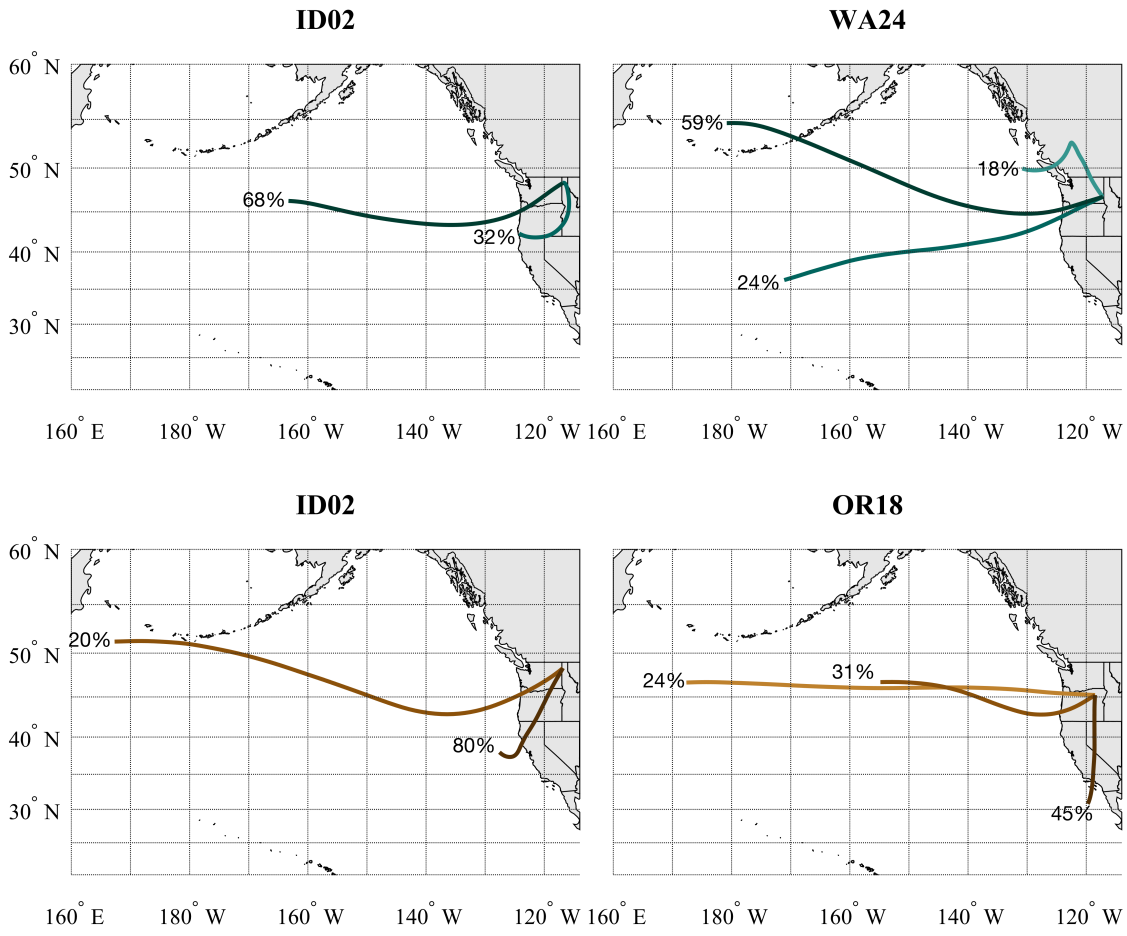

Figure 2.13. Selected cluster mean trajectories that produced precipitation with low $\delta^{18}O$ values (top) and high $\delta^{18}O$ values (bottom) precipitation during June-September. Each cluster mean is labeled with the percentage of trajectories represented by the given cluster.

Discussion

Our findings suggest that a combination of distance inland and position on the windward versus leeward side of the Cascades impact the quantitative and qualitative characteristics of period mean trajectories. The absence of high-elevation sites on the western side of the Cascades and lower-elevation sites on the eastern side of the Cascades complicates untangling the

influence of elevation versus distance inland. However, our findings align with the extensively documented impacts of complex topography and the resulting orographic effect on precipitation patterns (Leung *et al.*, 2003; Minder *et al.*, 2010) and the continental effect on the stable isotope composition of precipitation (Winnick *et al.*, 2014). Both of these effects lead to precipitation with lower $\delta^{18}O$ values with movement inland and provide a process-based framework for interpreting our results.

Vachon *et al.* (2010b) suggested that local conditions (namely condensation and evaporation temperatures) likely exert more influence on the isotope ratio of precipitation in mountainous areas than does moisture source. However, more recent studies suggest that temperature only emerges as a strong control on precipitation isotope values when seasonal temperature changes are incorporated (Akers *et al*. 2017; Bailey *et al*. 2019). We find that seasonal variation in deuterium-excess values on the windward and leeward sides of the range suggests that the dry sites on the leeward side of the Cascades experience more convective conditions and moisture recycling than the sites on the windward side of the range during the summer months, pointing to local conditions as a dominant factor. This finding also helps to contextualize the instances where some northerly cluster mean trajectories, which would be expected to lead to precipitation with lower $\delta^{18}O$ values due to the temperature effect, lead to precipitation with higher $\delta^{18}O$ values at OR18 and ID02. We also find that trajectories that originated farther north, which are likely to be colder than those originating farther south, often produce precipitation with lower $\delta^{18}O$ values at our sites, suggesting that both local conditions and moisture source considerably impact the stable isotope ratios of precipitation at our sites. Changes in moisture source over the course of the year may also play an important role and have been suggested as a driving factor behind isotope slopes, which measure the rate of change in

$\delta^{18}O$ with distance inland and are one means of quantifying the continental effect (Rozanski *et al*., 1993), particularly in coastal regions (Vachon *et al.*, 2010b). This may help to explain why we find more distinct shifts between moisture sources at our two relatively coastal sites than at our three inland sites.

Our isotope ratios and $\delta^{18}O$ slope (‰ per 100 km of movement inland) align with existing research in the Pacific Northwest. We found, on average, a 5‰ difference between $\delta^{18}O$ values on the windward and leeward side of the Cascades, which is comparable with the differences reported by Liu *et al.* (2013) for weekly USNIP precipitation samples during January-March 1990 and 1992. The values are also similar to those identified by Smith *et al*. (2005) for streamflow water samples taken from a longitudinal gradient from 120.22°W to 123.97°W across Oregon during June-July 2003, though three of our sites lie farther east. Latitude is unlikely to have much effect on isotope slopes in the Pacific Northwest, as the latitudinal isotopic gradient is weak in this region (Vachon *et al.*, 2010a). These findings are consistent with the concept of "orographic airmass transformation" (Smith, 2018) and the preferential loss of heavier isotopologues as air passes over a mountain range and rainout occurs (Dansgaard, 1964; Gat, 1996). The isotope ratios we measured for OR18 align with those found at the same site by Welker (2000), who suggested that the site is representative of a temperate moisture source. However, we found a much smaller decrease in $\delta^{18}O$ values with inland movement across the PNW, with a site difference between WA98 and WA24 (which lie at nearly identical latitudes) of 0.7‰ per 100 km in contrast with Welker's decrease of 1.2‰ per 100 km between NADP sites OR02 and OR18 (Welker, 2000). This gradient is still more dramatic than that reported by Rozanski (1993) for movement across Europe and South America and suggests

that complex topography likely drives this difference, though differences in moisture source region may also play a role.

In our analysis of air mass trajectories, we capture synoptic-scale atmospheric circulation that is typical of the region during different times of the year. While the Pacific storm track is generally zonal (Chang *et al.,* 2002), it shifts toward the equator in cooler months and toward the poles in warmer months (Chang *et al.,* 2002; Mesquita *et al.*, 2010), typically meandering between about 35 and 50°N (Nakamura, 1992). This aligns closely with the range of latitudes we found, with the trajectories of some individual precipitation events originating at higher latitudes, especially in the warm season (Figure 2.2). Birks and Edwards (2009) also noted that zonal flow is associated with negative isotope anomalies in western Canada, and that large-scale atmospheric circulation is partially responsible for the stable isotope ratios of precipitation in the region, especially in the winter months, which also aligns with our findings.

Although variations in moisture source and air mass trajectories are likely responsible for many of the patterns described in our results, the amount effect confounds these results during heavy precipitation events. For example, additional back-trajectory analyses for a heavy rainfall event (7.4 cm in 48 hours) at WA99 from March 14th through 16th, 2015, suggested a southerly moisture source that produced a precipitation sample with a low $\delta^{18}O$ value. The framework proposed by Dansgaard (1964) suggests that in heavy rainfall events like this, the relatively low $\delta^{18}O$ values recorded are likely to be indicative of extensive rainout during a heavy precipitation event rather than indicating a colder, more northerly moisture source. Based on analyses of our data, amount effect impacts at our sites are prominent mostly during the warm season and when daily precipitation exceeds 1.5 inches/3.8 centimeters (analyses not shown). Although our approach to the identification of moisture source that combines methods in stable isotope

geochemistry with meteorological records and back-trajectory analysis helps to remedy this issue, it does not remove all uncertainty, as is demonstrated by the wide variety of paths taken by cluster mean trajectories leading to precipitation with both low and high $\delta^{18}O$ values across all seasons.

Summary and Conclusions

In this study, we used the stable isotope ratios of weekly precipitation samples to guide the selection of dates for back-trajectory modeling with the goal of better understanding the relationship between the stable isotope ratio of precipitation and air mass trajectories for five sites in the U.S. Pacific Northwest. We investigated trends at the seasonal level to produce a narrative of variability in zonal to meridional flow in correspondence with changes in the season and resultant stable isotope ratio of rainfall. We found statistically significant differences between the period mean trajectories that produced the highest and lowest decile of $\delta^{18}O$ values in precipitation samples for all but two of the twenty-five combinations of sites and periods ($\alpha \leq 0.05$). We also found a wide range of time spent over land by different trajectories across periods, with an overall trend toward more time spent over land during the fall and summer and within trajectories delivering precipitation with lower $\delta^{18}O$ values.

In general, air masses trajectories that lead to precipitation with higher $\delta^{18}O$ values in our study region more frequently originate in southerly regions and follow more meridional paths, whereas air masses trajectories that lead to precipitation with lower $\delta^{18}O$ values often originate in northerly regions and spend considerable time over the continental interior. We suggest that stable isotope ratios of precipitation in the Pacific Northwest are largely driven by moisture source and the air mass trajectory followed by that precipitation in the 72 hours leading to

rainout. These trajectories largely reflect seasonal changes in storm tracks that drive much of the region's annual precipitation, highlighting the linkages between synoptic-scale flow and the resulting stable isotope ratio of precipitation.

Our results demonstrate considerable nuance among sites and periods and suggest that complexity may arise from a variety of factors including rainout and topography. We find that the amount effect impacts our ability to infer moisture source when daily precipitation exceeds 1.5 inches/3.8 centimeters, and finer-scale effects cannot be completely untangled using the weekly dataset we used in this study. Future research using event-based precipitation samples would significantly enhance the ability to directly link the stable isotope ratios of rainfall with the air mass trajectories and meteorological conditions that produced that rainfall. In addition, while our findings highlight the ability of stable isotope ratios to capture a variety of signals and represent various processes, they also demonstrate a complicated relationship between air mass trajectories and the stable isotope ratio of precipitation that must be considered when interpreting isotope records in the region. This outcome highlights the importance of considering meteorological data and local precipitation records to contextualize the outcomes of back-trajectory analyses, especially those involving cluster analyses. It also highlights that while different air mass trajectories drive isotopically distinct rainfall in the study area, the relationship between the two variables is complex and warrants further investigation.

Stable isotope ratios in tree rings (McCarroll and Loader, 2004), speleothems (McDermott, 2004), bone (Hedges *et al.*, 2004), corals (Lough, 2010), and other natural archives (Ghosh and Brand, 2003) provide critical information about paleoclimate and enable climate reconstruction at a variety of spatial and temporal scales. While technological advancements have recently improved measurement precision (Ghosh and Brand, 2003), the interpretation of

individual proxies in different regions requires additional study. For example, assessment of the connections between synoptic-scale circulation (and coupled ocean-atmosphere dynamics more broadly) and the stable isotope ratio of precipitation is one key step toward building a framework to enable the interpretation of paleoclimate records within a given region (Bailey *et al*., 2015). The patterns identified here will help improve interpretation of seasonal tree-ring proxy records in the Pacific Northwest, which can capture unique and fine-scale climate information. This is especially important in our study region and others where traditional tree-ring width records may not capture adequate climate information for reconstruction. More generally, an enhanced understanding of the relationship between the stable isotope ratio of precipitation and the air mass trajectory that likely produced it can help to guide interpretation of isotope records and support more robust inferences about how storm tracks and moisture source shift across seasons and locations, providing context for current conditions and improving future projections in a changing climate.

CHAPTER 3: SUB-ANNUAL RING-WIDTH MEASUREMENTS ADD SEASONAL CLIMATE INFORMATION ACROSS AN ARIDITY GRADIENT IN THE U.S. PACIFIC NORTHWEST

Introduction

In June and July 2021, extreme heat, extended drought, and resulting wildfires in the Pacific Northwest of North America caused hundreds of excess deaths, destroyed infrastructure, and triggered crop failure. A rapid attribution analysis of the event suggested that climate change made the heat wave 2°C hotter than it would have been in preindustrial times and forecast that similar "1000-year events" could occur every five to ten years in a world with 2°C of global warming (Philip *et al.*, 2021). This event and resultant analyses of its contributing factors highlight the rapid changes taking place in the Pacific Northwest (PNW, defined here as the U.S. states of Washington, Oregon, and Idaho and the Canadian province of British Columbia) and the need to understand seasonal climate patterns in the region and develop strategies for reacting to future changes, especially in the water supply.

Precipitation drives hydropower that accounts for over 50% of American energy and 92% of Canadian energy generated in the PNW (Bonneville Power Administration, 2019; Electricity Canada, 2012), and lack of winter precipitation and summer precipitation can both drive drought that threatens this resource (Littell *et al.*, 2016). The amount and seasonality of precipitation that drives the supply of and demand for hydropower are already changing in the PNW (Zhang *et al.*, 2021) and are likely to continue to change considerably due to climate change (Hamlet *et al.*, 2010; Bartos and Chester, 2015) in a heterogeneous pattern largely impacted by fine-scale

factors like land cover and topography (Diffenbaugh *et al.,* 2005). These changes further complicate water resource management: while peak demand and subsequent shortfalls in the PNW typically occur during winter cold snaps, hotter summers are leading to increased cooling demands while snowpack, summer precipitation, and subsequent hydropower generation decrease (Turner *et al.*, 2019). This compounding of temperature and precipitation changes is increasing the frequency of power shortfall events in the summer (Turner *et al*., 2019) while heat waves become more common and cities like Seattle experience a rapid adoption of air conditioning (United States Census Bureau, 2019; Balk, 2021). Therefore, it is crucial to improve the understanding of seasonal precipitation patterns in the PNW to better inform water resource management and provide more nuanced insight into how hydroclimate varies at different altitudes and locations within the region across time. Tree-ring width metrics provide a readily accessible means of contributing to this insight.

The variability in the width of trees' annual growth rings has been widely used to understand and reconstruct past climate due to the proxy's broad geographic distribution and annual resolution (Fritts, 1976). The reliance of tree growth and activity on climatic conditions, and particularly temperature and precipitation, along with their geographic distribution has long made them a favored high-resolution proxy for understanding local and regional climate (Briffa *et al*., 1996). In addition to total annual ring width (TRW), earlywood width (EW) and latewood width (LW) (e.g., Meko and Baisan, 2001; Stahle *et al*., 2009), maximum latewood density (MXD) (e.g., Briffa *et al.*, 1988; D'Arrigo *et al.*, 1992), measurements of blue intensity (BI) (e.g., McCarroll *et al.*, 2002; Buckley *et al.*, 2018), positioning of intra-annual density fluctuations (IADFs) (e.g., Campelo *et al.*, 2006; Vieira *et al*., 2010), and the isotopic composition of whole wood and wood components (primarily of $\delta^{18}O$ and $\delta^{13}C$ values of

cellulose) (e.g., Anderson *et al.*, 1998; Saurer *et al.*, 2008; Andreu-Hayles *et al*. 2017) may be used to isolate and enhance seasonal climate signals and provide finer-scale climate histories.

While MXD and isotopic analyses have proven useful for isolating seasonal signals, the time, training, labor, and expense required for these methods makes them difficult to deploy quickly and at large scales. Alternatively, simple measurements of EW and LW width are possible using basic dendrochronological equipment and procedures and are therefore more accessible and hold potential for widespread enhancement of the understanding of seasonal-scale climate variability. To this end, subannual index chronologies (of earlywood and latewood, referred to in earlier works as "spring wood" and "summer wood," respectively) for various species of *Pinus* (Soulé *et al.*, 2021), *Pseudotsuga* (Cleaveland, 1983; Meko and Baisan, 2001), *Quercus*, and others (Torbenson *et al.*, 2016) have been developed over the past several decades, especially in arid regions such as the U.S. southwest.

In comparison, studies of EW and LW in the PNW have been recent and limited (Robertson *et al.*, 1990; Watson and Luckman, 2002; Crawford *et al.* 2015; Dannenberg and Wise, 2016). Many EW and LW measurement efforts have focused on Douglas-fir (*Pseudotsuga menziesii*), mountain hemlock (*Tsuga mertensiana*), Engelmann spruce (*Picea engelmannii*), and Pacific silver fir (*Abies amabilis*) (ITRDB, 2021), though some studies have examined Ponderosa pine (*Pinus ponderosa*) (Watson and Luckman, 2002; Dannenberg and Wise, 2016). These studies largely found positive correlations between LW and summer precipitation, and they suggest that EW tends to capture prior growing season precipitation while LW more closely reflects current-growing-season precipitation amount (Watson and Luckman, 2002; Crawford *et al.* 2015; Dannenberg and Wise, 2016) or annual water deficit (Robertson *et al.*, 1990). However, they have produced conflicting results for two parameters: the strength of climate response in

EW and the utility of adjusted latewood width (LW_{adj}) as an improved indicator of summer precipitation variability. While the majority of studies in the PNW have found a significant climate response in EW, Robertson *et al.* (1990) noted that this response differed greatly between subhygric, submesic, and xeric sites on Vancouver Island. In their work on LW_{adj}, Crawford *et al*. (2015) found that LW_{adj} retained climate signals from the prior fall and early winter at sites in the northern Rocky Mountains despite the attempted removal of latewood dependence on antecedent earlywood. Therefore, further research is needed to examine the climate signals captured by these metrics at diverse sites in the PNW to understand how they vary across space and site aridity.

Here, we establish the extent to which seasonal variations in total precipitation and average temperature are captured by TRW, EW, LW, and LW_{adj} of *Pinus ponderosa* trees at three sites in the U.S. Pacific Northwest by testing the following hypotheses:

1) EW, LW, and LW_{adj} measurements enhance overall climate signal capture at our sites when compared with TRW alone
2) EW measurements reflect moisture from early in the growing season and prior to the growing season at our sites while LW and LW_{adj} measurements reflect moisture from later in the growing season
3) LW_{adj} isolates summer precipitation signals at our sites

We show that all four ring-width metrics do capture seasonal climate information in our study area, and all three subannual metrics add information that is not available from total annual ring widths alone.

Materials and Methods

Study sites and climatology

To examine the relationship between tree-ring width measurements and local and regional climate, we selected three field sites for tree core collection (Figure 3.1). The field sites are located in close proximity to the three leeward (eastern) NADP sites used and discussed in Chapter 2 and were selected for comparison between tree-ring width and climate data in this chapter and tree-ring isotope and climate data in the following chapter (Chapter 4). We retain the NADP naming scheme in this study: 1) to maintain consistency with previous studies of NADP data; 2) to facilitate direct comparison with NADP precipitation samples in Chapters 2 and 4; and 3) to clearly include the state in which each site is located in its name.

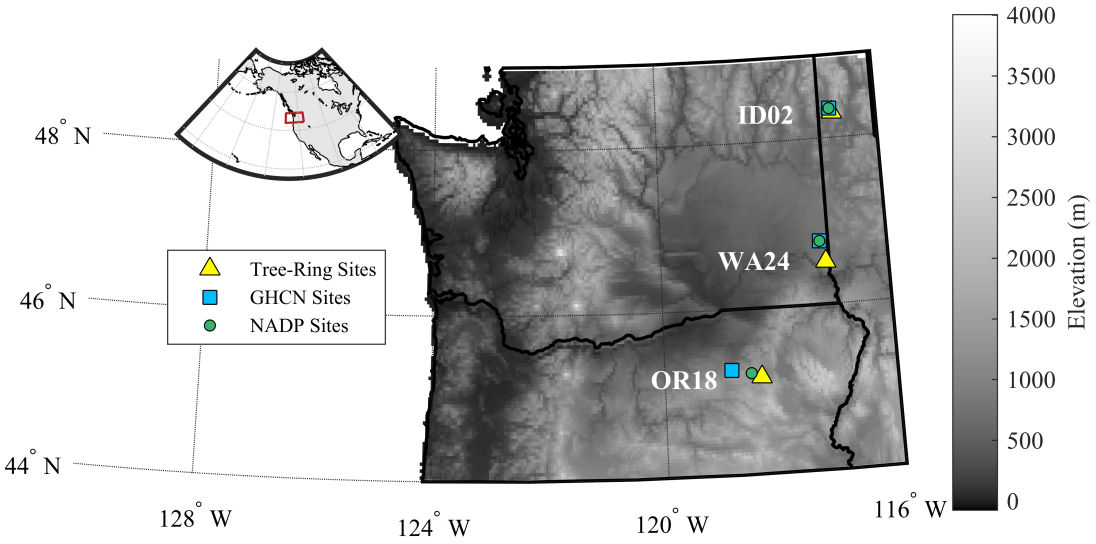

Figure 3.1. Location of study sites within the Pacific Northwest. All three tree-ring sites are located in close proximity to NADP climate data sites.

Winter storms are a predominant force in PNW climate and bring considerable precipitation from October through March and April (NOAA, 2013). The resulting snowpack

accounts for 50 to 70 percent of annual precipitation in mountainous regions of the western U.S., which subsequently determines streamflow during the warm season (Hunter *et al*., 2006). Summers in this region are generally dry, particularly east of the Cascade Range. Consequently, the Columbia River Basin in eastern Washington (which includes our driest site, WA24) is one of the most arid regions of the continental United States (NOAA, 2013). While winter months bring considerable precipitation with average temperatures near or below freezing at our sites, summer months bring low and often trace precipitation totals along with temperatures of 15°C or higher (Figure 3.2), with July and August exhibiting the highest temperature and water stress at all sites (Table A1).

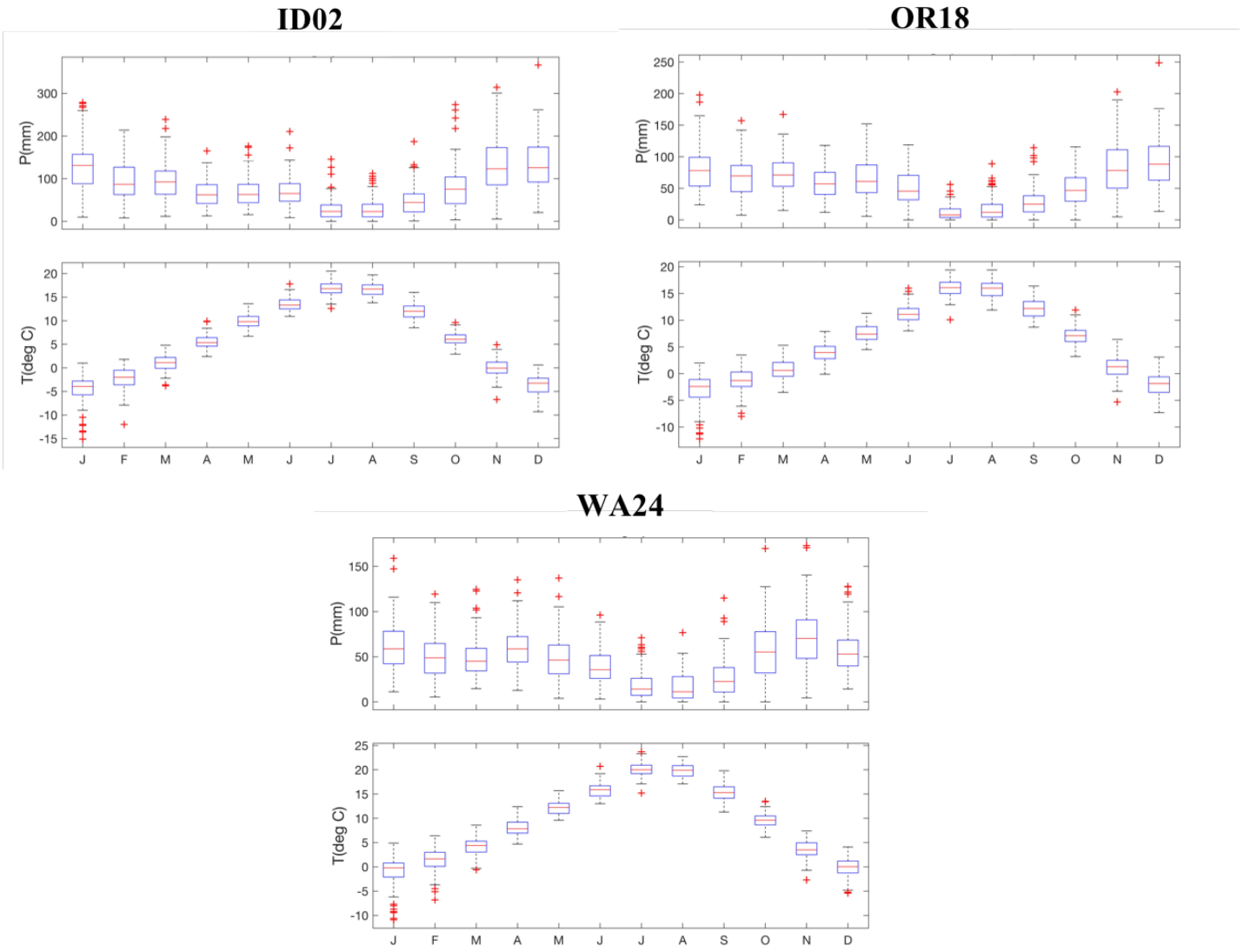

Figure 3.2. Climographs showing monthly temperature and total precipitation at the three tree collection sites over the study period at each site. Climate data retrieved from PRISM; see Table A1 for numerical inputs and additional climate variables.

Although the three sites have broadly similar climates, they represent a gradient of precipitation ranging from an annual average of 572 mm (WA24) to 971 mm (ID02) (Table A1). They also experience differing levels of water stress with considerably higher values of maximum vapor-pressure deficit at WA24 than at OR18 or ID02 (Table A1). We refer to a gradient from ID02 → OR18 → WA24 to indicate lower to higher water stress when comparing the three sites, and we present most results in this order to emphasize this gradient and its impacts on the climate-growth relationship. Precipitation and temperature are strongly intercorrelated at all three sites; the relationship is direct during the winter (November-February) and inverse during the spring, summer, and fall (Figure A1), and it is strongest at the monthly level and becomes weaker with longer seasonal subsets. Interestingly, the relationship remains relatively constant at OR18 at one-month through twelve-month seasonal subsets.

These broadly similar climates produce considerable overlap in dominant tree species. Washington state is dominated by four types of softwood conifer forests: Douglas-fir, fir/spruce/mountain hemlock, western hemlock/Sitka spruce, and ponderosa pine (Campbell *et al.*, 2010). Similarly, Oregon is dominated by Douglas-fir and western hemlock in the west and ponderosa pine, western juniper, and lodgepole pine in the east (Bansal *et al.*, 2017), and northern Idaho is dominated by Douglas-fir and various fir/spruce/hemlock species (Holte, 2012). We sampled *Pinus ponderosa* at each of our three sites as it is sensitive to climate, has been previously studied in the region and therefore can be meaningfully compared, and is abundant across much of our study area.

Tree ring-width measurements

We collected 12mm cores and 5.5mm cores from three sites across Washington State, Oregon, and Idaho (Figure 1) during July 2019. Two 12mm cores were collected from five to ten trees at each site to be isotopically analyzed for another study (Chapter 4), and additional 5.5mm cores were collected from at least six more trees at each site to assist with crossdating and ring-width chronology development. All cores were processed and crossdated using standard dendrochronological procedures (Stokes and Smiley, 1968). Earlywood and latewood boundaries were determined using the technique outlined by Stahle *et al*. (2009), and the annual EW and LW of each core were measured using Tellervo, which also calculates TRW (www.tellervo.org; Brewer, 2014). We used the program COFECHA (Holmes, 1983) to check for dating and measurement errors in the TRW series and detrended the resulting quality-controlled measurements in ARSTAN (Cook, 1985) with a cubic smoothing spline two-thirds the length of the series to produce index chronologies of TRW, EW, and LW at each site. Expressed population signal (EPS; Wigley *et al.*, 1984) for all total and partial ring-width chronologies was greater than 0.85 for all periods of overlap with climate data at ID02 and OR18 and from 1915 onward at WA24 (Table A2).

The dependence of LW on antecedent EW often obscures any unique climate signals in LW, so the removal of dependence on antecedent EW using linear regression is sometimes used in an attempt to isolate the climatic signal unique to LW (see Meko and Baisan, 2001; Stahle *et al.*, 2009). Because EW and LW of *Pinus ponderosa* have been shown to be highly correlated in western North America (Torbenson *et al.*, 2016) and were highly correlated at our sites ($0.53 < r < 0.61$), we regressed site-level detrended LW residual chronologies onto EW chronologies and calculated the residuals to attempt to isolate the variability that is unique to LW. We then added a

constant of 1.0 to the residuals to restore the original mean; the resulting variable is referred to as adjusted latewood (LW_{adj}) (Meko and Baisan, 2001; Stahle *et al.*, 2009).

Climate data and statistical analysis

We selected two climate datasets (*in situ* data near tree-ring collection sites and gridded data at tree-ring collection sites) for comparison with ring-width data to perform a preliminary investigation of which data type was most closely related with tree growth metrics. All available monthly mean temperature and precipitation totals were retrieved from the Global Historical Climate Network (GHCN) (Lawrimore *et al.*, 2011) for sites USC00107386 (Priest River/ID02), USS0018D06S (Lucky Strike/OR18), and USC00456789 (Pullman/WA24) to provide *in situ* data near tree-ring collection sites. We used NOAA's Climate Data Online search tool to examine historical data records in close proximity to our tree sampling sites (Figure 3.1) that overlap with our study period. With the exception of Lucky Strike, our selected sites provide *in situ* climate data since at least 1940 (Table 3.1). We also downloaded monthly mean temperature and precipitation totals from PRISM (PRISM Climate Group, 2004) from 1895-2018 for the location of each of the three GHCN sites and our tree collection sites. PRISM tree-collection-site data were analyzed independently. PRISM data for the GHCN site locations were used to fill any gaps in the GHCN time series, as the two series were highly correlated ($p \geq 0.97$ for precipitation and $p \geq 0.99$ for temperature at all sites), and the Seascorr function described below requires a dataset at least thirty years long and without any gaps. While we will present selected results from analyses of the GHCN data, we chose to focus primarily on the PRISM tree-collection-site data because of its continuity, similarity to GHCN data, and easier access for researchers who wish to conduct comparable work in the future.

Table 3.1. Summary of GHCN site records. Percentage of missing *P* (precipitation) and *T* (temperature) records refer to monthly values; percentage of missing daily values presented in supplementary material.

Site Name	Site Identifier	Coordinates	Tree Site	Start Month	Start Year	% *P* Values	% *T* Values
Priest River	USC00107386	48.35, -116.84	ID02	Feb.	1898	5.4	6.3
Lucky Strike	USS0018D06S	45.27, -118.85	OR18	Oct.	1978	0.0	29.6
Pullman	USC00456789	46.76, -117.19	WA24	Nov.	1940	1.0	3.4

We used the MATLAB function Seascorr (Meko *et al.*, 2011) to examine the monthly and seasonal climate signals captured by our annual and subannual ring-width chronologies at each site. Seascorr calculates a suite of Pearson correlation coefficients between monthly, seasonalized, and annual total precipitation and tree-ring growth chronologies (in our case TRW, EW, LW, and LW_{adj}) and partial correlations with temperature by controlling for the influence of precipitation. Exact simulation (in the form of Monte Carlo simulations) is used to provide confidence intervals for the correlations (Meko *et al.*, 2011); we conducted 1000 simulations to produce these estimates. Seascorr also produces a suite of descriptive statistics and figures to display and contextualize its results. September was selected as the last month of the growing season, and we examined one-month, three-month, nine-month, and twelve-month seasons in the current and previous year using all combinations of ring width metrics with GHCN climate data and PRISM climate data.

Results and Discussion

Overview

In general, EW and LW primarily reflect prior growing season and current growing season precipitation signals, respectively (Figures 3.3-3.5). All four metrics capture precipitation

from the driest part of the year (July-August) at our sites, though at WA24 these signals are mostly apparent at the composite, multi-month level. Precipitation signals are considerably stronger than temperature signals, though temperature signals are robust during select summer months, particularly at WA24, the driest and most water-stressed site (Figures 3.6-3.8). Both precipitation and temperature signals are generally strongest at the one- and three-month seasonal level, though precipitation signals remain robust at the nine- and twelve-month seasonal levels while temperature signals largely disappear (note that seasons are defined here for use within Seascorr as one-month, three-month, nine-month, and twelve-month composites). Relationships between EW and climate closely mirror those between TRW and climate, and LW and LW_{adj} produce similar relationships to each other, though LW_{adj} captures temperature signals from later in the season than LW (Figures 3.6-3.8). Correlations of tree-ring metrics with the GHCN and PRISM climate datasets exhibit differences in both the strength and seasonality of the climate-growth relationship, with trees capturing stronger summer temperature signals from the GHCN data than from the PRISM data at two sites but failing to capture precipitation signals from the GHCN site paired with OR18, which was farthest from its accompanying GHCN site.

Precipitation capture

All four tree growth metrics (TRW, EW, LW, and LW_{adj}) capture monthly precipitation from the current and previous warm season with varying degrees of significance (Figures 3.3-3.5). LW and LW_{adj} also capture a considerable cool-season signal, particularly at WA24. Many of these relationships are strengthened by compositing precipitation into three-month, nine-month, and twelve-month totals, though tree growth metrics tend to correlate most strongly with

one- and three-month precipitation composites (Figures A2-A4). An exception is WA24, where three of the four width metrics exhibit their strongest correlations with twelve-month composites.

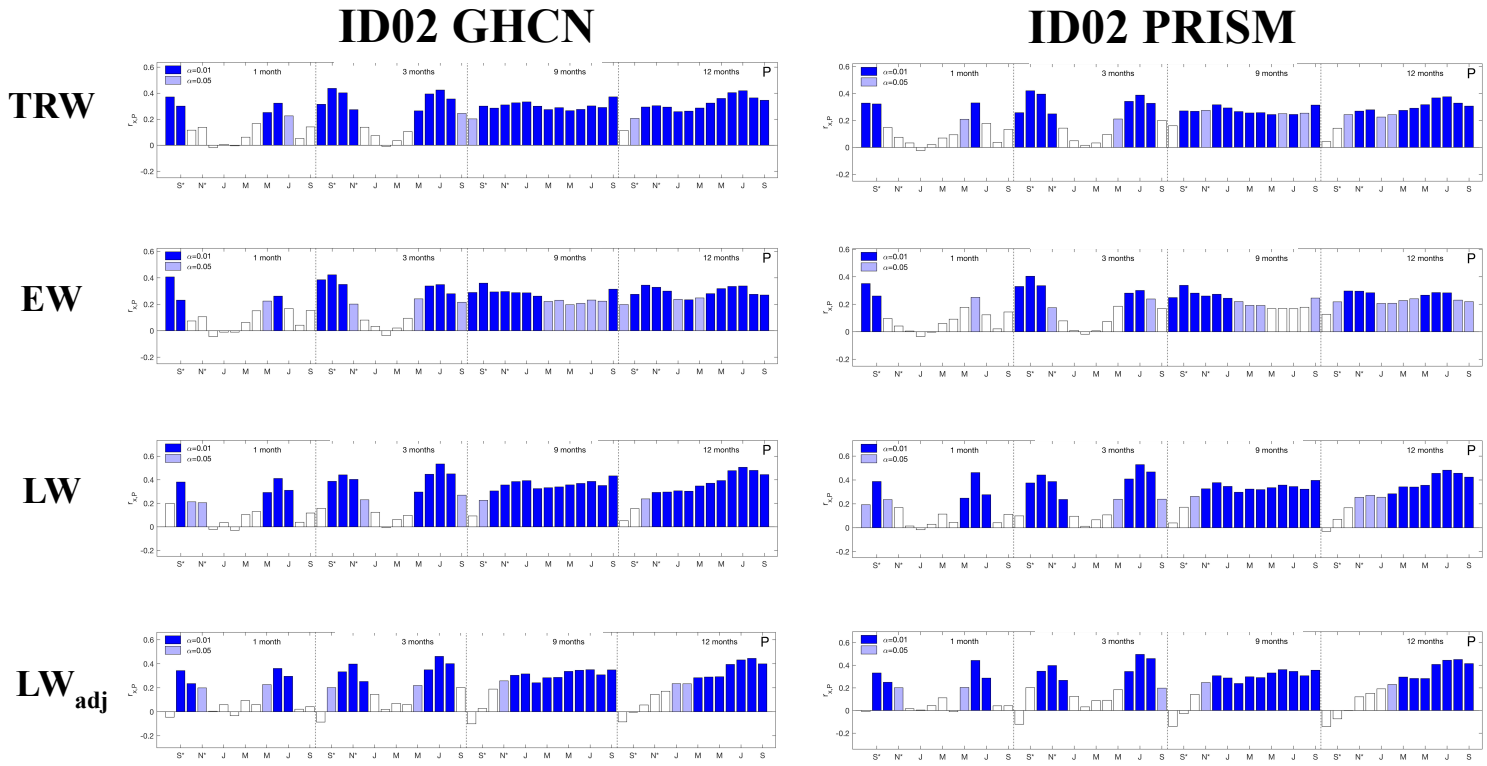

Figure 3.3. Summary of results from Seascorr for GHCN and PRISM data with TRW, EW, LW, and LW_{adj} for ID02/Priest River. Vertical bars represent correlations with seasonal precipitation totals; light (dark) blue bars indicate significance at $\alpha = 0.05$ ($\alpha = 0.01$).

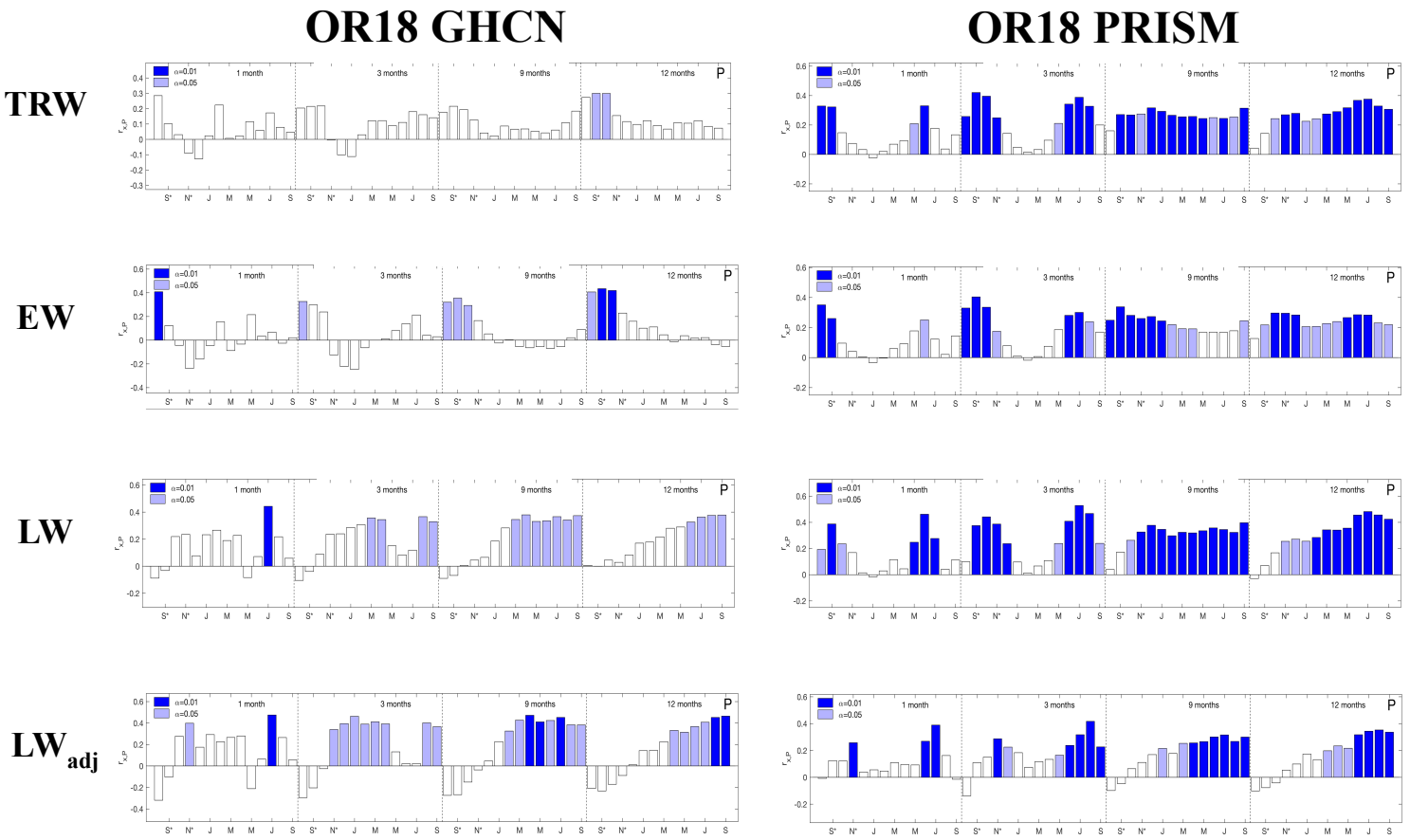

Figure 3.4. Summary of results from Seascorr for GHCN and PRISM data with TRW, EW, LW, and LW_{adj} for OR18/Lucky Strike. Vertical bars represent correlations with seasonal precipitation totals; light (dark) blue bars indicate significance at $\alpha = 0.05$ ($\alpha = 0.01$).

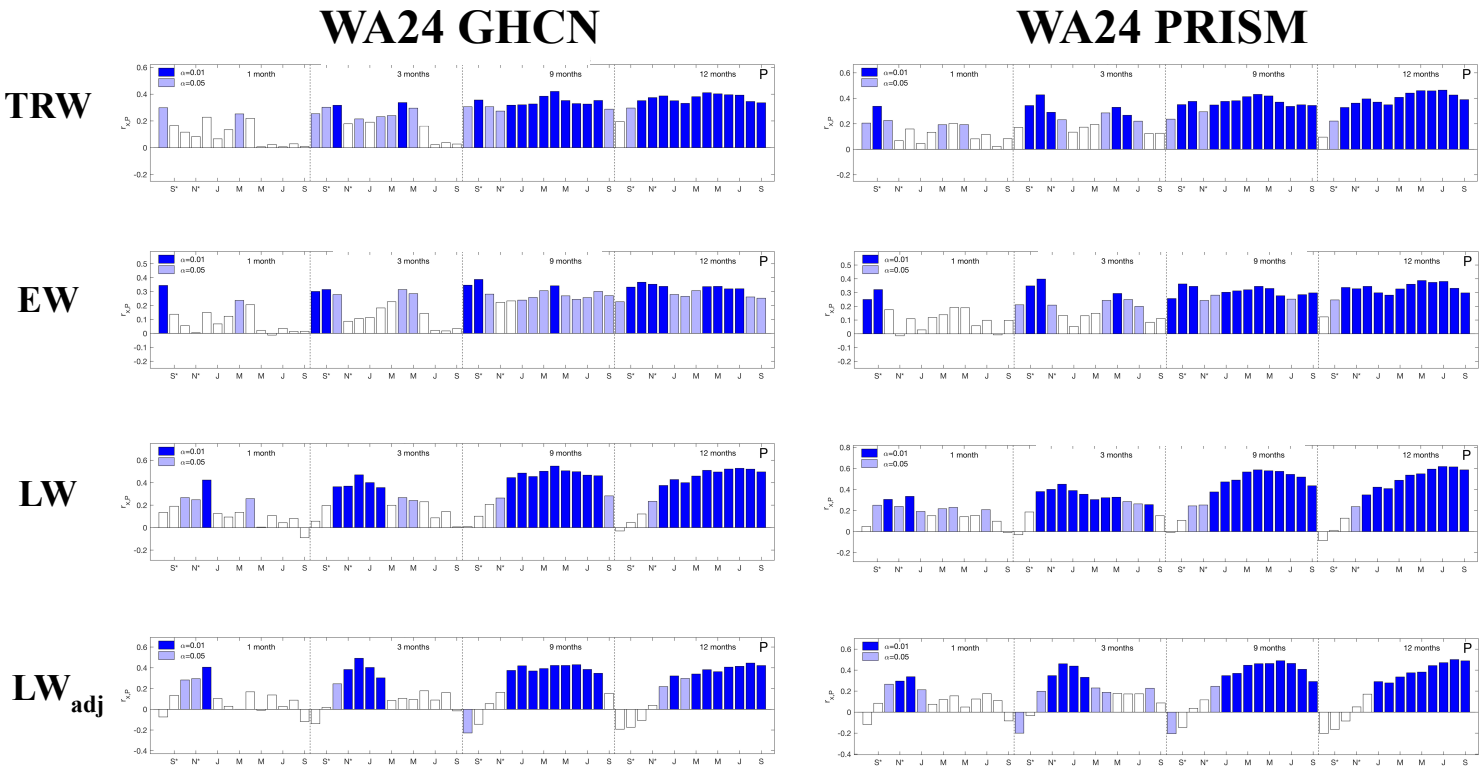

Figure 3.5. Summary of results from Seascorr for GHCN and PRISM data with TRW, EW, LW, and LW_{adj} for WA24/Pullman. Vertical bars represent correlations with seasonal precipitation totals; light (dark) blue bars indicate significance at $\alpha = 0.05$ ($\alpha = 0.01$).

In general, summer precipitation (both in the current and prior year) is the dominant limiting factor of total and partial ring widths across our sites (Figures 3.3-3.5). This is likely because of the seasonal distribution of precipitation at these sites, where the cool season is very wet and the warm season accounts for very little of the precipitation received in a given year (Figure 3.2; Table A1). Therefore, the relative scarcity of summer precipitation is the main limitation to tree growth at our sites in a given year, as evidenced by the strong correlation between current- and previous-year summer precipitation and our tree-ring metrics (Figures 3.3-3.5; Tables A3-A14). TRW and EW correlate strongly and significantly with prior-summer precipitation at all three sites, especially with July-September composites and August single-month totals (Figures 3.3-3.5). However, LW generally correlates most strongly with current-summer precipitation (current-year June and July and current-year May-July and June-August composites), and these correlations are often as strong as or stronger than those between the other two metrics and prior-summer precipitation.

Interestingly, LW and LW_{adj} capture some prior-winter precipitation signals, especially at WA24 (Figures 3.3-3.5). It is likely that the degree of capture at WA24 is enhanced by the lower precipitation amounts and higher vapor pressure deficits at this site both during the winter and year-round, as these conditions induce stronger moisture stress at WA24 than at the other two sites that may in turn limit tree growth. It is unlikely that the degree of capture is enhanced by its elevation relative to the other two sites, as ID02 and WA24 are located at similar elevations (ID02: 726 m, WA24: 766 m) while OR18 is located at a higher elevation (1253 m). The particular importance of antecedent water stored in soil at the start of the growing season in the PNW (Grier and Running, 1977) and hydraulic distribution of stored water in dry conditions (Brooks *et al.*, 2002) may also help to explain this pattern, as the trees at these sites rely on

antecedent conditions for growth beyond the beginning of the growing season. This phenomenon has been observed in PNW coniferous forests, where water extraction moves progressively deeper with summer drought (Warren *et al.*, 2005). At all three sites, LW_{adj} significantly captures prior-November precipitation, though the relationship is generally weak (Figures 3.3-3.5). LW also significantly captures prior-November precipitation at two of the three sites while this metric is not captured by EW or TRW metrics at any site.

These findings suggest that in addition to capturing current-summer precipitation more robustly than EW or TRW, LW and LW_{adj} in the PNW may also capture a certain degree of prior-winter precipitation. The ability of LW to capture both current-year late-summer precipitation and prior-winter precipitation makes it especially valuable for understanding precipitation patterns in the PNW in the context of hydropower. It provides proxy data for the winter, when precipitation determines snowpack that drives warm-season streamflow, and the late summer, when hydropower demand is greatest. This is important for our sites because strong winter and late-summer/early fall (primarily September) signals are absent from the EW and TRW record but are present within LW and LW_{adj}. For sites with a strong tree-climate relationship, this could allow for reconstruction of winter and late-summer/early-fall precipitation to contextualize current conditions within long-term variability and extremes.

The monthly precipitation-growth relationships at our sites are of a similar magnitude to those found at six sites in southwestern Montana and north-central Idaho by Crawford *et al.* (2015), though we find comparatively few significant, negative precipitation-growth relationships at our sites. It should be noted that Crawford *et al.*'s study area lies in the eastern Rocky Mountains, which is dominated by spring and summer precipitation (Mock, 1996) rather than winter precipitation as our sites are, and is also located at higher elevation (1634-1903 m)

than our sites (ID02: 726 m, OR18: 1253 m, and WA24: 766 m). Unlike Crawford *et al.* (2015), who found negative precipitation-growth relationships in February and March for all four growth metrics, we only find significant negative relationships between precipitation and growth in the case of LW_{adj} at WA24 with prior-summer precipitation; Crawford *et al.* (2015) found this relationship in the prior August with LW and LW_{adj} only. We also note that the compositing of climate variables into three-, nine-, and twelve-month seasons in our study enhances the precipitation signal in many cases, especially for the twelve-month season at WA24, while the Crawford study only examined monthly relationships.

Crawford *et al.* (2015) suggest a lagged relationship between cool-season precipitation and tree growth may be driven by soil moisture recharge during the cool season, and it is likely that the enhanced signal at the twelve-month seasonal level at WA24 is also due to the influence of soil moisture recharge and the importance of antecedent moisture conditions at this relatively arid site. The persistent impact of spring rain and snowmelt throughout the year has been well-documented in the western U.S., and even apparently normal water years can lead to low runoff in rivers that experienced low snowpack and spring rainfall (Konrad, 2019), further highlighting the importance of examining the water-tree growth relationship at a variety of temporal scales.

While our findings broadly agree with Dannenberg and Wise (2016) finding that current-summer precipitation is the primary signal embedded in the first principle component of TRW and EW with some input from the previous summer and winter, TRW and EW do not significantly capture cool-season precipitation at our sites (Figures 3.3-3.5) at the three-month seasonal level as they did at the Dannenberg and Wise (2016) sites. However, this could be due to different aridity levels at our sites—WA24, our most arid site, does show winter precipitation capture, though it is captured by LW and LW_{adj} rather than TRW or EW. The strong capture of

climate signals by LW in comparison with EW is not unique to our site or study area and has been noted in locations as diverse as western France (Lebourgeois, 2000). However, EW has been shown to be more sensitive to climate variability than LW at sites in both temperate, humid climates (Cabral-Alemán, 2017) and colder, semi-arid climates (Chen *et al.*, 2010), and the climate-growth relationship with EW and LW can vary considerably within a single species at different sites (Torbenson *et al.*, 2016).

Overall, we find that LW demonstrates a stronger relationship with current-summer precipitation than that provided by TRW or EW at our sites, which corroborates the findings in other disparate but water-limited regions (e.g., Meko and Baisan, 2001; Griffin *et al.*, 2013); the significant and coherent relationship between LW and precipitation at ID02 and OR18 suggests that these sites could be used as part of a network-based construction such as that performed by Griffin *et al.* (2013) in the North American Monsoon region. LW_{adj} shifts the captured signal from earlier in the summer to later in the summer, and this shift to later in the growing season captures a critical period for hydropower supply and demand in the PNW and emphasizes the utility of these metrics for the reconstruction of summer precipitation.

Temperature capture

Partial correlations with temperature are generally weak (Figures 3.6-3.8), which is unsurprising due to the probable dominance of annual water deficit (Robertson *et al.*, 1990) and precipitation controls more broadly (Watson and Luckman, 2001) on tree growth in the PNW. However, significant current-year and prior-year relationships do exist between temperature and all four tree-ring width metrics for at least part of the year at all sites (Figures 3.6-3.8). These relationships are positive in the winter through early summer (previous November through May)

at all sites and year-round at the wettest site (ID02). The temperature-growth relationship becomes negative during the growing season (June-August) at OR18 and WA24, with WA24 exhibiting the most sensitive and consistent response (Figures 3.6-3.8). This finding is typical for western arid-site conifers (Fritts, 1974) and also aligns with more recent findings from the northern Rocky Mountains (Crawford *et al.*, 2015). The fact that the inverse summertime temperature-growth relationship only exists at our more arid sites and is notably strongest at our most arid site also emphasizes the degree to which our three sites capture a range of precipitation and overall aridity that represent common conditions across the study area.

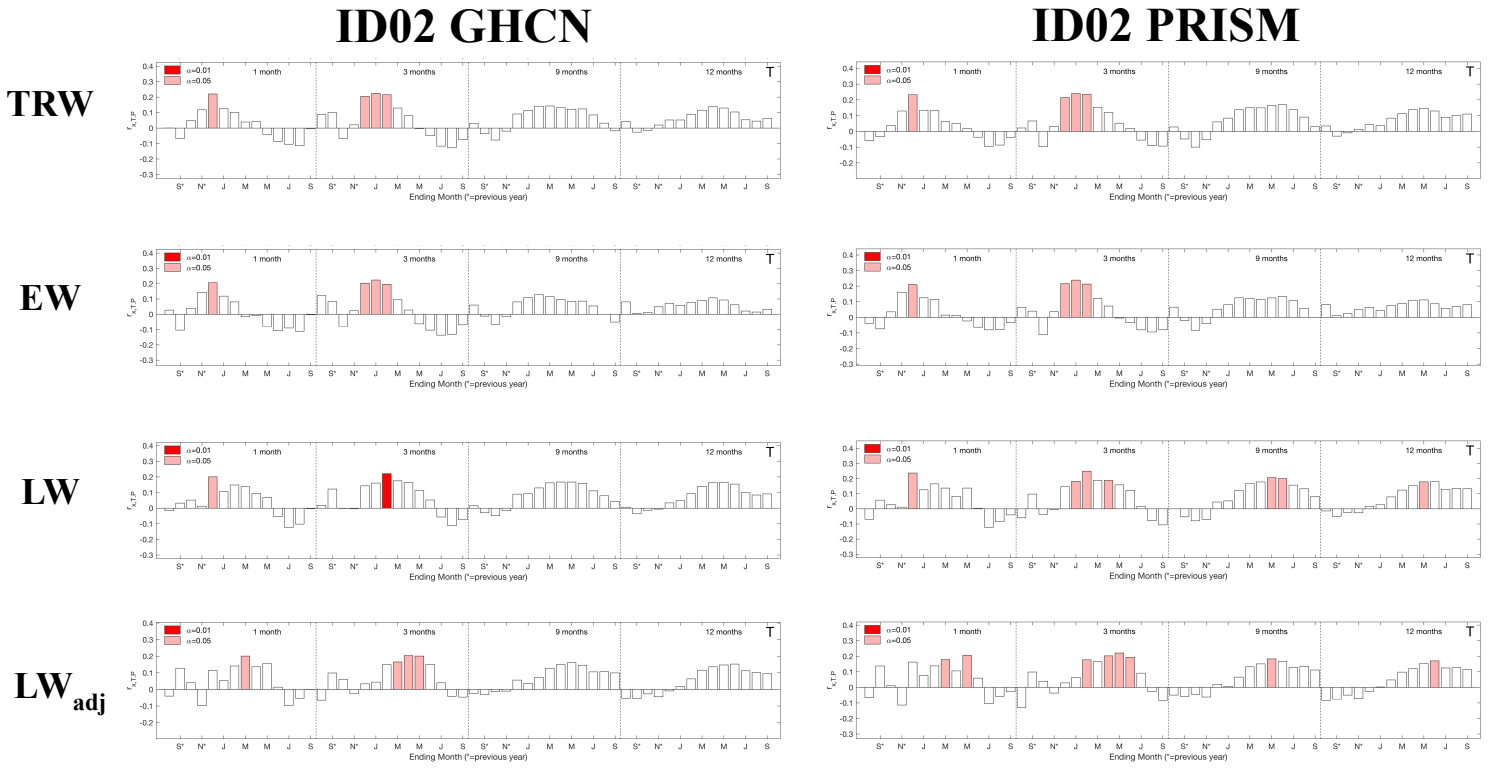

Figure 3.6. Summary of results from Seascorr for GHCN and PRISM data with TRW, EW, LW, and LW_{adj} for ID02/Priest River. Vertical bars represent partial correlations (controlling for precipitation) with seasonal temperature; light (dark) red bars indicate significance at $\alpha = 0.05$ ($\alpha = 0.01$).

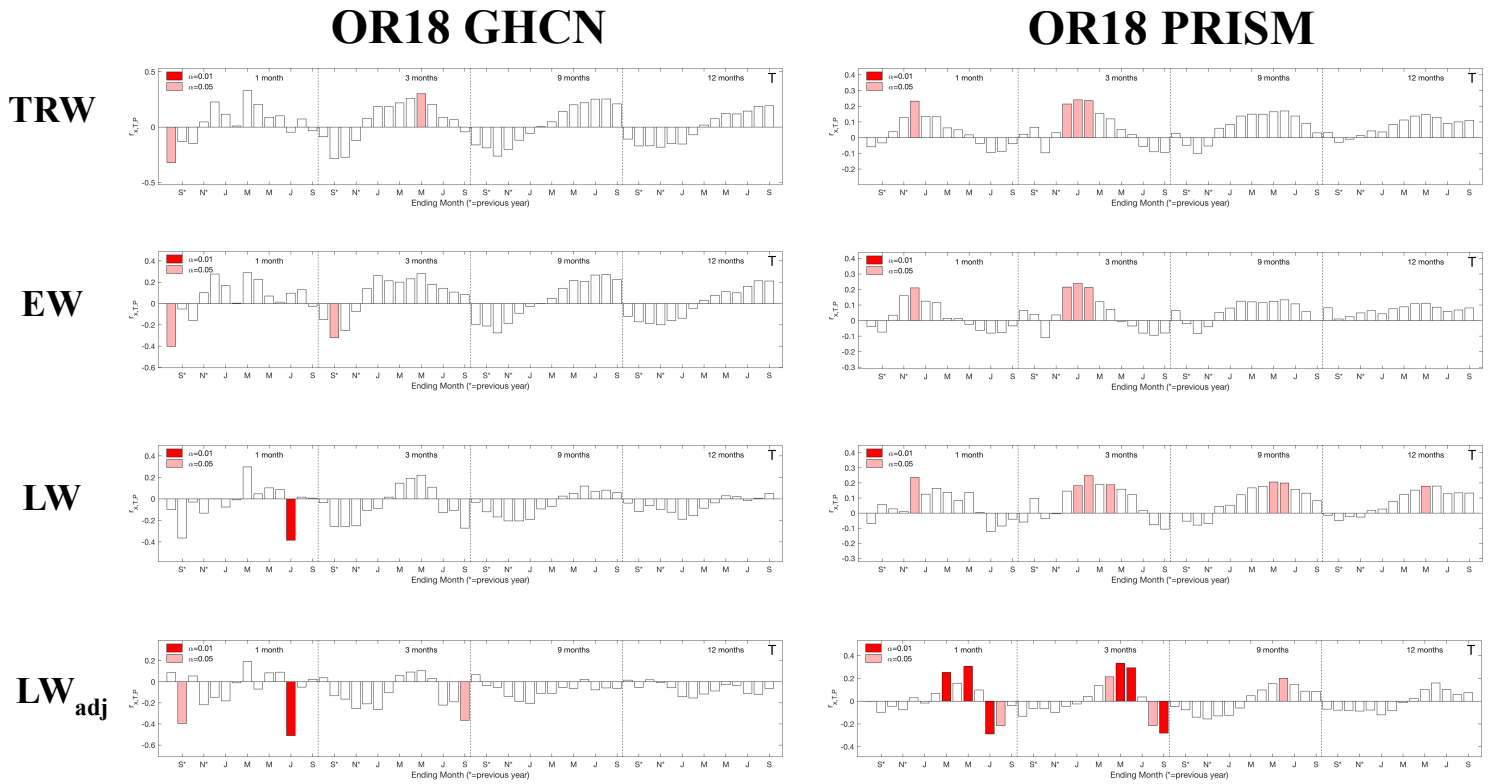

Figure 3.7. Summary of results from Seascorr for GHCN and PRISM data with TRW, EW, LW, and LW_{adj} for OR18/Lucky Strike. Vertical bars represent partial correlations (controlling for precipitation) with seasonal temperature; light (dark) red bars indicate significance at $\alpha = 0.05$ ($\alpha = 0.01$).

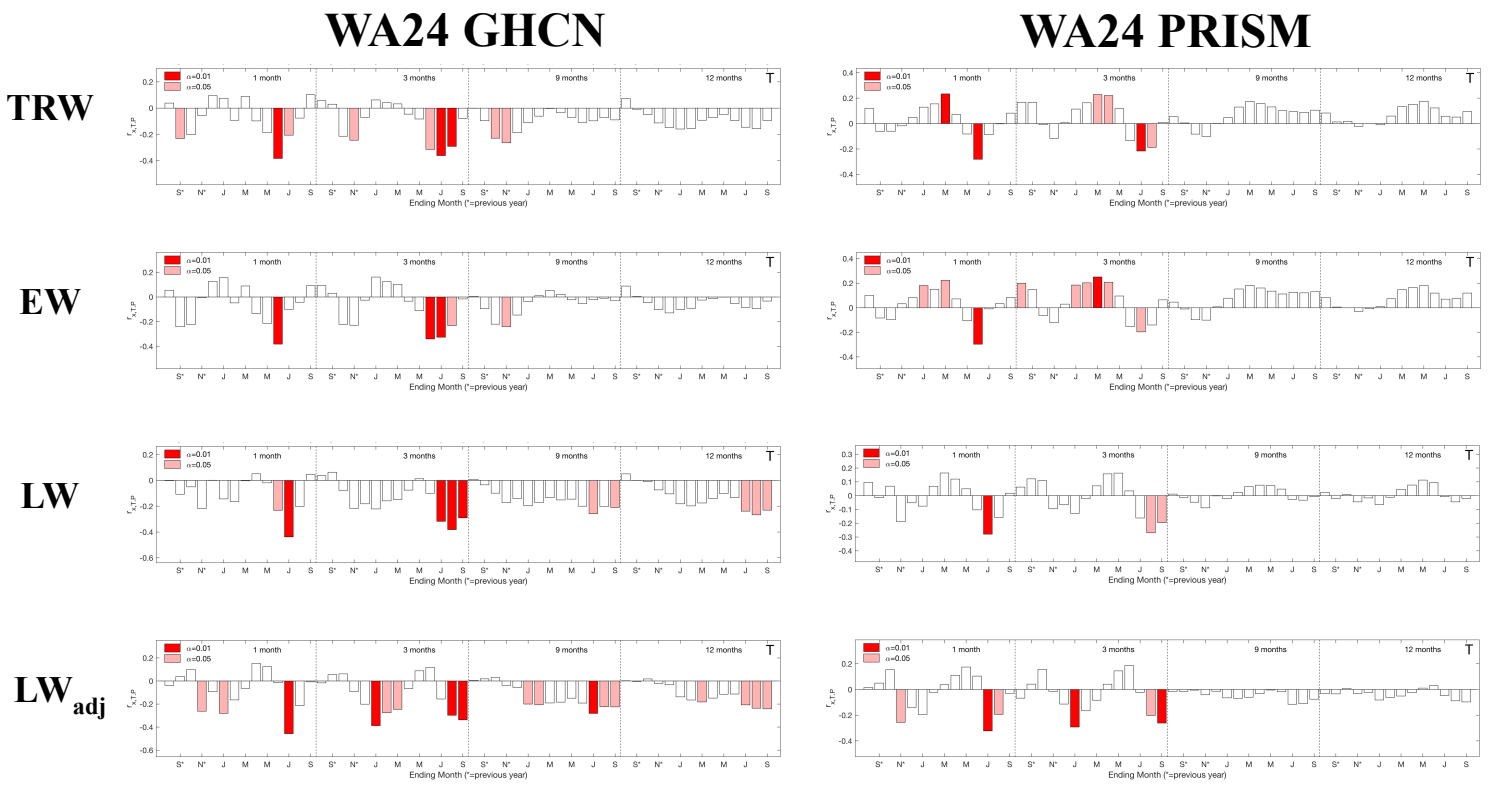

Figure 3.8. Summary of results from Seascorr for GHCN and PRISM data with TRW, EW, LW, and LW_{adj} for WA24/Pullman. Vertical bars represent partial correlations (controlling for precipitation) with seasonal temperature; light (dark) red bars indicate significance at $\alpha = 0.05$ ($\alpha = 0.01$).

In general, the temperature-growth relationship is most prominent during single-month and three-month seasons and is sparse or absent in nine- and twelve-month composites (Figures 3.6-3.8). This signal contrasts with the pattern of the precipitation-growth relationship, which is significant for more nine- and twelve-month seasons than one- and three-month seasons and is often stronger in the nine- and twelve-month composites. This difference in patterns is likely due to the persistence of precipitation in the form of snowpack (during the cool season) and groundwater recharge (during the warm season) that can then impact tree growth for months after a rainfall event. In contrast, temperature does not always express the same type of persistence, and heat wave events create a shorter "pulse" rather than a longer "press" response (Harris *et al.*, 2018); a temperature spike within a given month may exacerbate drought, which is known to produce water stress in the PNW during the summer due to reliance on stored water from prior to the current growing season (Brubaker, 1980). High air and soil temperatures reduce photosynthesis rates in Oregon (Emmingham and Waring, 1977) and transpiration rates in *Pinus ponderosa* specifically (Lopushinsky and Klock, 1974), further supporting the idea that temperature both directly and indirectly hinders growth in trees at our study sites. It is logical that this impact appears primarily within LW and LW_{adj} since temperatures that are likely to limit ponderosa pine growth appear later in the growing season; in contrast, positive temperature-growth relationships earlier in the season are present within all four growth metrics.

The highest-magnitude correlation between temperature and growth occurs in July at WA24, where the correlation between LW_{adj} and temperature reaches $p = -0.32$ ($\alpha = 0.01$) for the PRISM dataset and $p = -0.46$ ($\alpha = 0.01$) for the GHCN dataset (Table A14). Similarly, Robertson *et al.* (1990) found that high August temperatures decreased LW on Vancouver Island, with the impact increasing from a subhygric site to a xeric site, and increased water deficit (aided by high

temperatures) was the dominant signal within LW. The relative strength of the temperature–LW relationship at WA24 is unsurprising in this context because WA24 is both the driest and warmest site, with average maximum monthly temperatures in July and August exceeding 28°C (Table A1). However, site elevation may also play a role in climate signal capture amongst our sites, as trees at higher-latitude and higher-elevation sites tend to be more limited by climate and therefore capture stronger climate signals (Carrer *et al.*, 2012). For example, OR18 captures a comparably strong temperature signal in latewood and is located at a considerably higher elevation than WA24 while being cooler and less dry. It is also notable that the magnitude of negative temperature-growth relationships is consistently greater than that of the positive relationships. Therefore, these findings likely indicate that higher temperatures contribute to relatively high levels of evaporative stress and vapor pressure deficit that limit tree growth at these sites during the summer; they also suggest that slightly warmer winter temperatures encourage tree growth, perhaps due to the warmer air holding more water and contributing to increased snowpack and subsequent streamflow during the following growing season.

LW vs. LW_{adj}

Although we hypothesized that the calculation of site-level LW_{adj} should improve warm-season climate signals by removing statistical reliance on preceding EW (e.g., Griffin *et al.*, 2013; Dannenberg and Wise, 2016), we find that LW_{adj} does not provide vastly different climate information from the other three metrics at our sites, and it most closely resembles traditional LW measurements (Figures 3.3-3.8). LW_{adj} also retains climate signals from the prior summer at all sites and the prior winter at WA24. This finding suggests that the linear regression approach to removing biological persistence from LW may not completely remove autocorrelation, which

aligns with Crawford *et al.*'s (2015) findings and their suggestion that some autocorrelation may be "embedded within the time series structure of precipitation" and therefore not removable through linear regression. In addition, our results may have been impacted by our choice to perform linear regression at the site level rather than the core level; however, both site- and core-level regressions are common and no particular regression method appears to confer a significant advantage in removal of dependence on antecedent EW (Stahle *et al*., 2009).

Notably, the current-year temperature signal is strengthened and shifted later in the growing season with the removal of LW dependence on EW, and some of the persistent impact of antecedent precipitation is removed at the twelve-month seasonal level (Figures 3.6-3.8). July and August are the warmest and driest months at all three of our sites, and a negative temperature-growth relationship in LW and LW_{adj} is relatively well-captured for one-month and three-month seasons. This suggests that despite an incomplete removal of dependence on antecedent EW, LW_{adj} does preserve some unique climate signals not apparent within traditional tree-ring width measurements and provides information about temperature during the time of year when a combination of increased temperatures and low precipitation produce high vapor pressure deficits that are likely to impact hydropower supply and demand. Especially when considering the ease and simplicity of measuring LW when compared with more time-consuming and cost-intensive methods such as maximum latewood density and stable isotope analysis, it is prudent to measure both full ring widths and partial ring widths (particularly latewood) of *Pinus ponderosa* in our study region.

Summary of comparison between sites

WA24, which is the most water-stressed site, shows the strongest influence of temperature on tree growth, particularly during the current growing season. Along with the aforementioned comparison, this also aligns with Robertson *et al.*'s (1990) finding that EW at xeric and submesic sites in British Columbia is significantly reduced with increased summer (May) temperatures; this impact is apparent at all three of their sites but is less apparent at the wettest (subhygric) site. Interestingly, only LW and LW_{adj} at ID02 and OR18 demonstrate temperature signal capture at the nine- and twelve-month seasonal levels. Because this relationship is positive and leads to the current growing season, it is possible that this signal represents favorable temperature conditions that are integrated over the course of the current and prior growing season, though it could also be interpreted as a diluted version of the "pulse" response captured by the monthly- and three-month relationships.

WA24 also exhibits little precipitation signal at the monthly level, particularly during the current summer; however, the precipitation signal is strengthened within LW and LW_{adj} for most of the current and prior year at the three-month level. The consistent cool-season signal at WA24 is absent at the other sites, and it is possible the presence of this signal at WA24 represents an increased dependence on stored precipitation, especially during the summer months when vapor pressure deficits peak and temperatures approach 30°C. Overall, increased water deficit leads to an increasingly stronger (and often positive) summer precipitation signal at our sites, especially in LW and LW_{adj}, while enhancing a more integrated precipitation signal at a longer seasonal level at the expense of monthly signal strength.

Lastly, it is important to note that elevation is also likely to be an influential factor at our sites, as the growth of trees at higher-elevation and higher-latitude sites tends to be more strongly

limited by climate (Carrer *et al.*, 2012). This may explain why our highest-elevation site (OR18) often captures stronger climate signals than WA24 despite OR18 experiencing milder temperatures and less water stress. Therefore, ID02 and WA24 may represent a more comparable pairing for understanding the role of aridity in climate capture, as the two sites are located at nearly the same elevation but experience different levels of water stress.

Climate data comparison: GHCN vs. PRISM

The GHCN data set, which was retrieved from a database of climate summaries from land surface stations (NCEI, 2022), and the PRISM data set, which is available for the conterminous United States and relies on an elevation-based interpolation model (Daly *et al.*, 2008; PRISM Climate Group, 2022), are highly correlated with each other and exhibit similar correlations with tree-ring metrics (Figures 3.3-3.8), suggesting that they are both suitable for comparison with tree-ring width data. However, correlations of tree-ring metrics with the two datasets do exhibit some differences in both the strength and seasonality of the climate-growth relationship, and these differences vary across sites. At OR18, EW and TRW are more strongly correlated with PRISM data, while LW and LW_{adj} are more strongly correlated with GHCN data. However, GHCN precipitation is not well-captured by the trees at OR18, which is likely due to the spatial heterogeneity of precipitation and the two locations being over 40 kilometers apart. Of all the combinations examined at this site, the strongest relationships exist between current-July GHCN precipitation and LW_{adj} and previous-August PRISM precipitation and EW ($r = 0.47$ for both combinations, $p < 0.01$). OR18 LW_{adj} also captures considerable current-July temperature at Lucky Strike despite the two sites' distance, but this is likely an artefact, as Lucky Strike is missing a significant amount of temperature data that were then supplemented from PRISM. At

ID02, EW and TRW are slightly more strongly correlated with GHCN data than with PRISM data, while LW and LW_{adj} show slightly stronger correlations with PRISM data than with GHCN data. At WA24, temperature signals are captured by all tree-ring metrics in the current growing season, but the temperature-growth relationship is considerably stronger with the GHCN data than the PRISM data, and only negative relationships are captured from the GHCN data.

It is possible that these different relationships are driven by the varying influence of local-scale versus synoptic-scale factors at the sites across seasons, as common signals across the GHCN and PRISM networks (which are highly correlated) are likely to reflect larger-scale atmospheric circulation. Watson and Luckman (2001) noted the likelihood of trees capturing regional climate patterns driven by synoptic-scale climate in the nearby southern Canadian Cordillera, especially in years producing extreme tree-ring widths, further supporting this hypothesis. Differences in capture between local- and synoptic-scale climate would most likely affect the comparison for OR18 because this site has the greatest distance between the GHCN and tree-ring collection sites. However, it is also possible that these differences are an artefact, particularly since they are not strikingly disparate for any given comparison. Overall, while comparisons of tree-ring width data with GHCN data may reveal some additional nuance in the climate-growth relationship where available, we find that the PRISM dataset captures similar climate-growth relationships with the advantage of being readily available for use at any site within the conterminous United States from 1895 to the present.

Conclusion

The escalating threat of summer heat waves and their devastating effects in the PNW underscore the importance of understanding seasonal precipitation patterns and water stress in

the region, and the widths of annual tree rings are a well-established means of elucidating these patterns to contextualize present climate within long-term variability and improve projections of future climate. However, traditional tree-ring studies using TRW often fail to capture the nuances of climate at the seasonal level. The use of multiple tree-ring metrics has already been proposed as one means of gathering additional climate information for a site to improve seasonal reconstructions (Wise, 2021), and here we explore this method by examining four of these metrics across an aridity gradient in the PNW.

We find that EW, LW, and LW_{adj} measurements enhance overall climate signal capture at our sites when compared with TRW alone. These subannual tree-ring width measurements capture local monthly- and seasonal-scale precipitation signals at our sites, with EW primarily reflecting prior-summer precipitation signals and LW and LW_{adj} primarily reflecting current-summer precipitation. We also find that subannual ring widths (and particularly LW) capture more robust climate signals than total annual ring widths, and all four metrics capture precipitation from the driest part of the current growing year. These findings agree with previous studies in western North America (Crawford *et al.*, 2015; Dannenberg and Wise, 2016). There is also significant capture of temperature signals during the growing season at all sites, particularly by LW and LW_{adj}. This signal strengthens and becomes increasingly negative with increased site aridity, which is unsurprising in the context of similar research in the region (Robertson *et al.*, 1990). Like Crawford *et al.* (2015), we also find that LW_{adj} does not exclusively reflect summer precipitation signals at our sites, but it does strengthen the current-year temperature signal and shifts it later in the growing season, and it also strengthens the prior-winter climate signal. Therefore, LW_{adj} provides unique climatic information that is not present in EW or LW

measurements, and LW and LW_{adj} are likely to be particularly fruitful avenues for both warm-season and cool-season climate studies in the PNW.

We demonstrate that subannual tree-ring width metrics capture some temperature and precipitation signals during the winter months that fuel recharge and drive spring streamflow as well as the summer months when high water stress increasingly threatens hydropower production and health and human safety. The relatively low costs involved, both in labor and specialized equipment, make the measurement of subannual ring-width metrics a particularly exciting and accessible approach. The combination of these metrics with other, more cost-intensive metrics such as stable isotope analyses stands to maximize the use of the rich climatic information stored within trees and further improve our understanding of climate variability in the PNW. By better understanding the capture of these variables within subannual tree-ring widths, we aim to improve interpretation of tree-ring paleoclimate proxy records and subsequent climate reconstructions in the PNW to examine the seasonality of precipitation and how it is shifting in a changing climate.

CHAPTER 4: SUBANNUAL $\delta^{18}O$ VALUES OF *PINUS PONDEROSA* AS INDICATORS OF SOURCE WATER $\delta^{18}O$ AND SEASONAL CLIMATE VARIABILITY IN THE U.S. PACIFIC NORTHWEST

Introduction

Although annual tree-ring widths have been used as a climate proxy for over a century, most prior research has been focused on arid environments and trees growing at their ecological limits due to the enhanced capture of climatic signals by trees growing under these conditions (Briffa *et al.*, 2002). In locations where trees are not growing at their ecological limits, a complex array of climatic and biological factors may obscure the climate-growth signal (Anderson *et al*., 1998). This limited signal hinders the ability to use ring width measurements to contextualize some aspects of current local and regional climate within longer-term variability. It also points to the need to investigate other climate proxies and tree-ring variables in these regions to more fully understand past climate (Saurer *et al*., 2008). The stable isotope composition of tree-ring cellulose provides one promising means for obtaining this information.

Because trees' primary moisture source is meteoric water, they can capture and store the isotopic composition of precipitation within cellulose produced from this water (Edwards and Fritz, 1986; Reynolds-Henne *et al.*, 2007). Trees tend to dampen the isotopic signals from precipitation (Anderson et al., 1998), and hydraulic redistribution and differential rooting depths can further complicate this relationship (Brooks et al., 2006; Brooks and Coulombe, 2009). However, trees with extensive shallow root systems exhibit less of this dampening and therefore can capture a relatively strong precipitation signal (Anderson et al., 2002). Annual ring widths

and the isotopic composition of cellulose may store different climate information (Gagen *et al*. 2011), and in some cases isotope chronologies show significant correlations with climate variables when ring widths do not (Anderson *et al.*, 1998). Isotopic chronologies have also been shown to reflect climate in trees not growing at their ecological limits (Anderson *et al*., 1998), representing a unique benefit of isotopic analyses in these regions.

Anderson *et al*. (1998) suggested that terrestrial proxies including trees can capture information related to the variability of dominant air masses and the westerly jet stream. This information is particularly important in regions like the U.S. Pacific Northwest, where precipitation is highly seasonal, driven by large-scale atmospheric circulation, and has already begun to shift due to climate change (Abatzoglou *et al.*, 2014). However, studies directly relating moisture source variability or atmospheric circulation (often in the form of indices of El Niño-Southern Oscillation, the Atlantic Multidecadal Oscillation, or the Pacific Decadal Oscillation) with isotopic analyses of tree-ring cellulose remain relatively scarce. Some of these studies have been used to examine centennial- or millennial-scale climate patterns (Edwards *et al.*, 2008; Wernicke *et al.*, 2017), though annual examinations and reconstructions are more common.

Most studies of this type that have examined annual- or seasonal-scale climate have used whole annual rings (Feng *et al.*, 2007; Reynolds-Henne *et al.*, 2007; Berkelhammer and Stott, 2008, 2011, but see also Bale *et al*., 2010; Porter *et al.*, 2009; Xu *et al.*, 2013), though some have used latewood (Liu *et al.*, 2009), earlywood (Zhu *et al.*, 2021), separate earlywood and latewood (An *et al.*, 2012; Labotka *et al.*, 2016) or even middlewood (Voelker *et al.*, 2019). Whole rings are often used when rings are narrow and therefore difficult to separate or extract sufficient material for analysis (Reynolds-Henne *et al.*, 2007; Porter *et al.*, 2009; Xu *et al.*, 2013). However, separate earlywood and latewood components have been found to confer an advantage

when attempting to isolate seasonal climate signals (Liu *et al.*, 2009; An *et al.*, 2012; Labotka *et al.*, 2016; Zhu *et al.*, 2021) and therefore are especially promising for the PNW where precipitation is highly seasonal. These studies point to some of the advantages afforded by subannual measurements of the $\delta^{18}O$ values of tree-ring cellulose to infer atmospheric circulation patterns, which in turn is linked with the meteoric water and soil water used by trees.

While source water can refer to air mass source region as discussed above, the term more frequently refers to stem water. Stem water is assumed to represent meteoric water because fractionation does not occur during uptake (Wershaw *et al*., 1966), though as previously mentioned, hydraulic redistribution and differential rooting depths also impact trees' representation of meteoric water (Brooks *et al.*, 2006; Brooks and Coulombe, 2009). Hydrologic processes also often alter and dampen this signal (Tang and Feng, 2001) and evaporative enrichment can occur within the soil, making soil moisture the ultimate determinant of tree source water (McCarroll and Loader, 2004). The degree of oxygen isotope exchange during cellulose formation determines the extent to which the source water signal is captured (Roden *et al*., 2000), highlighting the importance of understanding the extent to which this signal is captured in different environments (McCarroll and Loader, 2004).

Previous studies in the PNW have found a statistically significant relationship between $\delta^{18}O$ values of source water and tree cellulose even when there is not a significant relationship between ring width and precipitation amount (Roden *et al*., 2005; Roden and Ehleringer, 2007). Although the source-water-cellulose relationship is promising, it is also complex and requires further investigation in a variety of settings to better understand the spatial variability of past climate in this and other temperate regions (Anderson *et al*., 1998). *Pinus ponderosa* trees demonstrated no significant autocorrelation within $\delta^{18}O_{cellulose}$ values and likely took up

relatively shallow soil water when studied at a site in Idaho (Marshall and Monserud, 2006); hence, they provide an ideal target for this investigation. In addition, long-term weekly meteoric water samples collected by sites as part of the National Atmospheric Deposition Network (NADP) provide the means to investigate the source-water-cellulose relationship at fine spatial and temporal scales in a temperate region with complex terrain in the PNW.

In this study, we examine the extent to which climatic variables, primarily seasonal precipitation and temperature and atmospheric circulation, are captured by the $\delta^{18}O$ values of tree-ring earlywood and latewood cellulose at three sites in the U.S. PNW. We also use our tree-ring isotopic measurements as inputs in a mechanistic model to estimate source water $\delta^{18}O$ values and compare our estimates with *in situ* values from nearby sites. We use a combination of weekly precipitation $\delta^{18}O$ values from January 2007-December 2016, subannual tree-ring $\delta^{18}O$ values from 2006-2018, and monthly mean temperature and precipitation totals from 2007-2018 to directly compare the isotopic signal captured by tree-ring cellulose to climate variables and the stable isotope composition of source water. By better understanding the capture of these variables within tree cellulose, we aim to improve interpretation of tree-ring paleoclimate proxy records and subsequent climate reconstructions in the PNW.

Materials and methods

Study sites and climatology

To examine the relationship between the isotopic composition of meteoric water at shorter timescales (monthly and seasonal) and tree cellulose at longer timescales (subannual in the form of earlywood and latewood), we selected three pairings of field sites for tree core

collection and NADP stations for collection of precipitation samples suitable for isotopic analysis (Figure 4.1).

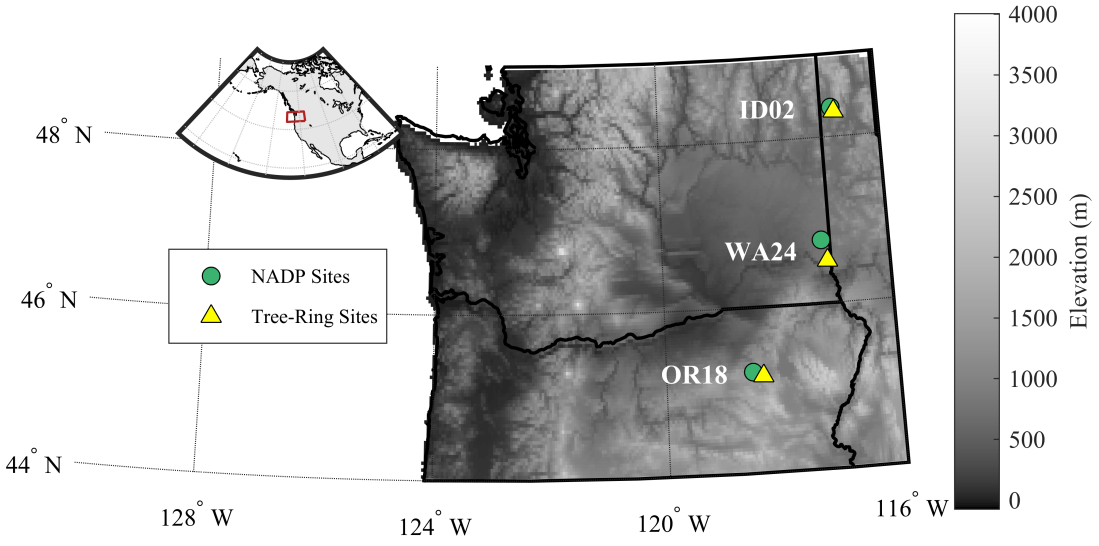

Figure 4.1. Location of study sites within the Pacific Northwest.

Tree cellulose samples and ring-width measurements

We collected and processed tree cores from three sites across Washington State, Oregon, and Idaho (Figure 4.1) following standard dendrochronological procedures as detailed in Chapter 3. Two 12mm cores were collected from six to twelve trees at each site to provide sufficient material for stable isotope analysis. A sample size of four or more trees has been demonstrated to accurately represent site trends in tree-ring isotopes in most cases (Leavitt, 2010), particularly for examining high-frequency (i.e., year-to-year) changes (Robertson *et al.*, 1997), and has been successfully used for *Pinus ponderosa* in Oregon (Roden and Ehleringer, 2007). Despite a small number of cores being omitted due to periods of indistinguishable growth rings, 12mm cores from at least five trees were retained at each site.

Following the sample preparation and measurement processes detailed in Chapter 3, the period from 2006-2018 from each 12mm core was then micromilled using a mounted Dremel rotary tool with a movable x- and y-stage (Acra Mill Plus, Vanda-Lay Industries, California) under a microscope to create separate annual earlywood ($\delta^{18}O_{EW}$) and latewood ($\delta^{18}O_{LW}$) samples for isotopic analysis. Six trees at ID02, five trees at OR18, and ten trees at WA24 were micromilled for isotopic analysis. We combined approximately equal amounts of material from each tree at each site to create a total of 26 pooled samples per site (one earlywood and one latewood sample for each of thirteen years at each site) before extracting the cellulose from each pooled sample using a modified version of the sodium chlorite method by Leavitt and Danzer (1993) and Rinne *et al*. (2005). Following cellulose extraction, individual tracheids from separate pieces of material were selected and combined within each sample (0.200mg ± 0.050) to enhance homogenization. Each sample was packaged in a silver capsule for analysis, and at least two replicates of each pooled cellulose sample were analyzed with the exception of three seasons at OR18 (2007 LW, 2008 LW, 2014 LW) and WA24 (2012 LW, 2014 LW, and 2015 LW) due to instrumental errors from autosampler use (total sample number: 151 out of possible 156).

Oxygen isotope ratios were determined using a Thermo Delta V Advantage interfaced with a Thermo Temperature Conversion/Elemental Analyzer (TC/EA) at the Center for Environmental Science and Technology at the University of Notre Dame. Stable isotope ratios are expressed in delta notation in per mil (‰) relative to Vienna Standard Mean Ocean Water (V-SMOW), and USGS standards 54 (Canadian lodgepole pine, $\delta^{18}O = +17.79 \pm 0.15$ ‰), 55 (Mexican ziricote, $\delta^{18}O = +19.12 \pm 0.07$ ‰), and 56 (South African red ivorywood, $\delta^{18}O = +27.23 \pm 0.03$ ‰) and IAEA standard 601 (benzoic acid, $\delta^{18}O = +23.14 \pm 0.19$‰) were used to calibrate each instrument to the VSMOW-SLAP scale, wherein Vienna Standard Mean Ocean

Water has a $\delta^{18}O$ value of 0 ‰. Instrumental drift was determined at the beginning, middle, and end of each run by running a sample set consisting of an empty sample, a blank silver capsule, and a combination of three to four standards.

Using the measurements of the USGS and IAEA standards, we performed sample correction using linear regression between standard data points (r^2 ranged from 0.98 to 0.99 across runs). To address the two missing seasons at OR18, we regressed corrected LW values onto EW values and used the resulting regression equation to predict the missing LW values. Unlike the tree-ring width measurements, we did not detrend the corrected $\delta^{18}O_{EW}$ and $\delta^{18}O_{LW}$ values. While age-related "juvenile effects" have been found in tree-ring $\delta^{18}O$ values (Treydte *et al.*, 2006), tree-ring oxygen isotope time series generally lack age-related trends (Holzkämper *et al.*, 2008), especially at the short time scales studied here. We also avoid potential age-related trends by using only the outermost growth rings of our samples.

Precipitation samples

We selected the NADP sample collection site nearest to each tree collection site and requested weekly precipitation samples from each site for January 2007 through December 2016. These precipitation samples were analyzed for $\delta^{18}O$ values as described in Chapter 2. For this study, we calculated amount-weighted values from the resulting measurements at a variety of monthly, three-month, and longer seasonal scales for comparison with tree-ring isotopes and climate data.

Climate data

We retrieved monthly precipitation totals and mean temperatures for our three tree-ring collection sites from PRISM (PRISM Climate Group) from 1895-2018 for comparison with our subannual ring-width and tree-ring isotope measurements. We also downloaded monthly dew point temperatures to calculate growing-season relative humidity for use in the mechanistic model described later in this section. We used the MATLAB function Seascorr (Meko *et al.*, 2011) to perform correlation and temporal stability analyses using the subannual tree-ring width series for the length of the available climate record (see Chapter 3 for details) prior to the remainder of analyses.

Mechanistic modeling

To determine the extent to which tree-ring cellulose captures source water $\delta^{18}O$ values at each site, we used the following mechanistic model developed by Anderson *et al.* (2002) based on earlier leaf-water modeling work by Dongmann *et al.* (1974) and Craig and Gordon (1965) to estimate source water (in this case, xylem water) $\delta^{18}O$ values (i.e., the oxygen isotope ratio of source water; $\delta^{18}O_{SW}$) using our seasonal tree-cellulose $\delta^{18}O$ values. This model considers factors that impact both the physical and biochemical fractionation that occur due to influences and processes including vapor pressure, the evaporative enrichment of leaf water, and isotopic exchange between carbohydrates and xylem water during cellulose synthesis (Anderson *et al.*, 2002). The simplified model (similar to those defined by Yapp and Epstein (1982) and Saurer *et al.* (1997)) is as follows:

$$\delta_{sw} \approx \delta^{18}O_{cellulose} - (1-f)(1-h)(\varepsilon_e + \varepsilon_k) - \varepsilon_{biochem}$$

where δ_{sw} is the isotopic composition of source water, $\delta^{18}O_{cellulose}$ is the isotopic composition of tree-ring cellulose, h is growing-season relative humidity, ε_e is the liquid–vapor equilibrium fractionation for water (Majoube, 1971), ε_k is the liquid–vapor kinetic fractionation at the leaf boundary layer held constant at 28‰ (Buhay *et al*., 1996), and $\varepsilon_{biochem}$ is a biologic fractionation factor held constant at 27‰ (Anderson *et al.*, 2002). Although dampening factors are sometimes held constant for simplicity, we calculated a variable dampening factor, represented as the variable *f*, for each year as shown below to estimate the fraction of water re-exchanging with source water (xylem water) prior to cellulose synthesis:

$$f = -1.47 \times RH + 0.03 \times T + 0.11 \times TRX + 0.62$$

where *RH* is mean growing-season (May-September) relative humidity at the growth site (calculated using mean growing-season T and T_d from PRISM), *T* is mean growing-season temperature, and *TRX* is the total tree-ring width index for a given year. Of the three approaches they tested (constant *f,* linear regression using only RH, and multivariate regression as used here), Anderson *et al.* (2002) found that the multivariate model we selected produced the best fit with $\delta^{18}O_P$ values. By using tree-ring cellulose $\delta^{18}O$ values as inputs in the model, we can directly compare the modeled outputs with seasonal *in situ* amount-weighted $\delta^{18}O_P$ values from the NADP sites that theoretically represent source water for our trees. We also compare the resulting $\delta^{18}O_{SW}$ values with monthly and seasonal composites of temperature and precipitation. However, when interpreting relationships between modeled $\delta^{18}O_{SW}$ values and growing-season climate, it is important to consider that growing-season (March-September) temperature and relative humidity are used as predictors in the mechanistic model. As a result, a certain degree of

growing-season climate conditions are therefore intrinsically embedded within the modeled $\delta^{18}O_{SW}$ values, which may inflate correlations between climate variables and $\delta^{18}O_{SW}$ values.

Statistical analyses

We used the R package treeclim (Zang and Biondi, 2015) to calculate correlations between the tree-ring isotope time series and various seasonal averages of precipitation and temperature during the year of growth and the preceding summer, fall, and winter. Treeclim was selected for this analysis despite its more simplified output because, unlike Seascorr (used in Chapter 3), it permits analyses of time series shorter than 30 years. A thirty-year analysis period has officially been the standard for calculations of climate normals for nearly a century (NCEI, 2022) and has generally been considered an "acceptable trade-off" between increased noise in shorter time series and considerable changes in the normal over longer periods (Livezey *et al.*, 2007). Therefore, the shorter time series used here may exhibit a lower signal-to-noise ratio than a longer series. This smaller sample size also results in a larger confidence interval, but it does likely capture the general relationship between the two variables assuming they are normally distributed (de Winter *et al.*, 2016).

Because the $\delta^{18}O$ value of tree-ring cellulose is influenced by both environmental and physiological factors, we also chose to compare temperature and precipitation records with modeled $\delta^{18}O_{SW}$ values to extract the source water signal, which is theoretically more directly related to climate, in addition to comparisons with measured $\delta^{18}O_{EW/LW}$ values. We used our preliminary analyses in treeclim to identify target seasons for comparisons between modeled $\delta^{18}O_{SW}$ values, temperature, and precipitation. From the PRISM climate dataset, we computed monthly and seasonal (i.e., prior August-October, prior October-December, current May-August

and current Mar-May) averages of temperature and precipitation, and we calculated monthly and seasonal amount averages of $\delta^{18}O_P$ values from our NADP series at each site.

We then calculated Pearson's correlation coefficient between each climate variable and 1) modeled $\delta^{18}O_{SW}$ values and 2) measured $\delta^{18}O_{EW/LW}$ values using the treeclim package. The advantage of using treeclim rather than only performing simple correlation calculations is that its dcc function performs bootstrap resampling to test for significant correlations and exact simulation to produce confidence intervals (Zang and Biondi, 2015). To do this, treeclim uses the input series to generate 1000 simulations of the proxy time series (generally tree-ring width indices but in this case $\delta^{18}O_{EW/LW}$ values). which is particularly valuable in this study because our EW and LW $\delta^{18}O$ time series are of limited length (thirteen years). The dcc function accomplishes this simulation by using a Fourier transform and periodogram to estimate the spectrum of the proxy time series and then compute the predictand and estimate significance (Zang and Biondi, 2015) using the percentile range method (Dixon, 2001) and empirical nonexceedance probabilities using the Weibull formula (Stedinger *et al.*, 1993). Overall, using this exact simulation approach allows us to better contextualize the resulting correlations and estimate significance and confidence intervals despite the limited length of our dataset.

Synoptic analyses

To examine the relationship between synoptic conditions and tree-ring $\delta^{18}O$ values, we generated composite maps of 500 mb height anomalies for seasons that we hypothesized to most impact the isotopic composition of tree rings based on our findings from treeclim (this chapter) and Seascorr (Chapter 3). These maps were derived from the NOAA Physical Sciences Laboratory and created using NCEP/NCAR Reanalysis products (Kalnay *et al.*, 1996). We

examined March-September in the current year to represent synoptic conditions during the growing season, prior-year October through current-year June to represent the time period that produces most of the precipitation available to trees at our sites, and prior-year December through current February to capture winter precipitation. To contextualize these maps within the context of important teleconnections in the region, we also obtained monthly values of the Pacific/North American Pattern index (PNAI), Southern Oscillation index (SOI), and West Pacific teleconnection index (WPI), as these teleconnections have been identified as exerting influence over geopotential heights and cool-season precipitation in our study area (Wise *et al.*, 2015).

Because of the limited length of our isotope records, we identified amount-weighted precipitation values and tree-ring $\delta^{18}O$ values that were at least one standard deviation above or below the mean to isolate more extreme values for comparison with synoptic drivers and each other. However, we note that several teleconnections are known to influence $\delta^{18}O_P$ values in multidecadal phases and suggest that a longer dataset would better represent these patterns over time. We also examined values from 2015, as this was a known snow drought year in the PNW (Marlier *et al.*, 2017) that was captured by $\delta^{18}O_{SW}$ values modeled from other tree-ring isotopic records in the region (A. Csank, personal communication).

Results and Discussion

Overview of tree-ring isotope time series

Tree-ring isotope ratios average 26.2 ± 1.1 ‰ and range from 22.2 to 29.2 ‰ across all sites (Figure 4.2). $\delta^{18}O_{EW}$ and $\delta^{18}O_{LW}$ values are slightly higher at our most xeric site (WA24) compared to the least xeric site (ID02), which aligns with the findings of other research on alpine

species (Lévesque et al., 2013). In addition, EW and LW isotope ratios are significantly correlated at WA24 but not at ID02 or OR18 ($\alpha = 0.05$). Because of the greater number of trees contributing to the pooled samples at WA24, it is possible that this correlation and smaller range of values is in fact more representative of tree response at the site. However, two other complications could explain this difference: 1) combining material from many different trees ($n = 10$) could introduce more opportunities for contamination and error; and 2) the experimental farm setting at WA24. Unlike the other two study sites, WA24 (Palouse Conservation Farm) is heavily managed and is home to ongoing environmental experiments (USDA, 2018) that could influence precipitation cycling and evaporative conditions.

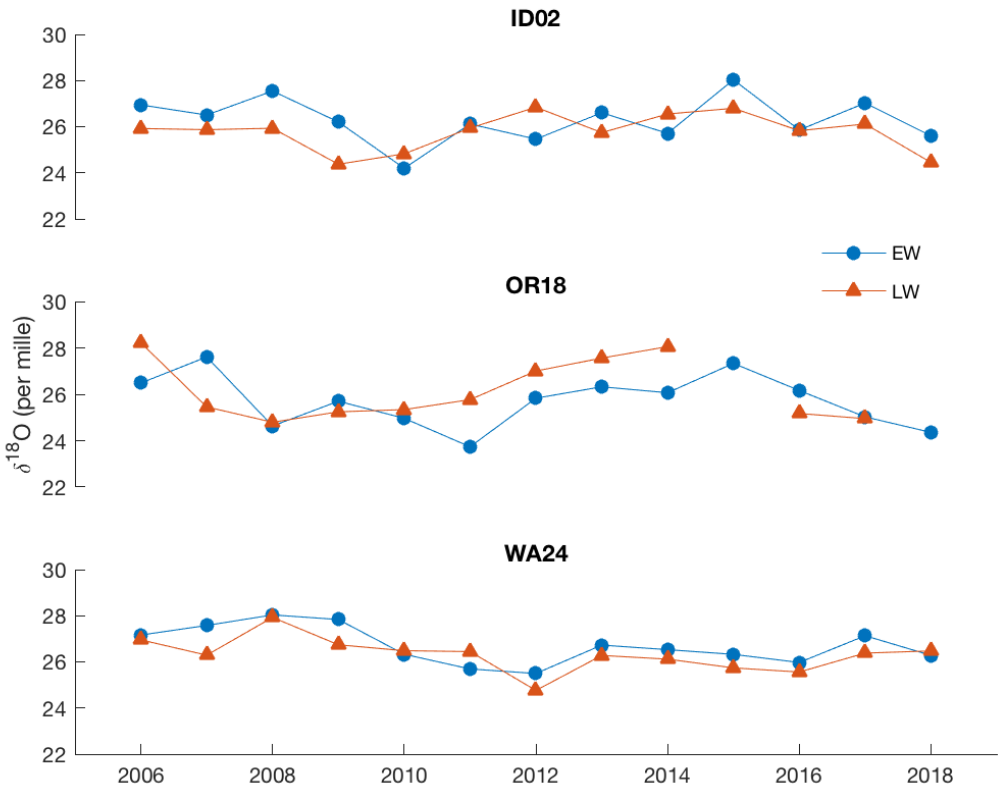

Figure 4.2. Time series of tree-ring oxygen isotope ratios. Blue circles represent earlywood, and orange triangles represent latewood.

At ID02 and WA24, $\delta^{18}O_{EW}$ values were higher than those for LW (Table 4.1); the difference was not statistically significant at $\alpha = 0.05$ at any site but was statistically significant at $\alpha = 0.10$ at ID02. This finding aligns with those of other studies suggesting that $\delta^{18}O$ values of latewood may reflect isotopically-lighter winter-spring precipitation (Zhu *et al.*, 2021) and therefore can be, on average, lower than those for earlywood. Tree-ring width indices and isotopic ratios for the same season (i.e., earlywood width and earlywood $\delta^{18}O$ values) are not significantly correlated at any site for either earlywood or latewood. TRW is also not significantly correlated with either earlywood $\delta^{18}O$ or latewood $\delta^{18}O$ values at either site, suggesting that these variables each provide unique climatic information.

Table 4.1. Site averages of earlywood and latewood $\delta^{18}O$ values of tree-ring cellulose at each of our three sites.

Site	EW/LW	$\delta^{18}O$ cellulose (‰ VSMOW)
ID02	EW	26.3 ± 1.0
	LW	25.8 ± 0.8
OR18	EW	25.7 ± 1.4
	LW	26.1 ± 1.3
WA24	EW	26.7 ± 0.9
	LW	26.4 ± 0.8

Overview of modeled source water isotope time series

The $\delta^{18}O_{SW}$ time series modeled from $\delta^{18}O_{EW}$ and $\delta^{18}O_{LW}$ values at ID02 and OR18 are generally well-matched with amount-weighted growing-season $\delta^{18}O_P$ values from their accompanying NADP stations (Figures 4.3, 4.4). Trees at both sites capture similar patterns, with low values during 2010-2011 and higher values in 2013 and 2015 (Figures 4.3, 4.4). 2015 was a snow drought year in the PNW where much of the winter precipitation fell as rain (Marlier *et al.*,

2017), which would be expected to produce higher $\delta^{18}O$ values as snow generally has much lower $\delta^{18}O$ values than rain (Gonfiantini and Picciotto, 1959). Therefore, it is possible that the higher $\delta^{18}O$ values captured by trees at these sites reflect this larger-scale phenomenon that was also captured by trees at other sites in the region (A. Csank, personal communication). It is also possible that this pattern is caused by an increased reliance on summer precipitation with higher $\delta^{18}O$ values; a longer time series would allow us to better understand which influence accounts for this pattern and is a promising avenue for future research.

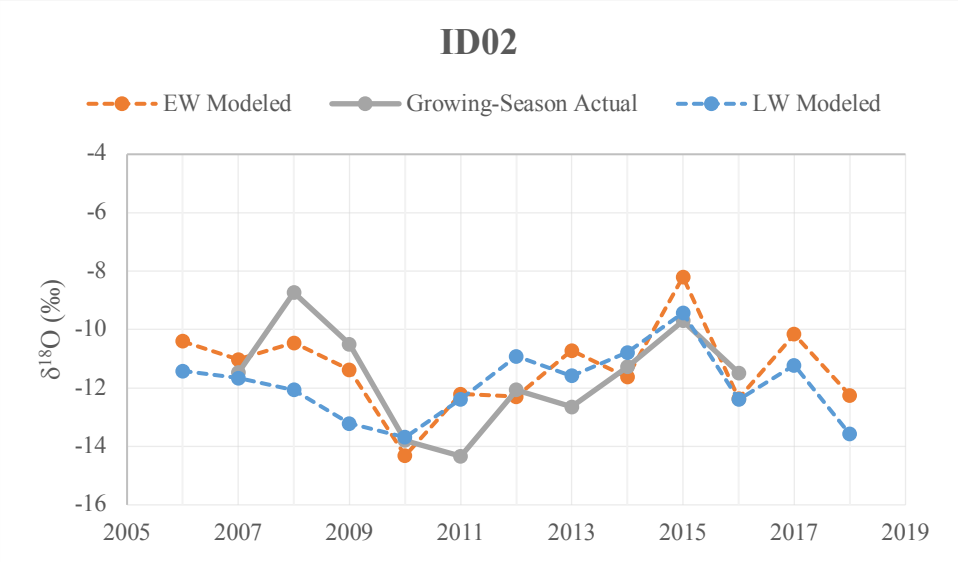

Figure 4.3. Comparison of $\delta^{18}O_{SW}$ values modeled from $\delta^{18}O_{EW}$ (orange line) and $\delta^{18}O_{LW}$ (blue line) values with actual amount-weighted growing-season $\delta^{18}O_P$ values (gray line) from NADP precipitation samples at ID02.

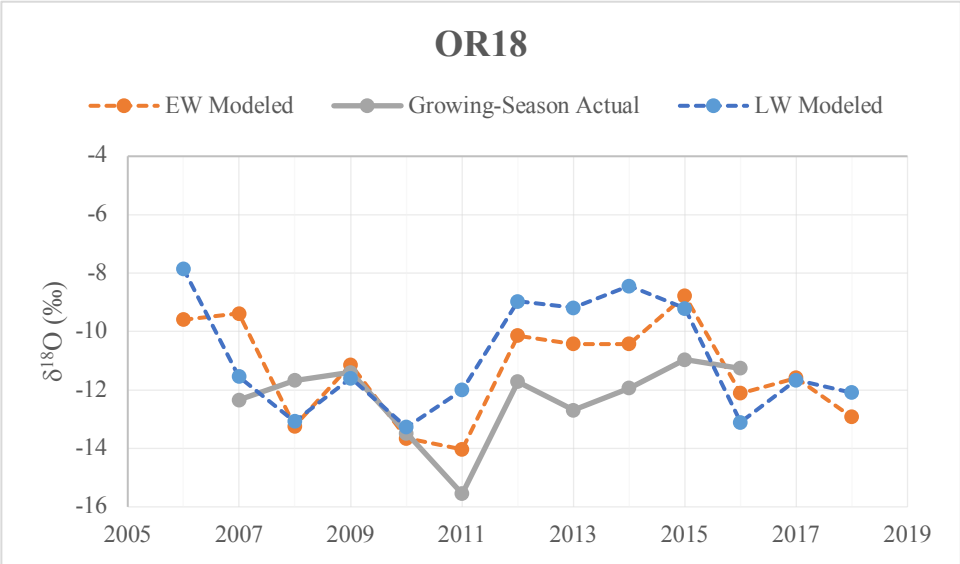

Figure 4.4. Comparison of $\delta^{18}O_{SW}$ values modeled from $\delta^{18}O_{EW}$ (orange line) and $\delta^{18}O_{LW}$ (blue line) values with actual amount-weighted growing-season $\delta^{18}O_P$ values (gray line) from NADP precipitation samples at OR18.

The modeled and *in situ* (growing-season) $\delta^{18}O$ time series at WA24 are not well-matched aside from 2009-2011, and *in situ* $\delta^{18}O_P$ values are considerably lower than predicted by the model (Figure 4.5). Overall, modeled $\delta^{18}O_{SW}$ values tend to increase with increasing site aridity (Figures 4.3-4.5), but the *in situ* $^{18}O_P$ values at WA24 break with this pattern. As previously mentioned, it is likely that interventions at the Palouse Conservation Farm may be responsible for these differences. However, the fact that modeled values based on actual $\delta^{18}O_{cellulose}$ values follow the expected trend while the precipitation values do not suggests more complexity in this relationship and a mismatch between growing-season precipitation and $\delta^{18}O_{cellulose}$ values at the site that will be examined in proceeding sections.

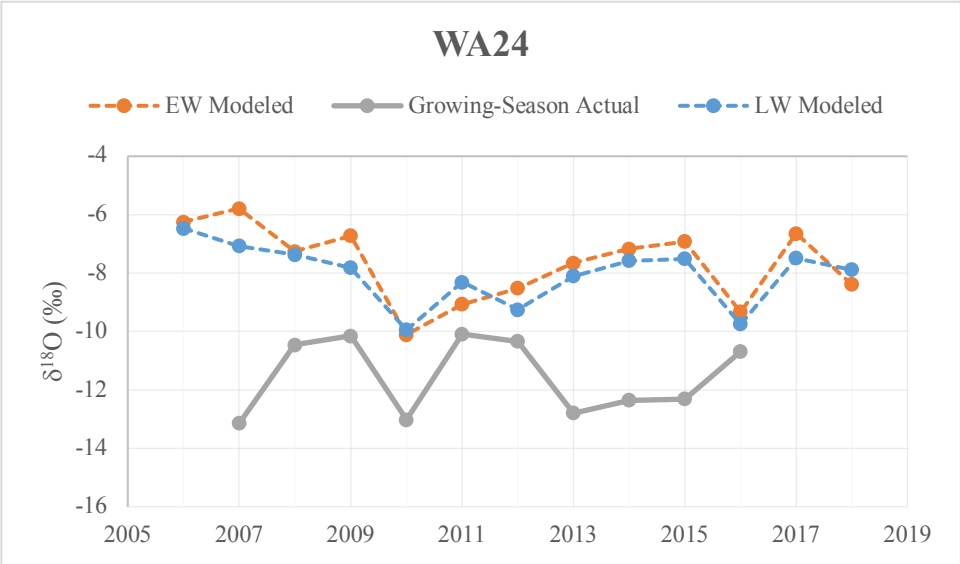

Figure 4.5. Comparison of $\delta^{18}O_{SW}$ values modeled from $\delta^{18}O_{EW}$ (orange line) and $\delta^{18}O_{LW}$ (blue line) values with actual amount-weighted growing-season $\delta^{18}O_P$ values (gray line) from NADP precipitation samples at WA24.

Capture of local precipitation and temperature by $\delta^{18}O_{EW}$ and $\delta^{18}O_{LW}$ values

We find that seasonal mean temperature exerts a more widespread and consistent influence over modeled $\delta^{18}O_{SW}$ and measured $\delta^{18}O_{cellulose}$ values than does seasonal precipitation amount (Tables 4.2, 4.3). This is unsurprising, as generally sites above 30°N/S latitude tend to exhibit significant correlation of $\delta^{18}O_P$ values with temperature, while sites below 30°N/S latitude exhibit correlation between $\delta^{18}O_P$ values and precipitation amount but not temperature (Bowen, 2008). There is a generally strong and significant relationship between $\delta^{18}O_{SW}$ values modeled from both EW and LW and May-September (growing season) temperature at our sites (Table 4.3). This relationship is consistently positive with the exception of our most arid site, WA24. Positive temperature-$\delta^{18}O_{SW}$ relationships are well-explained by the temperature effect, wherein increased temperature results in evaporative enrichment of ^{18}O in meteoric water (Dansgaard, 1964).

While generally weak, we do find correlations between $\delta^{18}O_{SW}$ values and precipitation amount at our sites, some of which are significant. With the exception of winter precipitation at ID02, these correlations are consistently negative. This negative relationship is likely due to the amount effect, wherein higher precipitation rates lead to lower $\delta^{18}O$ values of precipitation as ^{18}O preferentially rains out, leaving proportionally more ^{16}O and decreasing the $\delta^{18}O$ value (Dansgaard, 1964; Gat, 1971). This effect is apparent even for tropical and other wet climates where temperature is relatively constant and therefore does not significantly alter the $\delta^{18}O$ value of precipitation (Rozanski *et al.*, 1993; Kurita *et al.*, 2009). Therefore, it does seem likely that this relationship is not spurious. The positive relationship between precipitation amount and $\delta^{18}O_{LW}$ values does not fit this model and may either be spurious or due to factors not considered here.

Table 4.2. Summary of statistically-significant relationships between three-month precipitation composites and (bottom) measured tree-ring cellulose $\delta^{18}O$ values ["Tree Cellulose"] and (top) modeled source water $\delta^{18}O$ values ["Source Water"]. An asterisk denotes that a given season begins in the year prior to growth; i.e., *aso refers to total precipitation during August, September, and October of the year prior to growth. Statistically-significant relationships are shaded and include the sign (positive or negative) of the precipitation amount-isotope relationship.

	Precipitation	*aso	*son	*ond	*ndj	*djf	jfm	fma	mam	amj	mjj	jja	jas
Source Water	ID02 EW									-	-	-	
	ID02 LW												
	OR18 EW	-											
	OR18 LW												
	WA24 EW										-		
	WA24 LW										-		
Tree Cellulose	ID02 EW									-	-		
	ID02 LW						+	+					
	OR18 EW	-					-		-	-			
	OR18 LW												
	WA24 EW										-		
	WA24 LW										-		

Table 4.3. Summary of statistically-significant relationships between three-month temperature composites and (bottom) measured tree-ring cellulose $\delta^{18}O$ values ["Tree Cellulose"] and (top) modeled source water $\delta^{18}O$ values ["Source Water"]. An asterisk denotes that a given season begins in the year prior to growth; i.e., *aso refers to average temperature during August, September, and October of the year prior to growth. Statistically-significant relationships are shaded and include the sign (positive or negative) of the temperature-isotope relationship.

	Temperature	*aso	*son	*ond	*ndj	*djf	jfm	fma	mam	amj	mjj	jja	jas
Source Water	ID02 EW										+	+	
	ID02 LW											+	+
	OR18 EW		+						+	+	+	+	
	OR18 LW				+						+	+	+
	WA24 EW										+	+	+
	WA24 LW										+	+	
Tree Cellulose	ID02 EW												
	ID02 LW												
	OR18 EW			+		+	+	+	+	+	+	+	
	OR18 LW				+								
	WA24 EW	-				-							
	WA24 LW	-	-					-					

In general, our modeled $\delta^{18}O_{SW}$ values correlate strongly with *in situ* amount-weighted $\delta^{18}O_P$ values, though the strength of this relationship varies between sites, between earlywood and latewood from the same site, and depending on the season of $\delta^{18}O_P$ values used for the comparison (Table 4.4). At our two less-arid sites, ID02 and OR18, May-September (growing season) $\delta^{18}O_P$ values are highly correlated with $\delta^{18}O_{SW}$ values modeled from both EW and LW. Values of $\delta^{18}O_{SW}$ modeled from EW also significantly reflects growing-season temperature at OR18 and growing-season temperature and precipitation at ID02 and WA24.

Table 4.4. Pearson correlation coefficients between amount-weighted seasonal precipitation $\delta^{18}O_p$ values for prior October-current April, prior October-December, and current May-September and (bottom) measured tree-ring cellulose $\delta^{18}O$ values ["Tree Cellulose"] and (top) modeled source water $\delta^{18}O$ values ["Source Water"]. Earlywood values are shaded in light gray, and latewood values are unshaded.

		$\delta^{18}O_P$ *Oct-Apr	$\delta^{18}O_P$ *Oct-Dec	$\delta^{18}O_P$ May-Sep
Source Water	ID02 EW	-0.10	0.44	0.69
	ID02 LW	0.26	0.73	0.39
	OR18 EW	0.39	0.82	0.61
	OR18 LW	0.60	0.73	0.25
	WA24 EW	0.31	0.54	-0.20
	WA24 LW	0.42	0.43	-0.14
Tree Cellulose	ID02 EW	-0.35	0.30	0.71
	ID02 LW	0.13	0.19	0.67
	OR18 EW	0.26	0.72	0.64
	OR18 LW	0.63	0.64	0.09
	WA24 EW	0.15	-0.05	-0.09
	WA24 LW	0.19	-0.30	0.05

Although May-September $\delta^{18}O_P$ values are highly correlated with $\delta^{18}O_{SW}$ values modeled from both EW and LW, prior-year October-December $\delta^{18}O_P$ values are even more highly correlated in many cases. This relationship is particularly notable at WA24, where the relationship between May-September $\delta^{18}O_P$ and $\delta^{18}O_{SW}$ values modeled from both EW and LW

is very weak, but the relationship with prior October-December $\delta^{18}O_P$ values is strong. Other isotopic studies have found that trees in relatively dry regions with dominant winter precipitation often use winter precipitation (Leonelli *et al.*, 2017), particularly when facing summer drought conditions (Allen *et al.*, 2019), and that EW $\delta^{18}O$ values tends to directly reflect current-growing-season $\delta^{18}O_P$ while LW $\delta^{18}O$ values may incorporate meltwater and is generally more complicated (An *et al.*, 2012). Conifers in particular use "legacy water reservoirs" from prior seasons and show a preference for snowmelt, though this relationship may cycle over time (Berkelhammer *et al.*, 2020). Reliance on winter precipitation has even been found in relatively dry-summer Mediterranean climates (Brooks et al., 2010; Rempe and Dietrich, 2018), emphasizing the importance that dry summers play in driving trees to rely on stored precipitation later in the growing season. Therefore, while $\delta^{18}O_{LW}$ values may not represent current growing-season conditions, $\delta^{18}O_{SW}$ values modeled from this wood may provide information about the isotopic composition of precipitation during the prior winter, especially when trends are considered as a spatial network rather than a single site. Common climate signals in tree-ring $\delta^{18}O$ values have been found across large swaths of Europe (Treydte *et al.*, 2007), and even when signals differ across space, they have demonstrated influence from a common climate pattern (Szejner *et al.*, 2016).

Values of $\delta^{18}O_{SW}$ modeled from latewood are more highly correlated with amount-weighted October-December $\delta^{18}O_P$ values than with mean October-December temperature at all three sites. This suggests that latewood captures unique climate information in its isotopic composition that is not solely related to temperature. We also found a considerable prior-winter signal within latewood width and adjusted latewood width for the same sites, further supporting the finding that latewood metrics capture prior-winter climate. At ID02, modeled $\delta^{18}O_{SW}$ value

correlate most strongly with growing season $\delta^{18}O_P$ values, and the modeled $\delta^{18}O_{SW}$ values from $\delta^{18}O_{EW}$ values produce a stronger correlation than that modeled from $\delta^{18}O_{LW}$ values. This site shows little correlation with prior October-current June $\delta^{18}O_P$ for $\delta^{18}O_{EW}$ values but some for $\delta^{18}O_{LW}$ values. At OR18, modeled $\delta^{18}O_{SW}$ values based on both $\delta^{18}O_{EW}$ and $\delta^{18}O_{LW}$ values correlate strongly with prior October-current June $\delta^{18}O_P$ values and show some correlation with growing season $\delta^{18}O_P$ values. WA24 is the only site where $\delta^{18}O_{LW}$ values provide better estimates of growing season $\delta^{18}O_P$ than $\delta^{18}O_{EW}$ values, though correlations between $\delta^{18}O_{SW}$ and $\delta^{18}O_P$ values are weaker than at the other sites.

In summary, the strength of the climate-tree isotope relationship and the *in situ* precipitation isotope-tree isotope relationship is often improved by using mechanistically modeled $\delta^{18}O_{SW}$ values rather than tree-ring cellulose $\delta^{18}O$ values at our sites. This is unsurprising because the mechanistic model incorporates growing-season temperature and relative humidity and therefore is not solely based on the particular isotopic signal the tree was able to capture. However, we suggest that because modeled values can be easily calculated using mean temperatures and dew point temperatures that are readily available from PRISM for 1895 onward, the calculation of modeled $\delta^{18}O_{SW}$ values is a useful and accessible means of improving climate capture from measurements of tree-ring cellulose $\delta^{18}O$ values over at least the past 125 years.

Synoptic-scale influences

In light of the possible link between winter precipitation and $\delta^{18}O_{EW}$ and $\delta^{18}O_{LW}$ values, we focus our discussion here on synoptic-scale patterns during October-March. We identify years in which at least two sites demonstrate anomalously high or low $\delta^{18}O_{EW}$ and $\delta^{18}O_{LW}$ values

(± one standard deviation from the mean) to attempt to isolate synoptic-scale influence (Table 4.5). The years 2007, 2008, and 2015 meet the criteria for a positive $\delta^{18}O_{EW}$ and $\delta^{18}O_{LW}$ anomaly year, while 2011 and 2018 are identified as years with a negative anomaly. We find that the 2015 snow drought is well-captured by trees at ID02 and OR18 and that 2015 was characterized by anomalously high $\delta^{18}O_{EW}$ and $\delta^{18}O_{LW}$ values at these sites and a positive cool-season 500 mb height anomaly centered over the west coast of North America (Figure 4.6). This capture is particularly notable because the 2015 snow drought was a result of above-average temperatures causing most precipitation to fall as rain rather than snow, but winter precipitation in general was not anomalously low (Marlier *et al.*, 2017). This pattern is projected to become more frequent in the future (Marlier *et al.*, 2017), highlighting the complex interplay between temperature and precipitation in this region and how it impacts the snowpack that supplies summer hydropower. 2007 and 2008 do not exhibit a clear pressure anomaly pattern in line with that from 2015 (Figure 4.6), though 2007 does show positive height anomalies over the study area. In contrast, 2011 was characterized by anomalously low $\delta^{18}O_{EW}$ values and a negative cool-season 500 mb height anomaly centered over the PNW (Figure 4.7). 2018 does not express such a pattern, with no anomaly over the study area (Figure 4.7). These findings suggest that while there may be synoptic-scale influence on tree-ring isotopes, examination of a longer time series is needed to contextualize these findings as previously suggested by Liu *et al.* (2013).

Table 4.5. Identification of years that produced anomalous $\delta^{18}O_{EW}$ and $\delta^{18}O_{LW}$ values. $\delta^{18}O_{EW}$ and $\delta^{18}O_{LW}$ values that are at least one standard deviation above (below) the site mean [calculated separately for earlywood and latewood] are shaded in pink (blue). All $\delta^{18}O_{EW}$ and $\delta^{18}O_{LW}$ values are in ‰ relative to VSMOW.

	ID02		OR18		WA24		
Year	$\delta^{18}O_{EW}$	$\delta^{18}O_{LW}$	$\delta^{18}O_{EW}$	$\delta^{18}O_{LW}$	$\delta^{18}O_{EW}$	$\delta^{18}O_{LW}$	Anomaly
2006	26.9	25.9	26.5	28.2	27.2	27.0	
2007	26.5	25.9	27.6	25.5	27.6	26.3	+
2008	27.5	25.9	24.6	24.8	28.0	27.9	+
2009	26.2	24.4	25.7	25.2	27.8	26.7	
2010	24.2	24.8	25.0	25.3	26.3	26.5	
2011	26.1	25.9	23.7	25.8	25.7	26.4	-
2012	25.5	26.8	25.8	27.0	25.5	24.8	
2013	26.6	25.7	26.3	27.6	26.7	26.3	
2014	25.7	26.5	26.1	28.1	26.5	26.1	
2015	28.0	26.8	27.3	26.9	26.3	25.7	+
2016	25.9	25.8	26.2	25.2	26.0	25.6	
2017	27.0	26.1	25.0	24.9	27.1	26.4	
2018	25.6	24.4	24.4	25.5	26.3	26.5	-

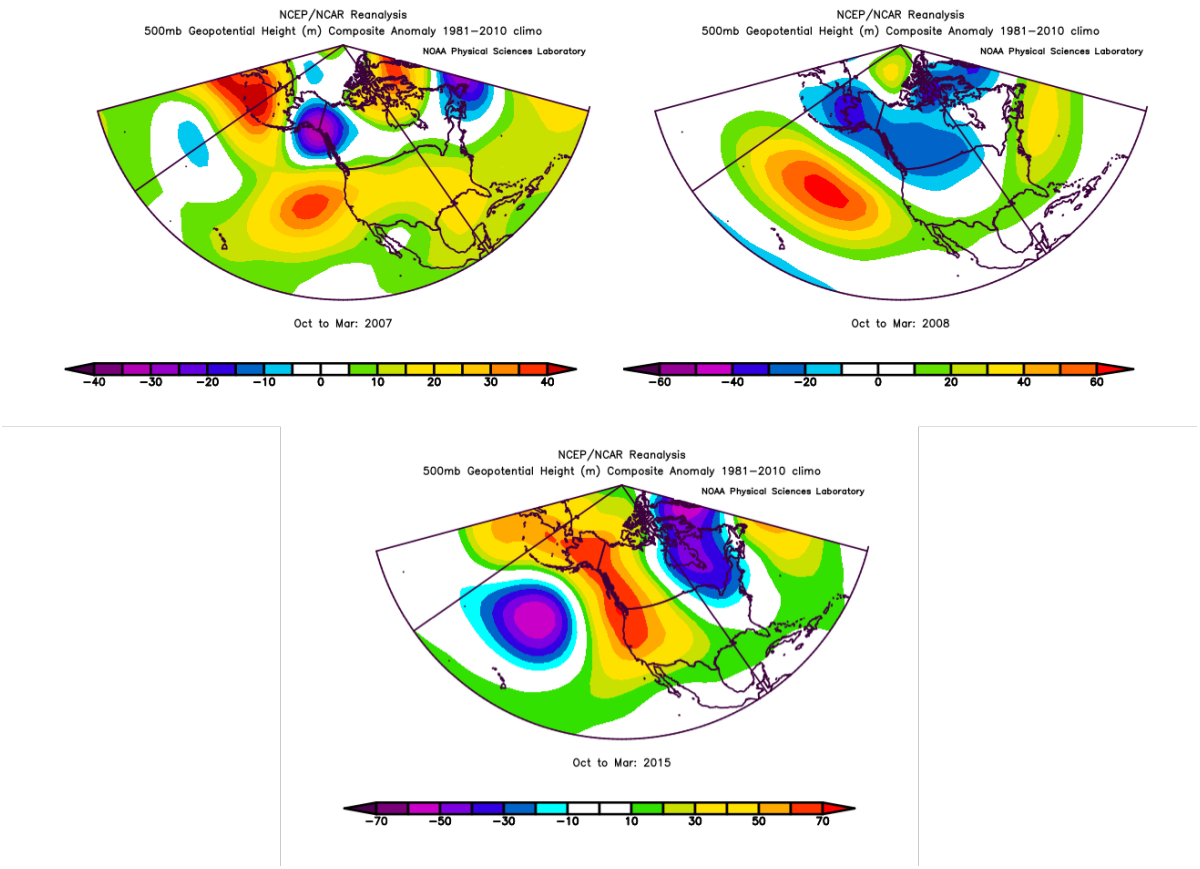

Figure 4.6. Composites of October-March 500 mb geopotential height anomalies in years that produced anomalously high tree-ring $\delta^{18}O$ values (2007, 2008, and 2015).

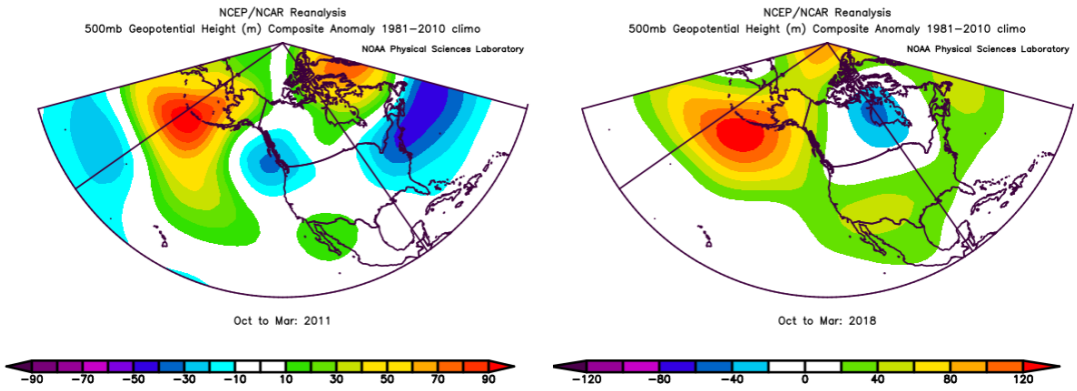

Figure 4.7. Composites of October-March 500 mb geopotential height anomalies in years that produced anomalously low tree-ring $\delta^{18}O$ values (2011 and 2018).

Although some tree-ring width records in western North America are sensitive to the Pacific/North American pattern (PNA) (Trouet and Taylor, 2010), this relationship is not universal. For example, out of twelve chronologies from the core region of PNA influence on winter climate that were tested for reconstruction, the three that were retained were from Montana and Alaska (Trouet and Taylor, 2010), indicating that chronologies in other parts of the region did not exhibit a robust relationship. Additionally, the overlapping of teleconnections in different phases can amplify, mute, or otherwise alter the influence of individual teleconnections (Liu *et al.*, 2013; Wise *et al.*, 2015), and this interplay is apparent in the PNW (Wise *et al.*, 2015). While we did not find a consistent relationship between tree-ring isotopic ratios and the PNA index over our short study period, it is notable that 2015 was a PNA+ year that produced both above-average winter temperatures and anomalously high $\delta^{18}O$ values captured by the trees we sampled. The increase in regional isotopic ratios during PNA+ years is related to a greater frequency of meridional flow and, subsequently, tropical air masses bringing isotopically heavy precipitation to the region (Liu *et al*. 2013). This further complicates interpretation of our findings in 2015, as the PNA connection suggests that above-average temperatures, isotopically enriched precipitation brought in by meridional flow, or a combination of the two factors could be responsible for the isotopically anomalous tree-ring cellulose from this year.

While these short-term findings for our study area are not definitive, it is possible that a longer time series would reveal clearer patterns. Many tree-ring width records are positively correlated with positive PNA and ENSO indices in the PNW, but these patterns vary in strength, sign, and significance across the region (St. George, 2014). Teleconnection influences may also be expressed in longer-term phases (Jouzel *et al.*, 1997) and the influence of overall climate forcing acts on precipitation isotopes on multiple scales (Berkelhammer *et al.*, 2012), both

suggesting that a combination of proxies with advantages for short- and longer-term climate capture is necessary. Tree-ring $\delta^{18}O$ chronologies stand to play an important role amongst these proxies because they do not generally express juvenile effects or other long-term trends that require detrending as in traditional tree-ring measurements. Consequently, tree-ring $\delta^{18}O$ chronologies are often able to retain more low-frequency signals (Young *et al.*, 2010; Rinne *et al.*, 2013), and tree-ring $\delta^{18}O$ chronologies in this region may hold promise for long-term reconstructions that preserve low-frequency variability (Edwards *et al.*, 2008).

Conclusion

In this study, we used $\delta^{18}O$ values of precipitation and subannual tree-ring cellulose from three sites in the U.S. Pacific Northwest to understand their relationship to climate and to each other. Through mechanistic modeling, correlation analyses with local climate data, and examination of synoptic conditions throughout the study period, we found that $\delta^{18}O_{cellulose}$ values appear to capture summer precipitation amounts at two sites and some prior-autumn and winter-spring precipitation signals. We also found that our tree-ring $\delta^{18}O$ values best reflect the $\delta^{18}O$ values of prior-winter and current-growing-season precipitation, though there are exceptions to this relationship. Tree-ring $\delta^{18}O$ values also captured temperature signals ranging from the prior summer through the current growing season. Many of these relationships were improved and somewhat shifted when the mechanistic model was applied to estimate source water, though relationships with summer temperature in particular should be viewed with caution since growing-season relative humidity and temperature are considered in the model. However, the fact that spring/summer and prior-winter influences are evident both in tree-ring $\delta^{18}O$ values and estimated source water improves the likelihood that these relationships are not artefacts. Taken

together, analyses of both subannual ring widths and $\delta^{18}O_{cellulose}$ values suggest that trees at our driest site, WA24, are particularly dependent on antecedent moisture and prior-winter precipitation, especially during the driest part of the year when latewood is formed.

As suggested by Anderson *et al.* (2002), a robust match between $\delta^{18}O_{cellulose}$ values and modeled $\delta^{18}O_{SW}$ values at a site indicates that source water could be reconstructed over a century or more in locations where estimates of relative humidity can be made. In the PNW where our study is situated, we used freely accessible PRISM data to demonstrate that the resulting modeled $\delta^{18}O_{SW}$ values from two of our three sites closely matches growing-season or prior October-December *in situ* measurements of $\delta^{18}O_P$ values from nearby stations. This study shows the potential for longer-term studies of $\delta^{18}O_{cellulose}$ values in our study region for reconstructing $\delta^{18}O_P$ values to at least 1895, the start of the PRISM coverage period. This would be particularly useful for examining climate forcings that act on decadal scales, as tree-ring isotope ratios retain more low-frequency variability than their ring-width counterparts because they generally do not require detrending. By combining studies of this type with tree-ring width measurements and stable isotope proxies such as speleothems and lake sediments, we can better understand the unique advantages of each proxy across time and space and how they work together to provide a more richly detailed understanding of the past.

CHAPTER 5: SUMMARY AND CONCLUSIONS

Water resources in the U.S. Pacific Northwest are intimately connected with the seasonality of precipitation and, in turn, with the hydropower that much of the region relies upon. As an increasing frequency of summer heat waves increases the need for ever more hydropower-driven air conditioning to sustain quality of life in the region (Philip *et al.*, 2021; Balk, 2021; United States Census Bureau, 2019), the need to understand precipitation patterns at a range of spatial and temporal scales becomes ever more apparent. A range of climate proxies provide a key to contextualizing these current conditions within long-term variability (Berkelhammer *et al.*, 2012) to better understand possible futures. In this dissertation, I explored the utility of three interconnected climate proxies—stable isotope ratios in precipitation, subannual tree-ring widths, and stable isotope ratios of tree-ring cellulose —to better understand their unique advantages and limitations across an aridity gradient in the PNW and the role they stand to play in reconstructing seasonal precipitation, temperature, and source water $\delta^{18}O$ patterns in the region.

In Chapter 2, I used back-trajectory analysis to examine the trajectories followed by air parcels that produced isotopically anomalous precipitation and identify patterns in these trajectories with the goal of understanding the trajectory-isotope relationship in the region's precipitation. In Chapter 3, I quantified the relationship between subannual tree-ring width measurements and seasonal climate data at sites near those explored in Chapter 2 to determine the extent to which simple ring-width measurements capture seasonal climate signals. Lastly, in

Chapter 4, I compared the stable isotope ratios of the tree rings studied in Chapter 3 with seasonal climate data and used the tree-ring isotope measurements to mechanistically model the source water used by those trees and compare the modeled source water with *in situ* precipitation from nearby sites and synoptic-scale climate patterns.

Taken together, the findings of this research on the connection between trees, oxygen isotope ratios, and climate in the U.S. Pacific Northwest make three main contributions to the fields of physical geography, dendroclimatology, and stable isotope geochemistry:

(1) Understanding the relationship between precipitation isotopes and air mass trajectories. While oxygen isotope ratios in precipitation have been extensively studied around the world (Rozanski *et al.*, 1993), much of this research has relied on short (a few years), discontinuous, or low-temporal-resolution (monthly) datasets that obscure finer details of the air mass-isotope relationship (e.g., Vachon *et al.* 2010a; Marchetti and Marchetti, 2019). In Chapter 2 of this dissertation, I used a ten-year-long weekly precipitation isotope dataset and back-trajectory analysis to examine the air mass-isotope relationship at five sites and determine spatial and seasonal patterns in this relationship. I found that although many precipitation samples with high (low) $\delta^{18}O$ values originated from air masses following southerly (northerly) trajectories as expected due to the temperature effect (Dansgaard, 1964), there are exceptions to this pattern that complicate the trajectory-isotope relationship in this region that are likely due to the amount effect, complex topography, and moisture recycling. Consequently, the interpretation of paleoclimate records that rely on an accurate understanding of this relationship must consider these influences and how they may impact the stable isotopic composition of precipitation across spatial and temporal scales.

(2) Improving seasonal reconstructions of past climate. Because trees are most sensitive to climate at their ecological limits (Briffa *et al.*, 2002), most tree-ring width studies have focused on these regions. Where traditional total-ring-width measurements are less sensitive, the exploration of other metrics stands to unlock additional climate information (Anderson *et al.*, 1998; Saurer *et al.*, 2008) and enable seasonal reconstructions, which are important for understanding precipitation patterns in regions with highly seasonal precipitation such as the U.S. PNW. In Chapter 3, I found that subannual ring-width measurements, which require little additional labor and no added equipment or expense beyond traditional tree-ring analyses, provide seasonal climate information that is not available through measurements of total ring widths alone. I found that latewood widths in particular are useful for isolating prior-winter and late-summer precipitation signals that are important for addressing summer water and hydropower availability in the PNW, which corroborates previous findings (Crawford *et al.*, 2015) and makes this metric a logical target for future research in the region. Performing similar analyses of the climate-proxy relationship in Chapter 4 allowed me to demonstrate that the stable isotope ratio of tree-ring cellulose at these same sites captures some unique information about local climate and therefore holds potential for reconstructing source water (Anderson *et al.*, 2002), which is linked with atmospheric circulation. Taken together, these findings demonstrate that subannual tree-ring width measurements and subannual tree-ring isotope ratios each provide distinct climatic information and therefore may be used in conjunction to enhance the reconstruction of seasonal climate signals.

(3) Understanding the relationship between source water and tree-ring isotope proxy records. Mechanistic models have been developed and refined to attempt to quantify the source water-tree isotope relationship, but these models must be field tested in diverse

environments to determine their accuracy, utility, and potential use in source water reconstructions (Roden *et al.*, 2000; Anderson *et al.*, 2002). Most work in this vein has been situated outside of the PNW, and studies of separate earlywood and latewood stable isotope proxies in the PNW have been limited (Roden and Ehleringer, 2000; Roden *et al.*, 2005; Roden and Ehleringer, 2007). Through mechanistic modeling in Chapter 4, I found that source water modeled from thirteen years of subannual tree-ring cellulose measurements captures the isotope signal of current-growing-season and prior-winter precipitation to varying degrees across sites and is likely linked with synoptic-scale climate patterns. I also found evidence to support the hypothesis that conifers, and trees in arid environments more broadly, rely heavily on prior-winter precipitation, especially when forming latewood (Robertson *et al.*, 2008; Allen *et al.*, 2019; Berkelhammer *et al.*, 2020; Szymczak *et al.*, 2020; Huang *et al.*, 2022). These findings suggest that tree-ring cellulose at our sites could be used to reconstruct the isotopic composition of growing-season and winter source water (Anderson *et al.*, 2002) since at least 1895, from which time PRISM data can be used to estimate relative humidity, and possibly be used to infer low-frequency atmospheric patterns that are often removed by necessary detrending in tree-ring-width chronologies (Briffa *et al.*, 1996).

Taken together, my findings suggest three main considerations for future research:

1) The stable isotope ratios of precipitation samples in the U.S. PNW are influenced by a complex array of factors that may be particularly difficult to untangle in this region, highlighting the need for more event-scale sample collection and analysis to fine-tune our understanding of this relationship.
2) Subannual tree-ring width measurements provide a means of accessing seasonal precipitation and temperature signals in the PNW, especially at more arid sites, without

the need for additional equipment or considerable time or labor. The use of latewood widths and adjusted latewood widths in particular stands to help isolate late-summer climate signals.

3) Despite the considerable time, labor, and expense required to perform stable isotope analyses of tree-ring cellulose, these analyses may provide information on the isotope ratios of annual winter- and growing-season precipitation that is not accessible through other proxies.

While proxy data have been used to reconstruct past climate conditions for over a century (Douglass, 1919), in recent decades, increasingly precise instrumentation and analyses have become the new frontier for advances in our understanding of past climates, bringing climate proxy research to the molecular level. With these exciting advancements comes the responsibility to acknowledge the complexity of information captured by these proxies and how this complexity impacts our interpretations of past climate. This dissertation contributes to this endeavor by considering three of these proxies at targeted sites in close proximity to one another as an inherently interconnected network of seasonal climate information in the context of the U.S. Pacific Northwest. This comparison allows for a better understanding of climate-proxy relationships in the region and a detailed assessment of the considerations that must be made to understand and apply these relationships across time and space.

APPENDIX 1: SUPPLEMENTAL FIGURES

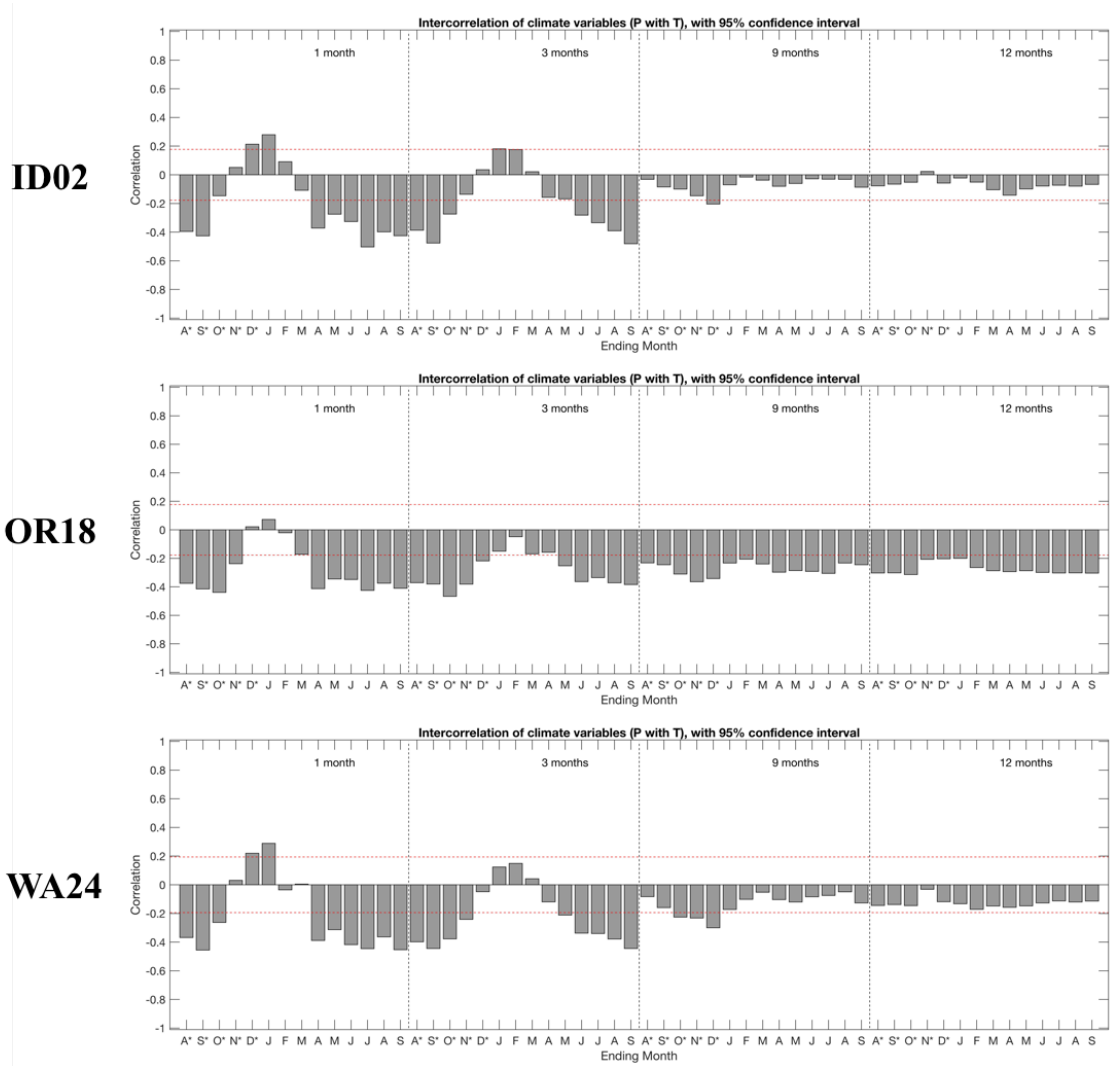

Figure A1. Intercorrelation of monthly temperature and precipitation data at our three study sites. Data retrieved from PRISM.

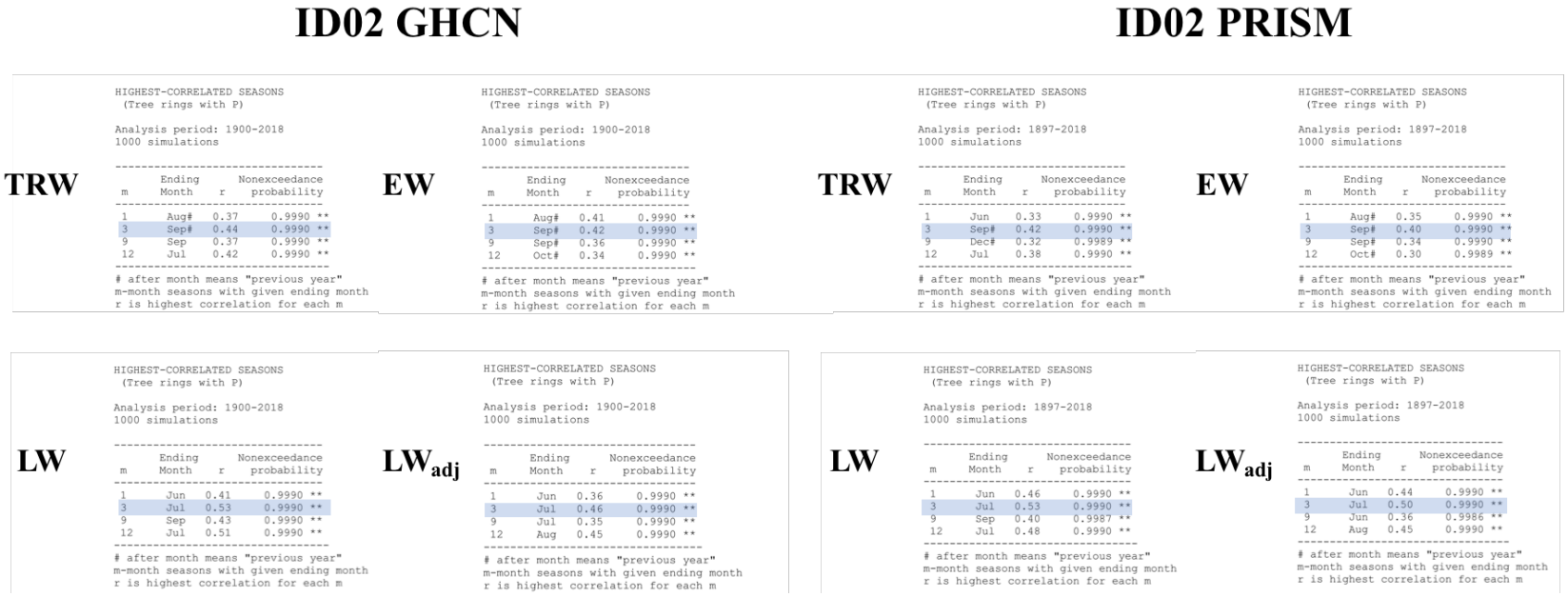

Figure A2. Highest one-, three-, nine-, and twelve-month seasonal correlations between precipitation and tree growth metrics at ID02. The highest overall correlation for each site/metric combination is highlighted in blue.

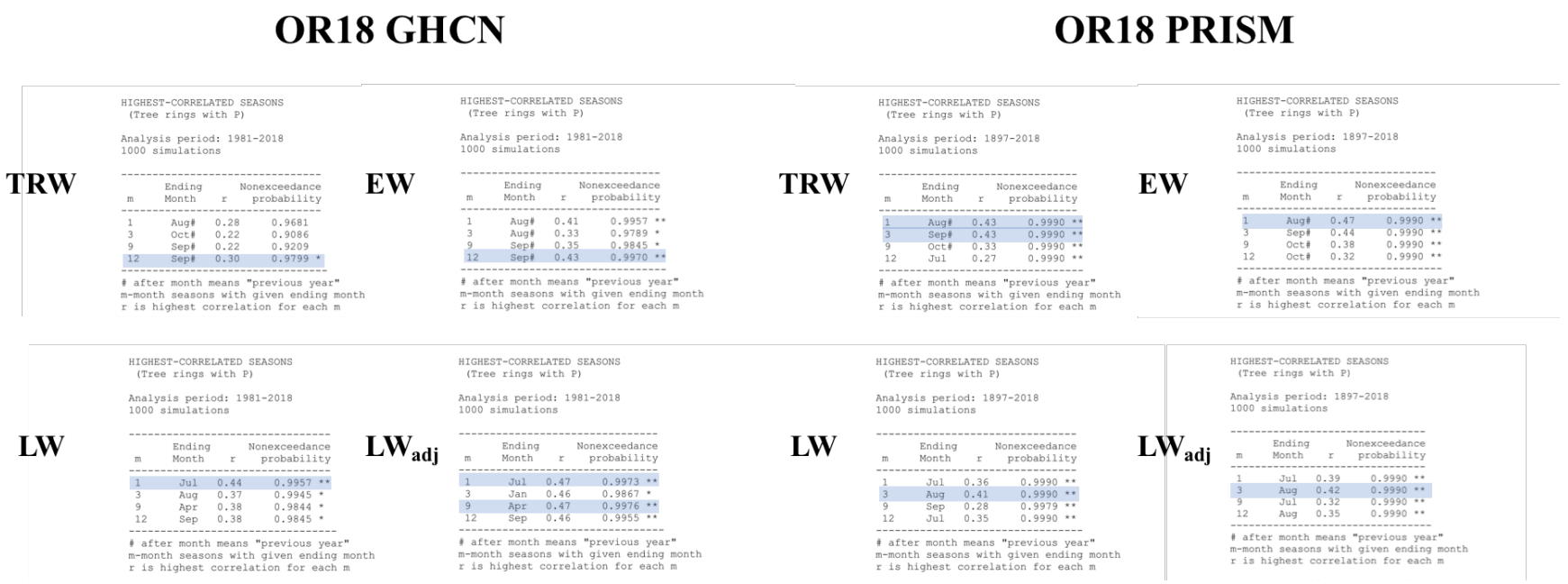

Figure A3. Highest one-, three-, nine-, and twelve-month seasonal correlations between precipitation and tree growth metrics at OR18. The highest overall correlation for each site/metric combination is highlighted in blue.

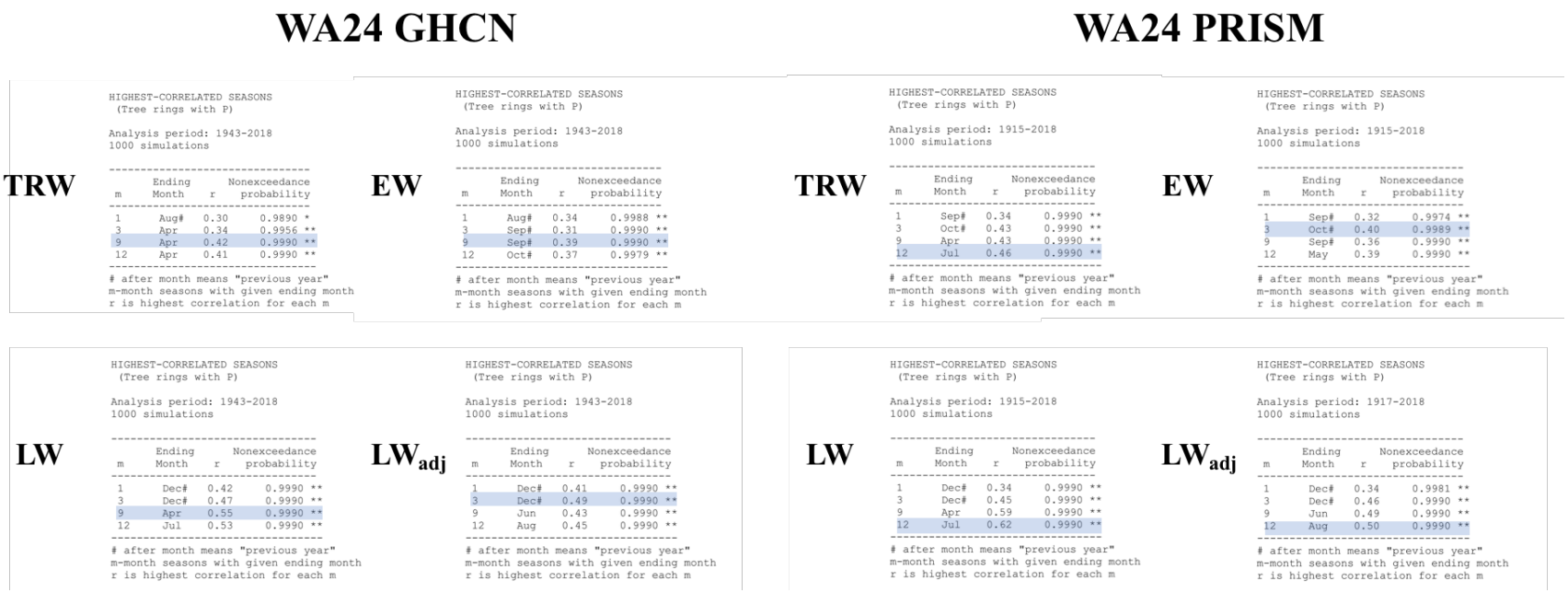

Figure A4. Highest one-, three-, nine-, and twelve-month seasonal correlations between precipitation and tree growth metrics at WA24. The highest overall correlation for each site/metric combination is highlighted in blue.

APPENDIX 2: SUPPLEMENTAL TABLES

Table A1. Summary of isotopically light (lowest 10% of $\delta^{18}O$ values) and isotopically heavy (highest 10% of $\delta^{18}O$ values) precipitation samples at ID02.

Isotopically Light				Isotopically Heavy			
Start Date	End Date	Precipitation (mm)	$\delta^{18}O$ (‰)	Start Date	End Date	Precipitation (mm)	$\delta^{18}O$ (‰)
11/22/10	11/30/10	38	-21.1	11/03/09	11/10/09	25	-9.8
11/24/09	11/30/09	10	-19.2	10/17/11	10/25/11	14	-8.7
11/06/12	11/13/12	14	-19.0	10/06/15	10/13/15	10	-8.1
11/20/07	11/27/07	11	-18.9	10/07/08	10/14/08	5	-7.8
11/12/13	11/19/13	48	-18.8	10/05/10	10/12/10	25	-7.0
11/17/09	11/24/09	21	-17.9	09/28/10	10/05/10	9	-6.6
12/28/10	01/04/11	10	-26.9	12/23/14	12/30/14	28	-12.8
12/08/09	12/15/09	24	-25.1	01/02/07	01/09/07	39	-12.7
01/28/14	02/04/14	18	-23.7	01/20/15	01/27/15	6	-12.4
12/30/14	01/06/15	38	-23.1	01/08/13	01/15/13	12	-12.3
01/26/10	02/02/10	8	-23.0	01/09/14	01/14/14	28	-11.0
12/30/08	01/06/09	43	-22.0	11/29/16	12/06/16	10	-10.9
02/27/07	03/06/07	10	-21.9	03/16/10	03/23/10	9	-11.9
02/03/09	02/10/09	8	-21.8	03/11/14	03/18/14	23	-11.7
02/02/10	02/09/10	6	-21.3	03/12/13	03/19/13	8	-11.4
02/10/09	02/17/09	5	-21.1	03/02/10	03/09/10	5	-11.3
03/25/08	04/01/08	22	-20.2	03/06/07	03/13/07	25	-10.4
02/13/07	02/20/07	26	-19.0	03/17/09	03/24/09	14	-9.5
02/17/09	02/24/09	20	-18.9	03/01/11	03/08/11	11	-8.9
03/31/15	04/07/15	19	-23.6	04/10/07	04/17/07	8	-9.1
05/24/11	05/31/11	42	-18.3	05/07/13	05/14/13	12	-8.2
04/21/09	04/28/09	18	-17.6	05/13/14	05/20/14	5	-7.5
04/26/11	05/03/11	14	-17.5	05/06/08	05/13/08	8	-6.6
05/10/11	05/17/11	27	-17.1	05/27/14	06/03/14	10	-6.2
03/31/09	04/07/09	11	-16.8	04/26/16	05/03/16	6	-3.5
06/17/14	06/24/14	12	-20.1	08/05/08	08/12/08	7	-6.5
09/25/07	10/02/07	29	-17.8	06/16/09	06/23/09	7	-6.5
06/10/08	06/17/08	14	-17.8	09/27/11	10/04/11	13	-5.5
06/26/12	07/03/12	12	-17.6	07/07/15	07/14/15	8	-5.0
06/01/10	06/08/10	38	-16.7	09/15/09	09/22/09	7	-4.7
06/18/13	06/25/13	78	-16.5	06/30/09	07/07/09	6	-4.6

Table A2. Summary of isotopically light (lowest 10% of $\delta^{18}O$ values) and isotopically heavy (highest 10% of $\delta^{18}O$ values) precipitation samples at OR18.

Isotopically Light				Isotopically Heavy			
Start Date	End Date	Precipitation (mm)	$\delta^{18}O$ (‰)	Start Date	End Date	Precipitation (mm)	$\delta^{18}O$ (‰)
11/23/10	11/30/10	41	-22.6	10/18/16	10/25/16	18	-8.4
11/12/14	11/18/14	18	-19.4	10/04/16	10/11/16	10	-8.4
11/16/10	11/23/10	30	-19.3	10/29/13	11/05/13	25	-8.3
11/10/09	11/17/09	20	-19.1	09/28/10	10/05/10	18	-8.1
11/27/07	12/04/07	36	-18.6	11/25/08	12/02/08	20	-7.9
11/02/10	11/09/10	20	-18.3	11/12/08	11/18/08	10	-6.1
12/28/10	01/04/11	18	-30.2	12/17/13	12/24/13	38	-13.1
12/18/12	12/26/12	43	-25.8	12/31/13	01/07/14	8	-12.9
12/08/09	12/15/09	38	-25.5	12/30/08	01/06/09	86	-12.8
12/14/10	12/21/10	23	-24.4	01/03/12	01/10/12	5	-12.0
01/02/08	01/08/08	36	-23.7	01/13/15	01/20/15	30	-11.6
01/19/10	01/26/10	30	-22.8	01/28/14	02/04/14	58	-10.0
02/10/09	02/17/09	5	-21.6	03/26/13	04/02/13	10	-10.1
03/15/11	03/22/11	36	-20.9	02/21/12	02/28/12	15	-9.7
03/22/11	03/29/11	41	-20.8	03/04/08	03/11/08	5	-9.3
01/29/08	02/05/08	36	-20.7	03/18/08	03/25/08	18	-9.2
02/03/09	02/10/09	18	-19.3	02/01/11	02/08/11	13	-8.9
02/28/12	03/06/12	20	-19.0	02/12/08	02/19/08	8	-7.9
02/20/07	02/27/07	23	-18.8	03/22/16	03/29/16	23	-4.7
04/17/07	04/24/07	18	-18.9	05/15/12	05/22/12	25	-9.2
03/30/10	04/06/10	36	-18.5	05/10/16	05/17/16	18	-8.6
04/12/11	04/19/11	43	-18.1	05/05/09	05/12/09	20	-7.9
05/10/11	05/17/11	69	-17.8	05/26/09	06/02/09	8	-7.4
05/19/15	05/26/15	20	-17.4	05/27/14	06/03/14	5	-6.5
05/04/10	05/11/10	38	-17.3	05/08/07	05/15/07	5	-5.5
04/03/12	04/10/12	13	-16.9	05/07/13	05/14/13	5	-3.9
09/25/07	10/02/07	15	-18.4	07/10/12	07/17/12	15	-7.7
08/11/09	08/18/09	8	-17.6	07/07/15	07/14/15	43	-7.6
06/01/10	06/08/10	64	-16.5	09/13/16	09/20/16	15	-6.8
07/12/11	07/19/11	15	-16.1	09/16/08	09/23/08	18	-6.8
09/18/12	09/25/12	5	-15.4	08/05/08	08/12/08	8	-4.5

Table A3. Summary of isotopically light (lowest 10% of $\delta^{18}O$ values) and isotopically heavy (highest 10% of $\delta^{18}O$ values) precipitation samples at WA24.

Isotopically Light				Isotopically Heavy			
Start Date	End Date	Precipitation (mm)	$\delta^{18}O$ (‰)	Start Date	End Date	Precipitation (mm)	$\delta^{18}O$ (‰)
11/17/09	11/24/09	20	-17.6	11/25/08	12/02/08	20	-8.3
10/30/12	11/06/12	7	-17.1	10/27/09	11/03/09	6	-7.9
10/16/12	10/23/12	7	-17.1	10/21/14	10/28/14	14	-7.8
11/02/10	11/09/10	10	-17.1	11/17/15	11/24/15	6	-7.5
10/04/11	10/11/11	22	-16.9	10/05/10	10/12/10	11	-7.2
11/24/09	12/01/09	7	-16.3	09/28/10	10/05/10	9	-7.1
12/08/09	12/15/09	11	-22.8	12/06/16	12/13/16	13	-9.2
01/26/10	02/02/10	11	-21.8	01/26/16	02/02/16	12	-8.7
12/16/08	12/23/08	23	-21.8	12/17/13	12/24/13	19	-8.5
12/04/07	12/11/07	6	-20.6	12/20/16	12/28/16	13	-8.4
01/11/11	01/18/11	32	-20.3	01/12/16	01/19/16	28	-7.6
01/04/11	01/11/11	5	-19.8	11/29/16	12/06/16	10	-6.8
03/01/16	03/08/16	15	-20.2	01/29/13	02/05/13	7	-9.4
03/27/12	04/03/12	29	-19.9	03/04/08	03/11/08	6	-9.3
01/30/07	02/06/07	5	-19.0	02/26/13	03/05/13	11	-9.3
03/20/12	03/27/12	57	-18.4	03/19/13	03/26/13	7	-8.9
03/24/15	03/31/15	16	-18.3	03/23/10	03/30/10	15	-8.3
02/23/10	03/02/10	10	-17.4	03/05/13	03/12/13	7	-6.4
04/07/15	04/14/15	8	-19.9	04/10/12	04/17/12	11	-9.3
04/21/09	04/28/09	7	-19.5	04/20/10	04/27/10	6	-9.2
05/15/07	05/22/07	20	-19.2	05/05/09	05/12/09	18	-9.0
05/06/14	05/13/14	9	-18.6	05/24/11	05/31/11	19	-5.8
04/26/16	05/03/16	17	-16.8	04/12/11	04/18/11	15	-4.6
05/04/10	05/11/10	9	-16.3	05/08/07	05/15/07	7	-4.5
06/01/10	06/08/10	30	-18.6	09/16/08	09/23/08	8	-7.5
06/10/08	06/17/08	16	-16.5	07/07/09	07/14/09	12	-7.4
09/24/13	10/01/13	33	-15.9	06/16/09	06/23/09	8	-7.0
09/23/14	09/30/14	8	-15.2	07/22/08	07/29/08	5	-6.7
08/14/07	08/21/07	7	-14.9	07/05/16	07/12/16	17	-4.7

Table A4. Summary of isotopically light (lowest 10% of $\delta^{18}O$ values) and isotopically heavy (highest 10% of $\delta^{18}O$ values) precipitation samples at WA98.

Isotopically Light				Isotopically Heavy			
Start Date	End Date	Precipitation (mm)	$\delta^{18}O$ (‰)	Start Date	End Date	Precipitation (mm)	$\delta^{18}O$ (‰)
11/12/14	11/19/14	5	-17.9	10/27/09	11/03/09	7	-5.4
11/01/16	11/08/16	40	-15.0	09/30/08	10/07/08	81	-5.2
10/28/08	11/04/08	55	-14.3	10/25/11	11/01/11	38	-5.1
11/22/11	11/29/11	60	-14.1	10/14/08	10/21/08	13	-5.1
11/22/16	11/29/16	138	-13.8	10/23/07	10/30/07	20	-4.8
11/17/09	11/24/09	94	-13.0	11/25/08	12/02/08	61	-4.7
11/27/12	12/03/12	60	-13.0	10/18/11	10/25/11	13	-4.0
12/28/10	01/04/11	5	-16.7	01/02/13	01/08/13	64	-7.3
01/26/10	02/02/10	27	-16.0	01/16/07	01/23/07	14	-6.7
01/17/12	01/25/12	236	-15.6	01/27/09	02/03/09	27	-6.6
01/19/10	01/26/10	45	-15.3	12/18/13	12/26/13	96	-6.4
12/18/12	12/25/12	123	-14.3	11/29/11	12/06/11	10	-6.3
01/22/08	01/29/08	52	-13.6	01/25/11	02/01/11	17	-5.5
03/05/13	03/12/13	35	-16.2	02/19/13	03/05/13	143	-5.8
03/20/12	03/27/12	44	-15.7	01/30/07	02/06/07	6	-5.8
03/07/12	03/13/12	62	-14.9	02/01/11	02/08/11	41	-5.6
01/29/08	02/05/08	129	-14.8	03/16/10	03/23/10	19	-5.6
02/27/07	03/06/07	76	-13.9	02/12/08	02/19/08	11	-5.1
02/06/07	02/13/07	27	-13.5	01/29/13	02/05/13	71	-4.8
05/01/12	05/09/12	53	-14.4	03/31/09	04/07/09	60	-5.6
04/13/10	04/20/10	14	-13.8	04/23/13	04/30/13	17	-5.6
05/21/13	05/28/13	172	-13.1	05/15/12	05/22/12	25	-5.2
04/28/09	05/05/09	80	-12.6	05/08/07	05/15/07	8	-4.9
05/20/08	05/27/08	46	-12.5	05/20/14	05/27/14	5	-4.9
04/12/16	04/19/16	44	-12.0	05/06/08	05/13/08	8	-4.7
04/26/11	05/03/11	33	-11.3	05/06/13	05/15/13	12	-2.1
06/19/12	06/26/12	47	-15.4	07/10/12	07/17/12	6	-4.2
09/25/07	10/02/07	77	-13.2	09/20/11	09/27/11	39	-3.9
06/01/10	06/08/10	87	-12.6	09/15/09	09/22/09	9	-3.7
09/03/13	09/10/13	43	-11.1	09/16/08	09/23/08	10	-3.7
08/14/07	08/21/07	28	-10.9	09/21/10	09/28/10	26	-3.4
07/12/11	07/19/11	39	-10.6	09/13/11	09/20/11	20	-3.3
05/29/12	06/05/12	52	-10.5	08/12/08	08/19/08	9	-3.1
06/22/16	06/28/16	41	-10.1	08/12/14	08/19/14	13	-2.7

Table A5. Summary of isotopically light (lowest 10% of $\delta^{18}O$ values) and isotopically heavy (highest 10% of $\delta^{18}O$ values) precipitation samples at WA99.

Isotopically Light				Isotopically Heavy			
Start Date	End Date	Precipitation (mm)	$\delta^{18}O$ (‰)	Start Date	End Date	Precipitation (mm)	$\delta^{18}O$ (‰)
11/15/11	11/22/11	117	-14.6	10/14/08	10/21/08	29	-5.9
11/01/16	11/08/16	6	-14.6	10/25/11	11/01/11	30	-5.8
11/27/07	12/04/07	176	-14.3	09/29/09	10/06/09	24	-5.7
11/16/10	11/23/10	74	-14.2	09/30/08	10/07/08	22	-5.7
11/24/09	12/01/09	33	-14.1	10/18/11	10/25/11	57	-5.4
11/22/16	11/29/16	45	-13.6	10/27/09	11/03/09	76	-4.7
11/01/11	11/08/11	14	-13.4	11/25/08	12/02/08	29	-4.6
01/17/12	01/19/12	48	-20.1	12/02/08	12/09/08	40	-8.4
12/28/10	01/04/11	18	-18.4	12/23/13	12/31/13	12	-8.3
12/08/09	12/15/09	27	-18.4	11/29/11	12/06/11	6	-7.5
12/18/12	12/26/12	63	-17.7	12/02/14	12/09/14	11	-7.4
01/22/08	01/29/08	38	-17.6	01/20/15	01/27/15	15	-7.3
12/09/08	12/16/08	52	-16.3	01/24/11	02/01/11	22	-7.1
03/27/12	04/03/12	15	-24.8	03/12/13	03/19/13	49	-7.3
03/22/11	03/29/11	29	-16.4	03/23/16	03/29/16	72	-7.2
03/10/15	03/17/15	26	-16.2	02/12/13	02/19/13	17	-6.9
02/27/07	03/06/07	60	-15.7	02/01/11	02/08/11	89	-6.2
03/06/12	03/13/12	23	-14.9	03/04/08	03/11/08	12	-6.1
03/24/09	03/31/09	82	-14.6	03/27/07	04/04/07	23	-5.9
02/28/12	03/06/12	57	-14.6	03/16/10	03/23/10	5	-5.6
02/20/07	02/27/07	32	-14.2	02/05/13	02/12/13	20	-5.5
05/10/11	05/17/11	47	-18.8	05/10/16	05/17/16	23	-6.0
05/27/08	06/03/08	16	-14.5	04/22/08	04/29/08	19	-5.9
05/25/10	06/01/10	78	-14.3	05/26/15	06/02/15	14	-5.7
05/15/07	05/22/07	35	-13.9	05/08/07	05/15/07	7	-5.4
05/21/13	05/28/13	66	-13.7	04/23/13	04/30/13	40	-5.2
05/01/12	05/08/12	48	-13.6	05/06/08	05/13/08	17	-5.1
04/19/11	04/26/11	32	-12.9	05/07/13	05/14/13	13	-4.3
06/19/12	06/26/12	39	-15.6	09/13/11	09/21/11	39	-5.1
09/03/13	09/10/13	58	-14.8	08/05/08	08/12/08	25	-5.0
08/14/07	08/21/07	20	-13.4	09/16/08	09/23/08	31	-4.9
06/01/10	06/09/10	72	-13.2	08/04/09	08/11/09	7	-4.6
07/05/16	07/12/16	28	-12.7	09/10/13	09/17/13	8	-4.4
09/25/07	10/02/07	64	-11.7	09/21/10	09/29/10	15	-4.3
06/10/14	06/17/14	46	-11.3	09/21/11	09/27/11	30	-4.2

Table A6. Site and seasonal summary statistics for weekly stable isotope ratios at ID02. All isotopic values are in ‰.

	Site		ON		DJ		FM		AM		JJAS	
	$\delta^{18}O$	$\delta^{2}H$	$\delta^{18}O$	$\delta^{2}H$	$\delta^{18}O$	$\delta^{2}H$	$\delta^{18}O$	$\delta^{2}H$	$\delta^{18}O$	$\delta^{2}H$	$\delta^{18}O$	$\delta^{2}H$
Mean	-13.8	-105.4	-13.8	-100.7	-18.1	-135.3	-15.3	-117.3	-12.5	-98.3	-10.5	-83.3
Std. Dev.	4.1	30.1	3.1	23.6	3.4	26.6	2.7	20.4	3.2	25.4	3.4	26.1
Range	23.3	192.0	14.5	104.3	15.9	129.8	13.1	93.3	20.1	170.2	15.5	123.1
Minimum	-26.9	-202.2	-21.1	-151.7	-26.9	-202.2	-21.9	-166.2	-23.6	-180.4	-20.1	-158.7
Maximum	-3.5	-10.2	-6.6	-47.4	-10.9	-72.4	-8.9	-72.9	-3.5	-10.2	-4.6	-35.6
n	340	340	65	65	58	58	70	70	66	66	81	81

Table A7. Site and seasonal summary statistics for weekly stable isotope ratios at OR18. All isotopic values are in ‰.

	Site		ON		DJ		FM		AM		JJAS	
	$\delta^{18}O$	$\delta^{2}H$	$\delta^{18}O$	$\delta^{2}H$	$\delta^{18}O$	$\delta^{2}H$	$\delta^{18}O$	$\delta^{2}H$	$\delta^{18}O$	$\delta^{2}H$	$\delta^{18}O$	$\delta^{2}H$
Mean	-13.5	-102.6	-13.3	-98.3	-17.2	-130.0	-14.2	-108.0	-12.3	-95.1	-11.2	-87.1
Std. Dev.	3.9	30.0	3.4	26.5	4.1	32.4	3.3	24.8	3.1	23.5	3.5	26.6
Range	26.6	200.0	16.5	124.4	20.2	165.1	16.9	137.2	15.0	120.5	14.8	107.4
Minimum	-30.2	-229.9	-22.6	-167.3	-30.2	-229.9	-21.6	-167.1	-18.9	-156.4	-18.4	-143.7
Maximum	-3.6	-29.9	-6.1	-42.9	-10.0	-64.8	-4.7	-29.9	-3.9	-36.0	-3.6	-36.3
n	333	333	68	68	55	55	70	70	73	73	69	69

Table A8. Site and seasonal summary statistics for weekly stable isotope ratios at WA24. All isotopic values are in ‰.

	Site		ON		DJ		FM		AM		JJAS	
	$\delta^{18}O$	$\delta^{2}H$	$\delta^{18}O$	$\delta^{2}H$	$\delta^{18}O$	$\delta^{2}H$	$\delta^{18}O$	$\delta^{2}H$	$\delta^{18}O$	$\delta^{2}H$	$\delta^{18}O$	$\delta^{2}H$
Mean	-12.6	-96.0	-12.1	-89.6	-14.1	-105.7	-13.5	-103.9	-12.5	-96.0	-11.0	-84.4
Std. Dev.	3.4	26.2	2.9	23.7	4.0	30.5	3.0	23.6	3.3	24.0	2.9	22.7
Range	19.2	140.3	11.1	89.6	16.0	125.6	13.9	109.7	15.4	113.5	14.0	117.3
Minimum	-22.8	-170.2	-18.2	-139.7	-22.8	-170.2	-20.2	-153.3	-19.9	-150.9	-18.6	-147.2
Maximum	-3.7	-29.9	-7.1	-50.1	-6.8	-44.6	-6.3	-43.6	-4.5	-37.4	-4.7	-29.9
n	330	323	61	61	65	64	72	71	63	63	62	62

Table A9. Site and seasonal summary statistics for weekly stable isotope ratios at WA98. All isotopic values are in ‰.

	Site		ON		DJ		FM		AM		JJAS	
	$\delta^{18}O$	$\delta^{2}H$	$\delta^{18}O$	$\delta^{2}H$	$\delta^{18}O$	$\delta^{2}H$	$\delta^{18}O$	$\delta^{2}H$	$\delta^{18}O$	$\delta^{2}H$	$\delta^{18}O$	$\delta^{2}H$
Mean	-8.9	-61.6	-9.2	-61.5	-10.4	-72.1	-9.5	-67.5	-8.5	-59.8	-7.2	-50.0
Std. Dev.	2.9	22.9	3.0	23.6	2.8	23.8	2.8	22.1	2.2	18.3	2.4	20.0
Range	17.4	134.0	13.9	109.7	14.1	113.3	11.4	102.6	12.3	98.8	12.7	100.8
Minimum	-19.6	-144.9	-17.9	-132.6	-19.6	-144.9	-16.2	-127.3	-14.4	-109.6	-15.4	-113.2
Maximum	-2.1	-10.8	-4.0	-22.9	-5.5	-31.6	-4.8	-24.7	-2.1	-10.8	-2.7	-12.4
n	348	348	68	68	58	58	62	62	72	72	82	82

Table A10. Site and seasonal summary statistics for weekly stable isotope ratios at WA99. All isotopic values are in ‰.

	Site		ON		DJ		FM		AM		JJAS	
	$\delta^{18}O$	$\delta^{2}H$	$\delta^{18}O$	$\delta^{2}H$	$\delta^{18}O$	$\delta^{2}H$	$\delta^{18}O$	$\delta^{2}H$	$\delta^{18}O$	$\delta^{2}H$	$\delta^{18}O$	$\delta^{2}H$
Mean	-9.9	-72.3	-9.6	-67.5	-11.9	-86.0	-10.8	-79.8	-9.2	-67.9	-8.2	-60.5
Std. Dev.	3.0	23.8	2.7	21.5	2.9	23.6	3.1	24.1	2.6	21.4	2.4	19.9
Range	21.3	167.8	10.0	80.8	13.1	104.0	19.3	152.5	14.5	110.0	12.1	101.3
Minimum	-24.8	-187.9	-14.6	-110.9	-20.1	-149.3	-24.8	-187.9	-18.8	-141.3	-15.6	-121.4
Maximum	-3.5	-20.1	-4.6	-30.1	-7.0	-45.3	-5.5	-35.4	-4.3	-31.3	-3.5	-20.1
n	381	381	74	74	64	64	79	79	75	75	81	81

Table A11. 30-year normals of monthly and annual total precipitation, minimum temperature, mean temperature, maximum temperature, mean dew point, minimum vapor-pressure deficit, and maximum vapor-pressure deficit at our tree collection sites. Climate data retrieved from PRISM.

ID02

Date	P (mm)	Tmin (°C)	Tmean (°C)	Tmax (°C)	Tdmean (°C)	VPDmin (hPa)	VPDmax (hPa)
January	124	-6.4	-3.2	0.1	-5.5	0.27	1.83
February	84	-5.9	-1.4	3.1	-4.4	0.21	3.12
March	96	-3.5	2.0	7.4	-2.7	0.31	5.31
April	72	-0.6	5.6	11.8	-0.9	0.64	8.87
May	77	2.9	9.9	16.9	2.8	0.74	13.25
June	76	6.4	13.5	20.6	6.5	0.93	16.05
July	35	8.3	16.9	25.6	8.0	1.86	23.99
August	30	8.5	17.1	25.7	6.9	2.28	25.06
September	41	4.6	12.4	20.2	4.3	1.33	16.94
October	71	0.2	5.9	11.6	1.1	0.49	7.34
November	136	-3.2	0.1	3.4	-1.8	0.20	2.27
December	130	-7.2	-4.1	-0.9	-5.4	0.17	1.36
Annual	971	0.3	6.2	12.1	0.7	0.79	10.45

OR18

Date	P (mm)	Tmin (°C)	Tmean (°C)	Tmax (°C)	Tdmean (°C)	VPDmin (hPa)	VPDmax (hPa)
January	88	-6.5	-2.8	0.9	-6.4	0.58	2.97
February	68	-6.1	-1.5	3.1	-6.4	0.67	4.20
March	76	-4.2	1.0	6.1	-4.7	0.69	5.80
April	69	-1.9	3.9	9.6	-2.6	0.88	7.94
May	73	1.4	7.7	13.9	0.4	1.32	11.07
June	55	4.7	11.5	18.4	2.9	2.01	15.07
July	20	8.8	16.6	24.5	4.1	4.36	25.29
August	25	9.1	16.9	24.7	3.0	4.62	26.46
September	28	5.8	13.0	20.2	0.6	3.57	20.04
October	46	1.0	6.8	12.6	-1.6	1.80	10.59
November	92	-3.5	0.3	4.1	-4.1	0.91	4.41
December	92	-6.8	-3.2	0.3	-6.5	0.59	2.74
Annual	732	0.2	5.9	11.5	-1.8	1.83	11.38

WA24

Date	P (mm)	Tmin (°C)	Tmean (°C)	Tmax (°C)	Tdmean (°C)	VPDmin (hPa)	VPDmax (hPa)
January	62	-2.9	0.4	3.7	-3.3	0.58	3.12
February	49	-2.3	1.9	6.1	-2.9	0.69	4.46
March	49	0.0	4.9	9.9	-1.2	0.93	6.58
April	62	2.5	8.1	13.8	0.9	1.21	9.47
May	57	6.0	12.1	18.2	3.8	1.97	13.59
June	40	9.2	15.7	22.2	6.3	2.64	18.13
July	25	11.7	19.9	28.1	6.6	4.90	29.55
August	19	11.8	20.1	28.3	5.5	5.68	30.99
September	25	7.6	15.3	23.0	3.5	3.77	21.90
October	52	3.6	9.4	15.1	1.6	1.78	10.70
November	79	-0.2	3.5	7.2	-0.9	0.76	4.51
December	52	-3.8	-0.6	2.6	-3.7	0.52	2.79
Annual	572	3.6	9.2	14.8	1.3	2.12	12.98

Table A12. Expressed population signal (EPS) and number of retained cores for 25-year periods as determined by ARSTAN. TRW statistics refer to the total ring width chronology, and EW and LW statistics refer to the earlywood width and latewood width chronologies, respectively. All EPS values during the period of overlap with climate data are > 0.85 with the exception of WA24, where values are > 0.85 beginning in 1915.

ID02

	TRW		EW		LW	
Start Year	EPS	Cores	EPS	Cores	EPS	Cores
1775	0.804	5.42	0.785	6.02	0.750	5.42
1800	0.823	6.76	0.764	7.76	0.817	6.76
1825	0.861	8.84	0.822	9.84	0.904	8.84
1850	0.871	11.28	0.837	12.28	0.898	11.28
1875	0.876	13.2	0.866	14.2	0.878	13.2
1900	0.902	14.14	0.903	15.14	0.888	14.14
1925	0.909	14.64	0.906	15.64	0.899	14.64
1950	0.876	15	0.874	16	0.860	15
1975	0.881	15	0.878	16	0.858	15

OR18

	TRW		EW		LW	
Start Year	EPS	Cores	EPS	Cores	EPS	Cores
1750	0.798	5.34	0.820	5.34	0.663	5.34
1775	0.890	7.04	0.887	7.04	0.878	7.04
1800	0.855	7.76	0.851	7.76	0.854	7.76
1825	0.900	9.74	0.899	9.74	0.888	9.74
1850	0.912	13.5	0.915	13.3	0.890	13.3
1875	0.929	17.72	0.916	17.1	0.915	17.1
1900	0.955	20.92	0.947	20	0.937	20
1925	0.958	22.62	0.947	21.62	0.945	21.62
1950	0.954	23	0.943	22	0.954	22
1975	0.926	23	0.911	22	0.927	22

WA24

	TRW		EW		LW	
Start Year	EPS	Cores	EPS	Cores	EPS	Cores
1790	0.531	2	0.387	2	-0.230	2
1815	0.723	2.08	0.151	2.08	-0.209	2.08
1840	0.801	3.84	-0.109	3.84	-1.420	3.84
1865	0.863	7.98	0.697	7.98	0.659	7.98
1890	0.878	12.12	0.833	12.12	0.771	12.12
1915	0.931	15.68	0.922	15.68	0.893	15.68
1940	0.933	19.68	0.933	19.68	0.898	19.68
1965	0.933	23.9	0.929	23.9	0.929	23.9
1990	0.946	26	0.933	26	0.948	26

Table A13. Summary of all Seascorr correlation outputs for ID02 TRW. Significant relationships with precipitation and temperature at $\alpha = 0.05$ ($\alpha = 0.01$) are highlighted in light (dark) blue for precipitation and orange for temperature; the strongest significant correlation for each season/variable combination is outlined in a thick black box.

PRISM								GHCN							
Precipitation				Temperature				Precipitation				Temperature			
End Month	*r*	NP	*p*	End Month	*r*	NP	*p*	End Month	*r*	NP	*p*	End Month	*r*	NP	*p*
1 month								1 month							
Aug_prev	0.33	0.9990	**	Aug_prev	-0.06	0.2403		Aug_prev	0.37	0.9990	**	Aug_prev	0.00	0.5376	
Sep_prev	0.32	0.9986	**	Sep_prev	-0.03	0.3719		Sep_prev	0.30	0.9990	**	Sep_prev	-0.07	0.2228	
Oct_prev	0.15	0.9447		Oct_prev	0.04	0.6647		Oct_prev	0.12	0.8953		Oct_prev	0.05	0.6813	
Nov_prev	0.08	0.8138		Nov_prev	0.13	0.9062		Nov_prev	0.14	0.9422		Nov_prev	0.12	0.9015	
Dec_prev	0.03	0.6321		Dec_prev	0.23	0.9889	*	Dec_prev	-0.02	0.4301		Dec_prev	0.22	0.9876	*
Jan	-0.02	0.4145		Jan	0.13	0.9321		Jan	0.01	0.5428		Jan	0.13	0.9030	
Feb	0.02	0.5759		Feb	0.13	0.9387		Feb	0.00	0.4819		Feb	0.10	0.8707	
Mar	0.07	0.7810		Mar	0.06	0.7507		Mar	0.06	0.7504		Mar	0.04	0.6693	
Apr	0.09	0.8176		Apr	0.05	0.7207		Apr	0.17	0.9623		Apr	0.04	0.6814	
May	0.21	0.9774	*	May	0.02	0.5659		May	0.25	0.9956	**	May	-0.04	0.3260	
Jun	0.33	0.9990	**	Jun	-0.04	0.3220		Jun	0.32	0.9975	**	Jun	-0.09	0.1484	
Jul	0.18	0.9604		Jul	-0.10	0.1842		Jul	0.23	0.9895	*	Jul	-0.10	0.1362	
Aug	0.04	0.6510		Aug	-0.09	0.1574		Aug	0.05	0.6896		Aug	-0.11	0.0988	
Sep	0.13	0.9091		Sep	-0.04	0.3332		Sep	0.14	0.9305		Sep	0.00	0.4939	
3 month								3 month							
Aug_prev	0.26	0.9975	**	Aug_prev	0.02	0.6178		Aug_prev	0.32	0.9990	**	Aug_prev	0.09	0.8377	
Sep_prev	0.42	0.9990	**	Sep_prev	0.07	0.7864		Sep_prev	0.44	0.9990	**	Sep_prev	0.10	0.8754	
Oct_prev	0.40	0.9990	**	Oct_prev	-0.10	0.1198		Oct_prev	0.40	0.9990	**	Oct_prev	-0.07	0.2007	
Nov_prev	0.25	0.9971	**	Nov_prev	0.03	0.6275		Nov_prev	0.27	0.9976	**	Nov_prev	0.02	0.5690	
Dec_prev	0.14	0.9510		Dec_prev	0.21	0.9848	*	Dec_prev	0.14	0.9370		Dec_prev	0.21	0.9839	*
Jan	0.05	0.7227		Jan	0.24	0.9923	*	Jan	0.07	0.7971		Jan	0.22	0.9875	*
Feb	0.02	0.5846		Feb	0.24	0.9950	*	Feb	-0.01	0.4613		Feb	0.22	0.9912	*
Mar	0.03	0.6550		Mar	0.15	0.9498		Mar	0.04	0.6429		Mar	0.13	0.9033	
Apr	0.10	0.8083		Apr	0.12	0.9220		Apr	0.10	0.8400		Apr	0.08	0.8143	
May	0.21	0.9852	*	May	0.05	0.7108		May	0.26	0.9955	**	May	0.00	0.4931	
Jun	0.34	0.9990	**	Jun	0.02	0.6017		Jun	0.39	0.9990	**	Jun	-0.05	0.2982	
Jul	0.39	0.9990	**	Jul	-0.06	0.2857		Jul	0.42	0.9990	**	Jul	-0.12	0.0913	
Aug	0.33	0.9990	**	Aug	-0.09	0.1537		Aug	0.36	0.9990	**	Aug	-0.13	0.0718	
Sep	0.20	0.9614		Sep	-0.09	0.1459		Sep	0.24	0.9867	*	Sep	-0.08	0.1938	
9 month								9 month							
Aug_prev	0.16	0.9664		Aug_prev	0.03	0.6111		Aug_prev	0.20	0.9797	*	Aug_prev	0.03	0.6029	
Sep_prev	0.27	0.9986	**	Sep_prev	-0.05	0.2917		Sep_prev	0.30	0.9981	**	Sep_prev	-0.04	0.3362	
Oct_prev	0.27	0.9954	**	Oct_prev	-0.10	0.1136		Oct_prev	0.29	0.9964	**	Oct_prev	-0.08	0.1844	
Nov_prev	0.28	0.9949	*	Nov_prev	-0.05	0.2387		Nov_prev	0.31	0.9985	**	Nov_prev	-0.02	0.4069	
Dec_prev	0.32	0.9989	**	Dec_prev	0.06	0.7412		Dec_prev	0.33	0.9990	**	Dec_prev	0.09	0.8187	
Jan	0.29	0.9990	**	Jan	0.08	0.8061		Jan	0.33	0.9990	**	Jan	0.11	0.8746	
Feb	0.27	0.9983	**	Feb	0.14	0.9208		Feb	0.30	0.9990	**	Feb	0.14	0.9254	
Mar	0.26	0.9978	**	Mar	0.15	0.9405		Mar	0.27	0.9990	**	Mar	0.14	0.9266	
Apr	0.26	0.9972	**	Apr	0.15	0.9471		Apr	0.29	0.9988	**	Apr	0.13	0.9131	
May	0.24	0.9975	**	May	0.16	0.9549		May	0.27	0.9973	**	May	0.12	0.8987	
Jun	0.25	0.9940	*	Jun	0.17	0.9656		Jun	0.28	0.9977	**	Jun	0.12	0.9038	
Jul	0.24	0.9952	**	Jul	0.14	0.9359		Jul	0.30	0.9986	**	Jul	0.08	0.8131	
Aug	0.25	0.9949	*	Aug	0.09	0.8542		Aug	0.29	0.9990	**	Aug	0.03	0.6304	
Sep	0.31	0.9986	**	Sep	0.03	0.6436		Sep	0.37	0.9990	**	Sep	-0.02	0.4167	
12 month								12 month							
Aug_prev	0.04	0.6966		Aug_prev	0.03	0.6266		Aug_prev	0.11	0.8755		Aug_prev	0.04	0.6632	
Sep_prev	0.14	0.9410		Sep_prev	-0.03	0.3657		Sep_prev	0.21	0.9785	*	Sep_prev	-0.03	0.3709	
Oct_prev	0.24	0.9943	*	Oct_prev	-0.01	0.4346		Oct_prev	0.29	0.9982	**	Oct_prev	-0.01	0.4166	
Nov_prev	0.27	0.9954	**	Nov_prev	0.01	0.5389		Nov_prev	0.30	0.9983	**	Nov_prev	0.02	0.5642	
Dec_prev	0.28	0.9982	**	Dec_prev	0.04	0.6649		Dec_prev	0.29	0.9984	**	Dec_prev	0.05	0.6970	
Jan	0.23	0.9915	*	Jan	0.04	0.6533		Jan	0.26	0.9960	**	Jan	0.05	0.6986	
Feb	0.24	0.9920	*	Feb	0.08	0.8075		Feb	0.26	0.9959	**	Feb	0.09	0.8135	
Mar	0.28	0.9967	**	Mar	0.11	0.8716		Mar	0.29	0.9989	**	Mar	0.12	0.8749	
Apr	0.29	0.9976	**	Apr	0.14	0.9255		Apr	0.32	0.9990	**	Apr	0.14	0.9273	
May	0.32	0.9990	**	May	0.15	0.9430		May	0.36	0.9990	**	May	0.13	0.9062	
Jun	0.37	0.9990	**	Jun	0.13	0.9093		Jun	0.40	0.9990	**	Jun	0.10	0.8564	
Jul	0.38	0.9990	**	Jul	0.09	0.8350		Jul	0.42	0.9990	**	Jul	0.05	0.7073	
Aug	0.33	0.9990	**	Aug	0.10	0.8640		Aug	0.36	0.9990	**	Aug	0.05	0.6910	
Sep	0.31	0.9990	**	Sep	0.11	0.8952		Sep	0.35	0.9990	**	Sep	0.06	0.7402	

Table A14. Summary of all Seascorr correlation outputs for ID02 EW. Significant relationships with precipitation and temperature at $\alpha = 0.05$ ($\alpha = 0.01$) are highlighted in light (dark) blue for precipitation and orange for temperature; the strongest significant correlation for each season/variable combination is outlined in a thick black box.

PRISM								GHCN							
Precipitation				Temperature				Precipitation				Temperature			
End Month	*r*	NP	*p*	End Month	*r*	NP	*p*	End Month	*r*	NP	*p*	End Month	*r*	NP	*p*
1 month								1 month							
Aug_prev	0.35	0.9990	**	Aug_prev	-0.04	0.3380		Aug_prev	0.41	0.9990	**	Aug_prev	0.03	0.6233	
Sep_prev	0.26	0.9955	**	Sep_prev	-0.07	0.2008		Sep_prev	0.23	0.9958	**	Sep_prev	-0.10	0.1243	
Oct_prev	0.10	0.8597		Oct_prev	0.04	0.6551		Oct_prev	0.07	0.7822		Oct_prev	0.04	0.6657	
Nov_prev	0.04	0.6779		Nov_prev	0.16	0.9684		Nov_prev	0.11	0.8687		Nov_prev	0.14	0.9388	
Dec_prev	0.01	0.5302		Dec_prev	0.21	0.9833	*	Dec_prev	-0.04	0.3219		Dec_prev	0.21	0.9761	*
Jan	-0.03	0.3314		Jan	0.13	0.9116		Jan	-0.01	0.4340		Jan	0.12	0.9050	
Feb	0.00	0.4931		Feb	0.11	0.8990		Feb	-0.01	0.4322		Feb	0.08	0.8245	
Mar	0.06	0.7157		Mar	0.01	0.5554		Mar	0.06	0.7302		Mar	-0.02	0.4307	
Apr	0.09	0.8546		Apr	0.01	0.5579		Apr	0.15	0.9438		Apr	-0.01	0.4534	
May	0.18	0.9668		May	-0.02	0.4162		May	0.22	0.9947	*	May	-0.08	0.1806	
Jun	0.25	0.9934	*	Jun	-0.06	0.2411		Jun	0.26	0.9971	**	Jun	-0.11	0.1159	
Jul	0.12	0.9017		Jul	-0.08	0.1767		Jul	0.17	0.9642		Jul	-0.09	0.1739	
Aug	0.02	0.5580		Aug	-0.08	0.1790		Aug	0.04	0.6807		Aug	-0.11	0.1124	
Sep	0.14	0.9214		Sep	-0.03	0.3446		Sep	0.15	0.9486		Sep	0.00	0.5046	
3 month								3 month							
Aug_prev	0.33	0.9990	**	Aug_prev	0.06	0.7737		Aug_prev	0.39	0.9990	**	Aug_prev	0.12	0.9238	
Sep_prev	0.40	0.9990	**	Sep_prev	0.04	0.6885		Sep_prev	0.42	0.9990	**	Sep_prev	0.08	0.8390	
Oct_prev	0.34	0.9990	**	Oct_prev	-0.11	0.1098		Oct_prev	0.35	0.9990	**	Oct_prev	-0.08	0.1739	
Nov_prev	0.17	0.9769	*	Nov_prev	0.04	0.6595		Nov_prev	0.20	0.9821	*	Nov_prev	0.02	0.5846	
Dec_prev	0.08	0.8289		Dec_prev	0.22	0.9867	*	Dec_prev	0.08	0.8139		Dec_prev	0.20	0.9792	*
Jan	0.01	0.5491		Jan	0.24	0.9933	*	Jan	0.03	0.6329		Jan	0.22	0.9904	*
Feb	-0.02	0.4097		Feb	0.21	0.9887	*	Feb	-0.04	0.3105		Feb	0.20	0.9768	*
Mar	0.01	0.5204		Mar	0.12	0.9089		Mar	0.02	0.5620		Mar	0.10	0.8529	
Apr	0.07	0.7624		Apr	0.07	0.8102		Apr	0.09	0.8219		Apr	0.03	0.6288	
May	0.19	0.9617		May	0.00	0.4976		May	0.24	0.9951	**	May	-0.06	0.2544	
Jun	0.28	0.9969	**	Jun	-0.03	0.3658		Jun	0.34	0.9990	**	Jun	-0.10	0.1230	
Jul	0.30	0.9971	**	Jul	-0.08	0.1938		Jul	0.35	0.9990	**	Jul	-0.14	0.0468	
Aug	0.24	0.9939	*	Aug	-0.09	0.1246		Aug	0.28	0.9966	**	Aug	-0.13	0.0795	
Sep	0.17	0.9370		Sep	-0.08	0.1539		Sep	0.22	0.9787	*	Sep	-0.07	0.2155	
9 month								9 month							
Aug_prev	0.25	0.9990	**	Aug_prev	0.07	0.7696		Aug_prev	0.29	0.9985	**	Aug_prev	0.06	0.7534	
Sep_prev	0.34	0.9990	**	Sep_prev	-0.02	0.4012		Sep_prev	0.36	0.9990	**	Sep_prev	-0.01	0.4861	
Oct_prev	0.28	0.9961	**	Oct_prev	-0.08	0.1612		Oct_prev	0.29	0.9968	**	Oct_prev	-0.06	0.2342	
Nov_prev	0.26	0.9982	**	Nov_prev	-0.04	0.3081		Nov_prev	0.30	0.9978	**	Nov_prev	-0.01	0.4631	
Dec_prev	0.27	0.9990	**	Dec_prev	0.05	0.7017		Dec_prev	0.29	0.9966	**	Dec_prev	0.08	0.7834	
Jan	0.24	0.9975	**	Jan	0.08	0.8124		Jan	0.29	0.9978	**	Jan	0.11	0.8618	
Feb	0.22	0.9932	*	Feb	0.13	0.9118		Feb	0.26	0.9967	**	Feb	0.13	0.9077	
Mar	0.19	0.9850	*	Mar	0.12	0.9093		Mar	0.22	0.9920	*	Mar	0.12	0.8858	
Apr	0.19	0.9788	*	Apr	0.12	0.9056		Apr	0.23	0.9963	**	Apr	0.10	0.8514	
May	0.17	0.9606		May	0.12	0.9188		May	0.20	0.9795	*	May	0.08	0.8098	
Jun	0.17	0.9577		Jun	0.13	0.9317		Jun	0.21	0.9801	*	Jun	0.09	0.8148	
Jul	0.17	0.9623		Jul	0.11	0.8874		Jul	0.23	0.9955	**	Jul	0.05	0.7169	
Aug	0.18	0.9714		Aug	0.06	0.7527		Aug	0.22	0.9949	*	Aug	0.00	0.4881	
Sep	0.25	0.9892	*	Sep	0.00	0.4975		Sep	0.31	0.9990	**	Sep	-0.05	0.2836	
12 month								12 month							
Aug_prev	0.13	0.9147		Aug_prev	0.08	0.8353		Aug_prev	0.20	0.9869	*	Aug_prev	0.08	0.8172	
Sep_prev	0.22	0.9908	*	Sep_prev	0.01	0.5457		Sep_prev	0.28	0.9971	**	Sep_prev	0.01	0.5561	
Oct_prev	0.30	0.9989	**	Oct_prev	0.02	0.6067		Oct_prev	0.34	0.9990	**	Oct_prev	0.01	0.5758	
Nov_prev	0.30	0.9990	**	Nov_prev	0.05	0.7027		Nov_prev	0.33	0.9990	**	Nov_prev	0.05	0.7140	
Dec_prev	0.28	0.9983	**	Dec_prev	0.06	0.7448		Dec_prev	0.30	0.9988	**	Dec_prev	0.07	0.7891	
Jan	0.21	0.9898	*	Jan	0.04	0.6928		Jan	0.24	0.9965	**	Jan	0.06	0.7355	
Feb	0.21	0.9910	*	Feb	0.08	0.8069		Feb	0.23	0.9955	**	Feb	0.08	0.7900	
Mar	0.23	0.9947	*	Mar	0.09	0.8358		Mar	0.25	0.9933	*	Mar	0.09	0.8308	
Apr	0.24	0.9942	*	Apr	0.11	0.8835		Apr	0.28	0.9970	**	Apr	0.11	0.8695	
May	0.27	0.9984	**	May	0.11	0.8961		May	0.32	0.9990	**	May	0.09	0.8368	
Jun	0.29	0.9990	**	Jun	0.09	0.8437		Jun	0.34	0.9990	**	Jun	0.06	0.7335	
Jul	0.28	0.9990	**	Jul	0.06	0.7547		Jul	0.34	0.9990	**	Jul	0.02	0.5711	
Aug	0.23	0.9925	*	Aug	0.07	0.7877		Aug	0.28	0.9979	**	Aug	0.01	0.5393	
Sep	0.22	0.9858	*	Sep	0.08	0.8397		Sep	0.27	0.9986	**	Sep	0.03	0.6193	

Table A15. Summary of all Seascorr correlation outputs for ID02 LW. Significant relationships with precipitation and temperature at $\alpha = 0.05$ ($\alpha = 0.01$) are highlighted in light (dark) blue for precipitation and orange for temperature; the strongest significant correlation for each season/variable combination is outlined in a thick black box.

PRISM								GHCN							
Precipitation				Temperature				Precipitation				Temperature			
End Month	*r*	NP	*p*	End Month	*r*	NP	*p*	End Month	*r*	NP	*p*	End Month	*r*	NP	*p*
1 month								1 month							
Aug_prev	0.19	0.9665		Aug_prev	-0.07	0.1943		Aug_prev	0.20	0.9758	*	Aug_prev	-0.02	0.4530	
Sep_prev	0.39	0.9990	**	Sep_prev	0.06	0.7700		Sep_prev	0.38	0.9990	**	Sep_prev	0.03	0.6441	
Oct_prev	0.24	0.9981	**	Oct_prev	0.03	0.6070		Oct_prev	0.21	0.9846	*	Oct_prev	0.05	0.7055	
Nov_prev	0.17	0.9627		Nov_prev	0.01	0.5525		Nov_prev	0.20	0.9878	*	Nov_prev	0.01	0.5442	
Dec_prev	0.01	0.5467		Dec_prev	0.24	0.9933	*	Dec_prev	-0.02	0.3936		Dec_prev	0.20	0.9873	*
Jan	-0.02	0.4445		Jan	0.13	0.9236		Jan	0.04	0.6524		Jan	0.11	0.8848	
Feb	0.03	0.6288		Feb	0.16	0.9602		Feb	-0.03	0.3730		Feb	0.15	0.9683	
Mar	0.12	0.8583		Mar	0.14	0.9224		Mar	0.10	0.8528		Mar	0.14	0.9422	
Apr	0.05	0.6638		Apr	0.08	0.8154		Apr	0.13	0.9128		Apr	0.09	0.8413	
May	0.25	0.9918	*	May	0.14	0.9337		May	0.29	0.9980	**	May	0.07	0.7897	
Jun	0.46	0.9990	**	Jun	0.00	0.5350		Jun	0.41	0.9990	**	Jun	-0.06	0.2611	
Jul	0.28	0.9990	**	Jul	-0.12	0.0922		Jul	0.31	0.9988	**	Jul	-0.12	0.1039	
Aug	0.04	0.6449		Aug	-0.09	0.1436		Aug	0.04	0.6429		Aug	-0.10	0.1176	
Sep	0.11	0.8675		Sep	-0.04	0.3225		Sep	0.12	0.8923		Sep	0.00	0.4912	
3 month								3 month							
Aug_prev	0.10	0.8243		Aug_prev	-0.06	0.2176		Aug_prev	0.16	0.9305		Aug_prev	0.02	0.5762	
Sep_prev	0.38	0.9990	**	Sep_prev	0.10	0.8762		Sep_prev	0.39	0.9990	**	Sep_prev	0.12	0.9217	
Oct_prev	0.44	0.9990	**	Oct_prev	-0.04	0.3439		Oct_prev	0.44	0.9990	**	Oct_prev	0.00	0.4714	
Nov_prev	0.39	0.9990	**	Nov_prev	0.00	0.4909		Nov_prev	0.40	0.9990	**	Nov_prev	0.00	0.4751	
Dec_prev	0.24	0.9953	**	Dec_prev	0.15	0.9456		Dec_prev	0.23	0.9947	*	Dec_prev	0.14	0.9481	
Jan	0.10	0.8887		Jan	0.18	0.9769	*	Jan	0.12	0.9127		Jan	0.16	0.9572	
Feb	0.01	0.5538		Feb	0.25	0.9940	*	Feb	-0.01	0.4658		Feb	0.22	0.9923	*
Mar	0.07	0.7361		Mar	0.19	0.9675		Mar	0.06	0.7357		Mar	0.17	0.9665	
Apr	0.11	0.8192		Apr	0.19	0.9795	*	Apr	0.10	0.8239		Apr	0.16	0.9664	
May	0.24	0.9894	*	May	0.16	0.9495		May	0.30	0.9990	**	May	0.11	0.8855	
Jun	0.41	0.9990	**	Jun	0.12	0.9054		Jun	0.45	0.9990	**	Jun	0.05	0.7296	
Jul	0.53	0.9990	**	Jul	0.02	0.5755		Jul	0.53	0.9990	**	Jul	-0.06	0.2615	
Aug	0.47	0.9990	**	Aug	-0.08	0.1880		Aug	0.45	0.9990	**	Aug	-0.11	0.1098	
Sep	0.24	0.9823	*	Sep	-0.11	0.1061		Sep	0.27	0.9967	**	Sep	-0.07	0.1998	
9 month								9 month							
Aug_prev	0.04	0.6634		Aug_prev	0.00	0.5068		Aug_prev	0.09	0.8009		Aug_prev	0.02	0.5947	
Sep_prev	0.17	0.9361		Sep_prev	-0.05	0.2902		Sep_prev	0.23	0.9769	*	Sep_prev	-0.03	0.3736	
Oct_prev	0.26	0.9858	*	Oct_prev	-0.08	0.1954		Oct_prev	0.31	0.9933	*	Oct_prev	-0.05	0.3046	
Nov_prev	0.33	0.9986	**	Nov_prev	-0.07	0.2087		Nov_prev	0.36	0.9987	**	Nov_prev	-0.02	0.4350	
Dec_prev	0.38	0.9990	**	Dec_prev	0.05	0.6637		Dec_prev	0.39	0.9990	**	Dec_prev	0.09	0.8385	
Jan	0.35	0.9990	**	Jan	0.05	0.6986		Jan	0.39	0.9990	**	Jan	0.09	0.8441	
Feb	0.30	0.9990	**	Feb	0.12	0.8964		Feb	0.32	0.9988	**	Feb	0.13	0.9236	
Mar	0.32	0.9990	**	Mar	0.17	0.9577		Mar	0.33	0.9980	**	Mar	0.16	0.9603	
Apr	0.32	0.9990	**	Apr	0.18	0.9712		Apr	0.34	0.9990	**	Apr	0.17	0.9663	
May	0.34	0.9990	**	May	0.21	0.9809	*	May	0.36	0.9990	**	May	0.17	0.9598	
Jun	0.36	0.9990	**	Jun	0.20	0.9803	*	Jun	0.37	0.9990	**	Jun	0.16	0.9589	
Jul	0.34	0.9990	**	Jul	0.16	0.9411		Jul	0.39	0.9990	**	Jul	0.11	0.8831	
Aug	0.32	0.9990	**	Aug	0.13	0.9046		Aug	0.35	0.9990	**	Aug	0.08	0.8141	
Sep	0.4	0.9990	**	Sep	0.08	0.7972		Sep	0.43	0.9990	**	Sep	0.04	0.6969	
12 month								12 month							
Aug_prev	-0.03	0.4014		Aug_prev	-0.01	0.4392		Aug_prev	0.05	0.6755		Aug_prev	0.01	0.5416	
Sep_prev	0.07	0.7692		Sep_prev	-0.05	0.2976		Sep_prev	0.16	0.9197		Sep_prev	-0.04	0.3716	
Oct_prev	0.17	0.9411		Oct_prev	-0.02	0.3910		Oct_prev	0.24	0.9878	*	Oct_prev	-0.01	0.4685	
Nov_prev	0.25	0.9858	*	Nov_prev	-0.03	0.3878		Nov_prev	0.29	0.9963	**	Nov_prev	-0.01	0.4903	
Dec_prev	0.27	0.9928	*	Dec_prev	0.02	0.5583		Dec_prev	0.30	0.9974	**	Dec_prev	0.03	0.6516	
Jan	0.26	0.9887	*	Jan	0.03	0.6004		Jan	0.31	0.9990	**	Jan	0.05	0.6942	
Feb	0.28	0.9959	**	Feb	0.08	0.7969		Feb	0.30	0.9981	**	Feb	0.09	0.8554	
Mar	0.34	0.9990	**	Mar	0.12	0.8983		Mar	0.35	0.9990	**	Mar	0.14	0.9409	
Apr	0.34	0.9990	**	Apr	0.15	0.9368		Apr	0.37	0.9990	**	Apr	0.17	0.9600	
May	0.36	0.9990	**	May	0.18	0.9638		May	0.39	0.9990	**	May	0.17	0.9641	
Jun	0.46	0.9990	**	Jun	0.18	0.9643		Jun	0.48	0.9990	**	Jun	0.15	0.9414	
Jul	0.48	0.9990	**	Jul	0.13	0.9076		Jul	0.51	0.9990	**	Jul	0.10	0.8586	
Aug	0.46	0.9990	**	Aug	0.13	0.9143		Aug	0.48	0.9990	**	Aug	0.08	0.8245	
Sep	0.42	0.9990	**	Sep	0.13	0.9133		Sep	0.44	0.9990	**	Sep	0.09	0.8333	

Table A16. Summary of all Seascorr correlation outputs for ID02 LW_{adj}. Significant relationships with precipitation and temperature at $\alpha = 0.05$ ($\alpha = 0.01$) are highlighted in light (dark) blue for precipitation and orange for temperature; the strongest significant correlation for each season/variable combination is outlined in a thick black box.

PRISM								GHCN							
Precipitation				Temperature				Precipitation				Temperature			
End Month	*r*	NP	*p*	End Month	*r*	NP	*p*	End Month	*r*	NP	*p*	End Month	*r*	NP	*p*
1 month								1 month							
Aug_prev	-0.01	0.4342		Aug_prev	-0.07	0.2084		Aug_prev	-0.05	0.3057		Aug_prev	-0.04	0.3285	
Sep_prev	0.33	0.9990	**	Sep_prev	0.14	0.9396		Sep_prev	0.34	0.9990	**	Sep_prev	0.13	0.9290	
Oct_prev	0.25	0.9990	**	Oct_prev	0.01	0.5657		Oct_prev	0.23	0.9962	**	Oct_prev	0.04	0.6712	
Nov_prev	0.20	0.9878	*	Nov_prev	-0.11	0.1097		Nov_prev	0.20	0.9905	*	Nov_prev	-0.10	0.1320	
Dec_prev	0.02	0.5814		Dec_prev	0.16	0.9625		Dec_prev	0.00	0.5393		Dec_prev	0.11	0.8930	
Jan	0.00	0.5326		Jan	0.08	0.7958		Jan	0.06	0.7242		Jan	0.05	0.7083	
Feb	0.04	0.6719		Feb	0.14	0.9550		Feb	-0.03	0.3824		Feb	0.14	0.9606	
Mar	0.11	0.9028		Mar	0.18	0.9639		Mar	0.09	0.8401		Mar	0.20	0.9840	*
Apr	-0.01	0.4552		Apr	0.11	0.8786		Apr	0.06	0.7043		Apr	0.14	0.9291	
May	0.20	0.9834	*	May	0.21	0.9941	*	May	0.23	0.9920	*	May	0.16	0.9735	
Jun	0.44	0.9990	**	Jun	0.06	0.7410		Jun	0.36	0.9990	**	Jun	0.01	0.5777	
Jul	0.29	0.9990	**	Jul	-0.10	0.1428		Jul	0.30	0.9988	**	Jul	-0.10	0.1674	
Aug	0.04	0.6557		Aug	-0.06	0.2580		Aug	0.02	0.6183		Aug	-0.05	0.2934	
Sep	0.04	0.6622		Sep	-0.03	0.3957		Sep	0.04	0.6850		Sep	0.00	0.4950	
3 month								3 month							
Aug_prev	-0.12	0.1211		Aug_prev	-0.13	0.0639		Aug_prev	-0.09	0.1997		Aug_prev	-0.06	0.2446	
Sep_prev	0.20	0.9626		Sep_prev	0.10	0.8866		Sep_prev	0.20	0.9720		Sep_prev	0.10	0.8869	
Oct_prev	0.35	0.9990	**	Oct_prev	0.04	0.7116		Oct_prev	0.33	0.9984	**	Oct_prev	0.06	0.7717	
Nov_prev	0.40	0.9990	**	Nov_prev	-0.04	0.3850		Nov_prev	0.40	0.9990	**	Nov_prev	-0.02	0.4053	
Dec_prev	0.27	0.9989	**	Dec_prev	0.03	0.6562		Dec_prev	0.25	0.9977	**	Dec_prev	0.03	0.6396	
Jan	0.13	0.9144		Jan	0.06	0.7568		Jan	0.14	0.9533		Jan	0.04	0.6597	
Feb	0.03	0.6532		Feb	0.18	0.9756	*	Feb	0.02	0.5952		Feb	0.15	0.9564	
Mar	0.09	0.8367		Mar	0.17	0.9682		Mar	0.07	0.7638		Mar	0.17	0.9682	
Apr	0.09	0.8224		Apr	0.20	0.9804	*	Apr	0.06	0.7149		Apr	0.20	0.9880	*
May	0.18	0.9742		May	0.22	0.9879	*	May	0.22	0.9919	*	May	0.20	0.9858	*
Jun	0.34	0.9990	**	Jun	0.19	0.9780	*	Jun	0.35	0.9990	**	Jun	0.15	0.9518	
Jul	0.50	0.9990	**	Jul	0.09	0.8464		Jul	0.46	0.9990	**	Jul	0.04	0.7009	
Aug	0.46	0.9990	**	Aug	-0.03	0.4051		Aug	0.40	0.9990	**	Aug	-0.04	0.3293	
Sep	0.20	0.9663		Sep	-0.08	0.1634		Sep	0.20	0.9743		Sep	-0.05	0.3020	
9 month								9 month							
Aug_prev	-0.14	0.0832		Aug_prev	-0.05	0.3018		Aug_prev	-0.10	0.1557		Aug_prev	-0.02	0.3792	
Sep_prev	-0.03	0.3927		Sep_prev	-0.06	0.2595		Sep_prev	0.03	0.5999		Sep_prev	-0.03	0.3613	
Oct_prev	0.14	0.8893		Oct_prev	-0.04	0.3175		Oct_prev	0.19	0.9544		Oct_prev	-0.01	0.4361	
Nov_prev	0.25	0.9920	*	Nov_prev	-0.06	0.2544		Nov_prev	0.26	0.9873	*	Nov_prev	-0.01	0.4563	
Dec_prev	0.31	0.9984	**	Dec_prev	0.02	0.6198		Dec_prev	0.30	0.9990	**	Dec_prev	0.06	0.7516	
Jan	0.29	0.9981	**	Jan	0.01	0.5421		Jan	0.32	0.9990	**	Jan	0.04	0.6694	
Feb	0.24	0.9944	*	Feb	0.07	0.7884		Feb	0.24	0.9964	**	Feb	0.07	0.7965	
Mar	0.30	0.9990	**	Mar	0.13	0.9461		Mar	0.28	0.9990	**	Mar	0.13	0.9324	
Apr	0.29	0.9990	**	Apr	0.15	0.9662		Apr	0.29	0.9990	**	Apr	0.15	0.9583	
May	0.33	0.9990	**	May	0.18	0.9814	*	May	0.34	0.9990	**	May	0.16	0.9641	
Jun	0.36	0.9990	**	Jun	0.17	0.9717		Jun	0.35	0.9990	**	Jun	0.15	0.9426	
Jul	0.35	0.9990	**	Jul	0.13	0.9108		Jul	0.35	0.9990	**	Jul	0.11	0.8955	
Aug	0.31	0.9980	**	Aug	0.14	0.9207		Aug	0.31	0.9990	**	Aug	0.11	0.8912	
Sep	0.36	0.9990	**	Sep	0.11	0.8784		Sep	0.35	0.9990	**	Sep	0.10	0.8782	
12 month								12 month							
Aug_prev	-0.14	0.0771		Aug_prev	-0.08	0.1920		Aug_prev	-0.08	0.1881		Aug_prev	-0.05	0.2540	
Sep_prev	-0.07	0.2277		Sep_prev	-0.08	0.2047		Sep_prev	0.00	0.4780		Sep_prev	-0.05	0.2570	
Oct_prev	0.00	0.4928		Oct_prev	-0.05	0.3136		Oct_prev	0.06	0.7066		Oct_prev	-0.03	0.3729	
Nov_prev	0.12	0.8841		Nov_prev	-0.07	0.2297		Nov_prev	0.14	0.9136		Nov_prev	-0.04	0.2954	
Dec_prev	0.15	0.9423		Dec_prev	-0.03	0.3979		Dec_prev	0.17	0.9619		Dec_prev	-0.01	0.4484	
Jan	0.19	0.9776	*	Jan	0.00	0.5188		Jan	0.23	0.9917	*	Jan	0.02	0.5791	
Feb	0.23	0.9893	*	Feb	0.05	0.7306		Feb	0.23	0.9892	*	Feb	0.06	0.7802	
Mar	0.30	0.9985	**	Mar	0.10	0.8876		Mar	0.28	0.9977	**	Mar	0.12	0.9087	
Apr	0.28	0.9963	**	Apr	0.12	0.9289		Apr	0.29	0.9980	**	Apr	0.14	0.9303	
May	0.28	0.9971	**	May	0.15	0.9688		May	0.29	0.9990	**	May	0.15	0.9519	
Jun	0.41	0.9990	**	Jun	0.17	0.9774	*	Jun	0.39	0.9990	**	Jun	0.15	0.9610	
Jul	0.44	0.9990	**	Jul	0.12	0.9199		Jul	0.43	0.9990	**	Jul	0.11	0.9055	
Aug	0.45	0.9990	**	Aug	0.13	0.9123		Aug	0.45	0.9990	**	Aug	0.10	0.8862	
Sep	0.42	0.9990	**	Sep	0.11	0.8920		Sep	0.40	0.9990	**	Sep	0.10	0.8697	

Table A17. Summary of all Seascorr correlation outputs for OR18 TRW. Significant relationships with precipitation and temperature at $\alpha = 0.05$ ($\alpha = 0.01$) are highlighted in light (dark) blue for precipitation and orange for temperature; the strongest significant correlation for each season/variable combination is outlined in a thick black box.

PRISM								GHCN							
Precipitation				Temperature				Precipitation				Temperature			
End Month	*r*	NP	*p*	End Month	*r*	NP	*p*	End Month	*r*	NP	*p*	End Month	*r*	NP	*p*
1 month								1 month							
Aug_prev	0.43	0.9990	**	Aug_prev	-0.22	0.0036	**	Aug_prev	0.28	0.9681		Aug_prev	-0.32	0.0183	*
Sep_prev	0.17	0.9502		Sep_prev	-0.01	0.4484		Sep_prev	0.10	0.7287		Sep_prev	-0.13	0.2188	
Oct_prev	0.11	0.8577		Oct_prev	-0.04	0.3162		Oct_prev	0.03	0.5853		Oct_prev	-0.15	0.2131	
Nov_prev	0.07	0.7857		Nov_prev	0.08	0.7942		Nov_prev	-0.09	0.3120		Nov_prev	0.05	0.6107	
Dec_prev	-0.01	0.4922		Dec_prev	0.24	0.9900	*	Dec_prev	-0.13	0.1849		Dec_prev	0.23	0.9456	
Jan	-0.08	0.2101		Jan	0.20	0.9892	*	Jan	0.02	0.5670		Jan	0.12	0.7867	
Feb	0.03	0.6202		Feb	0.06	0.7411		Feb	0.22	0.8789		Feb	0.01	0.5394	
Mar	0.07	0.7700		Mar	0.21	0.9947	*	Mar	0.01	0.5075		Mar	0.33	0.9725	
Apr	-0.03	0.3679		Apr	0.27	0.9969	**	Apr	0.02	0.5471		Apr	0.21	0.9364	
May	0.18	0.9512		May	0.23	0.9973	**	May	0.12	0.7685		May	0.09	0.7332	
Jun	0.27	0.9984	**	Jun	0.00	0.5214		Jun	0.06	0.6271		Jun	0.10	0.7293	
Jul	0.21	0.9873	*	Jul	-0.04	0.3012		Jul	0.17	0.8553		Jul	-0.05	0.3852	
Aug	0.06	0.7236		Aug	-0.01	0.4576		Aug	0.08	0.6878		Aug	0.07	0.6789	
Sep	-0.02	0.4412		Sep	-0.12	0.1048		Sep	0.05	0.6004		Sep	-0.03	0.4471	
3 month								3 month							
Aug_prev	0.27	0.9990	**	Aug_prev	-0.09	0.1808		Aug_prev	0.20	0.9072		Aug_prev	-0.09	0.2955	
Sep_prev	0.43	0.9990	**	Sep_prev	-0.05	0.3353		Sep_prev	0.22	0.9286		Sep_prev	-0.28	0.0417	
Oct_prev	0.37	0.9990	**	Oct_prev	-0.10	0.1435		Oct_prev	0.22	0.9086		Oct_prev	-0.27	0.0467	
Nov_prev	0.17	0.9591		Nov_prev	0.01	0.5421		Nov_prev	0.00	0.4923		Nov_prev	-0.12	0.2338	
Dec_prev	0.08	0.8196		Dec_prev	0.15	0.9513		Dec_prev	-0.10	0.2762		Dec_prev	0.08	0.7299	
Jan	0.00	0.5328		Jan	0.27	0.9990	**	Jan	-0.11	0.2677		Jan	0.18	0.9064	
Feb	-0.03	0.3771		Feb	0.25	0.9961	**	Feb	0.03	0.5753		Feb	0.18	0.8883	
Mar	0.00	0.5386		Mar	0.22	0.9929	*	Mar	0.12	0.7729		Mar	0.22	0.9341	
Apr	0.04	0.6636		Apr	0.24	0.9945	*	Apr	0.12	0.7828		Apr	0.26	0.9591	
May	0.14	0.9474		May	0.33	0.9990	**	May	0.09	0.7529		May	0.30	0.9792	*
Jun	0.24	0.9961	**	Jun	0.28	0.9990	**	Jun	0.11	0.7668		Jun	0.21	0.9458	
Jul	0.34	0.9990	**	Jul	0.09	0.8449		Jul	0.18	0.8601		Jul	0.09	0.7395	
Aug	0.31	0.9990	**	Aug	-0.01	0.4274		Aug	0.16	0.8663		Aug	0.07	0.6821	
Sep	0.10	0.8549		Sep	-0.10	0.1472		Sep	0.14	0.8285		Sep	-0.04	0.4130	
9 month								9 month							
Aug_prev	0.19	0.9887	*	Aug_prev	-0.04	0.3406		Aug_prev	0.18	0.8821		Aug_prev	-0.16	0.1474	
Sep_prev	0.28	0.9985	**	Sep_prev	-0.05	0.2763		Sep_prev	0.22	0.9209		Sep_prev	-0.19	0.1059	
Oct_prev	0.33	0.9990	**	Oct_prev	-0.13	0.0554		Oct_prev	0.19	0.9149		Oct_prev	-0.26	0.0453	
Nov_prev	0.28	0.9983	**	Nov_prev	-0.10	0.1193		Nov_prev	0.13	0.8237		Nov_prev	-0.20	0.0952	
Dec_prev	0.27	0.9990	**	Dec_prev	0.00	0.5121		Dec_prev	0.04	0.6295		Dec_prev	-0.12	0.2133	
Jan	0.23	0.9970	**	Jan	0.06	0.7206		Jan	0.02	0.5686		Jan	-0.06	0.3540	
Feb	0.18	0.9610		Feb	0.10	0.8495		Feb	0.09	0.7105		Feb	0.00	0.5183	
Mar	0.19	0.9710		Mar	0.16	0.9528		Mar	0.07	0.6513		Mar	0.05	0.6583	
Apr	0.16	0.9502		Apr	0.22	0.9920	*	Apr	0.07	0.6512		Apr	0.14	0.8562	
May	0.13	0.9275		May	0.31	0.9990	**	May	0.05	0.6241		May	0.20	0.9399	
Jun	0.16	0.9641		Jun	0.32	0.9990	**	Jun	0.04	0.6146		Jun	0.22	0.9454	
Jul	0.16	0.9713		Jul	0.32	0.9990	**	Jul	0.06	0.6582		Jul	0.25	0.9633	
Aug	0.15	0.9595		Aug	0.28	0.9981	**	Aug	0.11	0.7899		Aug	0.25	0.9681	
Sep	0.18	0.9805	*	Sep	0.21	0.9909	*	Sep	0.18	0.9199		Sep	0.21	0.9209	
12 month								12 month							
Aug_prev	0.16	0.9600		Aug_prev	0.00	0.4988		Aug_prev	0.27	0.9635		Aug_prev	-0.11	0.2446	
Sep_prev	0.21	0.9901	*	Sep_prev	-0.03	0.3556		Sep_prev	0.30	0.9799	*	Sep_prev	-0.17	0.1298	
Oct_prev	0.25	0.9964	**	Oct_prev	-0.04	0.3315		Oct_prev	0.30	0.9836	*	Oct_prev	-0.17	0.1301	
Nov_prev	0.26	0.9956	**	Nov_prev	-0.04	0.3207		Nov_prev	0.15	0.8689		Nov_prev	-0.18	0.1152	
Dec_prev	0.26	0.9971	**	Dec_prev	0.01	0.5202		Dec_prev	0.12	0.7999		Dec_prev	-0.15	0.1581	
Jan	0.24	0.9957	**	Jan	0.01	0.5340		Jan	0.10	0.7578		Jan	-0.15	0.1559	
Feb	0.20	0.9885	*	Feb	0.05	0.7124		Feb	0.12	0.8032		Feb	-0.07	0.3336	
Mar	0.23	0.9891	*	Mar	0.12	0.9081		Mar	0.09	0.7248		Mar	0.02	0.5754	
Apr	0.21	0.9858	*	Apr	0.18	0.9752	*	Apr	0.07	0.6664		Apr	0.08	0.7431	
May	0.21	0.9840	*	May	0.24	0.9938	*	May	0.11	0.7729		May	0.12	0.8305	
Jun	0.26	0.9985	**	Jun	0.25	0.9955	**	Jun	0.11	0.7791		Jun	0.12	0.8262	
Jul	0.27	0.9990	**	Jul	0.23	0.9925	*	Jul	0.12	0.8056		Jul	0.14	0.8753	
Aug	0.20	0.9897	*	Aug	0.26	0.9969	**	Aug	0.09	0.7201		Aug	0.19	0.9198	
Sep	0.17	0.9717		Sep	0.25	0.9957	**	Sep	0.07	0.7007		Sep	0.19	0.9153	

Table A18. Summary of all Seascorr correlation outputs for OR18 EW. Significant relationships with precipitation and temperature at $\alpha = 0.05$ ($\alpha = 0.01$) are highlighted in light (dark) blue for precipitation and orange for temperature; the strongest significant correlation for each season/variable combination is outlined in a thick black box.

PRISM								GHCN							
Precipitation				Temperature				Precipitation				Temperature			
End Month	*r*	NP	*p*	End Month	*r*	NP	*p*	End Month	*r*	NP	*p*	End Month	*r*	NP	*p*
1 month								1 month							
Aug_prev	0.47	0.9990	**	Aug_prev	-0.25	0.0015	**	Aug_prev	0.41	0.9930	*	Aug_prev	-0.40	0.0029	**
Sep_prev	0.14	0.9003		Sep_prev	-0.01	0.4638		Sep_prev	0.12	0.7895		Sep_prev	-0.05	0.3683	
Oct_prev	0.10	0.8591		Oct_prev	-0.04	0.3304		Oct_prev	-0.04	0.4269		Oct_prev	-0.16	0.1508	
Nov_prev	0.01	0.5395		Nov_prev	0.12	0.9179		Nov_prev	-0.24	0.0857		Nov_prev	0.10	0.7343	
Dec_prev	-0.04	0.3524		Dec_prev	0.25	0.9970	**	Dec_prev	-0.16	0.1798		Dec_prev	0.28	0.9526	
Jan	-0.12	0.1184		Jan	0.22	0.9873	*	Jan	-0.04	0.3602		Jan	0.17	0.8907	
Feb	0.02	0.5978		Feb	0.04	0.6462		Feb	0.15	0.8441		Feb	0.00	0.4888	
Mar	0.05	0.7007		Mar	0.16	0.9470		Mar	-0.09	0.2512		Mar	0.29	0.9489	
Apr	-0.05	0.3205		Apr	0.26	0.9939	*	Apr	-0.03	0.4152		Apr	0.23	0.9249	
May	0.20	0.9620		May	0.17	0.9825	*	May	0.21	0.9114		May	0.07	0.6897	
Jun	0.23	0.9927	*	Jun	-0.06	0.3208		Jun	0.03	0.5851		Jun	0.01	0.5242	
Jul	0.15	0.9362		Jul	0.03	0.6367		Jul	0.07	0.6669		Jul	0.10	0.7133	
Aug	-0.01	0.4864		Aug	0.06	0.6938		Aug	-0.03	0.4349		Aug	0.13	0.7782	
Sep	-0.01	0.4297		Sep	-0.11	0.1312		Sep	0.02	0.5484		Sep	-0.03	0.4270	
3 month								3 month							
Aug_prev	0.36	0.9990	**	Aug_prev	-0.08	0.2163		Aug_prev	0.33	0.9730		Aug_prev	-0.15	0.1706	
Sep_prev	0.44	0.9990	**	Sep_prev	-0.06	0.2982		Sep_prev	0.30	0.9705		Sep_prev	-0.32	0.0164	*
Oct_prev	0.37	0.9990	**	Oct_prev	-0.11	0.1313		Oct_prev	0.24	0.9452		Oct_prev	-0.25	0.0420	
Nov_prev	0.10	0.8601		Nov_prev	0.04	0.6548		Nov_prev	-0.12	0.2597		Nov_prev	-0.08	0.2947	
Dec_prev	0.02	0.5912		Dec_prev	0.17	0.9801	*	Dec_prev	-0.22	0.1241		Dec_prev	0.14	0.7939	
Jan	-0.07	0.2284		Jan	0.30	0.9984	**	Jan	-0.25	0.0747		Jan	0.26	0.9578	
Feb	-0.07	0.1988		Feb	0.25	0.9948	*	Feb	-0.06	0.3584		Feb	0.21	0.9186	
Mar	-0.04	0.3586		Mar	0.20	0.9830	*	Mar	0.00	0.4896		Mar	0.20	0.9114	
Apr	0.01	0.5947		Apr	0.21	0.9809	*	Apr	0.01	0.5160		Apr	0.23	0.9310	
May	0.13	0.9194		May	0.28	0.9990	**	May	0.08	0.7030		May	0.28	0.9701	
Jun	0.22	0.9844	*	Jun	0.21	0.9963	**	Jun	0.14	0.7967		Jun	0.18	0.8931	
Jul	0.32	0.9990	**	Jul	0.07	0.7973		Jul	0.21	0.8973		Jul	0.14	0.8251	
Aug	0.22	0.9848	*	Aug	0.03	0.6107		Aug	0.04	0.5981		Aug	0.11	0.7498	
Sep	0.04	0.6451		Sep	-0.03	0.3953		Sep	0.03	0.5769		Sep	0.08	0.6603	
9 month								9 month							
Aug_prev	0.27	0.9990	**	Aug_prev	-0.01	0.4297		Aug_prev	0.32	0.9776	*	Aug_prev	-0.20	0.0855	
Sep_prev	0.35	0.9990	**	Sep_prev	-0.03	0.3517		Sep_prev	0.35	0.9849	*	Sep_prev	-0.21	0.0612	
Oct_prev	0.38	0.9990	**	Oct_prev	-0.10	0.1373		Oct_prev	0.29	0.9820	*	Oct_prev	-0.28	0.0240	*
Nov_prev	0.31	0.9987	**	Nov_prev	-0.05	0.2802		Nov_prev	0.17	0.8859		Nov_prev	-0.19	0.0857	
Dec_prev	0.27	0.9979	**	Dec_prev	0.04	0.6656		Dec_prev	0.05	0.6555		Dec_prev	-0.09	0.2353	
Jan	0.20	0.9822	*	Jan	0.09	0.8215		Jan	-0.02	0.4531		Jan	-0.03	0.4161	
Feb	0.15	0.9313		Feb	0.11	0.8670		Feb	0.00	0.5216		Feb	0.00	0.5097	
Mar	0.13	0.9073		Mar	0.15	0.9400		Mar	-0.05	0.3785		Mar	0.05	0.6286	
Apr	0.10	0.8546		Apr	0.21	0.9879	*	Apr	-0.06	0.3625		Apr	0.14	0.8169	
May	0.07	0.8009		May	0.29	0.9982	**	May	-0.05	0.3681		May	0.22	0.9270	
Jun	0.10	0.8653		Jun	0.29	0.9980	**	Jun	-0.07	0.3343		Jun	0.21	0.9132	
Jul	0.09	0.8482		Jul	0.30	0.9982	**	Jul	-0.05	0.3609		Jul	0.27	0.9708	
Aug	0.09	0.8510		Aug	0.27	0.9981	**	Aug	0.02	0.5393		Aug	0.27	0.9751	*
Sep	0.13	0.8986		Sep	0.20	0.9756	*	Sep	0.09	0.7249		Sep	0.22	0.9386	
12 month								12 month							
Aug_prev	0.23	0.9945	*	Aug_prev	0.03	0.6030		Aug_prev	0.41	0.9935	*	Aug_prev	-0.12	0.2022	
Sep_prev	0.28	0.9984	**	Sep_prev	0.00	0.4637		Sep_prev	0.43	0.9939	*	Sep_prev	-0.17	0.1161	
Oct_prev	0.32	0.9990	**	Oct_prev	-0.01	0.4496		Oct_prev	0.42	0.9958	**	Oct_prev	-0.19	0.0937	
Nov_prev	0.29	0.9975	**	Nov_prev	-0.01	0.4455		Nov_prev	0.23	0.9552		Nov_prev	-0.20	0.0701	
Dec_prev	0.27	0.9971	**	Dec_prev	0.04	0.6388		Dec_prev	0.16	0.8708		Dec_prev	-0.16	0.1144	
Jan	0.23	0.9913	*	Jan	0.05	0.6879		Jan	0.10	0.7703		Jan	-0.14	0.1438	
Feb	0.20	0.9824	*	Feb	0.08	0.8144		Feb	0.11	0.7931		Feb	-0.04	0.3571	
Mar	0.21	0.9844	*	Mar	0.14	0.9195		Mar	0.05	0.6254		Mar	0.03	0.5830	
Apr	0.17	0.9593		Apr	0.18	0.9716		Apr	-0.01	0.4843		Apr	0.08	0.7018	
May	0.18	0.9593		May	0.22	0.9924	*	May	0.04	0.6063		May	0.11	0.7749	
Jun	0.21	0.9834	*	Jun	0.22	0.9909	*	Jun	0.02	0.5430		Jun	0.10	0.7522	
Jul	0.20	0.9819	*	Jul	0.21	0.9865	*	Jul	0.02	0.5477		Jul	0.16	0.8637	
Aug	0.12	0.9050		Aug	0.25	0.9980	**	Aug	-0.04	0.3977		Aug	0.21	0.9269	
Sep	0.10	0.8633		Sep	0.25	0.9959	**	Sep	-0.05	0.3775		Sep	0.21	0.9279	

Table A19. Summary of all Seascorr correlation outputs for OR18 LW. Significant relationships with precipitation and temperature at $\alpha = 0.05$ ($\alpha = 0.01$) are highlighted in light (dark) blue for precipitation and orange for temperature; the strongest significant correlation for each season/variable combination is outlined in a thick black box.

PRISM								GHCN							
Precipitation				Temperature				Precipitation				Temperature			
End Month	*r*	NP	*p*	End Month	*r*	NP	*p*	End Month	*r*	NP	*p*	End Month	*r*	NP	*p*
1 month								1 month							
Aug_prev	0.21	0.9934	*	Aug_prev	-0.10	0.1590		Aug_prev	-0.09	0.2929		Aug_prev	-0.10	0.2507	
Sep_prev	0.16	0.9581		Sep_prev	-0.08	0.2288		Sep_prev	-0.03	0.4414		Sep_prev	-0.36	0.0281	
Oct_prev	0.14	0.9191		Oct_prev	-0.05	0.2677		Oct_prev	0.22	0.9426		Oct_prev	-0.03	0.4163	
Nov_prev	0.19	0.9799	*	Nov_prev	0.00	0.4796		Nov_prev	0.24	0.9079		Nov_prev	-0.13	0.2301	
Dec_prev	0.01	0.5575		Dec_prev	0.14	0.9432		Dec_prev	0.08	0.6923		Dec_prev	0.00	0.5057	
Jan	-0.01	0.4518		Jan	0.09	0.8608		Jan	0.23	0.9436		Jan	-0.08	0.3371	
Feb	0.04	0.6417		Feb	0.07	0.7822		Feb	0.27	0.9225		Feb	-0.01	0.4749	
Mar	0.10	0.8482		Mar	0.26	0.9990	**	Mar	0.19	0.8919		Mar	0.30	0.9435	
Apr	0.05	0.7036		Apr	0.24	0.9896	*	Apr	0.23	0.9420		Apr	0.05	0.6031	
May	0.16	0.9348		May	0.31	0.9990	**	May	-0.08	0.2903		May	0.10	0.7345	
Jun	0.31	0.9990	**	Jun	0.05	0.6621		Jun	0.07	0.6562		Jun	0.09	0.6787	
Jul	0.36	0.9990	**	Jul	-0.20	0.0198	*	Jul	0.44	0.9971	**	Jul	-0.38	0.0031	**
Aug	0.12	0.9161		Aug	-0.13	0.0789		Aug	0.22	0.9136		Aug	0.02	0.5306	
Sep	-0.02	0.4410		Sep	-0.08	0.2016		Sep	0.06	0.6604		Sep	0.01	0.5263	
3 month								3 month							
Aug_prev	0.06	0.7312		Aug_prev	-0.13	0.1301		Aug_prev	-0.10	0.2710		Aug_prev	-0.03	0.4174	
Sep_prev	0.28	0.9988	**	Sep_prev	-0.07	0.2584		Sep_prev	-0.04	0.4146		Sep_prev	-0.25	0.0739	
Oct_prev	0.28	0.9928	*	Oct_prev	-0.10	0.1569		Oct_prev	0.09	0.7255		Oct_prev	-0.26	0.0748	
Nov_prev	0.26	0.9939	*	Nov_prev	-0.06	0.2735		Nov_prev	0.24	0.9440		Nov_prev	-0.25	0.0741	
Dec_prev	0.18	0.9614		Dec_prev	0.05	0.6690		Dec_prev	0.24	0.9355		Dec_prev	-0.11	0.2378	
Jan	0.11	0.8708		Jan	0.12	0.9084		Jan	0.29	0.9379		Jan	-0.09	0.2957	
Feb	0.02	0.5832		Feb	0.15	0.9358		Feb	0.31	0.9662		Feb	0.02	0.5366	
Mar	0.07	0.7473		Mar	0.19	0.9912	*	Mar	0.36	0.9864	*	Mar	0.15	0.8069	
Apr	0.11	0.8503		Apr	0.25	0.9990	**	Apr	0.34	0.9806	*	Apr	0.19	0.8857	
May	0.18	0.9833	*	May	0.38	0.9990	**	May	0.15	0.8675		May	0.22	0.8834	
Jun	0.28	0.9986	**	Jun	0.32	0.9990	**	Jun	0.08	0.7105		Jun	0.11	0.7604	
Jul	0.38	0.9990	**	Jul	0.06	0.7435		Jul	0.12	0.7716		Jul	-0.13	0.1875	
Aug	0.41	0.9990	**	Aug	-0.15	0.1205		Aug	0.37	0.9907	*	Aug	-0.11	0.2073	
Sep	0.19	0.9764	*	Sep	-0.22	0.0189	*	Sep	0.33	0.9723		Sep	-0.27	0.0571	
9 month								9 month							
Aug_prev	0.05	0.6902		Aug_prev	-0.04	0.3448		Aug_prev	-0.09	0.2949		Aug_prev	-0.03	0.4121	
Sep_prev	0.12	0.8906		Sep_prev	-0.07	0.2358		Sep_prev	-0.07	0.3434		Sep_prev	-0.12	0.2341	
Oct_prev	0.22	0.9820	*	Oct_prev	-0.15	0.0462		Oct_prev	0.01	0.5143		Oct_prev	-0.17	0.1470	
Nov_prev	0.22	0.9822	*	Nov_prev	-0.14	0.0630		Nov_prev	0.04	0.6239		Nov_prev	-0.20	0.0991	
Dec_prev	0.25	0.9939	*	Dec_prev	-0.08	0.2060		Dec_prev	0.07	0.6609		Dec_prev	-0.20	0.0962	
Jan	0.25	0.9989	**	Jan	-0.05	0.3289		Jan	0.19	0.8778		Jan	-0.19	0.1202	
Feb	0.20	0.9725		Feb	0.01	0.5297		Feb	0.28	0.9480		Feb	-0.09	0.2768	
Mar	0.25	0.9917	*	Mar	0.11	0.8612		Mar	0.35	0.9758	*	Mar	-0.07	0.3109	
Apr	0.23	0.9904	*	Apr	0.17	0.9691		Apr	0.38	0.9909	*	Apr	0.03	0.5702	
May	0.23	0.9894	*	May	0.25	0.9977	**	May	0.33	0.9852	*	May	0.05	0.6283	
Jun	0.27	0.9990	**	Jun	0.28	0.9990	**	Jun	0.34	0.9867	*	Jun	0.12	0.7565	
Jul	0.28	0.9990	**	Jul	0.25	0.9976	**	Jul	0.37	0.9901	*	Jul	0.07	0.6451	
Aug	0.24	0.9954	**	Aug	0.19	0.9877	*	Aug	0.34	0.9924	*	Aug	0.08	0.6740	
Sep	0.28	0.9982	**	Sep	0.16	0.9580		Sep	0.37	0.9959	**	Sep	0.06	0.6242	
12 month								12 month							
Aug_prev	0.03	0.6139		Aug_prev	-0.04	0.3748		Aug_prev	0.01	0.5109		Aug_prev	-0.04	0.4067	
Sep_prev	0.07	0.7623		Sep_prev	-0.06	0.2814		Sep_prev	0.00	0.4984		Sep_prev	-0.12	0.2333	
Oct_prev	0.12	0.8547		Oct_prev	-0.06	0.2614		Oct_prev	0.05	0.6051		Oct_prev	-0.06	0.3438	
Nov_prev	0.17	0.9346		Nov_prev	-0.07	0.2540		Nov_prev	0.03	0.5656		Nov_prev	-0.10	0.2760	
Dec_prev	0.20	0.9680		Dec_prev	-0.04	0.3172		Dec_prev	0.08	0.7194		Dec_prev	-0.12	0.2248	
Jan	0.23	0.9927	*	Jan	-0.07	0.2461		Jan	0.17	0.8521		Jan	-0.19	0.1327	
Feb	0.19	0.9600		Feb	-0.02	0.4067		Feb	0.18	0.8580		Feb	-0.16	0.1655	
Mar	0.24	0.9916	*	Mar	0.05	0.7111		Mar	0.22	0.9083		Mar	-0.09	0.2860	
Apr	0.25	0.9952	**	Apr	0.10	0.8544		Apr	0.28	0.9738		Apr	-0.04	0.4027	
May	0.24	0.9899	*	May	0.18	0.9742		May	0.29	0.9676		May	0.03	0.5716	
Jun	0.33	0.9990	**	Jun	0.22	0.9933	*	Jun	0.33	0.9853	*	Jun	0.02	0.5527	
Jul	0.35	0.9990	**	Jul	0.18	0.9714		Jul	0.36	0.9907	*	Jul	-0.01	0.4441	
Aug	0.32	0.9990	**	Aug	0.16	0.9639		Aug	0.38	0.9910	*	Aug	0.01	0.5226	
Sep	0.30	0.9990	**	Sep	0.17	0.9682		Sep	0.38	0.9906	*	Sep	0.05	0.6117	

Table A20. Summary of all Seascorr correlation outputs for OR18 LW_{adj}. Significant relationships with precipitation and temperature at $\alpha = 0.05$ ($\alpha = 0.01$) are highlighted in light (dark) blue for precipitation and orange for temperature; the strongest significant correlation for each season/variable combination is outlined in a thick black box.

PRISM								GHCN							
Precipitation				Temperature				Precipitation				Temperature			
End Month	*r*	NP	*p*	End Month	*r*	NP	*p*	End Month	*r*	NP	*p*	End Month	*r*	NP	*p*
1 month								1 month							
Aug_prev	-0.01	0.4687		Aug_prev	0.00	0.4926		Aug_prev	-0.32	0.0500		Aug_prev	0.09	0.7096	
Sep_prev	0.12	0.8973		Sep_prev	-0.10	0.1444		Sep_prev	-0.10	0.2920		Sep_prev	-0.39	0.0143	*
Oct_prev	0.12	0.8949		Oct_prev	-0.05	0.3125		Oct_prev	0.28	0.9472		Oct_prev	0.05	0.6324	
Nov_prev	0.26	0.9928	*	Nov_prev	-0.08	0.2356		Nov_prev	0.40	0.9877	*	Nov_prev	-0.22	0.1289	
Dec_prev	0.04	0.6496		Dec_prev	0.03	0.6229		Dec_prev	0.17	0.8683		Dec_prev	-0.15	0.2385	
Jan	0.06	0.7218		Jan	-0.02	0.4273		Jan	0.29	0.9585		Jan	-0.18	0.1851	
Feb	0.05	0.6740		Feb	0.07	0.7819		Feb	0.23	0.9026		Feb	-0.01	0.4613	
Mar	0.11	0.8710		Mar	0.25	0.9980	**	Mar	0.27	0.9470		Mar	0.19	0.8446	
Apr	0.10	0.8520		Apr	0.16	0.9450		Apr	0.28	0.9226		Apr	-0.07	0.3232	
May	0.09	0.8236		May	0.31	0.9990	**	May	-0.21	0.1160		May	0.08	0.7315	
Jun	0.27	0.9990	**	Jun	0.10	0.8281		Jun	0.06	0.6539		Jun	0.09	0.7074	
Jul	0.39	0.9990	**	Jul	-0.29	0.0010	**	Jul	0.47	0.9940	*	Jul	-0.51	0.0010	**
Aug	0.16	0.9718		Aug	-0.21	0.0093	*	Aug	0.26	0.9184		Aug	-0.05	0.3625	
Sep	-0.01	0.4497		Sep	-0.04	0.3434		Sep	0.06	0.6417		Sep	0.02	0.5365	
3 month								3 month							
Aug_prev	-0.14	0.0910		Aug_prev	-0.13	0.1042		Aug_prev	-0.29	0.0590		Aug_prev	0.04	0.5994	
Sep_prev	0.11	0.8682		Sep_prev	-0.06	0.2704		Sep_prev	-0.20	0.1863		Sep_prev	-0.13	0.2201	
Oct_prev	0.15	0.9250		Oct_prev	-0.07	0.2396		Oct_prev	-0.02	0.4421		Oct_prev	-0.16	0.1660	
Nov_prev	0.29	0.9950	*	Nov_prev	-0.10	0.1661		Nov_prev	0.34	0.9868	*	Nov_prev	-0.26	0.0954	
Dec_prev	0.22	0.9847	*	Dec_prev	-0.04	0.3242		Dec_prev	0.39	0.9858	*	Dec_prev	-0.21	0.1400	
Jan	0.18	0.9661		Jan	-0.02	0.4125		Jan	0.46	0.9906	*	Jan	-0.26	0.0803	
Feb	0.07	0.7881		Feb	0.04	0.6641		Feb	0.39	0.9845	*	Feb	-0.10	0.2883	
Mar	0.12	0.8851		Mar	0.14	0.9471		Mar	0.41	0.9953	**	Mar	0.06	0.6155	
Apr	0.13	0.9305		Apr	0.21	0.9961	**	Apr	0.39	0.9893	*	Apr	0.09	0.7226	
May	0.16	0.9754	*	May	0.33	0.9990	**	May	0.13	0.8134		May	0.10	0.7426	
Jun	0.24	0.9965	**	Jun	0.29	0.9990	**	Jun	0.02	0.5520		Jun	0.03	0.5944	
Jul	0.32	0.9990	**	Jul	0.04	0.6725		Jul	0.02	0.5660		Jul	-0.22	0.0598	
Aug	0.42	0.9990	**	Aug	-0.21	0.0127	*	Aug	0.40	0.9868	*	Aug	-0.19	0.0865	
Sep	0.23	0.9954	**	Sep	-0.28	0.0010	**	Sep	0.36	0.9648		Sep	-0.37	0.0073	*
9 month								9 month							
Aug_prev	-0.10	0.1455		Aug_prev	-0.05	0.3069		Aug_prev	-0.27	0.0918		Aug_prev	0.07	0.6230	
Sep_prev	-0.05	0.3112		Sep_prev	-0.08	0.1861		Sep_prev	-0.27	0.1080		Sep_prev	-0.03	0.4248	
Oct_prev	0.06	0.7402		Oct_prev	-0.14	0.0575		Oct_prev	-0.15	0.2056		Oct_prev	-0.05	0.3709	
Nov_prev	0.11	0.8731		Nov_prev	-0.16	0.0448		Nov_prev	-0.04	0.4044		Nov_prev	-0.14	0.1905	
Dec_prev	0.17	0.9690		Dec_prev	-0.13	0.0765		Dec_prev	0.05	0.6226		Dec_prev	-0.19	0.1086	
Jan	0.22	0.9896	*	Jan	-0.12	0.1020		Jan	0.23	0.9363		Jan	-0.21	0.1023	
Feb	0.18	0.9681		Feb	-0.06	0.2694		Feb	0.33	0.9747		Feb	-0.11	0.2598	
Mar	0.25	0.9972	**	Mar	0.05	0.7162		Mar	0.43	0.9947	*	Mar	-0.11	0.2515	
Apr	0.26	0.9976	**	Apr	0.10	0.8735		Apr	0.47	0.9977	**	Apr	-0.05	0.3647	
May	0.27	0.9990	**	May	0.15	0.9549		May	0.41	0.9926	*	May	-0.06	0.3486	
Jun	0.30	0.9990	**	Jun	0.20	0.9833	*	Jun	0.42	0.9896	*	Jun	0.02	0.5378	
Jul	0.32	0.9990	**	Jul	0.15	0.9510		Jul	0.45	0.9961	**	Jul	-0.08	0.3311	
Aug	0.27	0.9978	**	Aug	0.09	0.8375		Aug	0.38	0.9870	*	Aug	-0.06	0.3647	
Sep	0.30	0.9983	**	Sep	0.09	0.8453		Sep	0.38	0.9755	*	Sep	-0.06	0.3561	
12 month								12 month							
Aug_prev	-0.10	0.1475		Aug_prev	-0.07	0.1991		Aug_prev	-0.21	0.1485		Aug_prev	0.01	0.5405	
Sep_prev	-0.08	0.2295		Sep_prev	-0.08	0.1752		Sep_prev	-0.23	0.1500		Sep_prev	-0.05	0.3709	
Oct_prev	-0.04	0.3288		Oct_prev	-0.08	0.1657		Oct_prev	-0.17	0.2137		Oct_prev	0.02	0.5372	
Nov_prev	0.05	0.7039		Nov_prev	-0.09	0.1700		Nov_prev	-0.09	0.3054		Nov_prev	-0.01	0.4595	
Dec_prev	0.10	0.8585		Dec_prev	-0.08	0.1972		Dec_prev	0.01	0.5180		Dec_prev	-0.06	0.3725	
Jan	0.17	0.9704		Jan	-0.12	0.0992		Jan	0.14	0.8202		Jan	-0.14	0.1833	
Feb	0.13	0.9289		Feb	-0.08	0.1729		Feb	0.15	0.8237		Feb	-0.15	0.1643	
Mar	0.20	0.9863	*	Mar	-0.01	0.4703		Mar	0.23	0.9303		Mar	-0.12	0.2181	
Apr	0.23	0.9980	**	Apr	0.02	0.6241		Apr	0.33	0.9883	*	Apr	-0.09	0.2887	
May	0.22	0.9905	*	May	0.10	0.8861		May	0.31	0.9783	*	May	-0.03	0.4245	
Jun	0.32	0.9990	**	Jun	0.16	0.9625		Jun	0.37	0.9847	*	Jun	-0.03	0.4153	
Jul	0.34	0.9990	**	Jul	0.10	0.8780		Jul	0.41	0.9931	*	Jul	-0.11	0.2569	
Aug	0.35	0.9990	**	Aug	0.06	0.7451		Aug	0.45	0.9952	**	Aug	-0.12	0.2508	
Sep	0.34	0.9990	**	Sep	0.07	0.8009		Sep	0.46	0.9905	*	Sep	-0.06	0.3530	

Table A21. Summary of all Seascorr correlation outputs for WA24 TRW. Significant relationships with precipitation and temperature at $\alpha = 0.05$ ($\alpha = 0.01$) are highlighted in light (dark) blue for precipitation and orange for temperature; the strongest significant correlation for each season/variable combination is outlined in a thick black box.

PRISM								GHCN							
Precipitation				Temperature				Precipitation				Temperature			
End Month	*r*	NP	*p*	End Month	*r*	NP	*p*	End Month	*r*	NP	*p*	End Month	*r*	NP	*p*
1 month								1 month							
Aug_prev	0.21	0.9643		Aug_prev	0.12	0.9014		Aug_prev	0.30	0.9922	*	Aug_prev	0.04	0.6457	
Sep_prev	0.34	0.9990	**	Sep_prev	-0.06	0.2869		Sep_prev	0.17	0.9221		Sep_prev	-0.23	0.0290	
Oct_prev	0.23	0.9860	*	Oct_prev	-0.06	0.2527		Oct_prev	0.12	0.8717		Oct_prev	-0.20	0.0452	
Nov_prev	0.07	0.7772		Nov_prev	-0.02	0.4166		Nov_prev	0.08	0.7713		Nov_prev	-0.06	0.3235	
Dec_prev	0.16	0.9363		Dec_prev	0.05	0.6745		Dec_prev	0.23	0.9732		Dec_prev	0.10	0.8053	
Jan	0.04	0.6932		Jan	0.13	0.9041		Jan	0.07	0.7223		Jan	0.07	0.7416	
Feb	0.13	0.8878		Feb	0.15	0.9359		Feb	0.13	0.8712		Feb	-0.09	0.2214	
Mar	0.19	0.9709		Mar	0.23	0.9950	**	Mar	0.25	0.9857	*	Mar	0.09	0.7865	
Apr	0.20	0.9714		Apr	0.07	0.7760		Apr	0.22	0.9583		Apr	-0.10	0.2090	
May	0.19	0.9788	*	May	-0.08	0.1926		May	0.01	0.4917		May	-0.19	0.0679	
Jun	0.08	0.7830		Jun	-0.28	0.0042	**	Jun	0.02	0.5747		Jun	-0.38	0.0010	**
Jul	0.12	0.9165		Jul	-0.09	0.1520		Jul	0.01	0.5263		Jul	-0.21	0.0193	*
Aug	0.02	0.6039		Aug	0.00	0.4973		Aug	0.03	0.5999		Aug	-0.08	0.2445	
Sep	0.08	0.7460		Sep	0.08	0.7840		Sep	0.01	0.5116		Sep	0.10	0.7882	
3 month								3 month							
Aug_prev	0.17	0.9551		Aug_prev	0.17	0.9754	*	Aug_prev	0.25	0.9925	*	Aug_prev	0.06	0.6796	
Sep_prev	0.34	0.9990	**	Sep_prev	0.17	0.9792	*	Sep_prev	0.30	0.9934	*	Sep_prev	0.03	0.6122	
Oct_prev	0.43	0.9990	**	Oct_prev	-0.01	0.4664		Oct_prev	0.32	0.9964	**	Oct_prev	-0.21	0.0364	
Nov_prev	0.29	0.9990	**	Nov_prev	-0.12	0.1265		Nov_prev	0.18	0.9539		Nov_prev	-0.24	0.0271	
Dec_prev	0.23	0.9918	*	Dec_prev	0.01	0.5242		Dec_prev	0.22	0.9830	*	Dec_prev	-0.07	0.2714	
Jan	0.13	0.9215		Jan	0.11	0.8565		Jan	0.19	0.9588		Jan	0.06	0.6977	
Feb	0.17	0.9596		Feb	0.16	0.9416		Feb	0.23	0.9822	*	Feb	0.04	0.6448	
Mar	0.19	0.9738		Mar	0.23	0.9830	*	Mar	0.24	0.9822	*	Mar	0.03	0.6092	
Apr	0.29	0.9905	*	Apr	0.22	0.9874	*	Apr	0.34	0.9912	*	Apr	-0.05	0.3431	
May	0.33	0.9990	**	May	0.12	0.9014		May	0.30	0.9875	*	May	-0.08	0.2475	
Jun	0.27	0.9970	**	Jun	-0.13	0.0691		Jun	0.16	0.9183		Jun	-0.31	0.0083	*
Jul	0.22	0.9892	*	Jul	-0.22	0.0041	**	Jul	0.02	0.5623		Jul	-0.36	0.0010	**
Aug	0.12	0.9136		Aug	-0.19	0.0218	*	Aug	0.04	0.6640		Aug	-0.29	0.0058	*
Sep	0.13	0.8978		Sep	0.01	0.5628		Sep	0.03	0.5844		Sep	-0.08	0.2420	
9 month								9 month							
Aug_prev	0.24	0.9875	*	Aug_prev	0.05	0.7295		Aug_prev	0.31	0.9931	*	Aug_prev	0.00	0.4641	
Sep_prev	0.35	0.9990	**	Sep_prev	0.00	0.5318		Sep_prev	0.36	0.9977	**	Sep_prev	-0.10	0.1869	
Oct_prev	0.38	0.9988	**	Oct_prev	-0.08	0.1652		Oct_prev	0.31	0.9899	*	Oct_prev	-0.23	0.0294	
Nov_prev	0.29	0.9956	**	Nov_prev	-0.10	0.1195			0.27	0.9923	*	Nov_prev	-0.26	0.0156	*
Dec_prev	0.35	0.9990	**	Dec_prev	0.00	0.5094		Dec_prev	0.32	0.9979	**	Dec_prev	-0.19	0.0669	
Jan	0.38	0.9990	**	Jan	0.05	0.6807		Jan	0.32	0.9982	**	Jan	-0.11	0.2177	
Feb	0.38	0.9990	**	Feb	0.13	0.9104		Feb	0.33	0.9973	**	Feb	-0.06	0.3227	
Mar	0.41	0.9990	**	Mar	0.17	0.9655		Mar	0.39	0.9990	**	Mar	0.00	0.5069	
Apr	0.43	0.9990	**	Apr	0.16	0.9393		Apr	0.42	0.9990	**	Apr	-0.03	0.3967	
May	0.42	0.9990	**	May	0.13	0.8968		May	0.35	0.9970	**	May	-0.07	0.2841	
Jun	0.37	0.9990	**	Jun	0.10	0.8462		Jun	0.33	0.9957	**	Jun	-0.11	0.1853	
Jul	0.34	0.9989	**	Jul	0.09	0.8291		Jul	0.33	0.9948	*	Jul	-0.10	0.2069	
Aug	0.35	0.9990	**	Aug	0.09	0.8432		Aug	0.35	0.9983	**	Aug	-0.07	0.2680	
Sep	0.34	0.9990	**	Sep	0.11	0.8711		Sep	0.29	0.9880	*	Sep	-0.09	0.2141	
12 month								12 month							
Aug_prev	0.10	0.8202		Aug_prev	0.08	0.7889		Aug_prev	0.20	0.9566		Aug_prev	0.07	0.7102	
Sep_prev	0.22	0.9758	*	Sep_prev	0.01	0.5595		Sep_prev	0.30	0.9980	**	Sep_prev	-0.01	0.4284	
Oct_prev	0.33	0.9990	**	Oct_prev	0.02	0.5869		Oct_prev	0.35	0.9968	**	Oct_prev	-0.05	0.3112	
Nov_prev	0.36	0.9984	**	Nov_prev	-0.02	0.4055		Nov_prev	0.37	0.9983	**	Nov_prev	-0.11	0.1520	
Dec_prev	0.40	0.9990	**	Dec_prev	0.00	0.4950		Dec_prev	0.39	0.9990	**	Dec_prev	-0.15	0.1020	
Jan	0.37	0.9990	**	Jan	-0.01	0.4823		Jan	0.35	0.9974	**	Jan	-0.16	0.1089	
Feb	0.35	0.9990	**	Feb	0.06	0.7243		Feb	0.33	0.9973	**	Feb	-0.16	0.1161	
Mar	0.41	0.9990	**	Mar	0.13	0.9190		Mar	0.38	0.9984	**	Mar	-0.09	0.2370	
Apr	0.44	0.9990	**	Apr	0.15	0.9378		Apr	0.41	0.9990	**	Apr	-0.07	0.2941	
May	0.46	0.9990	**	May	0.18	0.9685		May	0.40	0.9990	**	May	-0.05	0.3448	
Jun	0.46	0.9990	**	Jun	0.12	0.8950		Jun	0.40	0.9990	**	Jun	-0.09	0.2265	
Jul	0.46	0.9990	**	Jul	0.06	0.7172		Jul	0.39	0.9990	**	Jul	-0.14	0.1170	
Aug	0.43	0.9990	**	Aug	0.05	0.6929		Aug	0.35	0.9976	**	Aug	-0.16	0.0913	
Sep	0.39	0.9989	**	Sep	0.10	0.8407		Sep	0.34	0.9964	**	Sep	-0.09	0.2209	

Table A22. Summary of all Seascorr correlation outputs for WA24 EW. Significant relationships with precipitation and temperature at $\alpha = 0.05$ ($\alpha = 0.01$) are highlighted in light (dark) blue for precipitation and orange for temperature; the strongest significant correlation for each season/variable combination is outlined in a thick black box.

PRISM								GHCN							
Precipitation				Temperature				Precipitation				Temperature			
End Month	*r*	NP	*p*	End Month	*r*	NP	*p*	End Month	*r*	NP	*p*	End Month	*r*	NP	*p*
1 month								1 month							
Aug_prev	0.25	0.9965	**	Aug_prev	0.10	0.8237		Aug_prev	0.34	0.9982	**	Aug_prev	0.05	0.7074	
Sep_prev	0.32	0.9964	**	Sep_prev	-0.08	0.2040		Sep_prev	0.14	0.8759		Sep_prev	-0.24	0.0270	
Oct_prev	0.18	0.9671		Oct_prev	-0.10	0.1668		Oct_prev	0.05	0.6858		Oct_prev	-0.22	0.0310	
Nov_prev	-0.01	0.4290		Nov_prev	0.03	0.6270		Nov_prev	0.00	0.5232		Nov_prev	-0.01	0.4654	
Dec_prev	0.11	0.8567		Dec_prev	0.08	0.8148		Dec_prev	0.15	0.8890		Dec_prev	0.13	0.8710	
Jan	0.03	0.6065		Jan	0.18	0.9708		Jan	0.07	0.7004		Jan	0.16	0.9170	
Feb	0.12	0.8556		Feb	0.15	0.9425		Feb	0.12	0.8443		Feb	-0.05	0.3441	
Mar	0.14	0.9163		Mar	0.22	0.9941	*	Mar	0.24	0.9736		Mar	0.09	0.8167	
Apr	0.19	0.9726		Apr	0.07	0.7979		Apr	0.21	0.9552		Apr	-0.13	0.1213	
May	0.19	0.9683		May	-0.11	0.1485		May	0.02	0.5887		May	-0.21	0.0394	
Jun	0.06	0.7169		Jun	-0.30	0.0010	**	Jun	-0.01	0.4561		Jun	-0.38	0.0010	**
Jul	0.10	0.8667		Jul	-0.01	0.4347		Jul	0.04	0.6580		Jul	-0.10	0.1755	
Aug	-0.01	0.4752		Aug	0.03	0.6587		Aug	0.01	0.5250		Aug	-0.04	0.3349	
Sep	0.10	0.8069		Sep	0.08	0.7980		Sep	0.02	0.5591		Sep	0.09	0.7449	
3 month								3 month							
Aug_prev	0.21	0.9826	*	Aug_prev	0.20	0.9854	*	Aug_prev	0.30	0.9990	**	Aug_prev	0.09	0.7991	
Sep_prev	0.35	0.9990	**	Sep_prev	0.15	0.9543		Sep_prev	0.31	0.9980	**	Sep_prev	0.03	0.6228	
Oct_prev	0.40	0.9990	**	Oct_prev	-0.06	0.2600		Oct_prev	0.28	0.9966	**	Oct_prev	-0.22	0.0422	
Nov_prev	0.21	0.9757	*	Nov_prev	-0.12	0.1034		Nov_prev	0.09	0.8125		Nov_prev	-0.23	0.0385	
Dec_prev	0.13	0.9082		Dec_prev	0.03	0.6328		Dec_prev	0.11	0.8302		Dec_prev	-0.03	0.4342	
Jan	0.05	0.7116		Jan	0.18	0.9723		Jan	0.11	0.8332		Jan	0.16	0.9204	
Feb	0.13	0.8769		Feb	0.20	0.9829	*	Feb	0.18	0.9379		Feb	0.12	0.8477	
Mar	0.15	0.9228		Mar	0.25	0.9939	*	Mar	0.23	0.9716		Mar	0.10	0.8290	
Apr	0.24	0.9820	*	Apr	0.21	0.9886	*	Apr	0.31	0.9943	*	Apr	-0.03	0.3830	
May	0.29	0.9970	**	May	0.10	0.8674		May	0.29	0.9912	*	May	-0.11	0.1581	
Jun	0.25	0.9951	**	Jun	-0.15	0.0503		Jun	0.14	0.9106		Jun	-0.34	0.0041	**
Jul	0.20	0.9861	*	Jul	-0.20	0.0099	*	Jul	0.02	0.6088		Jul	-0.33	0.0049	**
Aug	0.08	0.7839		Aug	-0.14	0.0651		Aug	0.02	0.5676		Aug	-0.23	0.0234	*
Sep	0.11	0.8519		Sep	0.06	0.7701		Sep	0.03	0.6233		Sep	-0.02	0.4112	
9 month								9 month							
Aug_prev	0.26	0.9935	*	Aug_prev	0.05	0.7012		Aug_prev	0.35	0.9990	**	Aug_prev	0.01	0.5353	
Sep_prev	0.36	0.9987	**	Sep_prev	-0.01	0.4657		Sep_prev	0.39	0.9990	**	Sep_prev	-0.09	0.1976	
Oct_prev	0.34	0.9980	**	Oct_prev	-0.10	0.1383		Oct_prev	0.28	0.9917	*	Oct_prev	-0.22	0.0352	
Nov_prev	0.24	0.9888	*	Nov_prev	-0.10	0.1249		Nov_prev	0.22	0.9722		Nov_prev	-0.24	0.0216	*
Dec_prev	0.28	0.9952	**	Dec_prev	0.01	0.5282		Dec_prev	0.23	0.9781	*	Dec_prev	-0.15	0.1209	
Jan	0.30	0.9983	**	Jan	0.08	0.7927		Jan	0.24	0.9852	*	Jan	-0.04	0.3868	
Feb	0.31	0.9973	**	Feb	0.15	0.9358		Feb	0.26	0.9908	*	Feb	0.01	0.5520	
Mar	0.32	0.9985	**	Mar	0.18	0.9689		Mar	0.31	0.9973	**	Mar	0.05	0.6876	
Apr	0.35	0.9990	**	Apr	0.16	0.9488		Apr	0.34	0.9990	**	Apr	0.02	0.5738	
May	0.33	0.9984	**	May	0.14	0.9381		May	0.27	0.9931	*	May	-0.02	0.4266	
Jun	0.28	0.9963	**	Jun	0.11	0.9057		Jun	0.24	0.9878	*	Jun	-0.05	0.3191	
Jul	0.25	0.9907	*	Jul	0.13	0.9291		Jul	0.26	0.9879	*	Jul	-0.02	0.4290	
Aug	0.28	0.9956	**	Aug	0.12	0.9326		Aug	0.30	0.9956	**	Aug	-0.01	0.4601	
Sep	0.30	0.9969	**	Sep	0.13	0.9427		Sep	0.27	0.9892	*	Sep	-0.03	0.3751	
12 month								12 month							
Aug_prev	0.12	0.8874		Aug_prev	0.08	0.8257		Aug_prev	0.23	0.9761	*	Aug_prev	0.09	0.7764	
Sep_prev	0.25	0.9873	*	Sep_prev	0.01	0.5421		Sep_prev	0.33	0.9990	**	Sep_prev	0.00	0.5418	
Oct_prev	0.34	0.9980	**	Oct_prev	0.00	0.5036		Oct_prev	0.37	0.9990	**	Oct_prev	-0.05	0.3601	
Nov_prev	0.33	0.9982	**	Nov_prev	-0.03	0.3917		Nov_prev	0.35	0.9990	**	Nov_prev	-0.10	0.1917	
Dec_prev	0.35	0.9982	**	Dec_prev	-0.01	0.4706		Dec_prev	0.34	0.9990	**	Dec_prev	-0.13	0.1429	
Jan	0.30	0.9917	*	Jan	0.01	0.5409		Jan	0.28	0.9922	*	Jan	-0.10	0.2146	
Feb	0.28	0.9920	*	Feb	0.07	0.8045		Feb	0.27	0.9893	*	Feb	-0.09	0.2376	
Mar	0.33	0.9974	**	Mar	0.15	0.9373		Mar	0.31	0.9955	**	Mar	-0.02	0.4336	
Apr	0.36	0.9986	**	Apr	0.16	0.9489		Apr	0.34	0.9970	**	Apr	-0.01	0.4665	
May	0.39	0.9988	**	May	0.18	0.9680		May	0.34	0.9971	**	May	0.00	0.5129	
Jun	0.37	0.9990	**	Jun	0.12	0.9099		Jun	0.32	0.9990	**	Jun	-0.05	0.3265	
Jul	0.38	0.9990	**	Jul	0.07	0.7770		Jul	0.32	0.9990	**	Jul	-0.08	0.2256	
Aug	0.33	0.9990	**	Aug	0.07	0.8057		Aug	0.26	0.9915	*	Aug	-0.09	0.1945	
Sep	0.30	0.9967	**	Sep	0.12	0.9199		Sep	0.25	0.9875	*	Sep	-0.03	0.3813	

Table A23. Summary of all Seascorr correlation outputs for WA24 LW. Significant relationships with precipitation and temperature at $\alpha = 0.05$ ($\alpha = 0.01$) are highlighted in light (dark) blue for precipitation and orange for temperature; the strongest significant correlation for each season/variable combination is outlined in a thick black box.

PRISM								GHCN							
Precipitation				Temperature				Precipitation				Temperature			
End Month	*r*	NP	*p*	End Month	*r*	NP	*p*	End Month	*r*	NP	*p*	End Month	*r*	NP	*p*
1 month								1 month							
Aug_prev	0.05	0.6583		Aug_prev	0.10	0.8463		Aug_prev	0.14	0.8580		Aug_prev	0.00	0.4591	
Sep_prev	0.25	0.9852	*	Sep_prev	-0.01	0.4262		Sep_prev	0.19	0.9524		Sep_prev	-0.11	0.1624	
Oct_prev	0.31	0.9983	**	Oct_prev	0.07	0.7624		Oct_prev	0.27	0.9873	*	Oct_prev	-0.05	0.2982	
Nov_prev	0.24	0.9948	*	Nov_prev	-0.19	0.0379		Nov_prev	0.25	0.9887	*	Nov_prev	-0.22	0.0273	
Dec_prev	0.34	0.9989	**	Dec_prev	-0.05	0.3024		Dec_prev	0.42	0.9990	**	Dec_prev	0.00	0.4911	
Jan	0.19	0.9765	*	Jan	-0.08	0.2317		Jan	0.12	0.8815		Jan	-0.14	0.0775	
Feb	0.15	0.9232		Feb	0.07	0.7264		Feb	0.09	0.7962		Feb	-0.16	0.0693	
Mar	0.22	0.9829	*	Mar	0.16	0.9509		Mar	0.14	0.8865		Mar	0.00	0.4827	
Apr	0.23	0.9905	*	Apr	0.12	0.8881		Apr	0.26	0.9785	*	Apr	0.05	0.6930	
May	0.14	0.9260		May	0.05	0.7160		May	0.00	0.5242		May	-0.02	0.4441	
Jun	0.15	0.9274		Jun	-0.10	0.1555		Jun	0.11	0.7917		Jun	-0.23	0.0126	*
Jul	0.21	0.9858	*	Jul	-0.28	0.0011	**	Jul	0.04	0.6033		Jul	-0.44	0.0010	**
Aug	0.10	0.8525		Aug	-0.16	0.0503		Aug	0.08	0.7588		Aug	-0.20	0.0317	
Sep	-0.01	0.4628		Sep	0.02	0.5678		Sep	-0.09	0.2125		Sep	0.05	0.6845	
3 month								3 month							
Aug_prev	-0.03	0.3564		Aug_prev	0.06	0.7463		Aug_prev	0.06	0.7221		Aug_prev	0.04	0.6355	
Sep_prev	0.19	0.9763	*	Sep_prev	0.12	0.9109		Sep_prev	0.20	0.9594		Sep_prev	0.06	0.7062	
Oct_prev	0.38	0.9990	**	Oct_prev	0.11	0.8707		Oct_prev	0.36	0.9974	**	Oct_prev	-0.08	0.2542	
Nov_prev	0.40	0.9990	**	Nov_prev	-0.10	0.1843		Nov_prev	0.37	0.9968	**	Nov_prev	-0.22	0.0239	*
Dec_prev	0.45	0.9990	**	Dec_prev	-0.07	0.2486		Dec_prev	0.47	0.9990	**	Dec_prev	-0.18	0.0637	
Jan	0.39	0.9990	**	Jan	-0.13	0.1059		Jan	0.40	0.9990	**	Jan	-0.22	0.0319	
Feb	0.35	0.9990	**	Feb	-0.02	0.4114		Feb	0.36	0.9990	**	Feb	-0.16	0.0946	
Mar	0.30	0.9990	**	Mar	0.07	0.7404		Mar	0.20	0.9597		Mar	-0.15	0.0905	
Apr	0.32	0.9990	**	Apr	0.16	0.9351		Apr	0.27	0.9797	*	Apr	-0.08	0.2493	
May	0.33	0.9988	**	May	0.16	0.9490		May	0.24	0.9778	*	May	0.01	0.5632	
Jun	0.29	0.9951	**	Jun	0.03	0.6611		Jun	0.23	0.9668		Jun	-0.10	0.1694	
Jul	0.26	0.9959	**	Jul	-0.16	0.0323		Jul	0.09	0.7511		Jul	-0.32	0.0025	**
Aug	0.26	0.9970	**	Aug	-0.27	0.0012	**	Aug	0.14	0.9041		Aug	-0.38	0.0010	**
Sep	0.15	0.9265		Sep	-0.20	0.0108	*	Sep	0.01	0.5182		Sep	-0.29	0.0039	**
9 month								9 month							
Aug_prev	-0.01	0.4585		Aug_prev	0.01	0.5313		Aug_prev	0.01	0.5407		Aug_prev	0.01	0.5338	
Sep_prev	0.11	0.8277		Sep_prev	-0.01	0.4502		Sep_prev	0.10	0.8264		Sep_prev	-0.03	0.3916	
Oct_prev	0.24	0.9922	*	Oct_prev	-0.05	0.3190		Oct_prev	0.21	0.9727		Oct_prev	-0.10	0.1943	
Nov_prev	0.25	0.9930	*	Nov_prev	-0.09	0.1780		Nov_prev	0.26	0.9846	*	Nov_prev	-0.17	0.0589	
Dec_prev	0.38	0.9990	**	Dec_prev	0.00	0.4873		Dec_prev	0.45	0.9990	**	Dec_prev	-0.14	0.1110	
Jan	0.47	0.9990	**	Jan	-0.02	0.4332		Jan	0.49	0.9990	**	Jan	-0.20	0.0412	
Feb	0.49	0.9990	**	Feb	0.02	0.5912		Feb	0.46	0.9990	**	Feb	-0.17	0.0734	
Mar	0.57	0.9990	**	Mar	0.06	0.7355		Mar	0.50	0.9990	**	Mar	-0.13	0.1118	
Apr	0.59	0.9990	**	Apr	0.08	0.7672		Apr	0.55	0.9990	**	Apr	-0.15	0.0875	
May	0.58	0.9990	**	May	0.07	0.7453		May	0.51	0.9990	**	May	-0.14	0.0995	
Jun	0.57	0.9990	**	Jun	0.05	0.6637		Jun	0.50	0.9990	**	Jun	-0.20	0.0437	
Jul	0.54	0.9990	**	Jul	-0.03	0.4177		Jul	0.47	0.9990	**	Jul	-0.26	0.0124	*
Aug	0.52	0.9990	**	Aug	-0.03	0.3816		Aug	0.46	0.9990	**	Aug	-0.20	0.0375	
Sep	0.44	0.9990	**	Sep	-0.01	0.4594		Sep	0.28	0.9979	**	Sep	-0.21	0.0189	*
12 month								12 month							
Aug_prev	-0.09	0.2100		Aug_prev	0.02	0.5664		Aug_prev	-0.03	0.4206		Aug_prev	0.05	0.6714	
Sep_prev	0.01	0.5148		Sep_prev	-0.02	0.4158		Sep_prev	0.05	0.6487		Sep_prev	0.00	0.4945	
Oct_prev	0.13	0.8495		Oct_prev	0.01	0.5090		Oct_prev	0.12	0.8461		Oct_prev	-0.01	0.4614	
Nov_prev	0.24	0.9912	*	Nov_prev	-0.05	0.3381		Nov_prev	0.23	0.9855	*	Nov_prev	-0.07	0.2727	
Dec_prev	0.35	0.9988	**	Dec_prev	-0.02	0.4214		Dec_prev	0.38	0.9988	**	Dec_prev	-0.10	0.1888	
Jan	0.42	0.9990	**	Jan	-0.07	0.2594		Jan	0.43	0.9990	**	Jan	-0.18	0.0550	
Feb	0.41	0.9990	**	Feb	-0.01	0.4619		Feb	0.40	0.9990	**	Feb	-0.20	0.0471	
Mar	0.49	0.9990	**	Mar	0.05	0.6642		Mar	0.46	0.9990	**	Mar	-0.18	0.0680	
Apr	0.54	0.9990	**	Apr	0.08	0.7808		Apr	0.51	0.9990	**	Apr	-0.14	0.0990	
May	0.55	0.9990	**	May	0.11	0.8548		May	0.50	0.9990	**	May	-0.10	0.1704	
Jun	0.59	0.9990	**	Jun	0.09	0.8232		Jun	0.52	0.9990	**	Jun	-0.13	0.1017	
Jul	0.62	0.9990	**	Jul	-0.01	0.4850		Jul	0.53	0.9990	**	Jul	-0.24	0.0170	*
Aug	0.61	0.9990	**	Aug	-0.05	0.3369		Aug	0.52	0.9990	**	Aug	-0.27	0.0078	*
Sep	0.59	0.9990	**	Sep	-0.02	0.4373		Sep	0.50	0.9990	**	Sep	-0.23	0.0172	*

Table A24. Summary of all Seascorr correlation outputs for WA24 LW_{adj}. Significant relationships with precipitation and temperature at $\alpha = 0.05$ ($\alpha = 0.01$) are highlighted in light (dark) blue for precipitation and orange for temperature; the strongest significant correlation for each season/variable combination is outlined in a thick black box.

PRISM								GHCN							
Precipitation				Temperature				Precipitation				Temperature			
End Month	*r*	NP	*p*	End Month	*r*	NP	*p*	End Month	*r*	NP	*p*	End Month	*r*	NP	*p*
1 month								1 month							
Aug_prev	-0.12	0.1042		Aug_prev	0.02	0.5128		Aug_prev	-0.07	0.2521		Aug_prev	-0.04	0.3645	
Sep_prev	0.09	0.8170		Sep_prev	0.05	0.6994		Sep_prev	0.13	0.9000		Sep_prev	0.04	0.6416	
Oct_prev	0.27	0.9905	*	Oct_prev	0.15	0.9265		Oct_prev	0.28	0.9867		Oct_prev	0.10	0.8100	
Nov_prev	0.30	0.9990	**	Nov_prev	-0.26	0.0065	*	Nov_prev	0.30	0.9913	*	Nov_prev	-0.26	0.0108	*
Dec_prev	0.34	0.9990	**	Dec_prev	-0.14	0.1065		Dec_prev	0.41	0.9990	*	Dec_prev	-0.09	0.2423	
Jan	0.21	0.9884	*	Jan	-0.19	0.0353		Jan	0.10	0.8387	**	Jan	-0.28	0.0043	**
Feb	0.08	0.7928		Feb	-0.02	0.4064		Feb	0.03	0.5864		Feb	-0.16	0.0837	
Mar	0.12	0.8887		Mar	0.04	0.6465		Mar	0.00	0.5140		Mar	-0.06	0.3025	
Apr	0.15	0.9379		Apr	0.11	0.8457		Apr	0.17	0.9253		Apr	0.15	0.9170	
May	0.05	0.6550		May	0.17	0.9616		May	-0.01	0.4715		May	0.12	0.8963	
Jun	0.13	0.8756		Jun	0.10	0.8286		Jun	0.14	0.8688		Jun	-0.01	0.4568	
Jul	0.18	0.9557		Jul	-0.32	0.0010	**	Jul	0.03	0.5810		Jul	-0.46	0.0010	**
Aug	0.11	0.9076		Aug	-0.19	0.0188	*	Aug	0.09	0.7784		Aug	-0.21	0.0308	
Sep	-0.08	0.1709		Sep	-0.03	0.3706		Sep	-0.12	0.1360		Sep	-0.01	0.4706	
3 month								3 month							
Aug_prev	-0.20	0.0245	*	Aug_prev	-0.07	0.2338		Aug_prev	-0.14	0.0857		Aug_prev	-0.02	0.4428	
Sep_prev	-0.03	0.3771		Sep_prev	0.04	0.6694		Sep_prev	0.02	0.5747		Sep_prev	0.06	0.6965	
Oct_prev	0.20	0.9779	*	Oct_prev	0.16	0.9245		Oct_prev	0.25	0.9660		Oct_prev	0.06	0.6966	
Nov_prev	0.35	0.9990	**	Nov_prev	-0.02	0.4488		Nov_prev	0.38	0.9984	**	Nov_prev	-0.09	0.2200	
Dec_prev	0.46	0.9990	**	Dec_prev	-0.11	0.1464		Dec_prev	0.49	0.9990	**	Dec_prev	-0.20	0.0557	
Jan	0.44	0.9990	**	Jan	-0.29	0.0048	**	Jan	0.40	0.9990	**	Jan	-0.39	0.0016	**
Feb	0.33	0.9990	**	Feb	-0.17	0.0645		Feb	0.30	0.9984	**	Feb	-0.28	0.0123	*
Mar	0.23	0.9951	**	Mar	-0.08	0.2049		Mar	0.08	0.7890		Mar	-0.25	0.0162	*
Apr	0.19	0.9862	*	Apr	0.04	0.6470		Apr	0.10	0.8495		Apr	-0.07	0.2856	
May	0.18	0.9643		May	0.14	0.9257		May	0.09	0.7886		May	0.09	0.8199	
Jun	0.17	0.9375		Jun	0.19	0.9685		Jun	0.18	0.9148		Jun	0.12	0.8797	
Jul	0.17	0.9334		Jul	-0.02	0.4159		Jul	0.09	0.7558		Jul	-0.16	0.0646	
Aug	0.23	0.9919	*	Aug	-0.20	0.0197	*	Aug	0.16	0.9441		Aug	-0.30	0.0037	**
Sep	0.09	0.8270		Sep	-0.26	0.0042	**	Sep	-0.02	0.4199		Sep	-0.34	0.0019	**
9 month								9 month							
Aug_prev	-0.21	0.0169	*	Aug_prev	-0.02	0.4390		Aug_prev	-0.23	0.0236	*	Aug_prev	0.01	0.5141	
Sep_prev	-0.14	0.0615		Sep_prev	-0.01	0.4363		Sep_prev	-0.14	0.0763		Sep_prev	0.02	0.5628	
Oct_prev	0.04	0.6603		Oct_prev	-0.01	0.4749		Oct_prev	0.05	0.7073		Oct_prev	0.03	0.6201	
Nov_prev	0.12	0.9013		Nov_prev	-0.04	0.3180		Nov_prev	0.16	0.9232		Nov_prev	-0.04	0.3704	
Dec_prev	0.25	0.9972	**	Dec_prev	-0.01	0.4522		Dec_prev	0.38	0.9986		Dec_prev	-0.06	0.3191	
Jan	0.35	0.9990	**	Jan	-0.07	0.2638		Jan	0.42	0.9990	**	Jan	-0.20	0.0310	
Feb	0.37	0.9990	**	Feb	-0.07	0.2526		Feb	0.37	0.9990	**	Feb	-0.21	0.0235	*
Mar	0.45	0.9990	**	Mar	-0.06	0.2599		Mar	0.39	0.9990	**	Mar	-0.19	0.0390	
Apr	0.46	0.9990	**	Apr	-0.03	0.3766		Apr	0.42	0.9990	**	Apr	-0.18	0.0488	
May	0.46	0.9990	**	May	0.00	0.5088		May	0.42	0.9990	**	May	-0.15	0.1025	
Jun	0.49	0.9990	**	Jun	-0.02	0.4592		Jun	0.43	0.9990	**	Jun	-0.19	0.0525	
Jul	0.46	0.9990	**	Jul	-0.11	0.1434		Jul	0.38	0.9990	**	Jul	-0.28	0.0112	*
Aug	0.41	0.9990	**	Aug	-0.11	0.1532		Aug	0.35	0.9990	**	Aug	-0.22	0.0239	*
Sep	0.29	0.9990	**	Sep	-0.08	0.2292		Sep	0.15	0.9191		Sep	-0.22	0.0194	*
12 month								12 month							
Aug_prev	-0.20	0.0403		Aug_prev	-0.03	0.3893		Aug_prev	-0.19	0.0575		Aug_prev	0.00	0.4939	
Sep_prev	-0.17	0.0781		Sep_prev	-0.03	0.3884		Sep_prev	-0.17	0.0788		Sep_prev	0.00	0.4805	
Oct_prev	-0.08	0.1930		Oct_prev	0.01	0.5254		Oct_prev	-0.11	0.1628		Oct_prev	0.02	0.5627	
Nov_prev	0.05	0.7076		Nov_prev	-0.03	0.3768		Nov_prev	0.04	0.6337		Nov_prev	-0.02	0.4165	
Dec_prev	0.17	0.9643		Dec_prev	-0.02	0.4100		Dec_prev	0.22	0.9819	*	Dec_prev	-0.03	0.3713	
Jan	0.29	0.9990	**	Jan	-0.08	0.2067		Jan	0.32	0.9970	**	Jan	-0.14	0.1027	
Feb	0.28	0.9963	**	Feb	-0.06	0.2583		Feb	0.30	0.9917	*	Feb	-0.16	0.0700	
Mar	0.34	0.9990	**	Mar	-0.05	0.2894		Mar	0.34	0.9978	**	Mar	-0.18	0.0429	
Apr	0.38	0.9990	**	Apr	-0.03	0.4078		Apr	0.38	0.9990	**	Apr	-0.15	0.0886	
May	0.38	0.9990	**	May	0.01	0.5406		May	0.36	0.9990	**	May	-0.11	0.1550	
Jun	0.44	0.9990	**	Jun	0.03	0.6186		Jun	0.41	0.9990	**	Jun	-0.11	0.1643	
Jul	0.47	0.9990	**	Jul	-0.05	0.3356		Jul	0.41	0.9990	**	Jul	-0.21	0.0290	
Aug	0.50	0.9990	**	Aug	-0.09	0.1997		Aug	0.45	0.9990	**	Aug	-0.24	0.0180	*
Sep	0.49	0.9990	**	Sep	-0.10	0.1759		Sep	0.42	0.9990	**	Sep	-0.24	0.0181	*

REFERENCES

Abatzoglou, J. T., Rupp, D. E., & Mote, P. W. (2014). Seasonal climate variability and change in the Pacific Northwest of the United States. *Journal of Climate*, *27*(5), 2125–2142, doi:10.1175/JCLI-D-13-00218.1.

Akers, P. D., Welker, J. M., & Brook, G. A. (2017). Reassessing the role of temperature in precipitation oxygen isotopes across the eastern and central United States through weekly precipitation-day data. *Water Resources Research*, *53*(9), 7644–7661, doi:10.1002/2017WR020569.

Allen, S. T., Kirchner, J. W., Braun, S., Siegwolf, R. T. W., & Goldsmith, G. R. (2019). Seasonal origins of soil water used by trees. *Hydrology and Earth System Sciences*, *23*(2), 1199–1210, doi:10.5194/hess-23-1199-2019.

An, W., Liu, X., Leavitt, StevenW., Ren, J., Sun, W., Wang, W., Wang, Y., Xu, G., Chen, T., & Qin, D. (2012). Specific climatic signals recorded in earlywood and latewood $\delta^{18}O$ of tree rings in southwestern China. *Tellus B: Chemical and Physical Meteorology*, *64*(1), 18703, doi:10.3402/tellusb.v64i0.18703.

Anderson, W. T., Bernasconi, S. M., McKenzie, J. A., & Saurer, M. (1998). Oxygen and carbon isotopic record of climatic variability in tree ring cellulose (*Picea abies*): An example from central Switzerland (1913-1995). *Journal of Geophysical Research: Atmospheres*, *103*(D24), 31625–31636, doi:10.1029/1998JD200040.

Anderson, W. T., Bernasconi, S. M., McKenzie, J. A., Saurer, M., & Schweingruber, F. (2002). Model evaluation for reconstructing the oxygen isotopic composition in precipitation from tree ring cellulose over the last century. *Chemical Geology*, *182*(2–4), 121–137, doi:10.1016/S0009-2541(01)00285-6.

Andreu-Hayles, L., Ummenhofer, C. C., Barriendos, M., Schleser, G. H., Helle, G., Leuenberger, M., Gutiérrez, E., & Cook, E. R. (2017). 400 Years of summer hydroclimate from stable isotopes in Iberian trees. *Climate Dynamics*, *49*(1–2), 143–161, doi:10.1007/s00382-016-3332-z.

Araguás-Araguás, L., Froehlich, K., & Rozanski, K. (1998). Stable isotope composition of precipitation over southeast Asia. *Journal of Geophysical Research: Atmospheres*, *103*(D22), 28721–28742, doi:10.1029/98JD02582.

Bailey, H. L., Kaufman, D. S., Henderson, A. C. G., & Leng, M. J. (2015). Synoptic scale controls on the $\delta^{18}O$ in precipitation across Beringia. *Geophysical Research Letters*, *42*(11), 4608–4616, doi:10.1002/2015GL063983.

Bailey, H. L., Klein, E. S., & Welker, J. M. (2019). Synoptic and mesoscale mechanisms drive winter precipitation $\delta^{18}O/\delta^{2}H$ in South-Central Alaska. *Journal of Geophysical Research: Atmospheres*, *124*(7), 4252–4266, doi:10.1029/2018JD030050.

Bale, R. J., Robertson, I., Leavitt, S. W., Loader, N. J., Harlan, T. P., Gagen, M., Young, G. H. F., Csank, A. Z., Froyd, C. A., & McCarroll, D. (2010). Temporal stability in bristlecone pine tree-ring stable oxygen isotope chronologies over the last two centuries. *The Holocene*, *20*(1), 3–6, doi:10.1177/0959683609348867.

Balk, Gene. (2021, June 25). Seattle is a lot more air-conditioned than it used to be. *Seattle Times*. <https://www.seattletimes.com/seattle-news/data/seattle-is-a-lot-more-air-conditioned-than-it-used-to-be/>

Bansal, S., Brodie, L., Stanton, S., Waddell, K., Palmer, M., Christensen, G., Kuegler, O., Chase, J., Thompson, J., Jovan, S., Gray, A., & Todd, M. (2017). *Oregon's forest resources, 2001–2010: Ten-year Forest Inventory and Analysis report* (PNW-GTR-958). U.S. Department of Agriculture, Forest Service, Pacific Northwest Research Station, doi:10.2737/PNW-GTR-958.

Bartos, M. D., & Chester, M. V. (2015). Impacts of climate change on electric power supply in the Western United States. *Nature Climate Change*, *5*(8), 748–752, doi:10.1038/nclimate2648.

Bazzano, A., Bertinetti, S., Ardini, F., Cappelletti, D., & Grotti, M. (2021). Potential source areas for atmospheric lead reaching Ny-Ålesund from 2010 to 2018. *Atmosphere*, *12*(3), 388, doi:10.3390/atmos12030388.

Berkelhammer, M. B., & Stott, L. D. (2008). Recent and dramatic changes in Pacific storm trajectories recorded in $\delta^{18}O$ from Bristlecone Pine tree ring cellulose. *Geochemistry, Geophysics, Geosystems*, *9*(4), doi:10.1029/2007GC001803.

Berkelhammer, M., & Stott, L. (2011). Correction to "Recent and dramatic changes in Pacific storm trajectories as recorded in the $\delta^{18}O$ of Bristlecone Pine tree ring cellulose." *Geochemistry, Geophysics, Geosystems*, *12*(9), doi:10.1029/2011GC003765.

Berkelhammer, M., & Stott, L. D. (2012). Secular temperature trends for the southern Rocky Mountains over the last five centuries. *Geophysical Research Letters*, *39*(17), doi:10.1029/2012GL052447.

Berkelhammer, M., Still, C. J., Ritter, F., Winnick, M., Anderson, L., Carroll, R., Carbone, M., & Williams, K. H. (2020). Persistence and plasticity in conifer water-use strategies. *Journal of Geophysical Research: Biogeosciences*, *125*(2), doi:10.1029/2018JG004845.

Birks, S. J., & Edwards, T. W. D. (2009). Atmospheric circulation controls on precipitation isotope–climate relations in western Canada. *Tellus B: Chemical and Physical Meteorology*, *61*(3), 566–576, doi:10.1111/j.1600-0889.2009.00423.x.

Bonneville Power Administration. (2019). *Value of the River*. <https://www.bpa.gov/publicinvolvement/communityeducation/valueoftheriver/pages/hydropower>

Bowen, G. J. (2008). Spatial analysis of the intra-annual variation of precipitation isotope ratios and its climatological corollaries. *Journal of Geophysical Research: Atmospheres*, *113*(D5), doi:10.1029/2007JD009295.

Brewer, P. W. (2014). Data management in dendroarchaeology using Tellervo. *Radiocarbon*, *56*(4), S79–S83, doi:10.2458/azu_rc.56.18320.

Briffa, K. R., Jones, P. D., & Schweingruber, F. H. (1988). Summer temperature patterns over Europe: A reconstruction from 1750 A.D. based on maximum latewood density indices of conifers. *Quaternary Research*, *30*(1), 36–52, doi:10.1016/0033-5894(88)90086-5.

Briffa, K. R., Jones, P. D., Schweingruber, F. H., Karlén, W., & Shiyatov, S. G. (1996). Tree-ring variables as proxy-climate indicators: Problems with low-frequency signals. In P. D. Jones, R. S. Bradley, & J. Jouzel (Eds.), *Climatic Variations and Forcing Mechanisms of the Last 2000 Years* (pp. 9–41). Springer Berlin Heidelberg, doi:10.1007/978-3-642-61113-1_2.

Briffa, K. R., Osborn, T. J., Schweingruber, F. H., Jones, P. D., Shiyatov, S. G., & Vaganov, E. A. (2002). Tree-ring width and density data around the Northern Hemisphere: Part 1, local and regional climate signals. *The Holocene*, *12*(6), 737–757, doi:10.1191/0959683602hl587rp.

Brimelow, J. C., & Reuter, G. W. (2005). Transport of atmospheric moisture during three extreme rainfall events over the Mackenzie River Basin. *Journal of Hydrometeorology*, *6*(4), 423–440, doi:10.1175/JHM430.1.

Brooks, J. R., & Coulombe, R. (2009). Physiological responses to fertilization recorded in tree rings: Isotopic lessons from a long-term fertilization trial. *Ecological Applications*, *19*(4), 1044–1060, doi:10.1890/08-0310.1.

Brooks, J. R., Meinzer, F. C., Coulombe, R., & Gregg, J. (2002). Hydraulic redistribution of soil water during summer drought in two contrasting Pacific Northwest coniferous forests. *Tree Physiology*, *22*(15–16), 1107–1117, doi:10.1093/treephys/22.15-16.1107.

Brooks, J. R., Meinzer, F. C., Warren, J. M., Domec, J.-C., & Coulombe, R. (2006). Hydraulic redistribution in a Douglas-fir forest: Lessons from system manipulations. *Plant, Cell and Environment*, *29*(1), 138–150, doi:10.1111/j.1365-3040.2005.01409.x.

Brooks, R. J., Barnard, H. R., Coulombe, R., & McDonnell, J. J. (2010). Ecohydrologic separation of water between trees and streams in a Mediterranean climate. *Nature Geoscience*, *3*(2), 100–104, doi:10.1038/ngeo722.

Brubaker, L. B. (1980). Spatial patterns of tree growth anomalies in the Pacific Northwest. *Ecology*, *61*(4), 798–807, doi:10.2307/1936750.

Buckley, B. M., Hansen, K. G., Griffin, K. L., Schmiege, S., Oelkers, R., D'Arrigo, R. D., Stahle, D. K., Davi, N., Nguyen, T. Q. T., Le, C. N., & Wilson, R. J. S. (2018). Blue intensity from a tropical conifer's annual rings for climate reconstruction: An ecophysiological perspective. *Dendrochronologia*, *50*, 10–22, doi:10.1016/j.dendro.2018.04.003.

Buda, A. R., & DeWalle, D. R. (2009). Using atmospheric chemistry and storm track information to explain the variation of nitrate stable isotopes in precipitation at a site in central Pennsylvania, USA. *Atmospheric Environment*, *43*(29), 4453–4464, doi:10.1016/j.atmosenv.2009.06.027.

Buhay, W. M., Edwards, T. W. D., & Aravena, R. (1996). Evaluating kinetic fractionation factors used for reconstructions from oxygen and hydrogen isotope ratios in plant water and cellulose. *Geochimica et Cosmochimica Acta*, *60*(12), 2209–2218, doi:10.1016/0016-7037(96)00073-7.

Burk, R. L., & Stuiver, M. (1981). Oxygen isotope ratios in trees reflect mean annual temperature and humidity. *Science*, *211*(4489), 1417–1419, doi:10.1126/science.211.4489.1417.

Cabral-Alemán, C., Pompa-García, M., Acosta-Hernández, A., Zúñiga-Vásquez, J., & Camarero, J. (2017). Earlywood and latewood widths of *Picea chihuahuana* show contrasting sensitivity to seasonal climate. *Forests*, *8*(5), 173, doi:10.3390/f8050173.

Campbell, S., Waddell, Karen, Gray, Andrew, & technical editors (Eds.). (2010). *Washington's forest resources, 2002–2006: Five-year Forest Inventory and Analysis report* (General Technical Report PNW-GTR-800; p. 189). U.S. Department of Agriculture, Forest Service, Pacific Northwest Research Station. <https://www.fs.fed.us/pnw/pubs/pnw_gtr800.pdf>

Campelo, F., Nabais, C., Freitas, H., & Gutiérrez, E. (2007). Climatic significance of tree-ring width and intra-annual density fluctuations in *Pinus pinea* from a dry Mediterranean area in Portugal. *Annals of Forest Science*, *64*(2), 229–238, doi:10.1051/forest:2006107.

Carrer, M., Motta, R., & Nola, P. (2012). Significant mean and extreme climate sensitivity of Norway spruce and silver fir at mid-elevation mesic sites in the Alps. *PLoS ONE*, *7*(11), e50755, doi:10.1371/journal.pone.0050755.

Chang, E. K. M. (2013). CMIP5 Projection of significant reduction in extratropical cyclone activity over North America. *Journal of Climate*, *26*(24), 9903–9922, doi:10.1175/JCLI-D-13-00209.1.

Chang, E. K. M. (2014). Impacts of background field removal on CMIP5 projected changes in Pacific winter cyclone activity. *Journal of Geophysical Research: Atmospheres*, *119*(8), 4626–4639, doi:10.1002/2013JD020746.

Chang, E. K. M., Guo, Y., & Xia, X. (2012). CMIP5 multimodel ensemble projection of storm track change under global warming. *Journal of Geophysical Research: Atmospheres*, *117*(D23), doi:10.1029/2012JD018578.

Chang, E. K. M., Lee, S., & Swanson, K. L. (2002). Storm track dynamics. *Journal of Climate*, *15*(16), 2163–2183, doi:10.1175/1520-0442(2002)015<02163:STD>2.0.CO;2.

Chen, F., Yuan, Y., Wei, W., Yu, S., Li, Y., Zhang, R., Zhang, T., & Shang, H. (2010). Chronology development and climate response analysis of Schrenk spruce (*Picea Schrenkiana*) tree-ring parameters in the Urumqi River Basin, China. *Geochronometria*, *36*(1), 17–22, doi:10.2478/v10003-010-0014-4.

Clark, I. D., & Fritz, P. (1997). *Environmental Isotopes in Hydrogeology*. CRC Press, doi:10.1201/9781482242911.

Cleaveland, M.K. (1983). *X-ray densitometric measurement of climatic influence on the intra-annual characteristics of southwestern semiarid conifer tree rings*. University of Arizona.

Cook, E.R. (1985). *A time series analysis approach to tree-ring standardization* [Dissertation]. University of Arizona.

Coplen, T. B. (1996). New guidelines for reporting stable hydrogen, carbon, and oxygen isotope-ratio data. *Geochimica et Cosmochimica Acta*, *60*(17), 3359–3360, doi:10.1016/0016-7037(96)00263-3.

Covert, D. S., Kapustin, V. N., Bates, T. S., & Quinn, P. K. (1996). Physical properties of marine boundary layer aerosol particles of the mid-Pacific in relation to sources and meteorological transport. *Journal of Geophysical Research: Atmospheres*, *101*(D3), 6919–6930, doi:10.1029/95JD03068.

Craig, H. (1961). Isotopic variations in meteoric waters. *Science*, *133*(3465), 1702–1703, doi:10.1126/science.133.3465.1702

Craig, H., & Gordon, L. (1965). Deuterium and oxygen-18 variations in the ocean and the marine atmosphere. *Proceedings of a Conference on Stable Isotopes in Oceanographic Studies and Paleotemperatures*, 9–130.

Crawford, C. J., Griffin, D., & Kipfmueller, K. F. (2015). Capturing season-specific precipitation signals in the northern Rocky Mountains, USA, using earlywood and latewood tree rings. *Journal of Geophysical Research: Biogeosciences*, *120*(3), 428–440, doi:10.1002/2014JG002740.

Csank, A. Z., Fortier, D., & Leavitt, S. W. (2013). Annually resolved temperature reconstructions from a late Pliocene–early Pleistocene polar forest on Bylot Island, Canada. *Palaeogeography, Palaeoclimatology, Palaeoecology*, *369*, 313–322, doi:10.1016/j.palaeo.2012.10.040.

Daly, C., Halbleib, M., Smith, J. I., Gibson, W. P., Doggett, M. K., Taylor, G. H., Curtis, J., & Pasteris, P. P. (2008). Physiographically sensitive mapping of climatological temperature and precipitation across the conterminous United States. *International Journal of Climatology*, *28*(15), 2031–2064, doi:10.1002/joc.1688

Dannenberg, M. P., & Wise, E. K. (2016). Seasonal climate signals from multiple tree ring metrics: A case study of *Pinus ponderosa* in the upper Columbia River Basin. *Journal of Geophysical Research: Biogeosciences*, *121*(4), 1178–1189, doi:10.1002/2015JG003155.

Dansgaard, W. (1964). Stable isotopes in precipitation. *Tellus*, *16*(4), 436–468, doi:10.3402/tellusa.v16i4.8993.

D'Arrigo, R. D., Jacoby, G. C., & Free, R. M. (1992). Tree-ring width and maximum latewood density at the North American tree line: Parameters of climatic change. *Canadian Journal of Forest Research*, *22*(9), 1290–1296, doi:10.1139/x92-171.

Dayem, K. E., Molnar, P., Battisti, D. S., & Roe, G. H. (2010). Lessons learned from oxygen isotopes in modern precipitation applied to interpretation of speleothem records of paleoclimate from eastern Asia. *Earth and Planetary Science Letters*, *295*(1–2), 219–230, doi:10.1016/j.epsl.2010.04.003.

de Boer, H. J., Robertson, I., Clisby, R., Loader, N. J., Gagen, M., Young, G. H. F., Wagner-Cremer, F., Hipkin, C. R., & McCarroll, D. (2019). Tree-ring isotopes suggest atmospheric drying limits temperature–growth responses of treeline bristlecone pine. *Tree Physiology*, *39*(6), 983–999, doi:10.1093/treephys/tpz018.

de Winter, J. C. F., Gosling, S. D., & Potter, J. (2016). Comparing the Pearson and Spearman correlation coefficients across distributions and sample sizes: A tutorial using simulations and empirical data. *Psychological Methods*, *21*(3), 273–290, doi:10.1037/met0000079.

Diem, J. E., & Brown, D. P. (2006). Tropospheric moisture and monsoonal rainfall over the southwestern United States. *Journal of Geophysical Research*, *111*(D16), doi:10.1029/2005JD006836.

Diem, J. E., Sung, H. S., Konecky, B. L., Palace, M. W., Salerno, J., & Hartter, J. (2019). Rainfall characteristics and trends—and the role of Congo westerlies—in the western Uganda transition zone of equatorial Africa from 1983 to 2017. *Journal of Geophysical Research: Atmospheres*, *124*(20), 10712–10729, doi:10.1029/2019JD031243.

Diffenbaugh, N. S., Pal, J. S., Trapp, R. J., & Giorgi, F. (2005). Fine-scale processes regulate the response of extreme events to global climate change. *Proceedings of the National Academy of Sciences*, *102*(44), 15774–15778, doi:10.1073/pnas.0506042102.

Dixon, P. M. (2001). Bootstrap resampling. In *The encyclopedia of environmetrics* (pp. 212–220). Wiley.

Dongmann, G., Nürnberg, H. W., Förstel, H., & Wagener, K. (1974). On the enrichment of $H_2{}^{18}O$ in the leaves of transpiring plants. *Radiation and Environmental Biophysics*, *11*(1), 41–52, doi:10.1007/BF01323099.

Douglass, A. E. (1919). *Climatic cycles and tree-growth: A study of the annual rings of trees in relation to climate and solar activity*. Carnegie Institution of Washington, doi:10.5962/bhl.title.121855.

Draxler, R. R., & Hess, G. D. (1997). *NOAA technical memorandum ERL ARL-224: Description of the HYSPLIT_4 modeling system* (pp. 1–24).

Draxler, R. R., & Hess, G. D. (1998). An overview of the HYSPLIT_4 modelling system for trajectories, dispersion, and deposition. *Australian Meteorological Magazine*, *47*, 295–308.

Draxler, R. R., Stunder, B., Rolph, G., & Taylor, A. (1999). *HYSPLIT_4 user's guide*. US Department of Commerce, National Oceanic and Atmospheric Administration, Environmental Research Laboratories, Air Resources Laboratory.

Dutton, A., Wilkinson, B. H., Welker, J. M., Bowen, G. J., & Lohmann, K. C. (2005). Spatial distribution and seasonal variation in $^{18}O/^{16}O$ of modern precipitation and river water across the conterminous USA. *Hydrological Processes*, *19*(20), 4121–4146, doi:10.1002/hyp.5876.

Eastoe, C. J., & Dettman, D. L. (2016). Isotope amount effects in hydrologic and climate reconstructions of monsoon climates: Implications of some long-term datasets for precipitation. *Chemical Geology*, *430*, 78–89, doi:10.1016/j.chemgeo.2016.03.022.

Edwards, T. W. D., Birks, S. J., Luckman, B. H., & MacDonald, G. M. (2008). Climatic and hydrologic variability during the past millennium in the eastern Rocky Mountains and northern Great Plains of western Canada. *Quaternary Research*, *70*(2), 188–197, doi:10.1016/j.yqres.2008.04.013.

Edwards, T. W. D., & Fritz, P. (1986). Assessing meteoric water composition and relative humidity from ^{18}O and ^{2}H in wood cellulose: Paleoclimatic implications for southern Ontario, Canada. *Applied Geochemistry*, *1*(6), 715–723, doi:10.1016/0883-2927(86)90093-4.

Electricity Canada. (2012). *Industry Data and Electricity*. <https://www.electricity.ca/media/Industry%20Data%20and%20Electricity%20101%20May%202012/KeyCanadianElectricityStatistics_2012.pdf>

Emmingham, W. H., & Waring, R. H. (1977). An index of photosynthesis for comparing forest sites in western Oregon. *Canadian Journal of Forest Research*, *7*(1), 165–174, doi:10.1139/x77-023.

Epstein, S., & Mayeda, T. (1953). Variation of O^{18} content of waters from natural sources. *Geochimica et Cosmochimica Acta*, *4*(5), 213–224, doi:10.1016/0016-7037(53)90051-9.

Ersek, V., Mix, A. C., & Clark, P. U. (2010). Variations of $\delta^{18}O$ in rainwater from southwestern Oregon. *Journal of Geophysical Research*, *115*(D9), doi:10.1029/2009JD013345.

Feng, X., Reddington, A. L., Faiia, A. M., Posmentier, E. S., Shu, Y., & Xu, X. (2007). The changes in North American atmospheric circulation patterns indicated by wood cellulose. *Geology*, *35*(2), 163, doi:10.1130/G22884A.1.

Ferguson, S. A. (1999). *Climatology of the interior Columbia River basin.* (PNW-GTR-445; p. PNW-GTR-445). U.S. Department of Agriculture, Forest Service, Pacific Northwest Research Station, doi:10.2737/PNW-GTR-445.

Fernau, M. E., & Samson, P. J. (1990). Use of cluster analysis to define periods of similar meteorology and precipitation chemistry in eastern North America, Part I: Transport patterns. *Journal of Applied Meteorology*, *29*(8), 735–750, doi:10.1175/1520-0450(1990)029<0735:UOCATD>2.0.CO;2.

Field, R. D. (2010). Observed and modeled controls on precipitation $\delta^{18}O$ over Europe: From local temperature to the Northern Annular Mode. *Journal of Geophysical Research*, *115*(D12), doi:10.1029/2009JD013370.

Flanagan, L. B., Comstock, J. P., & Ehleringer, J. R. (1991). Comparison of modeled and observed environmental influences on the stable oxygen and hydrogen isotope composition of leaf water in *Phaseolus vulgaris* L. *Plant Physiology*, *96*(2), 588–596, doi:10.1104/pp.96.2.588.

Friedman, I. (1953). Deuterium content of natural waters and other substances. *Geochimica et Cosmochimica Acta*, *4*(1–2), 89–103, doi:10.1016/0016-7037(53)90066-0.

Friedman, I. (2002). Stable isotope composition of waters in the Great Basin, United States, 1: Air-mass trajectories. *Journal of Geophysical Research*, *107*(D19), doi:10.1029/2001JD000565.

Fritts, H. C. (1974). Relationships of ring widths in arid-site conifers to variations in monthly temperature and precipitation. *Ecological Monographs*, *44*(4), 411–440, doi:10.2307/1942448.

Fritts, H. C. (1976). *Tree Rings and Climate*. Academic Press.

Gagen, M., McCarroll, D., Loader, N. J., & Robertson, I. (2011). Stable isotopes in dendroclimatology: Moving beyond 'potential.' In M. K. Hughes, T. W. Swetnam, & H. F. Diaz (Eds.), *Dendroclimatology* (Vol. 11, pp. 147–172). Springer Netherlands, doi:10.1007/978-1-4020-5725-0_6.

Gat, J. R. (1971). Comments on the stable isotope method in regional groundwater investigations. *Water Resources Research*, *7*(4), 980–993, doi:10.1029/WR007i004p00980.

Gat, J. R. (1996). Oxygen and hydrogen isotopes in the hydrologic cycle. *Annual Review of Earth and Planetary Sciences*, *24*(1), 225–262, doi:10.1146/annurev.earth.24.1.225.

Ghosh, P., & Brand, W. A. (2003). Stable isotope ratio mass spectrometry in global climate change research. *International Journal of Mass Spectrometry*, *228*(1), 1–33, doi:10.1016/S1387-3806(03)00289-6.

Gonfiantini, R., & Picciotto, E. (1959). Oxygen isotope variations in Antarctic snow samples. *Nature*, *184*(4698), 1557–1558, doi:10.1038/1841557a0.

Grier, C. G., & Running, S. W. (1977). Leaf area of mature northwestern coniferous forests: Relation to site water balance. *Ecology*, *58*(4), 893–899, doi:10.2307/1936225.

Grießinger, J., Bräuning, A., Helle, G., Hochreuther, P., & Schleser, G. (2017). Late Holocene relative humidity history on the southeastern Tibetan plateau inferred from a tree-ring $\delta^{18}O$ record: Recent decrease and conditions during the last 1500 years. *Quaternary International*, *430*, 52–59, doi:10.1016/j.quaint.2016.02.011.

Griffin, D., Woodhouse, C. A., Meko, D. M., Stahle, D. W., Faulstich, H. L., Carrillo, C., Touchan, R., Castro, C. L., & Leavitt, S. W. (2013). North American monsoon precipitation reconstructed from tree-ring latewood. *Geophysical Research Letters*, *40*(5), 954–958, doi:10.1002/grl.50184.

Guan, H., Zhang, X., Skrzypek, G., Sun, Z., & Xu, X. (2013). Deuterium excess variations of rainfall events in a coastal area of South Australia and its relationship with synoptic weather systems and atmospheric moisture sources. *Journal of Geophysical Research: Atmospheres*, *118*(2), 1123–1138, doi:10.1002/jgrd.50137.

Hamlet, A. F., Lee, S.-Y., Mickelson, K. E. B., & Elsner, M. M. (2010). Effects of projected climate change on energy supply and demand in the Pacific Northwest and Washington State. *Climatic Change*, *102*(1–2), 103–128, doi:10.1007/s10584-010-9857-y.

Hamlet, A. F., Mote, P. W., Clark, M. P., & Lettenmaier, D. P. (2005). Effects of temperature and precipitation variability on snowpack trends in the western United States. *Journal of Climate*, *18*(21), 4545–4561, doi:10.1175/JCLI3538.1

Harris, R. M. B., Beaumont, L. J., Vance, T. R., Tozer, C. R., Remenyi, T. A., Perkins-Kirkpatrick, S. E., Mitchell, P. J., Nicotra, A. B., McGregor, S., Andrew, N. R., Letnic, M., Kearney, M. R., Wernberg, T., Hutley, L. B., Chambers, L. E., Fletcher, M.-S., Keatley, M. R., Woodward, C. A., Williamson, G., … Bowman, D. M. J. S. (2018). Biological responses to the press and pulse of climate trends and extreme events. *Nature Climate Change*, *8*(7), 579–587, doi:10.1038/s41558-018-0187-9.

Hedges, R. E. M., Stevens, R. E., & Richards, Michael. P. (2004). Bone as a stable isotope archive for local climatic information. *Quaternary Science Reviews*, *23*(7–8), 959–965, doi:10.1016/j.quascirev.2003.06.022.

Hoefs, J. (2018). *Stable Isotope Geochemistry*. Springer International Publishing, doi:10.1007/978-3-319-78527-1.

Holmes, R.L. (1983). Computer-assisted quality control in tree ring dating and measurement. *Tree-Ring Bulletin*, *43*, 69–78.

Holte, J. C. (2012). *Forest resources of the Idaho Panhandle National Forest*. <https://www.fs.fed.us/rm/pubs_series/forest_resources/idaho_panhandle.pdf>

Holzkämper, S., Kuhry, P., Kultti, S., Gunnarson, B., & Sonninen, E. (2008). Stable isotopes in tree rings as proxies for winter precipitation changes in the Russian Arctic over the past 150 years. *Geochronometria*, *32*(1), 37–46, doi:10.2478/v10003-008-0025-6.

Hondula, D. M., Sitka, L., Davis, R. E., Knight, D. B., Gawtry, S. D., Deaton, M. L., Lee, T. R., Normile, C. P., & Stenger, P. J. (2010). A back-trajectory and air mass climatology for the northern Shenandoah Valley. *International Journal of Climatology*, *30*(4), 569–581, doi:10.1002/joc.1896.

Huang, R., Zhu, H., Liang, E., Bräuning, A., Zhong, L., Xu, C., Feng, X., Asad, F., Sigdel, S. R., Li, L., & Grießinger, J. (2022). Contribution of winter precipitation to tree growth persists until the late growing season in the Karakoram of northern Pakistan. *Journal of Hydrology*, *607*, 127513, doi:10.1016/j.jhydrol.2022.127513.

Hunter, T., Tootle, G., & Piechota, T. (2006). Oceanic-atmospheric variability and western U.S. snowfall. *Geophysical Research Letters*, *33*(13), doi:10.1029/2006GL026600.

International Tree-Ring Data Bank. (2021). < https://www.ncei.noaa.gov/products/paleoclimatology/tree-ring>

Jacoby, G. C. (1989). Overview of tree-ring analysis in tropical regions. *IAWA Journal*, *10*(2), 99–108, doi:10.1163/22941932-90000478.

Jouzel, J., Alley, R. B., Cuffey, K. M., Dansgaard, W., Grootes, P., Hoffmann, G., Johnsen, S. J., Koster, R. D., Peel, D., Shuman, C. A., Stievenard, M., Stuiver, M., & White, J. (1997). Validity of the temperature reconstruction from water isotopes in ice cores. *Journal of Geophysical Research: Oceans*, *102*(C12), 26471–26487, doi:10.1029/97JC01283.

Kalnay, E., Kanamitsu, M., Kistler, R., Collins, W., Deaven, D., Gandin, L., Iredell, M., Saha, S., White, G., Woollen, J., Zhu, Y., Leetmaa, A., Reynolds, R., Chelliah, M., Ebisuzaki, W., Higgins, W., Janowiak, J., Mo, K. C., Ropelewski, C., … Joseph, D. (1996). The NCEP/NCAR 40-year reanalysis project. *Bulletin of the American Meteorological Society*, *77*(3), 437–471, doi:10.1175/1520-0477(1996)077<0437:TNYRP>2.0.CO;2.

Karaca, F., Alagha, O., & Ertürk, F. (2005). Statistical characterization of atmospheric PM10 and PM2.5 concentrations at a non-impacted suburban site of Istanbul, Turkey. *Chemosphere*, *59*(8), 1183–1190, doi:10.1016/j.chemosphere.2004.11.062.

Kohn, M. J., & Welker, J. M. (2005). On the temperature correlation of $\delta^{18}O$ in modern precipitation. *Earth and Planetary Science Letters*, *231*(1–2), 87–96, doi:10.1016/j.epsl.2004.12.004.

Konrad, C. P. (2019). Seasonal precipitation influences streamflow vulnerability to the 2015 drought in the western United States. *Journal of Hydrometeorology*, *20*(7), 1261–1274, doi:10.1175/JHM-D-18-0121.1.

Kurita, N., Nakatsuka, T., Ohnishi, K., Mitsutani, T., & Kumagai, T. (2016). Analysis of the interdecadal variability of summer precipitation in central Japan using a reconstructed 106 year long oxygen isotope record from tree ring cellulose. *Journal of Geophysical Research: Atmospheres*, *121*(20), 12,089-12,107, doi:10.1002/2016JD025463.

Kurita, N., Ichiyanagi, K., Matsumoto, J., Yamanaka, M. D., & Ohata, T. (2009). The relationship between the isotopic content of precipitation and the precipitation amount in tropical regions. *Journal of Geochemical Exploration*, *102*(3), 113–122, doi:10.1016/j.gexplo.2009.03.002.

Labotka, D. M., Mora, C. I., & Johnson, E. J. (2016). Patterns of moisture source and climate variability in the southeastern United States: A four-century seasonally resolved tree-ring oxygen-isotope record. *Climate Dynamics*, *46*(7–8), 2145–2154, doi:10.1007/s00382-015-2694-y.

Lawrimore, J. H., Menne, M. J., Gleason, B. E., Williams, C. N., Wuertz, D. B., Vose, R. S., & Rennie, J. (2011). An overview of the Global Historical Climatology Network monthly mean temperature data set, version 3. *Journal of Geophysical Research*, *116*(D19), doi:10.1029/2011JD016187.

Leavitt, S. W. (2010). Tree-ring C–H–O isotope variability and sampling. *Science of The Total Environment*, *408*(22), 5244–5253, doi:10.1016/j.scitotenv.2010.07.057.

Leavitt, S. W., & Danzer, S. R. (1993). Method for batch processing small wood samples to holocellulose for stable-carbon isotope analysis. *Analytical Chemistry*, *65*(1), 87–89, doi:10.1021/ac00049a017.

Lebourgeois, F. (2000). Climatic signals in earlywood, latewood and total ring width of Corsican pine from western France. *Annals of Forest Science*, *57*(2), 155–164, doi:10.1051/forest:2000166.

LeGrande, A. N., & Schmidt, G. A. (2009). Sources of Holocene variability of oxygen isotopes in paleoclimate archives. *Climate of the Past*, *5*(3), 441–455, doi:10.5194/cp-5-441-2009.

Leonelli, G., Battipaglia, G., Cherubini, P., Saurer, M., Siegwolf, R. T. W., Maugeri, M., Stenni, B., Fusco, S., Maggi, V., & Pelfini, M. (2017). *Larix decidua* $\delta^{18}O$ tree-ring cellulose mainly reflects the isotopic signature of winter snow in a high-altitude glacial valley of the European Alps. *Science of The Total Environment*, *579*, 230–237, doi:10.1016/j.scitotenv.2016.11.129.

Leung, L. R., Qian, Y., Bian, X., & Hunt, A. (2003). Hydroclimate of the western United States based on observations and regional climate simulation of 1981–2000. Part II: Mesoscale ENSO anomalies. *Journal of Climate*, *16*(12), 1912–1928, doi:10.1175/1520-0442(2003)016<1912:HOTWUS>2.0.CO;2.

Lévesque, M., Saurer, M., Siegwolf, R., Eilmann, B., Brang, P., Bugmann, H., & Rigling, A. (2013). Drought response of five conifer species under contrasting water availability suggests high vulnerability of Norway spruce and European larch. *Global Change Biology*, *19*(10), 3184–3199, doi:10.1111/gcb.12268.

Lewis, S. C., LeGrande, A. N., Kelley, M., & Schmidt, G. A. (2010). Water vapour source impacts on oxygen isotope variability in tropical precipitation during Heinrich events. *Climate of the Past*, *6*(3), 325–343, doi:10.5194/cp-6-325-2010.

Lipp, J., Trimborn, P., Fritz, P., Moser, H., Becker, B., & Frenzel, B. (1991). Stable isotopes in tree ring cellulose and climatic change. *Tellus B*, *43*(3), 322–330, doi:/10.1034/j.1600-0889.1991.t01-2-00005.x.

Littell, J. S., Pederson, G. T., Gray, S. T., Tjoelker, M., Hamlet, A. F., & Woodhouse, C. A. (2016). Reconstructions of Columbia River streamflow from tree-ring chronologies in the Pacific Northwest, USA. *JAWRA Journal of the American Water Resources Association*, *52*(5), 1121–1141, doi:10.1111/1752-1688.12442.

Liu, Y., Wang, L., Li, Q., Cai, Q., Song, H., Sun, C., Liu, R., & Mei, R. (2019). Asian Summer Monsoon-related relative humidity recorded by tree ring $\delta^{18}O$ during last 205 years. *Journal of Geophysical Research: Atmospheres*, *124*(17–18), 9824–9838, doi:10.1029/2019JD030512.

Liu, X., Xu, G., Grießinger, J., An, W., Wang, W., Zeng, X., Wu, G., & Qin, D. (2014). A shift in cloud cover over the southeastern Tibetan Plateau since 1600: Evidence from regional tree-ring $\delta^{18}O$ and its linkages to tropical oceans. *Quaternary Science Reviews*, *88*, 55–68, doi:10.1016/j.quascirev.2014.01.009.

Liu, Z., Bowen, G. J., Welker, J. M., & Yoshimura, K. (2013). Winter precipitation isotope slopes of the contiguous USA and their relationship to the Pacific/North American (PNA) pattern. *Climate Dynamics*, *41*(2), 403–420, doi:10.1007/s00382-012-1548-0.

Liu, Z., Kennedy, C. D., & Bowen, G. J. (2011). Pacific/North American teleconnection controls on precipitation isotope ratios across the contiguous United States. *Earth and Planetary Science Letters*, *310*(3–4), 319–326, doi:10.1016/j.epsl.2011.08.037.

Livezey, R. E., Vinnikov, K. Y., Timofeyeva, M. M., Tinker, R., & van den Dool, H. M. (2007). Estimation and extrapolation of climate normals and climatic trends. *Journal of Applied Meteorology and Climatology*, *46*(11), 1759–1776, doi:10.1175/2007JAMC1666.1.

Loader, N. J., Robertson, I., & McCarroll, D. (2003). Comparison of stable carbon isotope ratios in the whole wood, cellulose and lignin of oak tree-rings. *Palaeogeography, Palaeoclimatology, Palaeoecology*, *196*(3–4), 395–407, doi:10.1016/S0031-0182(03)00466-8.

Lopushinsky, W. & Klock, G.O. (1974). Transpiration of conifer seedlings in relation to soil water potential. *Forest Science*, *20*(2), 181–186.

Lorrey, A. M., Brookman, T. H., Evans, M. N., Fauchereau, N. C., Macinnis-Ng, C., Barbour, M. M., Criscitiello, A., Eischeid, G., Fowler, A. M., Horton, T. W., & Schrag, D. P. (2016). Stable oxygen isotope signatures of early season wood in New Zealand kauri (*Agathis australis*) tree rings: Prospects for palaeoclimate reconstruction. *Dendrochronologia*, *40*, 50–63, doi:10.1016/j.dendro.2016.03.012.

Lough, J. M. (2010). Climate records from corals. *Wiley Interdisciplinary Reviews: Climate Change*, *1*(3), 318–331, doi:10.1002/wcc.39.

Majoube, M. (1971). Oxygen-18 and deuterium fractionation between water and steam. *Journal de Chimie Physique et de Physico-Chimie Biologique*, *68*, 1423–1436.

Mann, M. E., Rutherford, S., Wahl, E., & Ammann, C. (2005). Testing the fidelity of methods used in proxy-based reconstructions of past climate. *Journal of Climate*, 18(20), 4097–4107, doi:10.1175/JCLI3564.1.

Marchetti, D. W., & Marchetti, S. B. (2019). Stable isotope compositions of precipitation from Gunnison, Colorado 2007–2016: Implications for the climatology of a high-elevation valley. *Heliyon*, *5*(7), e02120, doi:10.1016/j.heliyon.2019.e02120.

Marlier, M. E., Xiao, M., Engel, R., Livneh, B., Abatzoglou, J. T., & Lettenmaier, D. P. (2017). The 2015 drought in Washington State: A harbinger of things to come? *Environmental Research Letters*, *12*(11), 114008, doi:10.1088/1748-9326/aa8fde.

Marshall, J. D., & Monserud, R. A. (2006). Co-occurring species differ in tree-ring $\delta^{18}O$ trends. *Tree Physiology*, *26*(8), 1055–1066, doi:10.1093/treephys/26.8.1055.

McAfee, S. A., & Wise, E. K. (2016). Intra-seasonal and inter-decadal variability in ENSO impacts on the Pacific Northwest. *International Journal of Climatology*, *36*(1), 508–516, doi:10.1002/joc.4351.

McCabe-Glynn, S., Johnson, K. R., Strong, C., Zou, Y., Yu, J.-Y., Sellars, S., & Welker, J. M. (2016). Isotopic signature of extreme precipitation events in the western U.S. and associated phases of Arctic and tropical climate modes. *Journal of Geophysical Research: Atmospheres*, *121*(15), 8913–8924, doi:10.1002/2016JD025524.

McCarroll, D., & Loader, N. J. (2004). Stable isotopes in tree rings. *Quaternary Science Reviews*, *23*(7–8), 771–801, doi:10.1016/j.quascirev.2003.06.017.

McCarroll, D., Pettigrew, E., Luckman, A., Guibal, F., & Edouard, J.-L. (2002). Blue reflectance provides a surrogate for latewood density of high-latitude pine tree rings. *Arctic, Antarctic, and Alpine Research*, *34*(4), 450–453, doi:10.1080/15230430.2002.12003516.

McDermott, F. (2004). Palaeo-climate reconstruction from stable isotope variations in speleothems: A review. *Quaternary Science Reviews*, *23*(7–8), 901–918, doi:10.1016/j.quascirev.2003.06.021.

Meko, D. M., & Baisan, C. H. (2001). Pilot study of latewood-width of conifers as an indicator of variability of summer rainfall in the North American monsoon region. *International Journal of Climatology*, *21*(6), 697–708, doi:10.1002/joc.646.

Meko, D. M., Touchan, R., & Anchukaitis, K. J. (2011). Seascorr: A MATLAB program for identifying the seasonal climate signal in an annual tree-ring time series. *Computers & Geosciences*, *37*(9), 1234–1241, doi:10.1016/j.cageo.2011.01.013.

Mesinger, F., DiMego, G., Kalnay, E., Mitchell, K., Shafran, P. C., Ebisuzaki, W., Jović, D., Woollen, J., Rogers, E., Berbery, E. H., Ek, M. B., Fan, Y., Grumbine, R., Higgins, W., Li, H., Lin, Y., Manikin, G., Parrish, D., & Shi, W. (2006). North American Regional Reanalysis. *Bulletin of the American Meteorological Society*, *87*(3), 343–360, doi:10.1175/BAMS-87-3-343.

Mesquita, M. D. S., Atkinson, D. E., & Hodges, K. I. (2010). Characteristics and variability of storm tracks in the North Pacific, Bering Sea, and Alaska. *Journal of Climate*, *23*(2), 294–311, doi:10.1175/2009JCLI3019.1.

Minder, J. R., Mote, P. W., & Lundquist, J. D. (2010). Surface temperature lapse rates over complex terrain: Lessons from the Cascade Mountains. *Journal of Geophysical Research*, *115*(D14), doi:10.1029/2009JD013493.

Mock, C. J. (1996). Climatic controls and spatial variations of precipitation in the western United States. *Journal of Climate*, *9*(5), 1111–1125, doi:10.1175/1520-0442(1996)009<1111:CCASVO>2.0.CO;2.

Moore, B. J., Neiman, P. J., Ralph, F. M., & Barthold, F. E. (2012). Physical processes associated with heavy flooding rainfall in Nashville, Tennessee, and vicinity during 1–2

May 2010: The role of an atmospheric river and mesoscale convective systems. *Monthly Weather Review*, *140*(2), 358–378, doi:10.1175/MWR-D-11-00126.1.

Moore, M., Blossey, P. N., Muhlbauer, A., & Kuang, Z. (2016). Microphysical controls on the isotopic composition of wintertime orographic precipitation. *Journal of Geophysical Research: Atmospheres*, *121*(12), 7235–7253, doi:10.1002/2015JD023763.

Mote, P., Snover, A. K., Capalbo, S., Eigenbrode, S. D., Glick, P., Littell, J., ... & Reeder, S. (2014). Ch. 21: Northwest. *Climate Change Impacts in the United States: The Third National Climate Assessment, JM Melillo, TC Richmond, and GW Yohe, Eds., US Global Change Research Program*, 487-513.

Nakamura, H. (1992). Midwinter suppression of baroclinic wave activity in the Pacific. *Journal of the Atmospheric Sciences*, *49*(17), 1629–1642, doi:10.1175/1520-0469(1992)049<1629:MSOBWA>2.0.CO;2.

National Atmospheric Deposition Program. (2020a). *NTN Field Methods*. <http://nadp.slh.wisc.edu/NTN/NTNfield.aspx>

National Atmospheric Deposition Program. (2020b). *Quality Assurance Support for the NADP*. <http://nadp.slh.wisc.edu/QA/>

National Centers for Environmental Information. (2022). *What Are "Proxy" Data?* <https://www.ncdc.noaa.gov/news/what-are-proxy-data>

NOAA Technical Report NESDIS 142-6: Regional climate trends and scenarios for the U.S. National Climate Assessment Part 5. Climate of the Northwest U.S. (2013). <https://www.nesdis.noaa.gov/sites/default/files/asset/document/NOAA_NESDIS_Tech_Report_142-6-Climate_of_the_Northwest_U.S.pdf>

Ogée, J., Barbour, M. M., Wingate, L., Bert, D., Bosc, A., Stievenard, M., Lambrot, C., Pierre, M., Bariac, T., Loustau, D., & Dewar, R. C. (2009). A single-substrate model to interpret intra-annual stable isotope signals in tree-ring cellulose. *Plant, Cell & Environment*, *32*(8), 1071–1090, doi:10.1111/j.1365-3040.2009.01989.x.

Philip, S. Y., Kew, S. F., van Oldenborgh, G. J., Anslow, F. S., Seneviratne, S. I., Vautard, R., Coumou, D., Ebi, K. L., Arrighi, J., Singh, R., van Aalst, M., Pereira Marghidan, C., Wehner, M., Yang, W., Li, S., Schumacher, D. L., Hauser, M., Bonnet, R., Luu, L. N., … Otto, F. E. L. (2021). *Rapid attribution analysis of the extraordinary heatwave on the Pacific Coast of the US and Canada June 2021* [Preprint]. Earth system change: climate scenarios, doi:10.5194/esd-2021-90.

Poage, M. A., & Chamberlain, C. P. (2001). Empirical relationships between elevation and the stable isotope composition of precipitation and surface waters: Considerations for studies of paleoelevation change. *American Journal of Science*, *301*(1), 1–15, doi:10.2475/ajs.301.1.1.

Porter, T. J., Pisaric, M. F. J., Kokelj, S. V., & Edwards, T. W. D. (2009). Climatic signals in $\delta^{13}C$ and $\delta^{18}O$ of tree-rings from white spruce in the Mackenzie Delta Region, northern Canada. *Arctic, Antarctic, and Alpine Research*, *41*(4), 497–505, doi:10.1657/1938-4246-41.4.497.

Porter, T. J., Pisaric, M. F. J., Field, R. D., Kokelj, S. V., Edwards, T. W. D., deMontigny, P., Healy, R., & LeGrande, A. N. (2014). Spring-summer temperatures since AD 1780 reconstructed from stable oxygen isotope ratios in white spruce tree-rings from the Mackenzie Delta, northwestern Canada. *Climate Dynamics*, *42*(3–4), 771–785, doi:10.1007/s00382-013-1674-3.

PRISM Climate Group, Oregon State University. <http://prism.oregonstate.edu>

Puntsag, T., Mitchell, M. J., Campbell, J. L., Klein, E. S., Likens, G. E., & Welker, J. M. (2016). Arctic Vortex changes alter the sources and isotopic values of precipitation in northeastern US. *Scientific Reports*, *6*(1), doi:10.1038/srep22647.

Putman, A. L., Feng, X., Sonder, L. J., & Posmentier, E. S. (2017). Annual variation in event-scale precipitation $\delta^{2}H$ at Barrow, AK, reflects vapor source region. *Atmospheric Chemistry and Physics*, *17*(7), 4627–4639, doi:10.5194/acp-17-4627-2017.

Qin, C., Yang, B., Bräuning, A., Grießinger, J., & Wernicke, J. (2015). Drought signals in tree-ring stable oxygen isotope series of Qilian juniper from the arid northeastern Tibetan Plateau. *Global and Planetary Change*, *125*, 48–59, doi:10.1016/j.gloplacha.2014.12.002.

Ramesh, R., Bhattacharya, S. K., & Gopalan, K. (1986). Climatic correlations in the stable isotope records of silver fir (*Abies pindrow*) trees from Kashmir, India. *Earth and Planetary Science Letters*, *79*(1–2), 66–74, doi:10.1016/0012-821X(86)90041-5.

Rempe, D. M., & Dietrich, W. E. (2018). Direct observations of rock moisture, a hidden component of the hydrologic cycle. *Proceedings of the National Academy of Sciences*, *115*(11), 2664–2669, doi:10.1073/pnas.1800141115.

Reynolds-Henne, C. E., Siegwolf, R. T. W., Treydte, K. S., Esper, J., Henne, S., & Saurer, M. (2007). Temporal stability of climate-isotope relationships in tree rings of oak and pine (Ticino, Switzerland). *Global Biogeochemical Cycles*, *21*(4), doi:10.1029/2007GB002945.

Rinne, K. T., Boettger, T., Loader, N. J., Robertson, I., Switsur, V. R., & Waterhouse, J. S. (2005). On the purification of α-cellulose from resinous wood for stable isotope (H, C and O) analysis. *Chemical Geology*, *222*(1–2), 75–82, doi:10.1016/j.chemgeo.2005.06.010.

Rinne, K. T., Loader, N. J., Switsur, V. R., & Waterhouse, J. S. (2013). 400-year May–August precipitation reconstruction for Southern England using oxygen isotopes in tree rings. *Quaternary Science Reviews*, *60*, 13–25, doi:10.1016/j.quascirev.2012.10.048.

Robertson, E. O., Jozsa, L. A., & Spittlehouse, D. L. (1990). Estimating Douglas-fir wood production from soil and climate data. *Canadian Journal of Forest Research*, *20*(3), 357–364, doi:10.1139/x90-052.

Robertson, I., Switsur, V. R., Carter, A. H. C., Barker, A. C., Waterhouse, J. S., Briffa, K. R., & Jones, P. D. (1997). Signal strength and climate relationships in $^{13}C/^{12}C$ ratios of tree ring cellulose from oak in east England. *Journal of Geophysical Research: Atmospheres*, *102*(D16), 19507–19516, doi:10.1029/97JD01226.

Robertson, I., Waterhouse, J. S., Barker, A. C., Carter, A. H. C., & Switsur, V. R. (2001). Oxygen isotope ratios of oak in east England: Implications for reconstructing the isotopic composition of precipitation. *Earth and Planetary Science Letters*, *191*(1–2), 21–31, doi:10.1016/S0012-821X(01)00399-5.

Robertson, I., Leavitt, S. W., Loader, N. J., & Buhay, W. (2008). Progress in isotope dendroclimatology. *Chemical Geology*, *252*(1–2), EX1–EX4, doi:10.1016/S0009-2541(08)00177-0.

Roden, J. S., Bowling, D. R., McDowell, N. G., Bond, B. J., & Ehleringer, J. R. (2005). Carbon and oxygen isotope ratios of tree ring cellulose along a precipitation transect in Oregon, United States. *Journal of Geophysical Research: Biogeosciences*, *110*(G2), doi:10.1029/2005JG000033.

Roden, J. S., & Ehleringer, J. R. (2000). Hydrogen and oxygen isotope ratios of tree ring cellulose for field-grown riparian trees. *Oecologia*, *123*(4), 481–489, doi:10.1007/s004420000349.

Roden, J. S., & Ehleringer, J. R. (2007). Summer precipitation influences the stable oxygen and carbon isotopic composition of tree-ring cellulose in *Pinus ponderosa*. *Tree Physiology*, *27*(4), 491–501, doi:10.1093/treephys/27.4.491.

Roden, J. S., Lin, G., & Ehleringer, J. R. (2000). A mechanistic model for interpretation of hydrogen and oxygen isotope ratios in tree-ring cellulose. *Geochimica et Cosmochimica Acta*, *64*(1), 21–35, doi:10.1016/S0016-7037(99)00195-7.

Rozanski, K., Araguás-Araguás, L., & Gonfiantini, R. (1993). Isotopic patterns in modern global precipitation. In P. K. Swart, K. C. Lohmann, J. Mckenzie, & S. Savin (Eds.), *Geophysical Monograph Series* (pp. 1–36). American Geophysical Union, doi:10.1029/GM078p0001.

Rozendaal, D. M. A., & Zuidema, P. A. (2011). Dendroecology in the tropics: A review. *Trees*, *25*(1), 3–16, doi:10.1007/s00468-010-0480-3.

Rupp, D. E., Abatzoglou, J. T., Hegewisch, K. C., & Mote, P. W. (2013). Evaluation of CMIP5 20th century climate simulations for the Pacific Northwest USA. *Journal of Geophysical Research: Atmospheres*, *118*(19), 10,884-10,906, doi:10.1002/jgrd.50843.

Sánchez-Murillo, R., Esquivel-Hernández, G., Welsh, K., Brooks, E. S., Boll, J., Alfaro-Solís, R., & Valdés-González, J. (2013). Spatial and temporal variation of stable isotopes in precipitation across Costa Rica: An analysis of historic GNIP records. *Open Journal of Modern Hydrology*, *03*(04), 226–240, doi:10.4236/ojmh.2013.34027.

Sano, M., Xu, C., & Nakatsuka, T. (2012). A 300-year Vietnam hydroclimate and ENSO variability record reconstructed from tree ring $\delta^{18}O$. *Journal of Geophysical Research: Atmospheres*, *117*(D12), doi:10.1029/2012JD017749.

Saurer, M., Borella, S., & Leuenberger, M. (1997). $\delta^{18}O$ of tree rings of beech (*Fagus silvatica*) as a record of $\delta^{18}O$ of the growing season precipitation. *Tellus B: Chemical and Physical Meteorology*, *49*(1), 80–92, doi:10.3402/tellusb.v49i1.15952.

Saurer, M., Cherubini, P., Reynolds-Henne, C. E., Treydte, K. S., Anderson, W. T., & Siegwolf, R. T. W. (2008). An investigation of the common signal in tree ring stable isotope chronologies at temperate sites. *Journal of Geophysical Research: Biogeosciences*, *113*(G4), doi:10.1029/2008JG000689.

Saurer, M., Kress, A., Leuenberger, M., Rinne, K. T., Treydte, K. S., & Siegwolf, R. T. W. (2012). Influence of atmospheric circulation patterns on the oxygen isotope ratio of tree rings in the Alpine region. *Journal of Geophysical Research: Atmospheres*, *117*(D5), doi:10.1029/2011JD016861.

Schmidt, G. A., LeGrande, A. N., & Hoffmann, G. (2007). Water isotope expressions of intrinsic and forced variability in a coupled ocean-atmosphere model. *Journal of Geophysical Research: Atmospheres*, *112*(D10), doi:10.1029/2006JD007781.

Schubert, B. A., & Jahren, A. H. (2015). Seasonal temperature and precipitation recorded in the intra-annual oxygen isotope pattern of meteoric water and tree-ring cellulose. *Quaternary Science Reviews*, *125*, 1–14, doi:10.1016/j.quascirev.2015.07.024.

Shi, C., Daux, V., Zhang, Q.-B., Risi, C., Hou, S.-G., Stievenard, M., Pierre, M., Li, Z., & Masson-Delmotte, V. (2012). Reconstruction of southeast Tibetan Plateau summer climate using tree ring $\delta^{18}O$: Moisture variability over the past two centuries. *Climate of the Past*, *8*(1), 205–213, doi:10.5194/cp-8-205-2012.

Shu, Y., Feng, X., Gazis, C., Anderson, D., Faiia, A. M., Tang, K., & Ettl, G. J. (2005). Relative humidity recorded in tree rings: A study along a precipitation gradient in the Olympic Mountains, Washington, USA. *Geochimica et Cosmochimica Acta*, *69*(4), 791–799, doi:10.1016/j.gca.2004.08.013.

Sidorova, O. V., Siegwolf, R. T. W., Saurer, M., Naurzbaev, M. M., Shashkin, A. V., & Vaganov, E. A. (2010). Spatial patterns of climatic changes in the Eurasian north reflected in Siberian larch tree-ring parameters and stable isotopes. *Global Change Biology*, *16*(3), 1003–1018, doi:10.1111/j.1365-2486.2009.02008.x.

Sjostrom, D. J., & Welker, J. M. (2009). The influence of air mass source on the seasonal isotopic composition of precipitation, eastern USA. *Journal of Geochemical Exploration*, *102*(3), 103–112, doi:10.1016/j.gexplo.2009.03.001.

Smith, R. B. (2019). 100 years of progress on mountain meteorology research. *Meteorological Monographs*, *59*, 20.1-20.73, doi:10.1175/AMSMONOGRAPHS-D-18-0022.1.

Smith, R. B., Barstad, I., & Bonneau, L. (2005). Orographic precipitation and Oregon's climate transition. *Journal of the Atmospheric Sciences*, *62*(1), 177–191, doi:10.1175/JAS-3376.1.

Soulé, P. T., Knapp, P. A., Maxwell, J. T., & Mitchell, T. J. (2021). A comparison of the climate response of longleaf pine (*Pinus palustris Mill.*) trees among standardized measures of earlywood, latewood, adjusted latewood, and totalwood radial growth. *Trees*, *35*(3), 1065–1074, doi:10.1007/s00468-021-02093-z.

St. George, S. (2014). An overview of tree-ring width records across the Northern Hemisphere. *Quaternary Science Reviews*, *95*, 132–150, doi:10.1016/j.quascirev.2014.04.029.

Stahle, D. W., Cleaveland, M. K., Griffin, R. D., Fye, F. K., Therrell, M. D., Burnette, D. J., Meko, D. M., & Villanueva Diaz, J. (2009). Cool- and warm-season precipitation reconstructions over western New Mexico. *Journal of Climate*, *22*(13), 3729–3750, doi:10.1175/2008JCLI2752.1.

Stedinger, J. R., et al. (1993). Frequency analysis of extreme events. In *Handbook of hydrology* (pp. 18.1-18.66). McGraw Hill.

Stein, A. F., Draxler, R. R., Rolph, G. D., Stunder, B. J. B., Cohen, M. D., & Ngan, F. (2015). NOAA's HYSPLIT atmospheric transport and dispersion modeling system. *Bulletin of the American Meteorological Society*, *96*(12), 2059–2077, doi:10.1175/BAMS-D-14-00110.1.

Stohl, A. (1998). Computation, accuracy and applications of trajectories—A review and bibliography. *Atmospheric Environment*, *32*(6), 947–966, doi:10.1016/S1352-2310(97)00457-3.

Stokes, M.A. & Smiley, T.L. (1968). *An Introduction to Tree-Ring Dating*. University of Chicago Press.

Strong, M., Sharp, Z. D., & Gutzler, D. S. (2007). Diagnosing moisture transport using D/H ratios of water vapor. *Geophysical Research Letters*, *34*(3), doi:10.1029/2006GL028307.

Su, L., Yuan, Z., Fung, J. C. H., & Lau, A. K. H. (2015). A comparison of HYSPLIT backward trajectories generated from two GDAS datasets. *Science of The Total Environment*, *506–507*, 527–537, doi:10.1016/j.scitotenv.2014.11.072.

Szejner, P., Wright, W. E., Babst, F., Belmecheri, S., Trouet, V., Leavitt, S. W., Ehleringer, J. R., & Monson, R. K. (2016). Latitudinal gradients in tree ring stable carbon and oxygen isotopes reveal differential climate influences of the North American Monsoon System. *Journal of Geophysical Research: Biogeosciences*, *121*(7), 1978–1991, doi:10.1002/2016JG003460.

Szymczak, S., Barth, J., Bendix, J., Huneau, F., Garel, E., Häusser, M., Juhlke, T., Knerr, I., Santoni, S., Mayr, C., Trachte, K., van Geldern, R., & Bräuning, A. (2020). First indications of seasonal and spatial variations of water sources in pine trees along an elevation gradient in a Mediterranean ecosystem derived from $\delta^{18}O$. *Chemical Geology*, *549*, 119695, doi:10.1016/j.chemgeo.2020.119695.

Tang, K., & Feng, X. (2001). The effect of soil hydrology on the oxygen and hydrogen isotopic compositions of plants' source water. *Earth and Planetary Science Letters*, *185*(3–4), 355–367, doi:10.1016/S0012-821X(00)00385-X.

Tindall, J. C., Valdes, P. J., & Sime, L. C. (2009). Stable water isotopes in HadCM3: Isotopic signature of El Niño–Southern Oscillation and the tropical amount effect. *Journal of Geophysical Research*, *114*(D4), D04111, doi:10.1029/2008JD010825.

Tohver, I. M., Hamlet, A. F., & Lee, S.-Y. (2014). Impacts of 21st-century climate change on hydrologic extremes in the Pacific Northwest region of North America. *JAWRA Journal of the American Water Resources Association*, *50*(6), 1461–1476, doi:10.1111/jawr.12199.

Torbenson, M. C. A., Stahle, D. W., Villanueva Díaz, J., Cook, E. R., & Griffin, D. (2016). The relationship between earlywood and latewood ring-growth across North America. *Tree-Ring Research*, *72*(2), 53–66, doi:10.3959/1536-1098-72.02.53.

Treydte, K. S., Schleser, G. H., Helle, G., Frank, D. C., Winiger, M., Haug, G. H., & Esper, J. (2006). The twentieth century was the wettest period in northern Pakistan over the past millennium. *Nature*, *440*(7088), 1179–1182, doi:10.1038/nature04743.

Treydte, K., Frank, D., Esper, J., Andreu, L., Bednarz, Z., Berninger, F., Boettger, T., D'Alessandro, C. M., Etien, N., Filot, M., Grabner, M., Guillemin, M. T., Gutierrez, E., Haupt, M., Helle, G., Hilasvuori, E., Jungner, H., Kalela-Brundin, M., Krapiec, M., … Schleser, G. H. (2007). Signal strength and climate calibration of a European tree-ring isotope network. *Geophysical Research Letters*, *34*(24), L24302, doi:10.1029/2007GL031106.

Trouet, V., & Taylor, A. H. (2010). Multi-century variability in the Pacific North American circulation pattern reconstructed from tree rings. *Climate Dynamics*, *35*(6), 953–963, doi:10.1007/s00382-009-0605-9.

Turner, S. W. D., Voisin, N., Fazio, J., Hua, D., & Jourabchi, M. (2019). Compound climate events transform electrical power shortfall risk in the Pacific Northwest. *Nature Communications*, *10*(1), 8, doi:10.1038/s41467-018-07894-4.

U.S. Energy Information Administration. (2021). *Mixed water supply conditions expected to affect hydropower outlook in Pacific Northwest*. <https://www.eia.gov/todayinenergy/detail.php?id=47456>

United States Census Bureau. (2019). *American Housing Survey (AHS)*. <https://www.census.gov/programs-surveys/ahs.html>

United States Department of Agriculture. (2018). *Palouse Conservation Field Station*. <https://www.ars.usda.gov/pacific-west-area/pullman-wa/northwest-sustainable-agroecosystems-research/docs/palouse-conservation-field-station/>

Vachon, R. W., Welker, J. M., White, J. W. C., & Vaughn, B. H. (2010a). Moisture source temperatures and precipitation $\delta^{18}O$-temperature relationships across the United States. *Water Resources Research*, *46*(7), doi:10.1029/2009WR008558.

Vachon, R. W., Welker, J. M., White, J. W. C., & Vaughn, B. H. (2010b). Monthly precipitation isoscapes ($\delta^{18}O$) of the United States: Connections with surface temperatures, moisture source conditions, and air mass trajectories. *Journal of Geophysical Research*, *115*(D21), doi:10.1029/2010JD014105.

Vaz de Oliveira, A. C., & da Silva Lima, A. (2010). Spatial variability in the stable isotopes of modern precipitation in the northwest of Iberia. *Isotopes in Environmental and Health Studies*, *46*(1), 13–26, doi:10.1080/10256010903388154.

Vieira, J., Campelo, F., & Nabais, C. (2010). Intra-annual density fluctuations of *Pinus pinaster* are a record of climatic changes in the western Mediterranean region. *Canadian Journal of Forest Research*, *40*(8), 1567–1575, doi:10.1139/X10-096.

Voelker, S. L., Brooks, J. R., Meinzer, F. C., Roden, J., Pazdur, A., Pawelczyk, S., Hartsough, P., Snyder, K., Plavcová, L., & Šantrůček, J. (2014). Reconstructing relative humidity from plant $\delta^{18}O$ and δD as deuterium deviations from the global meteoric water line. *Ecological Applications*, *24*(5), 960–975, doi:10.1890/13-0988.1.

Voelker, S. L., Wang, S.-Y. S., Dawson, T. E., Roden, J. S., Still, C. J., Longstaffe, F. J., & Ayalon, A. (2019). Tree-ring isotopes adjacent to Lake Superior reveal cold winter anomalies for the Great Lakes region of North America. *Scientific Reports*, *9*(1), 4412, doi:10.1038/s41598-019-40907-w.

Wallace, J. M., & Gutzler, D. S. (1981). Teleconnections in the geopotential height field during the Northern Hemisphere winter. *Monthly Weather Review*, *109*(4), 784–812, doi:10.1175/1520-0493(1981)109<0784:TITGHF>2.0.CO;2.

Wang, F., Chen, D. S., Cheng, S. Y., Li, J. B., Li, M. J., & Ren, Z. H. (2010). Identification of regional atmospheric PM10 transport pathways using HYSPLIT, MM5-CMAQ and synoptic pressure pattern analysis. *Environmental Modelling & Software*, *25*(8), 927–934, doi:10.1016/j.envsoft.2010.02.004.

Warner, M. D., Mass, C. F., & Salathé, E. P. (2015). Changes in winter atmospheric rivers along the North American West Coast in CMIP5 climate models. *Journal of Hydrometeorology*, *16*(1), 118–128, doi:10.1175/JHM-D-14-0080.1.

Warren, J. M., Meinzer, F. C., Brooks, J. R., & Domec, J. C. (2005). Vertical stratification of soil water storage and release dynamics in Pacific Northwest coniferous forests. *Agricultural and Forest Meteorology*, *130*(1–2), 39–58, doi:10.1016/j.agrformet.2005.01.004.

Watson, E. & Luckman, B.H. (2001). Dendroclimatic reconstruction of precipitation for sites in the southern Canadian Rockies. *Holocene*, *11*(2), 203–213.

Watson, E., & Luckman, B. H. (2002). The dendroclimatic signal in Douglas-fir and ponderosa pine tree-ring chronologies from the southern Canadian Cordillera. *Canadian Journal of Forest Research*, *32*, 1858–1874.

Welker, J. M. (2000). Isotopic ($\delta^{18}O$) characteristics of weekly precipitation collected across the USA: An initial analysis with application to water source studies. *Hydrological Processes*, *14*(8), 1449–1464, doi:10.1002/1099-1085(20000615)14:8<1449::AID-HYP993>3.0.CO;2-7.

Wernicke, J., Hochreuther, P., Grießinger, J., Zhu, H., Wang, L., & Bräuning, A. (2017). Multi-century humidity reconstructions from the southeastern Tibetan Plateau inferred from tree-ring $\delta^{18}O$. *Global and Planetary Change*, *149*, 26–35, doi:10.1016/j.gloplacha.2016.12.013.

Wershaw, R.L., Friedman, I., Heller, S.J., & Frank, P.A. (1966). Hydrogen isotopic fractionation of water passing through trees. In *Advances in Organic Geochemistry* (pp. 55–67).

Wigley, T. M. L., Briffa, K. R., & Jones, P. D. (1984). On the average value of correlated time series, with applications in dendroclimatology and hydrometeorology. *Journal of Applied Meteorology and Climatology*, *23*(2), 201–213, doi:10.1175/1520-0450(1984)023<0201:OTAVOC>2.0.CO;2.

Winnick, M. J., Chamberlain, C. P., Caves, J. K., & Welker, J. M. (2014). Quantifying the isotopic 'continental effect.' *Earth and Planetary Science Letters*, *406*, 123–133, doi:10.1016/j.epsl.2014.09.005.

Wise, E. K. (2021). Sub-seasonal tree-ring reconstructions for more comprehensive climate records in U.S. West Coast watersheds. *Geophysical Research Letters*, *48*(2), doi:10.1029/2020GL091598.

Wise, E. K., Wrzesien, M. L., Dannenberg, M. P., & McGinnis, D. L. (2015). Cool-season precipitation patterns associated with teleconnection interactions in the United States. *Journal of Applied Meteorology and Climatology*, *54*(2), 494–505, doi:10.1175/JAMC-D-14-0040.1.

Xu, C., Zheng, H., Nakatsuka, T., & Sano, M. (2013). Oxygen isotope signatures preserved in tree ring cellulose as a proxy for April-September precipitation in Fujian, the subtropical region of southeast China. *Journal of Geophysical Research: Atmospheres*, *118*(23), 12,805-12,815, doi:10.1002/2013JD019803.

Yapp, C. J., & Epstein, S. (1982). A reexamination of cellulose carbon-bound hydrogen δD measurements and some factors affecting plant-water D/H relationships. *Geochimica et Cosmochimica Acta*, *46*(6), 955–965, doi:10.1016/0016-7037(82)90051-5.

Yerramilli, A., Dodla, V. B. R., Challa, V. S., Myles, L., Pendergrass, W. R., Vogel, C. A., Dasari, H. P., Tuluri, F., Baham, J. M., Hughes, R. L., Patrick, C., Young, J. H., Swanier, S. J., & Hardy, M. G. (2012). An integrated WRF/HYSPLIT modeling approach for the assessment of PM2.5 source regions over the Mississippi Gulf Coast region. *Air Quality, Atmosphere & Health*, *5*(4), 401–412, doi:10.1007/s11869-010-0132-1.

Young, G. H. F., Loader, N. J., McCarroll, D., Bale, R. J., Demmler, J. C., Miles, D., Nayling, N. T., Rinne, K. T., Robertson, I., Watts, C., & Whitney, M. (2015). Oxygen stable isotope ratios from British oak tree-rings provide a strong and consistent record of past changes in summer rainfall. *Climate Dynamics*, *45*(11–12), 3609–3622, doi:10.1007/s00382-015-2559-4.

Young, G. H. F., McCarroll, D., Loader, N. J., & Kirchhefer, A. J. (2010). A 500-year record of summer near-ground solar radiation from tree-ring stable carbon isotopes. *The Holocene*, *20*(3), 315–324, doi:10.1177/0959683609351902.

Zang, C., & Biondi, F. (2015). treeclim: An R package for the numerical calibration of proxy-climate relationships. *Ecography*, *38*(4), 431–436, doi:10.1111/ecog.01335.

Zhang, F., Biederman, J. A., Dannenberg, M. P., Yan, D., Reed, S. C., & Smith, W. K. (2021). Five decades of observed daily precipitation reveal longer and more variable drought events across much of the western United States. *Geophysical Research Letters*, *48*(7), doi:10.1029/2020GL092293.

Zhang, X.-P., Liu, J.-M., Wang, X.-Y., Nakawo, M., Xie, Z.-C., Zhang, J.-M., & Zhang, X.-Z. (2010). Climatological significance of stable isotopes in precipitation over south-west China. *International Journal of Climatology*, *30*(14), 2229–2239, doi:10.1002/joc.2037.

Zhu, H., Huang, R., Asad, F., Liang, E., Bräuning, A., Zhang, X., Dawadi, B., Man, W., & Grießinger, J. (2021). Unexpected climate variability inferred from a 380-year tree-ring earlywood oxygen isotope record in the Karakoram, Northern Pakistan. *Climate Dynamics*, *57*(3–4), 701–715, doi:10.1007/s00382-021-05736-6.

Ziaco, E., Miley, N., & Biondi, F. (2020). Reconstruction of seasonal and water-year precipitation anomalies from tree-ring records of the southwestern United States. *Palaeogeography, Palaeoclimatology, Palaeoecology*, *547*, 109689, doi:10.1016/j.palaeo.2020.109689.